Thesis submitted as partial fulfilment of the requirements for the degree of

Doctor of Philosophy at University College London

Acoustic and X-ray Characterisation of Lithium-Ion Battery Failure

Martin Pham

Electrochemical Innovation Lab,

Department of Chemical Engineering,

University College London

2023

Declaration

I, Martin T.M. Pham confirm that the work presented in this thesis is my own. Where information has been derived from other sources, I confirm that this has been indicated in the thesis.

_____

Signature

_____

Date

Acknowledgements

First and foremost, I would like to express my gratitude for the thorough guidance, incredible steadfast support and unique opportunities offered to me by Paul Shearing since the email I sent him regarding battery research. I would also like to express my appreciation for Dan Brett for his support as a personal tutor since my first day as an undergraduate, for his engaging and lively talk during his lecture which presented the prospect of research within the EIL. Both Paul and Dan have been instrumental with excellent resources, facilities and making the EIL an amazing environment which makes this research possible.

Furthermore, I would like to thank Gareth Hinds from the National Physical Laboratory who played a fundamental role in the funding which made this opportunity possible as well as his advice, guidance, support and welcoming supervisory role.

After my first half a day in the office, I was introduced to Donal ‘Little Eric’ Finegan and Tom Heenan, who both have been fantastic in their counsel which has defined my research during our drives to synchrotron facilities in a conspicuous white van. I would like to thank them both for their instrumental influence, the hysterical memories from these beamtimes and the countless future advice they have imparted, least of all the ‘Finegan manoeuvre’ – not for the faint hearted!

During the collaborative work conducted and presented in this thesis, there were the enormous presence of two significant people; Eric Darcy and Jacob Darst. I would like to express great thanks to both especially during my research trips to the Johnson Space Centre, where they both welcomed, immersed and involved me in fascinating and highly impactful projects, some of which are detailed in this thesis. I would like to also give further thanks to Eric, for his constant guidance during my time at NASA where he provided unique and unparalleled insights, especially of a ‘Union Llama’. I’d like to express further appreciation to Jacob for his thoughtfulness, honesty, philosophical discussions! I’d like to thank Zoran Bilc separately for his candour, help, humour, kindness and welcoming nature during

my time in Houston. Those who know Zoran, know that he creates an unmatched and lively atmosphere in every room he is in.

The unique environment and culture which Dan and Paul cultivate and those in the EIL produce has been immense in contributing to the work in this thesis, especially with the more senior researchers who have been very approachable and generous with their time as I started my research. Francesco Iacoviello and Xueken Lu, I would like to thank both very much for the countless times they have lent their wealth of knowledge on CT systems as well as their chats. James Robinson, Rhodri Owen and Julia Weaving for their approachability on anything acoustic and battery related, their guidance and critical insights have been extremely helpful. I also thank Toby Neville, for his attitude and role as a co-conspirator to ensure research is possible within the lab. Finally, as a whole, the entire EIL group who have been wonderful to work with, enjoyable to celebrate many a “Christmas Party” with and amenable to jager.

Finally, an understated appreciation of the continual support from my family. Words can’t begin to describe the memories and bonds I’ve made with my family I’ve made during the research, so as I’ve learnt during my thesis regarding characterisation, a picture is far more insightful than any words, so thankfully I have a collage which I’m happy to share! Zahra Rana, Alice Llewellyn, Keenan Smith, Emanuele Magliocca, Harry Michael, Michael Johnson, Chun Tan, Thomas Heenan, Jacob Darst who all I consider family, thank you!

Abstract

Lithium-ion batteries have become synonymous with modern consumer electronics and potentially, are the cornerstone to development of integrated electrified infrastructure that can support a clean and renewable national energy grid. Despite the widespread applications due to the favourable performance parameters, recent events have elevated the safety concerns associated with lithium-ion batteries. However, there is great difficulty in rapid diagnostic analysis outside specialised laboratories which can hinder the review of functional safety- and novel energy dense- materials for lithium-ion energy storage.

The dynamic evolution of internal architectures and novel active materials across multiple length scales are investigated in this thesis; with *in-situ* and *operando* acoustic spectroscopy (AS) via ultrasonic time of flight (ToF) probing, high speed synchrotron X-ray imaging, computed tomography and fractional thermal runaway calorimetry. The identification of characteristic precursor events such as gas-induced delamination in degradation mechanisms before eventual failure by AS; is correlated with X-ray imaging and post-mortem computed tomography (CT), highlighting the potential for battery management systems. Mitigation and prevention of failure with plasticized current collectors and thermally stable cellulose separators was also investigated at multiple length scales, with the transient mechanical structure compared with their commercial counterparts in cylindrical cells. Further work investigating the robustness of acoustic spectroscopy and polymer current collectors were applied to pure silicon nanowire negative electrodes.

The studies reported in this thesis assess novel materials in lithium-ion batteries, and the potential impact of the work is highlighted. Development of AS via ToF probing offers another unique and field deployable insight allowing more complete and comprehensive understanding of batteries as they continue to evolve in complexity. Lithium-ion failure characterisation techniques and literature have evolved and provided insights into the function of polymer current collectors in different cell formats and chemistries. Findings presented in this thesis are anticipated to augment future inherently safer battery design and characterisation of lithium-ion energy storage thermal runaway.

Publications

Primary Publications

1. Pham MTM, Darst JJ, Finegan DP, Robinson JB, Heenan TMM, Kok MDR, Iacoviello F, Owen R, Walker WQ, Magdysyuk OV, Connolley T, Darcy ED, Hinds G, Brett DJL, Shearing PR. ***Correlative acoustic time-of-flight spectroscopy and X-ray imaging to investigate gas-induced delamination in lithium-ion pouch cells during thermal runaway.*** J Power Sources. 2020; 470:228039. doi:10.1016/j.jpowsour.2020.228039.

2. Pham MTM, Darst JJ, Walker WQ, Heenan TMM, Patel D, Iacoviello F, Rack A, Olbinado MP, Hinds G, Brett DJL, Darcy ED, Finegan DP, Shearing PR. ***Prevention of lithium-ion battery thermal runaway using polymer-substrate current collectors.*** Cell Reports Phys Sci. 2021. doi:10.1016/j.xcrp.2021.100360.

Secondary Publications

1. Kok MDR, Robinson JB, Weaving JS, Jnawali A, Pham MTM, Iacoviello F, Brett DJL, Shearing PR. ***Virtual unrolling of spirally-wound lithium-ion cells for correlative degradation studies and predictive fault detection.*** Sustain Energy Fuels. 2019. doi:10.1039/c9se00500e.

2. Amietszajew T, Fleming J, Roberts AJ, Widanalage DW, Greenwood D, Kok MDR, Pham MTM, Brett DJL, Shearing PR, Bhagat R. ***Hybrid Thermo-Electrochemical In Situ***

Instrumentation for Lithium-Ion Energy Storage. Batter Supercaps. 2019. doi:10.1002/batt.201900109.

3. Robinson JB, Pham M, Kok MDR, Heenan TMM, Brett DJL, Shearing PR. ***Examining the Cycling Behaviour of Li-Ion Batteries Using Ultrasonic Time-of-Flight Measurements.*** J Power Sources. 2019; 444. doi:10.1016/j.jpowsour.2019.227318.

4. Maier M, Owen RE, Pham MTM, Dodwell J, Majasan J, Robinson JB, Hinds G, Shearing PR, Brett DJL. ***Acoustic time-of-flight imaging of polymer electrolyte membrane water electrolysers to probe internal structure and flow characteristics.*** Int J Hydrogen Energy. 2021. doi:10.1016/j.ijhydene.2021.01.077.

5. Majasan JO, Robinson JB, Owen RE, Maier M, Radhakrishnan ANP, Pham MTM, Tranter TG, Zhang Y, Shearing PR, Brett DJL. ***Recent advances in acoustic diagnostics for electrochemical power systems.*** JPhys Energy. 2021. doi:10.1088/2515-7655/abfb4a.

6. Radhakrishnan ANP., Buckwell M, Pham, MTM, Finegan, DP, Rack A, Hinds G, Brett DJL, Shearing PR. ***Quantitative spatiotemporal mapping of thermal runaway propagation rates in lithium-ion cells using cross-correlated Gabor filtering.*** ChemRxiv. 2021. doi:10.26434/chemrxiv-2021-jpp7l.

7. Sharp M, Darst JJ, Hughes P, Billman J, Pham MTM, Petrushenko D, Heenan TMM, Jervis R, Owen R, Patel D, Du W, Michael H, Rack A, Magdysyuk OV, Connolley T, Brett DJL, Hinds G, Keyser M, Darcy ED, Shearing PR, Walker WQ, Finegan DP. ***Thermal Runaway of Li-Ion Cells: How Internal Dynamics, Mass Ejection, and Heat Vary with Cell Geometry and Abuse Type.*** J Electrochem Soc. 2022. doi:10.1149/1945-7111/ac4fef.

8. Walker WQ, Cooper K, Hughes P, Doemling I, Akhnoukh M, Taylor S, Darst JJ, Billman J, Sharp M, Petrushenko D, Owen R, Pham MTM, Heenan TMM, Rack A, Magdysyuk OV, Connolley T, Brett DJL, Shearing PR, Finegan DP, Darcy ED. ***The effect of cell geometry and***

trigger method on the risks associated with thermal runaway of lithium-ion batteries. J Power Sources. 2022. doi:10.1016/j.jpowsour.2021.230645.

9. Owen RE, Robinson JB, Weaving JS, Pham MTM, Tranter TG, Neville TP, Billson D, Braglia M, Stocker R, Tidblad AA, Shearing PR, Brett DJL. ***Operando Ultrasonic Monitoring of Lithium-Ion Battery Temperature and Behaviour at Different Cycling Rates and under Drive Cycle Conditions.*** 2022:1-35. doi:10.31224/2130.

Conferences Attended, Talks Given:

- March 2019 STFC Early Career Researchers Conference, Abingdon, UK. Presentation Title: ***Acoustic Time-of-Flight and X-ray Imaging: Probing the internal phenomena of lithium-ion batteries***

- May – June 2022 241st ECS Meeting, Vancouver, Canada. Presentation Title: ***Prevention, Mitigation and Correlative Acoustic Spectroscopy of Lithium-Ion Battery Thermal Runaway***

Table of Contents

List of Abbreviations

Symbol	Definition
ΔG^o	Gibbs Free Energy Change [kJ]
F	Faraday Constant [96485 C·mol^{-1}]
E^o	Standard Electromotive Force [V]
q	Capacity [Ah]
M	Number of electrons involved in the electrochemical reaction
k	Rate constant
A	Pre-exponential factor
E_q	Activation energy and orientation [J·mol^{-1}]
R	Universal Gas Constant [J·mol^{-1}·K^{-1}]
T	Absolute Temperature [K]
B	Brilliance [p.p.s. ·mm^{-2}·mrad^{-2}]
μ	Linear Attenuation Coefficient
I_0	Incident Beam Intensity [W·m^{-2}]
I	Expected Beam Intensity [W·m^{-2}]
η	Distance through a material [m]
ρ	Density [kg·m^{-3}]
N_A	Avogadro's Constant [6.022 ×10^{23} mol^{-1}]
m_A	Atomic Molar Mass [kg·mol$^{—1}$]
σ_{tot}	Total Photon Atomic Cross Section [m^2]
σ_{el}	Elastic Scattering Cross Section [m^2]
σ_{comp}	Inelastic Compton Scattering Cross Section [m^2]
σ_{pe}	Photoelectric Cross Section [m^2]
N_{proj}	Minimum Number of Projections
$\Delta\theta$	Angular Increments Between Projections
b_{vox}	Voxel Size
U_a	Accelerating Voltage [V]

c	Speed of sound [$m \cdot s^{-1}$]
E	Elastic Modulus [Pa]
ΔZ	Acoustic Impedance
Q	Quantity of heat [J]
m_i	Mass of species, i [kg]
$C_{p,i}$	Specific heat capacity of species, I [$J \cdot K^{-1} \cdot kg^{-1}$]
ΔT_i	Change in absolute temperature of species, i

Abbreviations	Definition
Al CC	Aluminium (Commercial) Current Collector
Al PCC	Aluminium Polymer Current Collector
Al + Cu PCC	Aluminium and Copper Polymer Current Collector
ARC	Accelerating Rate Calorimetry
AU	Arbitrary Units
AS	Acoustic Spectroscopy
BMS	Battery Management Systems
CC	Current Collector
CMC	Carboxymethyl cellulose
CMOS	Complementary Metal-Oxide Semiconductors
CT	Computed Tomography
Cu CC	Copper (Commercial) Current Collector
Cu PCC	Copper Polymer Current Collector
DLS	Diamond Light Source
DoD	Depth of Discharge
EDX	Energy Dispersive X-ray Spectroscopy
EIS	Electrochemical Impedance Spectroscopy
ESRF	European Synchrotron Radiation Facility
ESTA	Energy Storage Test Area
EVs	Electric Vehicles
FBP	Filtered Back Projection
FDK	Feldkamp-David-Kress
FOV	Field of View
FTRC	Fractional Thermal Runaway Calorimetry
HEVs	Hybrid Electric Vehicles
IEA	International Energy Agency
ISC	Internal Short Circuit
ISCD	Internal Short Circuit Device
JSC	Johnson Space Centre
LCO	Lithium Cobalt Oxide
LIBs	Lithium-Ion Batteries

LFP	Lithium Iron Phosphate
LMO	Lithium Manganese Oxide
LTO	Lithium Titanate
NASA	National Aeronautics Space Administration
NESC	NASA Engineering and Safety Centre
NCA	Nickel Cobalt Aluminium Oxide
NMC	Nickel Manganese Cobalt
OCV	Open Circuit Voltage
PCC(s)	Polymer Current Collector(s)
PE	Polyethylene
PP	Polypropylene
PTFE	Polytetrafluoroethylene / Teflon
PVDF	Polyvinylidene Fluoride
SEI	Solid Electrolyte Interface
SEM	Scanning Electron Microscopy
Si-NW	Silicon Nanowires
SOC	State of Charge
SOH	State of Health
TEM	Transmission Electron Microscopy
ToF	Time of Flight
TR	Thermal Runaway
TSS	Thermally Stable Separator
XRM	X-ray Microscopy

List of Tables

List of Figures

1 Introduction

1.1 The Importance of Lithium Ion Batteries

Lithium-ion energy storage has been the fundamental energy storage technology of modern consumer electronics, moreover, they hold an increasing influence in the transportation sector with legislative change and modern perspectives on electric vehicles (EVs) in decarbonisation of global energy consumption. The trend of electricity generation through renewable energy sources and technologies has increased to over 27% [1–3] globally, with projections to see this increase substantially since the recent COP-26 climate agreement to accomplish target reductions in greenhouse gas emissions. Proposals for further integration of the renewable energy sources and a smart grid network [4–9] have been made to reduce the climate impact of electricity generation through fossil fuels. These prospective decarbonisation strategies would be highly influential in reducing the emissions from the energy utilisation in agriculture, industry, transport and energy sectors, therefore their reliance on finite fossil fuel resources and their volatile prices.

For these objectives to be realized, the challenges posed by the mismatch of supply and demand through these inherently intermittent renewable energy sources could be mitigated with grid scale electric storage with lithium-ion batteries. Lithium-ion batteries have demonstrated the ability to immediately respond to energy consumption demands with long cycle life, high energy efficiency, high energy- and power- densities and ease of modularization for installation. Thus, this highlights the importance of lithium-ion batteries to integrate current renewable energy sources and technologies to achieve a sustainable, low- or non- pollution emissive energy future. However, to achieve such targets and infrastructural change to electrochemical energy storage, will require further legislative changes to implement, coupled with significant investments in lithium-ion and renewable energy sources technologies.

1.2 Thesis Overview

The ubiquitous applications of lithium-ion technology stems from their versatile performance parameters, which has seen continuous advancements; which is reflected in the broad uptake in aerospace, consumer electronics, electric vehicles, military and space uses [10–12]. However, the environmental and operational demands imposed upon lithium-ion batteries has seen well-reported high profile failures from a range of these applications [13–15]. Moreover, increasingly energy and power dense lithium-ion energy storage for EVs, and greater functionality electronics, escalate the risks associated with battery failure. Thus, there is an impetus for improvements in battery safety to prevent and mitigate these potentially severe consequences.

Typically the length- and time- scales for which nucleation of these failure occur presents difficulties in characterising and understanding the complex mechanical and thermal evolution within the cell. The work presented in this thesis aims to explore and target the sequence of events leading to thermal runaway, through understanding of the complex internal phenomena through fractional thermal runaway calorimetry (FTRC), X-ray radiography, CT and the development of AS as a low-cost field-deployable robust rapid diagnostics technique in battery safety evaluation. These characterisation techniques present unique insights into the structural and thermal evolution preceding widespread thermal runaway, which facilitates the linking of these observations to the extent of cell degradation and failure.

After this thesis introduction, Chapter 1 is concluded with a contextual outline on how lithium-ion batteries operate, the descriptors of performances which are usually referred to in comparison of lithium-ion batteries, then, an introduction into degradation and thermal runaway of lithium-ion batteries.

Chapter 2, describes the literature survey of relevant lithium-ion components and their influence on battery safety and failure. As understanding of the influence of these components and their contribution to the sequences of event that can occur during thermal runaway is fundamental to explaining the mechanisms by which components with additional safety functionality are impacting the mitigation and prevention of failure.

Subsequently, the fundamental principles and methodology of the characterisation techniques used in this thesis will be discussed in Chapter 3, including discussion of the information presented by high-speed X-ray radiography at synchrotron facilities, laboratory-based CT to linking internal structural changes during failure to thermal output measured by FTRC. The mechanisms of acoustic spectroscopy is described via fundamental scientific principles and the potential for correlative analysis with X-ray radiography and thermal data is articulated.

The results section consists of four main chapters; the first of which (Chapter 4) is split into two parts, the first part examines the use of laboratory X-ray radiography and AS to identify gas generation and electrode delamination in a lithium-ion pouch cell during routine cycling due to manufacturing defects. The second part of this chapter builds upon the characteristic acoustic signals observed with these architectural changes and investigates lithium-ion battery failure with correlative high-speed synchrotron radiography and AS.

Chapter 5 examines the prevention of thermal runaway through the implementation of a metal-coated polymer current collector (PCC), which are designed to disconnect internal short circuits by withdrawing from the heating region during nail penetration experiments. In these experiments, commercial 18650-geometry cells and their PCC counterparts are nail penetrated at 100% state of charge and in all instances with the Al PCC, prevention of failure was observed and cells retained voltage above 4.00 V. High speed synchrotron X-ray radiography of 18650-cells during nail penetration testing, in tandem with pre- and post- mortem X-ray CT, provides insights into the function of the novel current collectors which are compared with their commercial counterparts.

Chapter 6 investigates the mitigation of thermal runaway with thermal and electrical abuse techniques with PCC and a thermally stable separator (TSS). These materials are tested individually and in tandem to evaluate the effectiveness of these materials in reducing the total heat output during failure through FTRC. Cells with the PCCs and with both PCCs and TSS components, exhibited a 19.6% and 41.4% reduction in total energy released during failure compared to their industry standard counterparts. A respective reduction of 24.7% and 30.3% in thermal output was also measured during internal short circuit originated failure.

Chapter 7 is the final results chapter, where the microstructure and thermal runaway of a pure silicon nano-wire electrode microstructure is explored in a commercial lithium-ion pouch cell format.

Si technology is widely believed to be amongst the most promising next generation anode technologies, and these safety investigations will contribute to their deployment. Si cells with PCC counterparts are also investigated with AS and high-speed synchrotron X-ray radiography.

Chapter 8 concludes with a summary of the results presented in this thesis and a description of ongoing and potential future work which can be derived from the findings here, such as the investigations into other components with additional safety functionality such as a thermally stable polymer current collector and expanding the scope and robustness of AS to cylindrical cell formats and further degradation types to enhance lithium-ion characterisation.

1.3 Lithium-Ion Batteries: How Does a Cell Work?

A lithium-ion cell is an electrochemical energy storage device, where the fundamental principles of storing chemical potential energy is governed by electrochemistry, a branch of chemistry which dictates the relationship between chemical and electrical phenomena. Put simply, batteries are energy storage devices which convert electrical energy received via charging to store as chemical energy during charge.

Charging is achieved by reversing the cell's electrochemical equilibrium reaction through reduction and oxidation reactions at the electrodes within the cell. These reactions are reviewed in further depth in Chapter 2. This causes transport of lithium-ions from the positive electrode to the negative electrode to store the energy for later discharge. This chemical energy is then converted to electrical energy during use, whereby, the reverse reactions of the charging process occurs.

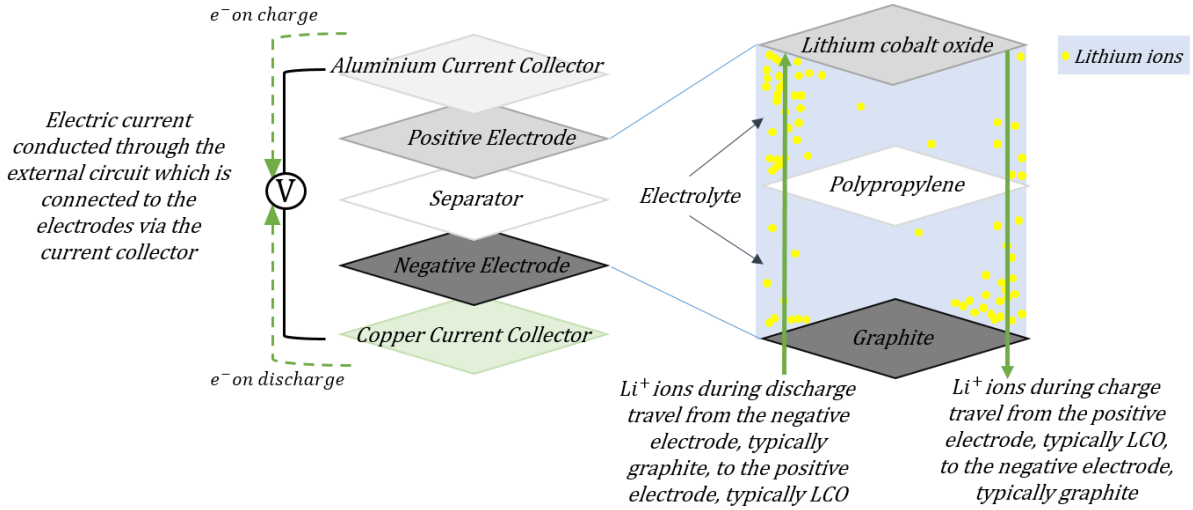

Figure 1-1: A simplified illustration of the components and processes of a lithium-ion battery with a lithium cobalt-oxide cathode and graphite anode.

1.4 Lithium-Ion Batteries: Why Lithium

Lithium is the third lightest element after hydrogen and helium with one of the smallest ionic radii, therefore, it is the lightest metal. It offers very favourable ionic conductivity and lightweight properties, combined with a standard electrode potential of -3.0401 V. Consequently, lithium-ion batteries are very energy dense, especially when compared to competing battery technologies. The low atomic weight and atom size also promotes a higher rate of intercalation of lithium-ions within the electrodes via the electrolyte. Lithium batteries do not suffer from the 'memory effect' as nickel-cadmium batteries may when continuous partial discharges and subsequent recharging reduces the battery capacity, thus there is no need for maintenance by individual cell deep charge and discharge cycles.

However, lithium is a highly reactive alkali metal which partakes in an exothermic reaction with water until all lithium is consumed, forming lithium hydroxide and highly flammable hydrogen gas. Thus, water must be assiduously eliminated from non-aqueous lithium-ion batteries to prevent corrosion, damage of internal components and materials and undesirable reactions. Much effort is expended to minimise the moisture content in lithium cells, including rigorously drying battery components and assembling cells in extremely low humidity environments. Lithium metal electrodes are not used due to continual 'stripping and plating' leading to dendritic formation. These can puncture through the polymer separator, therefore, there is a potential for lithium dendrites to electrically connect the anode and cathode, to cause battery short circuiting and propagation of thermal runaway to neighbouring batteries. Typically, rechargeable commercial lithium-ion batteries have lithium intercalated structures, therefore, the lithium-ions which are exchanged between electrodes.

1.5 Lithium-Ion Batteries: Background

In their early development, rechargeable lithium batteries were inundated with electrochemical instabilities. Dendritic formation and growth penetrating the separator causing catastrophic short-circuit induced thermal runaway, until Sony commercialized the first lithium-ion battery in 1991 [16]. The impact of this was revolutionary, especially in portable electronics, with the high-energy density, higher power performance and no memory effect as observed in nickel-cadmium or nickel-hydride batteries.

Table 1-1: Various rechargeable lithium metal battery electrochemical systems developed before 1991. Table reproduced from [16].

Chemistry	**Voltage (V)**	**Wh·kg^{-1}**	**Wh·L^{-1}**	**Company**
Li/TiS_2	2.1	130	280	1978 Exxon
LiAl/TiS_2				1979 Hitachi
Li/$LiAlCl_4$-SO_2/C	3.2	63	208	1981-85 Duracell
Li/V_2O_5	1.5	10	40	1989 Toshiba
Li/$NbSe_3$	2.0	95	250	1983-86 Bell Labs
LiAl/Polyaniline	3.0	-	180	1987 Bridgestone
LiAl/Polypyrolle	3.0	-	180	1989 Kanebo
Li/Al/Polyacene	3.0	-	-	1991 Kanebo/Seiko
Li/MoS_2	1.8	52	140	1987 Moli Energy
Li/CDMO(Li_xMnO_2)	3.0	-	-	1989 Sanyo
Li/$Li_{0.3}MnO_2$	3.0	50	140	1989 Tadiran
Li/VO_x	3.2	200	300	1990 Hydro-Quebec

Previously unsuccessful attempts at rechargeable lithium-based electrochemical energy storage systems are shown in Table 1-1, with a plethora of cathodes and electrolytes. The common use of lithium metal anodes resulted in failures and subsequent safety concerns, and consequently research shifted from lithium metal to lithium-intercalation anode materials. Ikeda of Sanyo first patented lithiation of graphite with non-aqueous solvents, 'Graphite/Li in non-aqueous solvents' Japan 1769661, on 18th June 1981. The use of transition metal oxides as a potential cathode was led by Goodenough, who filed his 'Transition metal oxides as cathode, $LiCoO_2$' US patent (US: 4302518, 31st March 1980) [16]. By 1985, Kuribayashi and Yoshino of Asahi Chemical Industries developed a cell which consisted of $LiCoO_2$ cathode, with an intercalation carbon anode, filing patents worldwide – Japan 1989293, 10th May 1985 [16]. The patent was the basis for Sony to begin to produce the commercial lithium-ion battery

which resembles modern rechargeable cells. Since then, means of improving the performance parameters of lithium-ion batteries have been the focus of research. The initial cylindrical cells of an 18650-format, had a capacity of 800 mAh and a fully charged voltage of 4.1 V [16]. Cells of an 18650-format are of approximately 18 mm in diameter and 65 mm in length. The early hard-carbon anode 18650-cells saw capacity rapidly improved with electrolyte additives, change to a graphite anode and subsequent doping [16].

Generally the myriad of modern lithium-ion batteries are defined by the array of lithium compounds used as the cathode. The improvements in rechargeable lithium-ion battery technology has manifested many variations in design and chemistry. Recently, as the technology has matured, manufacturing costs have decreased allowing a wide range of applications due to the versatile and robust qualities of the Li-ion battery; such as the wide operating temperature range, extended capacity retention despite complete depth of discharge, greater longevity, very high energy density, minimal maintenance, lower self-discharge and the size and weight advantages over other competing battery chemistries.

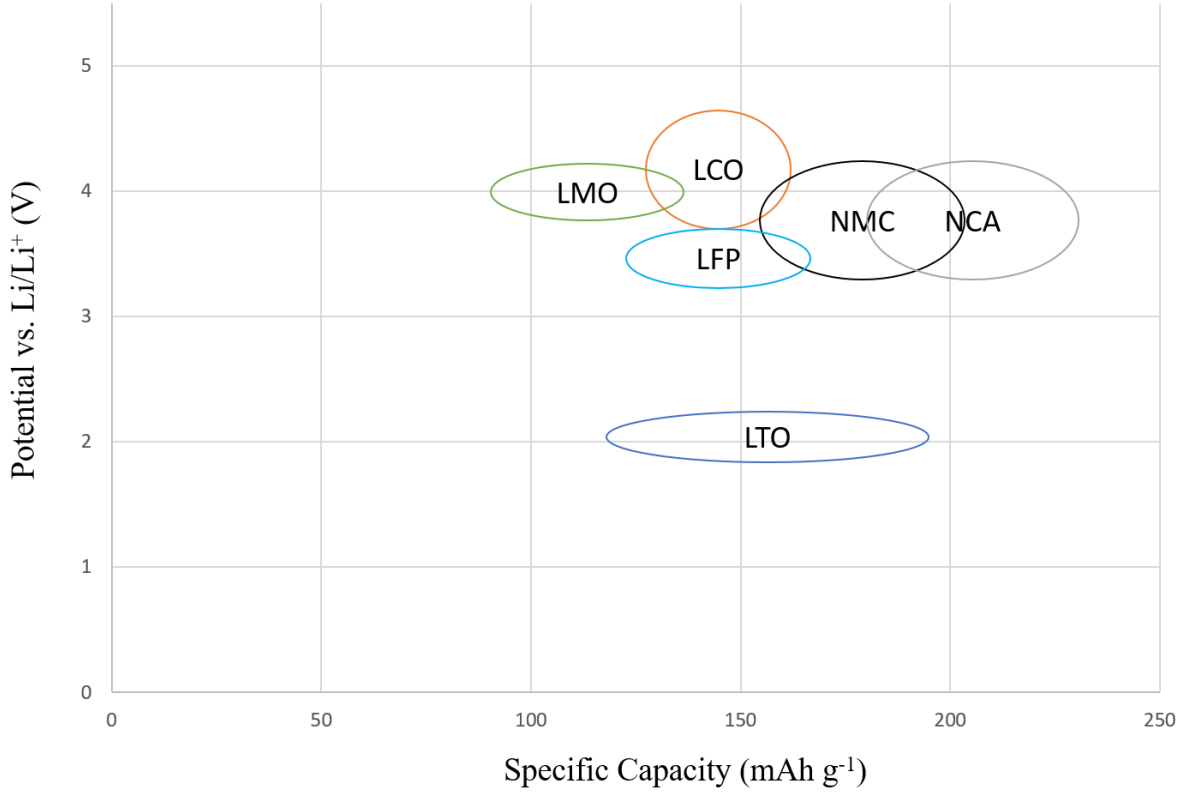

Figure 1-2: Approximate range of potentials and specific capacity some common types of cathodes are plotted for comparison. Figure reproduced with data from [17].

Although many current lithium based battery chemistries exist commercially, initially it was a lithium cobalt oxide (LCO) cathode and graphite electrode structure, which is still widely used today. Aside from LCO, lithium manganese oxide (LMO), lithium iron phosphate (LFP), lithium nickel manganese cobalt oxide (NMC) and lithium nickel cobalt aluminium oxide (NCA) dominate the commercial battery market as the cathode compounds. In stark contrast however, the graphite negative electrode in lithium-ion batteries has remained constant and almost ubiquitous.

Lithium ion cells exist in a range of architectures for different applications, these shapes can be roughly quantified into four groups, small coin cells such as those found in hearing aids and medical equipment, larger cylindrical cells such as the 18650-cells found in laptop battery packs and electric vehicles, pouch cells such as those used in mobile phones batteries and prismatic cells with large threaded terminals.

1.6 Cell Components - Introduction

All cells require three fundamental active components to function electrochemically; the electrolyte, the positive and negative electrodes. In addition to these, to prevent the electrodes from connecting electrically, separators are electrical insulators, which are placed between the electrodes, however, they are required to be ionic conductors for the transfer of lithium-ions. The positive and negative electrodes must allow lithium to insert or intercalate, which is the mechanism for lithium to move within and insert into the layered electrode structures. The electrolyte role is as an ionic transfer medium for lithium-ions while preventing electron transfer.

Typically, a commercial cell consists of a graphitic carbon negative electrode and a positive electrode; consisting of lithium and transition metal oxide compound, a range of cathodes are explored further in later in Chapter 1. These metal oxides are hugely influential in performance parameters and may also take the form of different structures. A layered oxide electrode is seen in lithium cobalt oxide cells, poly-anion structures are found in lithium iron phosphate cells or a spinel structure found in lithium manganese oxide cells. Electrolytes are non-aqueous, commonly lithium based anion complexes from salts and organic carbonates such as ethylene carbonate or diethyl carbonate. Equation 1-1 chemically defines an overall electrochemical reaction during the charge and discharge processes of a LCO chemistry:

$$Li_{1-x}CoO_2 + Li_xC \underset{charge}{\overset{discharge}{\rightleftarrows}} LiCoO_2 + C \qquad [1\text{-}1]$$

Where *x* is the fractional amount of lithium removed from the cobalt oxide layers that intercalates into the carbon electrode.

In a completely charged lithium-ion cell, lithium is intercalated into the negative graphite electrode – also described as fully lithiated graphite – and releases an electron into the external electric circuit during discharge. Simultaneously, the resultant lithium-ion is ionically conducted across the electrolyte to the positive electrode of cobalt oxide. Lithium then intercalates into the structure as shown in the electrochemical reaction previously, this is known as a galvanic process, a spontaneous electrochemical driving force and reaction to produce Faradaic current. During charging of rechargeable lithium cells, this process is reversed and this is classed as electrolytic, whereby an outside electrical source is required to drive the reverse electrochemical reaction which is non-spontaneous. The electromotive force must be greater than the cell potential for the reverse flow of electrons and lithium

transfer back and intercalation in the negative graphitic carbon electrode, this additional requirement of voltage is known as over-potential.

1.7 Lithium-Ion Batteries: Descriptors of Performance

With the plethora of applications in which batteries are involved, each circumstance will demand contrasting performance criteria, thus it is imperative that depending on the designated operating parameters, the most suitable batteries are chosen. When comparing differing cell chemistries, it is important to have defined performance parameters which can be evaluated especially when taking into consideration every characteristic to determine the appropriateness for application. Simpler specifications such as voltage and current can be achieved by a combination of cells in parallel and series, especially to ensure if one cell fails, adjacent cells in parallel will still ensure the module is functional.

Specific energy and volumetric energy density, refers to energy stored per unit mass or volume respectively (generally defined as $Wh \cdot kg^{-1}$ and $Wh \cdot L^{-1}$). Depending on the circumstances in which the cell will be operated, there are appropriate chemistries or commercial cells which can be selected which are more suited to that specification, as each tends to have particular performance characteristics. Thus, consumer electronic applications usually prefer very energy dense materials for the positive electrode, as this allows more energy to be stored per given volume or the same amount of energy but with a much more lightweight cell. Chemistries are discussed in further detail in Chapter 1.9 – Lithium Ion Batteries – Components: Positive Electrode.

Specific power or gravimetric power density is the amount of energy per second which can be exerted for applications per unit mass, $W \cdot kg^{-1}$.

Although the theoretical maximum energy associated with both electrolytic and galvanic (recharge and discharge respectively) processes is determined by the Gibbs free energy change (ΔG) of the system as defined in Equation 1-1, the practical capacity is much less.

$$\Delta G^o = -nFE^o \qquad [1\text{-}2]$$

Where n is the number of electrons per mole of product, F is the Faraday constant, 96485 $C \cdot mol^{-1}$ and E^o is the standard electromotive force, V, and can be calculated and is defined by the Nernst equation. In practice not all chemical energy stored can be converted to electrical energy as there are

losses accumulating from activation, ohmic and mass transport losses. Activation losses arise due to impeded reaction kinetics by activation energies, parasitic current losses and potentially unwanted side reactions. Ohmic losses due to ionic and internal electrical resistances are apparent in virtually all materials thus this intrinsic resistance opposing charge flow in transfer processes must also be accounted for. Thus, capacity is the total charge that the cell can deliver at the rated voltage, which is directly proportional to the amount of the limiting active electrode material in the battery. Faraday's law defines the equation for calculating the capacity for various electrode materials, which states the quantity of electrical charge, the capacity, *Q (Ah)*, is determined by the number of moles of active material, *M*, and the number of electrons involved in the electrochemical reaction, *n*:

$$Q = \frac{n \cdot F}{3600 \cdot M} \qquad [1\text{-}3]$$

The capacity retention focuses on the discharge capacity of a cell after a given number of cycles compared to that of that initial discharge capacity. Diminishing capacity over time, due to degradation of internal battery components such as cracking and deformation of electrode structures, is commonly experienced in consumer electronics. Current lithium-ion battery technology preferentially favours cell chemistries which display capacity retention for such applications, as manufacturers and consumers are conscious of longer lasting batteries which will continue to allow devices to retain full functionality and performance.

C-rates govern the charge and discharge rate of a cell with respect to the cell capacity, for example: a rating of 1 C implies the fully charged battery at 1 Ah provides 1 A current for 1 hour. The same 1 Ah capacity battery operating at 5 C should provide 5 A current for one fifth of an hour. Fast charging technology of lithium-ion batteries is critical to the commercial application of electrical vehicles, with consumer attitude to electronics also trending towards a fast charging mechanism. Traditionally low current charging is favoured to enhance lifetime to as higher charging current can possibly instigate lithium plating, resulting in accelerated degradation [18]. Furthermore, high current operation will cause both increased heat generation rate and thus raise cell temperature, another factor in accelerated battery degradation [19].

Although not strictly a performance parameter, chemical, mechanical and thermal stability as well as wider safety considerations are paramount to electrochemical cell designs which incorporate inherently safe design features. The chemistry and internal components must be able to withstand high

operating temperatures at a range of operating voltages: chemical stability is especially important to avoid degradation, unwanted additional side reactions and ensure longevity.

1.8 Lithium Ion Batteries: Components – Negative Electrode

1.8.1 Lithium Ion Batteries: Graphite and Commonly Studied Anodes

The first commercially feasible lithium-ion cell utilised disordered hard carbon as the negative electrode material but poor capacity ensued, until the adoption of graphite; since then virtually all commercial lithium-ion cells use variations of ordered graphene layers. Particles of graphitic carbon are typically less than 30 microns in diameter and profoundly influence the specific capacity, performance and electrochemical properties of a cell. Graphite has a theoretical specific capacity of 372 $mAh \cdot g^{-1}$, a maximum loading of one lithium-ion for every six carbon within graphite: LiC_6. However, in commercial reality, the observed specific capacity of graphite is ca. 300 to 350 $mAh \cdot g^{-1}$ [20] thus doping graphite with silicon or SiO_x [21], which has a theoretical specific capacity of 4200 $mAh \cdot g^{-1}$ [22], has shown greater capacity, which has been observed for example in the INR18650 MJ1 cell.

Table 1-2: Table of commonly studied anode materials in lithium-ion cells. Table adapted from [17].

Properties of some commonly studied anode materials				
Material	Lithiation Potential	Delithiation Potential	D ($cm^2 \cdot s^{-1}$)	Volume Change
Graphite [23–29]	0.07, 0.10, 0.19	0.10, 0.14, 0.23	$10^{-11} – 10^{-7}$	10%
LTO [30–34]	1.55	1.58	$10^{-12} – 10^{-11}$	0.20%
Si [35–44]	0.05, 0.21	0.31, 0.47	$10^{-13} – 10^{-11}$	ca. 300-400%
Li_2O [45] **(Amorphous)**	N/A	N/A	$5 \times 10^{-12} – 5 \times 10^{-10}$	N/A

One of the final challenges posed during the development of the first commercially viable cell was the identification of a material for the electrodes which permit intercalation to freely lithiate the structures without altering it. The negative electrode is fully intercalated with lithium at the full state of charge cell and over the lifetime, this structure is degraded via the transfer of lithium and irreversibly reduces the specific capacity of the cell. During the initial charge cycle, the formation of the solid electrolyte interphase (SEI) irreversibly reduces the capacity of the cell as the lithium reacts with the electrolyte, thus permanently depleting the maximum amount of lithium for the electrochemical reaction hence reducing capacity. Over an operating lifetime, gradual degradation of perform is expected due to the thickening of the SEI layer, dendritic growth and electrode fracturing.

1.8.2 Lithium Ion Batteries: Silicon and Silicon Nanowires (Si-NW)

The favourable theoretical specific capacity of silicon is an order of magnitude greater than that of graphite (4200 $mAh \cdot g^{-1}$ to 372 $mAh \cdot g^{-1}$), however during lithiation, silicon expands volumetrically by up to 400% (shown in Table 1-2) depending on microstructure. This is due to the highly favourable ratio of lithium-ions to silicon atoms once fully lithiated, $Li_{4.4}Si$, compared to the LiC_6 of graphite. However, in practice at room temperature, it has been observed that $Li_{3.75}Si$ is the highest lithiated phase, yielding a gravimetric capacity of 3579 $mAh \cdot g^{-1}$ [41,46–49].

In traditional, relatively rigid carbonaceous electrode structures, lithiation is the movement into and the occupation of interstitial sites. However, silicon alloys with lithium transforming from a crystalline to an amorphous phase [46]. Misra *et al*. [50] performed in-situ X-ray diffraction (XRD) studies of the lithiation mechanism in silicon nanowires to identify a metastable $Li_{15}S_4$ phase which was linked to degradation, cycling performance and the effect of Si-NW growth temperature on performance. The lithiation kinetics of silicon have been investigated by Pharr *et al.* [41], who identified differing velocities for different crystalline silicon wafer structures and developed a model to account for anisotropic morphologies and fracture patterns.

Alloying silicon electrodes undergo significant volume changes during cycling. The significant volume expansion after lithiation is well reported in literature [35–44] and induces mechanical deformations, degradation and severe capacity loss leading to battery failure by two principal mechanisms. Firstly, the continuous formation of a SEI due to the volume changes which causes separation from the bulk silicon electrode, thus the reformation of the SEI. Secondly, the volumes changes also induce cracks of the active material bulk phase, primarily the active material particles which separate from the bulk silicon phase leading to the loss of continuity of active material from the binder, conductive carbon and current collector.

Many mitigative strategies have been proposed, most prominently the influence of the morphology to alleviate this by introducing an established and stable structure with a well-defined void space for expansion. Liu *et al*. [51] previously proposed a yolk-shell design and 1D limited expansion of high performance pure silicon nanowires was proposed by Chan *et al.* [52]. The formation of the battery manufacturing company Amprius based upon this research has produced pure silicon anode lithium-ion battery based on the Si-NW morphology, as part of an effort partially funded by the US Department of Energy [53–55].

Further results by Chan *et al.* with ex-situ XRD and Transmission Electron Microscopy (TEM) have shown that the silicon nanowires structure were completely amorphous by the end of the first lithiation cycle. Shen *et al.* [56] investigated the favourable lithiation characteristics of both porous silicon nanoparticles and NWs compared with their solid counterparts by use of *in-situ* and *ex-situ* TEM. NWs produced on a current substrate with low tortuosity exhibited high rate conductivity, with high mass loading (2-3 $mg \cdot cm^{-2}$) and high first cycle efficiency [57] – performance parameters which can be adjusted with the nanowire porosity, depth of charge, discharge and maximum cell voltage. Applications thus far have been limited by the substantially higher price, therefore those applications requiring extremely high energy density to be viable such as aerospace, mission critical or military purposes [57].

1.8.3 Lithium Ion Batteries: Lithium Titanate (LTO)

The LTO chemistry replaces the graphite as the negative electrode with a spinel LTO structure. The positive electrode is generally LMO or NMC, both of which are discussed later in Chapter 1.9. LTO nano-crystal anode batteries can be rapidly charged, deliver discharge C-rates of 10 C and have reputed capacity retention over 7000 cycles. This is significantly more than competing commercial lithium-ion batteries as a result of the slight (0.2%) change in volume during cycling, thus LTO electrode are generally considered to have a zero-strain property.

Furthermore, distinguishing characteristics of the LTO electrode are the low internal resistance, the lack of SEI film formation due to the high equilibrium potential window and no lithium plating during rapid cycling at low temperatures. Hence, an operational capacity of 80% of the maximum at -30ºC. Thermal stability also at high temperatures is unmatched by competing lithium-ion battery chemistries, thus all these favourable qualities contribute to perhaps one of the naturally safest, durable and longest lasting lithium battery technologies.

Several limitations exist which have hindered widespread LTO battery applications, such as the uncompetitive specific capacity (175 $mAh \cdot g^{-1}$) [17], lower cell voltage (2.40 V typically) and the prohibitive cost of titanium required. Despite that, further research into LTO batteries has seen applications in electric powertrains for the Mitsubishi i-MiEV, the Honda Fit EV, Honda EV-neo bike and solar-powered applications. Commercially focused research will hope to improve performance parameters and exploit the high C-rate in charging and discharging. Expanding applications to electric charging stations, larger transportation powertrains such as coaches and ferries, electrical energy storage systems especially for communication, national grid and hospitals as critical backup power systems due to the reliability and durability of this battery technology.

1.9 Lithium Ion Batteries: Components – Positive Electrode

Positive electrode materials tend to be a compound of transition metal oxide or several metals in a more complex oxide due to their favourable properties, such examples being thermal stability, high-rate capabilities and high specific capacity. These preferred transition metals have high energy density and many commercial chemistries have an intercalation (insertion and extraction) mechanism during lithiation. Alloying and conversion reaction mechanisms are also commonly studied – the latter has shown promise for future energy-dense specific capacity [17]. Commonly studied intercalation lithium-ion positive electrode compounds are shown in Table 1-3.

Table 1-3: Properties of commonly studied commercial intercalation cathode compounds. Adapted from [17].

Crystal Structure	**Compound**	**Specific Capacity ($mAh \cdot g^{-1}$), theoretical/experimental/ commercial**	**Average Voltage**	**Degree of development**
Layered	NCA	279 / 199 / 200 [58]	3.7	Commercialized
	$LiCoO_2$	274 / 148 / 145 [59]	3.8	Commercialized
	NMC-111	280 / 160 / 170 [60]	3.7	Commercialized
Spinel	$LiMn_2O_4$	148 / 120 [61]	4.1	Commercialized
Olivine	$LiFePO_4$	170 / 165 [62]	3.4	Commercialized

Solid positive electrodes are typically in powder form or a porous solid structure, however, the poor electrical conductivities require an additional conductivity promoting matrix of carbon well dispersed through-out the positive electrode. Conductive carbon additives improve the electrical contact and thus transfer of electrons from the electrode particles and the current collector, hence improving the rated power potential of the cell.

Binder materials found in electrodes act as an adhesive which bonds the electrode together at the microscopic length scale, a fundamental component in cells as electrodes endure significant expansion during lithiation thus the binder acts to maintain the structural integrity of these during the

operating lifetime. Typical requirements for binder materials are the chemical stability, cohesiveness with neighbouring particles, low weight, low relative cost, wettability with the electrolyte and a degree of elasticity and robustness. Common binders are polymeric materials such as polytetrafluoroethylene (PTFE or Teflon) or polyvinylidene fluoride (PVDF).

Porous or powder-based electrodes have electrolyte imbibed throughout which maximise the interfacial surface area exposed to electrolyte and therefore greater discharging rates compared to a solid electrode surface for the same given volume. Thicker porous electrodes exhibit higher resistance that limits it maximum theoretical power output however yields greater capacity.

Electrochemical cell designers must consider the balance of energy against power when defining electrode thickness, as thicker electrodes usually mean more active electrode material in a given volume thus higher capacity. Alternatively, cells consisting of thinner electrodes have a greater proportion of current collectors and separators to active material, which can facilitate high-rate cycling capabilities without risks associated with higher temperatures, however, reduced cell capacity due to less active material. An example of this is in legacy designs of cylindrical cells, where two main architectures are the bobbin and spiral wound structures. Bobbin cells typically consist of a central cylindrical anode core with a polymer separator outer layer surrounded by a cathode. Bobbin cells are designed to optimise energy density at low power loads or intermittent operation thus thicker electrodes of electrode powder blend compressed into either a solid or hollow cylinder. Thinner porous electrodes can be found in spiral wound cells, printed onto the metallic current collectors, as applications require high power delivery, these relatively thin electrodes provide more rapid charge transport. In porous electrodes, tortuosity is an influential factor in ion transfer to the electrolyte phase, lithium mass transport can be a rate limiting step in the charge and discharge of a battery. Thicker porous structures for electrodes yield more energy storage capacity however these complex porous frameworks causes expected resistance to mass transport, thus the rate of lithium-ion transfer become increasingly important especially in power delivery.

1.9.1 Lithium-Ion Batteries: Lithium Cobalt Oxide (LCO)

Lithium cobalt oxide has historically been prevalent amongst portable electronic applications such as mobile phones, laptops and digital cameras. First introduced commercially in 1991 by Sony, the LCO positive electrode with the graphite negative electrode gained widespread acclaim and revolutionised consumer electronics. The LCO electrochemistry offers many advantages such as its recharging capabilities and performance parameters especially when the demand of the time was a greater rechargeable capacity for longer runtimes. Thus, the high voltage discharge, a theoretical specific capacity (274 $mAh \cdot g^{-1}$) [17] were highly favourable.

During discharge at the anode, lithium-ions are produced by oxidation of intercalated lithium in the graphite carbon negative electrode along with electrons:

$$LiC_6 \rightarrow xLi^+ + xe^- + C_6 \qquad [1\text{-}4]$$

At the cathode, the lithium-ions are absorbed by the lithium dioxide and the electrode is reduced by the electrons received from the circuit:

$$Li_{1-x}CoO_2 + xLi^+ + xe^- \rightarrow LiCoO_2 \qquad [1\text{-}5]$$

Thus, the overall chemical reaction for an LCO chemistry:

$$Li_{1-x}CoO_2 + Li_xC_6 \underset{charge}{\overset{discharge}{\rightleftarrows}} LiCoO_2 + C_6 \qquad [1\text{-}6]$$

Despite the energy density, LCO suffers low practical capacity [17] compared to theoretical specific capacity especially with greater depth of charge and discharge cycling causing lattice distortion [63]. There are also environmental and health concerns over the use of cobalt. Of the transition metal oxides, LCO is the most susceptible to high temperature instability which causes safety concerns due to the exothermic release of oxygen which can cause explosions with highly flammable electrolyte.

An additional commercial consideration for the LCO chemistry is the cobalt supply chain, the astronomical demand for batteries and in turn the raw materials to produce these batteries have led to high and unstable cobalt prices. Research into alternatives have started with recycling end of life batteries as a source of scarce materials as well as other battery chemistries such as NMC with significantly less cobalt compositions.

1.9.2 Lithium Ion Batteries: Lithium Ion Phosphate (LFP)

In the early 1990s, lithium iron phosphate was discovered as a viable positive electrode material for rechargeable lithium batteries. As part of the polyanion compound class, large polyanions occupy lattice positions and increase cathode redox potential while also stabilizing its olivine structure [63]. Progress made since has offered nano-scale structures which promote electrochemical performance with low resistance, high current rating, long cycle life and great high temperature thermal stability which permits high discharge rates and an intrinsically greater battery safety. Similarities in negative electrode and electrolyte with LCO have enabled transferable material components. The more stable LFP positive electrode arises due to the bonding within the structure, thus oxygen that is normally produced at high temperatures in the LCO chemistry, is still tightly bonded into the LFP structure thus providing a much greater chemical stability. The LFP cathode structure also ensures no lithium-ions remain in the iron phosphate electrode of a fully charged cell. As the lithium-ions can intercalate freely in and out of the iron phosphate cathode through well-defined tunnel framework without altering the structure.

However, a significantly lower energy density compared to lithium cobalt batteries and higher self-discharge rates are drawbacks to this battery chemistry which can cause balancing issues with aging. Common applications include replacement to the lead acid battery as lithium phosphate is more tolerant to full charge conditions and is less stressed than rival lithium-ion systems if kept at high voltage for prolonged periods. Excellent intrinsic safety, the potential for high load currents and longevity of the battery are qualities which promote the use of lithium-ion phosphate batteries, however, the substantially lower capacity has seen applications principally in niche markets.

During discharge at the graphite anode, lithium-ions are produced by the oxidation of lithium, releasing electrons shown in Equation 1-2.

At the cathode:

$$LiFe(III)PO_4 + Li^+ + e^- \rightarrow LiFe(II)PO_4 \quad [1\text{-}7]$$

$$FePO_4 + Li^+ + e^- \rightarrow LiFePO_4 \quad [1\text{-}8]$$

The overall reaction:

$$LiFePO_4 + 6C \rightarrow LiC_6 + FePO_4 \quad [1\text{-}9]$$

1.9.3 Lithium Ion Batteries: Lithium Nickel Manganese Cobalt Oxide (NMC)

NMC amalgamations have shown promise as an alternative to existing positive electrode materials, which combined the favourable properties of the constituent elements. Blends of NMC can vary significantly, with NMC-811 meaning 80% nickel, 10% manganese and 10% cobalt composition or NMC-111 which is equal parts of each respective element. Such differences in compositions are also reflected in the electrochemical performance, stability and thus a variety of energy storage applications may favour a given NMC composition as a result.

Nickel provides a high specific capacity (234 $mAh \cdot g^{-1}$) [63], and the electrochemically inactive Mn^{4+} ions offer greater thermal stability. Additionally, depending on the manganese content, the one-electron process of the $Co^{3+/4+}$ redox while the $Ni^{2+/4+}$ offers a two electron redox process [64]. NMC compounds with higher nickel content tend to have higher specific capacity; NMC-111 (160 $mAh \cdot g^{-1}$) [64] and NMC-811 (200 $mAh \cdot g^{-1}$) [64]. However, due to the high nickel composition, NMC-811 suffers from significantly short cycle life and lower thermal stability.

A promising approach [65,66] to increase the energy density (beyond 200 $mAh \cdot g^{-1}$) [67] of layer oxides of NMC is the synthesis of spherical nickel-rich cores and manganese rich shells – which provides both high capacity and enhanced stability within the electrolyte. Nickel and manganese rich NMC compounds provide exceptionally high specific capacities (300 $mAh \cdot g^{-1}$) [64], however, conversion from the layered to spinel structure upon cycling [68] which causes capacity and voltage fade. Further disadvantages are slow kinetics and voltage hysteresis caused by anionic redox activity [68,69].

Nickel and manganese rich compositions of NMC are especially favourable economically, with the cobalt market climate looking increasingly expensive when compared to the abundant, cheaper and environmentally friendlier manganese. Also, despite the lower voltage, recent developments of new electrolytes and additives have produced NMC cells capable of charging up to 4.50 V and a greater capacity [17]. The inherent advantage of NMC is the ability to produce a mixture of differing compositions, thus the properties of NMC are versatile and can be tailored for the application, meanwhile compensating for the limitations of each element individually.

The overall promising performance of NMC is due to; the high specific capacity, high cycling rates, low internal resistance, and commercially feasibility. This is coupled with the lowest self-heating

rate of competitive battery chemistries and good materials thermal stability up to 250 ^{o}C thus making NMC cells inherently safer. NMC batteries are experiencing a surge in growth in market share within lithium-ion batteries, especially in EVs, medical applications and energy storage systems.

1.9.4 Lithium Ion Batteries: Lithium Nickel Cobalt Aluminium Oxide (NCA)

Sharing many qualities with NMC batteries, NCA chemistries offer high practical specific capacity (200 $mAh \cdot g^{-1}$) [17] , high power density, reasonably good specific power, and a lower relative diminishing capacity over the cycling lifetime compared to traditional cobalt based cathodes, such as LCO. NCA batteries are notably commercially used in present Tesla electric vehicles and grid energy storage systems [63]. The addition of aluminium in small quantities improves the stability of the battery to thermal abuse, however, typically composed of 80% nickel, 15% cobalt and 5% aluminium, the cobalt content consequently increases the manufacturing costs of NCA batteries. Compared with other battery chemistries, the inherent safety can be considered more marginal due to the absence of electrochemically inactive Mn^{4+} and the battery is less resistant to thermal abuse than the leading batteries in thermal stability. In addition to severe capacity fade reported at elevated temperatures (40 - 70 ˚C) due to SEI growth and grain boundary micro-crack growth.

1.10 Lithium Ion Batteries: Electrolyte

Electrolytes in lithium batteries have three fundamental specifications for feasibility; electron transfer across the electrolyte must be prevented, ionic conduction must be favourable and it is imperative that the electrolyte is completely anhydrous. Lithium ion batteries are non-aqueous as lithium metal reacts with water, thus organic solvents and dissolved electrolyte salts are common constituents.

Porous electrodes and separator materials must allow liquid electrolytes to be absorbed, a property which increases the interfacial surface area with active materials facilitating greater power outputs. Commercial cells almost exclusively use electrolytes based on 0.8 – 1.5 $mol \cdot L^{-1}$ lithium hexa-fluoro-phosphate ($LiPF_6$) [64] salt. This is dissolved in a mixture of organic solvents such as linear organic carbonates including ethylene carbonate, dimethyl carbonate and vinylene carbonate which are volatile and highly flammable, a key concern during catastrophic thermal runaway. Additives are used to improve performance, stability, lifespan and safety of the electrolyte by maximising the ionic conductivity. Electrolyte costs are driven by the fine $LiPF_6$ salt used only in electrochemical applications.

Current research into alternatives such as solid state electrolytes have been well reviewed [70,71] and have been considered as having significant potential for future evolution of electrolytes. Favourable properties include enhanced safety, performance retention over operational lifetime and versatile design freedom. However, this research has yet to have substantial commercial impact as solid state electrolytes have inherently slower diffusion of ions as due to the solid-state nature which also reduces power output, low chemical, mechanical or thermal stability. Hence, the overwhelming popularity of current non-aqueous liquid-phase electrolytes in commercial lithium-ion cells.

Electrolyte solutions are sensitive to external operating conditions, becoming very reactive with intercalating lithium and decomposing at elevated temperatures (60 ^{o}C). The reaction with lithium is what creates the important solid electrolyte interphase during the formation cycles of a lithium-ion cell. Growth of this passivating solid electrolyte interphase stops until the electrolyte is no longer subject to reduction from the electrode potential and lithium. As with the electrolyte sensitivity to higher temperatures, the solid electrolyte interphase also decomposes, consequently the formation of a reactive interface between the electrode and electrolyte.

1.11 Lithium Ion Batteries: Current Collectors

1.11.1 Commercial Current Collectors

The role of the current collector (CC) in a cell is to provide an electronic conduction pathway to the anode and cathode; metals such as aluminium and copper are typically used as they are electrochemically stable across the respective operating potential windows of the cathode and anode, thus preventing degradation [72,73]. Aluminium alloys with lithium at low potentials vs Li/Li^+, however, a thin dense passivation layer occurs with transition metal oxides at the cathode thus which can protect the Al CC, typical operating potential between 3.70 – 5.00 V vs Li/Li^+ [73,74]. Copper experiences corrosion and dissolution at potentials the cathode operates within, however, remains relatively stable at lower potentials ca. 0.01 – 2.00 vs Li/Li^+ [73,74]. Traditionally, a fifteen-micron film thick current collector binds both side of the double layer electrodes [75] and vice versa. Currently, relatively high thicknesses are used for conventional CCs to avoid tearing of the material during roll-to-roll manufacture which negatively affect the energy density of cells. Conventional current collectors can carry large currents and are thus a critical component for sustaining internal short circuits that can lead to thermal runaway.

Relative to other components such as electrode material research, current collectors have not seen the same rate of innovation and revolution since the introduction of commercial lithium-ion batteries. Research has been led into optimising the morphology of current collectors with the structures of novel electrodes, such as a method of hindering dendritic growth in pure lithium anodes [73,76–78]. Recently reported re-engineering of the current collector to improve battery safety by Naguib *et al.* [79] restructured the electrode and current collector design to produce impact-tolerant "slitted" construction which could withstand mechanical impact and Liu *et al.* [80] using a positive temperature coefficient material within a current collector configuration to isolate the region of short-circuit from the rest of the battery.

1.11.2 Polymer Substrate Current Collectors

Modern current collector thicknesses are widely accepted due to synergy with automated equipment. However, such thicknesses are said to be in great excess of what is required for lithium-ion batteries to perform adequately [75]. Recent research by the Soteria Battery Innovation Group has focused on plasticized current collectors, whereby an eight micron thick PE layer is coated on both sides by copper or aluminium. Each film of metal on either side of the polymer substrate is 1 micron thick, which has yielded an interesting alternate perspective on the manufacture and arguably, more importantly, the inherent safety of lithium-ion batteries. Current collectors are overdesigned for purpose with additional functionality, such as contributions to safety via the polymer current collector – with the hypothesized mechanisms during internal defect shown in Figure 1-3. These have been studied extensively in this thesis.

A 10 µm aluminium polymer film offers competitive tensile strength to that of a 15 µm thick aluminium foil typically quoted at 150 $N \cdot mm^{-2}$, in addition greater elasticity yields similar coating and handling properties on roll to roll coating equipment[75]. Considering other cell characteristics, with both metal film coated polymer current collectors, cell level energy density can be expected to increase in the region of 10 - 20% [75].

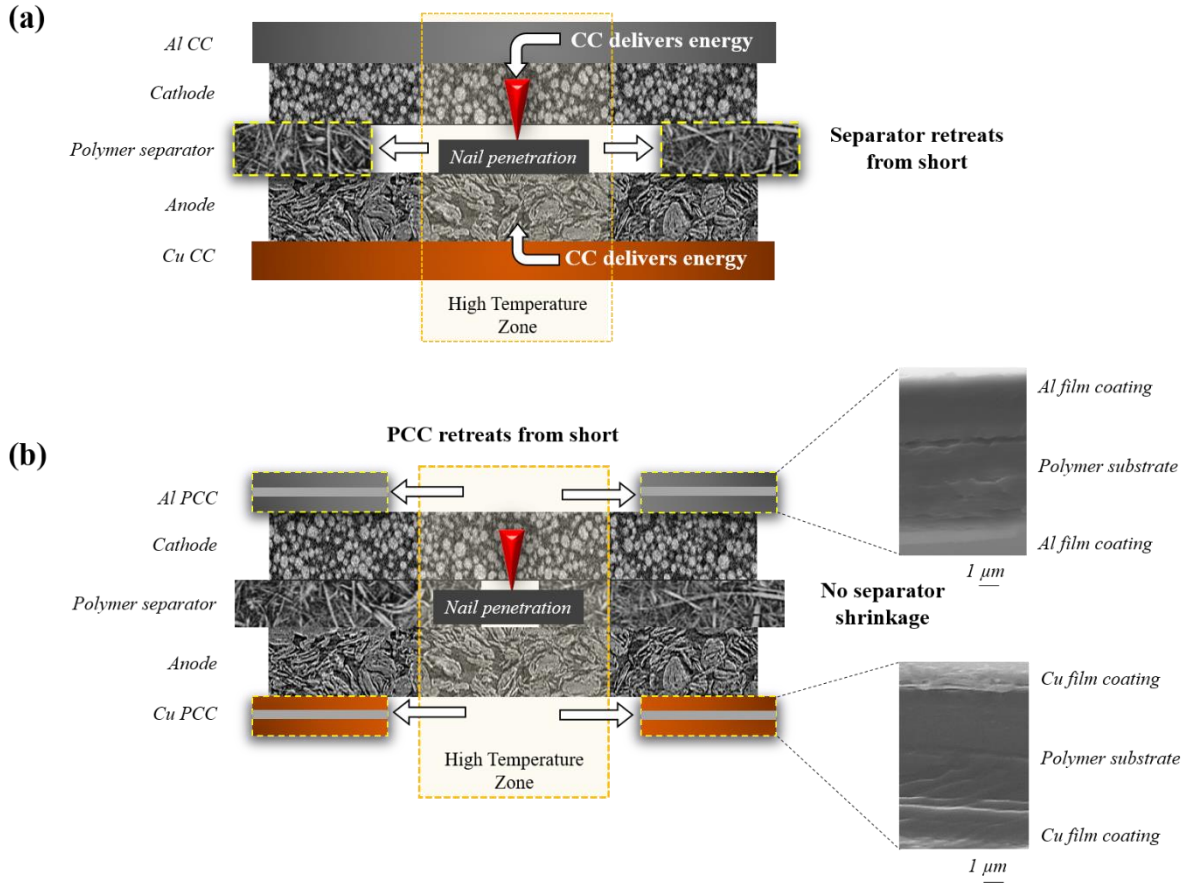

Figure 1-3: (a) Nail penetration of a standard commercial metal CC cell. (b) Failure mitigation mechanism of Al PCC + Cu PCC cell during nail penetration; SEM insets of the PCC cross-sections illustrate the ca. 8 µm polymer substrate 'core' and ca. 0.5 µm metal film coating.

The cathode coated aluminized plastic film and anode coated copperized plastic film of five micron thickness, prevent rapid and excessive current delivery to the local region of defect or short, this is especially important as shown in Figure 1-3. As the non-woven separator is stable, withstanding the local temperature rise without shrinking, the metallic coated film retreats from the origin of the short and isolates the electrochemically active materials within milliseconds.

1.12 Lithium Ion Batteries: Separator

1.12.1 Introduction and Commercial Separators

Placed between the positive and negative electrodes, a battery separator has two main functions, it must be an electrical insulator to prevent the short circuit between the electrodes but allow ions to pass through via the organic liquid electrolyte. Porous insulating materials like non-woven fabric, paper or microporous polymeric materials such as polyethylene are good electrical insulators which also allow ions in the electrolyte to pass through for the battery to function. Commercially common microporous polymeric membrane separators are manufactured from varying amounts of polyethylene (PE) and or polypropylene (PP) in single layer or multilayer designs. These commercial separators are separated into categories as: non-woven, ceramic coated and solid inorganic, polymeric or hybrid electrolytes functioning as an electrolyte and separator.

Further properties that are desirable in a cell separator are chemical, mechanical and thermal stability, permeability and wettability. As there are numerous species present in the lithium-ion batteries, the separator must be chemical and electrochemically inert in such potentially chemically volatile conditions. Mechanical stress has seen catastrophic failures in commercial applications [14,15,81], this underlines the importance of the separator to be resistant to strain, stress, tension and mechanical abuse such as punctures from lithium dendrites or internal shrapnel from structural collapse. Lithium ion batteries are required to operate in varying extremes of temperatures with minimal deviation from optimal performance, thus the separator must withstand these fluctuating temperatures without expansion or shrinkage and degradation while delivering the same performance. Electrolyte pore penetration occupation is essential for ion transport, gas pockets will result in a reduction in the available active surface areas regions which are inactive for ionic diffusion. Separator pore sizes should be evenly distributed, uniform and smaller than electrode particles to maintain a homogeneous constant current and prevent penetration of the separator by electrode particles. Highly tortuous separator structures assist in countering the risk of dendritic lithium growth which can short circuit the cell.

1.12.2 Thermally Stable Separators

Traditionally, due to the low melting point of polymer separators made from a blend of PP and PE, separators have been one of the first components within lithium-ion batteries to undergo thermal decomposition, shrinkage and later melting. This has a tendency to expose the opposing electrodes to one another and cause short circuit. Subsequent Ohmic heating provides energy for the material to rapidly react. This highly exothermic reaction which occurs instantaneously produces significant amount of heat, which causes oxygen to form from the cathode in an environment of oxygen, highly flammable electrolyte and elevated temperatures, thermal runaway occurs.

In response to this challenge, Dreamweaver have developed a non-woven blend of micro- and nano-fibres featuring aramid in their range of separators [82–84], which some have seen thermally stable architectures up to 300 ºC with zero shrinkage therefore thermal stability hence improved safety. Many favourable properties over that of traditional polymer separators include; greater efficiency due to the reduced internal resistance lowering energy dissipation due to greater wettability – especially over other non-woven separators. This also improves the ionic conductivity, thus greater electrode utilization at high C-rates. Also, this promotes higher energy density due to the more efficient ionic transfer, which permits greater flexibility in battery design with thicker electrodes and reducer separator area thus increasing energy density. These have been studied within the work presented in this thesis.

1.13 Thesis Motivation

Electrochemical degradation and poor capacity retention are common features of certain lithium-ion chemistries. There is considerable and diverse research into alternative materials to mitigate this, while improving upon other performance parameters such as specific capacity, cell energy and power density. These innovative active materials require greater understanding and characterisation during operation and failure before widespread commercial acceptance and uptake can occur.

There are many options for materials for positive electrodes, each with benefits and drawbacks. Positive electrodes such as the spinel based structures have shown excellent relative thermal stability and resistance to thermal runaway due to greater heat dissipation but are known to suffer from lower energy and power densities than competing cell chemistries such as the cobalt electrode compositions.

The widespread application and integration of lithium-ion batteries in the modern age has cemented the importance of the technology, however, when subjected to abusive operating or environmental conditions, catastrophic failure can occur. Recent high-profile lithium-ion battery failures have been observed and well reported [14,85] with media coverage of high profile failures often referred to as explosions. In many instances, the failure mechanisms were interrogated with characterisation methods such as X-ray imaging, however this is largely limited to post mortem investigation. Innovations into inherently safer battery architectures, to withstand adverse temperature because of electrical or mechanical abuse, external environmental heating sources such as adjacent cell failure in a battery powertrain module and abnormal localized internal heat accumulation are required. These innovations can be especially difficult to integrate as complex battery modules develop.

Thermal runaway is a consequence of heat generation greatly exceeding the heat dissipation and as a result, causing highly exothermic decomposition of active materials above a critical temperature. This accumulation of heat causes thermal degradation of the electrolyte, separator, cathode and anode [86–89] resulting in a catastrophic failure of the cell. During this sequence of events, it has been well reported that ca. 2 L of gas is generated per amp hour (Ah) [90,91] which induces cell swelling and later rupture of the battery. Ejection of flammable gases and materials from the cell casing at high temperature into the oxygen rich air tends to initiate a combustive reaction, which is a significant contributor to the thermal energy released by lithium-ion battery failure. Different cell chemistries will have a different range of critical temperatures of inevitable failure, once these temperatures occur within

the cell, the highly exothermic subsequent sequential collapse of cell structures induces an external heat effect on other neighbouring cells.

In this work, thermal runaway initiated with FTRC is used to determine the heat produced. FTRC has typically been used for higher-capacity cells and modular calorimetry to quantify and discern the heat output between ejected and non-ejected material during thermal runaway [86,92–94]. This is important for efficient battery module design and battery management systems (BMS) to prevent excess parasitic mass or volume but also to ensure that there is sufficient isolation of the characteristic ejection of heat from each cell. This can help to ensure that an individual cell failure does not propagate to widespread thermal runaway throughout the module.

In-depth insight into the dynamic mechanisms of thermal runaway with direct non-destructive, diagnostic imaging during thermal runaway has been respectively demonstrated by Finegan *et al.* [86,93–95] and Robinson *et al.* [96] with X-ray and thermal imaging. Feng *et al.* [14,97–99] have investigated failure with numerous abuse techniques, predominantly in large format prismatic cells. Yokoshima *et al.* [100] investigated the mechanisms during internal short circuit predicating thermal runaway using an laboratory micro X-ray scanner, Ruiz *et al.* [101] has reviewed the numerous abuse methods and Yang *et al.* [102] subjected a flexible lithium-ion battery to bending and cutting without catastrophic failure. Thermal management models have also been popular where numerous authors have investigated this in great depth [85,88,94,103–107].

Failure or abuse methods typically fall into three broad categories; thermal, mechanical and electrical abuse (external or internal short circuiting or excessive charge or discharge) with the majority of failure testing utilizing the first two [94]. However, disadvantages exist with these techniques [94,95,97,108] as the worst-case scenario of failure (whereby all the energy capacity is ejected in one direction), cannot be reliably induced. This is especially true for failure produced as a result of thermal abuse as there is a lack of precision in determining when and where thermal runaway will initiate. There are other experimental limitations which must be considered, but most prominent is the time taken to achieve the critical temperature to initiate thermal runaway as electrolyte may evaporate from initial venting. A drying electrode assembly [97] also poses challenges to other failure methods such as oven tests or accelerating rate calorimetry. These drawbacks are not observed in nail penetration failure tests, however: as a consequence of the nail penetration of the electrode assembly inside the cell casing, the nail provides a heat sink path from the cell, decreasing the total energy available released in thermal runaway thus a less violent failure event [93,109,110]. The third means of inducing failure is electrically, this

has been previously performed by a hard internal short-circuit [93,94,111], propagating widespread thermal runaway throughout the cell thus impeding the escape of electrolyte via venting. During the process of failure, surface temperatures in excess of 600 ˚C are common for an event which elapses within a few seconds [93–95]. Therefore in battery packs, the ability to forecast violent ruptures and failures will provide key insight into the safety and performance of such powertrains [112].

The most influential factor in determining the cell's thermal runaway behaviour is understanding the cell chemistry and influence of the components during operation, abnormal conditions and failure. The characterisation of this is crucial, as some chemistries and internal cell components are inherently more thermally stable than others; this acts as a basis from which inherently safe design can improve upon. [17,63,64].

The 18650-cylindrical cell format is popular in many applications, however, the protective exoskeleton can act as a pressure vessel. Lithium-ion 18650 thermal runaway experiments [86,93,94] have shown the rigid cylindrical steel casing of an 18650-cell can undergo explosive ruptures whereas pouch cells without such a rigid shell usually swell from internal gas production and ignite. Even among 18650-lithium-ion cells, similar cells can demonstrate very contrasting failures [86,93,94]. During failure, side wall ruptures provide an alternative path for a jet of flammable electrolyte and gases: catastrophic thermal runaway of this nature is of great concern when designing battery modules to prevent propagation of failure to adjacent cells. In EV battery packs, where it is common for these power trains to consist of approximately 7000 18650-cells [113], the mitigation of violent ruptures and failures must considered to eliminate or minimise the risk of catastrophic failure. New design innovations with the more energy dense 21700-batteries are expected as a standard in new electric vehicles [114].

The severity and consequences of these failures have provided the impetus for the development in rigorous *in-situ* and *operando* characterisation of failure in energy-dense high performance cells. The risks and consequences associated with batteries have increased with the greater capacity, energy and power densities seen in commercial applications, thus characterisation techniques to accelerate research into innovative cell designs and integrated safety mechanisms are crucial. High energy density batteries may be prone to catastrophic failure events rather than gradual performance decline and manufacturers need to be able to guarantee the safety and performance of a complex electrical power train, in a simple and cost effective manner.

1.14 Conclusions

Fundamental principles of components and mechanisms that construct and govern lithium-ion batteries are described in this first chapter with an introduction into the susceptibility of this electrochemical energy storage technology to failure under degradative conditions. Cell components redesigned with an active contribution to safety and investigated in this thesis were also described and a brief review of other technologies which provide additional battery safety in the event of failure propagation.

The sequence of component failure mechanisms and thereby the subsequent effect during failure are outlined briefly with the characterisation methods, which will be expounded upon in the following two chapters. Three abuse methods are described in this chapter and the effect of re-engineered components towards mitigation of each of these thermal runaway abuse methods during the precursor degradative events to failure are to be considered.

1.15 Thesis Aims and Objectives

The work presented in this thesis aims to establish the rapid responses of AS within battery safety characterisation methods, providing instantaneous insights into the electrode assembly structure, evolution and phase change throughout the process of thermal runaway. These responses can be identified *in-situ* and *operando* immediately with material properties changes which change attenuation and propagation of ultrasonic waves, before other battery safety and thermal runaway characterisation methods, such as calorimetry and X-ray radiography, for which relevant literature is examined in the following chapters.

Following this, a multi-faceted suite of characterisation are used to examine materials which target the important process of short-circuits which predicate ejection of material in thermal runaway and later exposure of high temperature combustible material to the oxygen-rich atmosphere. This focuses initially on commercial adjacent cylindrical cells, before the research scope is expanded upon for an innovative pure silicon nano-wire electrode to test the effectiveness in mitigation of the materials independent of different cell formats and cell chemistry, while providing initial insights into pure silicon anode thermal runaway.

2 Lithium Ion Batteries: Thermal Runaway

2.1 Thermal Runaway: Introduction

Thermal runaway is a consequence of heat generation greatly exceeding the heat dissipation and as a result, causing highly exothermic decomposition of active materials which is described in this chapter. It has been well reported that ca. 2 L of gas is generated per amp hour (Ah) [90,91] and the ejection of such large volumes of flammable gases and materials from the cell casing at high temperature into the oxygen rich air tends to initiate a combustive reaction, which is a significant contributor to the thermal energy released by lithium-ion battery failure and perhaps the greatest risk of power-train pack level propagation of failure. Different cell chemistries will have a different range of critical temperatures of inevitable failure, once these temperatures occur within the cell, the highly exothermic subsequent sequential collapse of cell structures induces an external heat effect on other neighbouring cells.

These effects on component failure through exothermic degradative reactions, propagation of the micro-scopic short-circuit, physical and mechanical considerations within the electrode assembly of the lithium-ion battery can be used as a comparative basis of standard reactions with typical commercialized components. The initial short-circuit is often the nucleation point for many failures and represents the greatest opportunity for mitigation and prevention of failure. There are typically two types of short-circuits which are referred to as ‘soft’ and ‘hard’. ‘Soft’ short-circuits are those which occur locally, with minimal damage to the electrode assembly, cells may experience voltage drop and recovery with cells displaying a degree of electrochemical operability thereafter. ‘Hard’ short-circuit refer to those where the initial Ohmic heating has continued to propagate heat transfer through the wider electrode assembly and cell, causing cell-level electrode damage, gas generation and permanent voltage losses with the cell beyond instability and electrochemical functionality.

2.2 Thermal Runaway: Characterisation and Mechanisms

2.2.1 Thermal runaway mechanisms and reactions

Given the complex combination of cell components within the cell, it can be difficult to ascertain a complete and comprehensive list of reactions and the rate at which these can occur. Abuse experiments such as the heat-wait-seek method from the ARC which can identify generation of heat within the cell combined with post-mortem cell disassembly with product material analysis, the most likely set of reactions can be inferred at a given temperature and the approximate or comparative proportion to the total calorific output during failure. Efforts have been made to utilise such measured datasets can be used to train and inform thermal runaway models given the challenges which are posed with abuse cell testing. However, spatial evolution of reactant surface areas as well as electrode particle size with variations in electrode composition, binder materials, electrolyte compositions are examples of variables which are difficult to quantify in such a circumstance. Post-mortem material, gases ejected and soot analysis also provides insight into the potential hazards and toxicity posed by the heavy transition metal oxides (typically cobalt, nickel, manganese oxides), carbon monoxide (CO), hydrogen fluoride (HF) [115–117] which are typically ejected. Chapter 2.2.2 discusses these gas generation reactions and the impact of these in cell failure. These insights can inform and aid future industry standards, government legislation for prevention, mitigation, storage and transportation.

There are other sources of heat which can contribute to the total calorific output of the cell not related to thermal runaway decomposition reactions, for example, combustion of high temperature flammable ejected gases, Ohmic heating during macroscopic cell short-circuit where high C-rates are observed and instances of failure for under- or over- charging. During the thermal decomposition of electrode assembly materials, there are typically five prominent reactions which can occur cause the cell to sustain heat generation until the critical temperature, whereby the cell undergoes failure [85,118,119]. The total heat output with respect to the individual decomposition reactions through the mechanisms described in the next section is defined as:

$$Q_{r,tot} = Q_{r,sei} + Q_{r,e} + Q_{r,ne} + Q_{r,pe} + Q_{nb} \quad [2\text{-}1]$$

Where the thermal decomposition of the SEI layer ($Q_{r,sei}$), decomposition of the electrolyte ($Q_{r,e}$), reaction between the negative electrode and electrolyte ($Q_{r,ne}$), reaction between the positive

electrode and electrolyte ($Q_{r,pe}$) and reaction between the negative electrode and the binder ($Q_{r,nb}$) are the five significant thermal runaway reactions. Each of these individual reactions can be described the general Arrhenius equation with their respective reaction kinetic parameters [85,118–120]:

$$k = Ae^{-\frac{E_a}{RT}} \quad [2\text{-}2]$$

Where k is the rate constant, A is the pre-exponential factor or frequency factor representing the proportion of collisions that have the energy to overcome the activation energy requirement, E_a is the activation energy and orientation, R is the universal gas constant and T is the absolute temperature. Given the transient internal environment with failure mechanics on the reaction conditions (temperature, reaction concentrations), the extent and rate of reaction can vary for each individual reaction between cells of the same specification and thereby the individual proportion of the total calorific output during failure. These reactions can occur non-exclusively however require each individually require an approximate temperature for onset of reaction due to occur due to activation energy or a failure mechanism to provide contact of reactants.

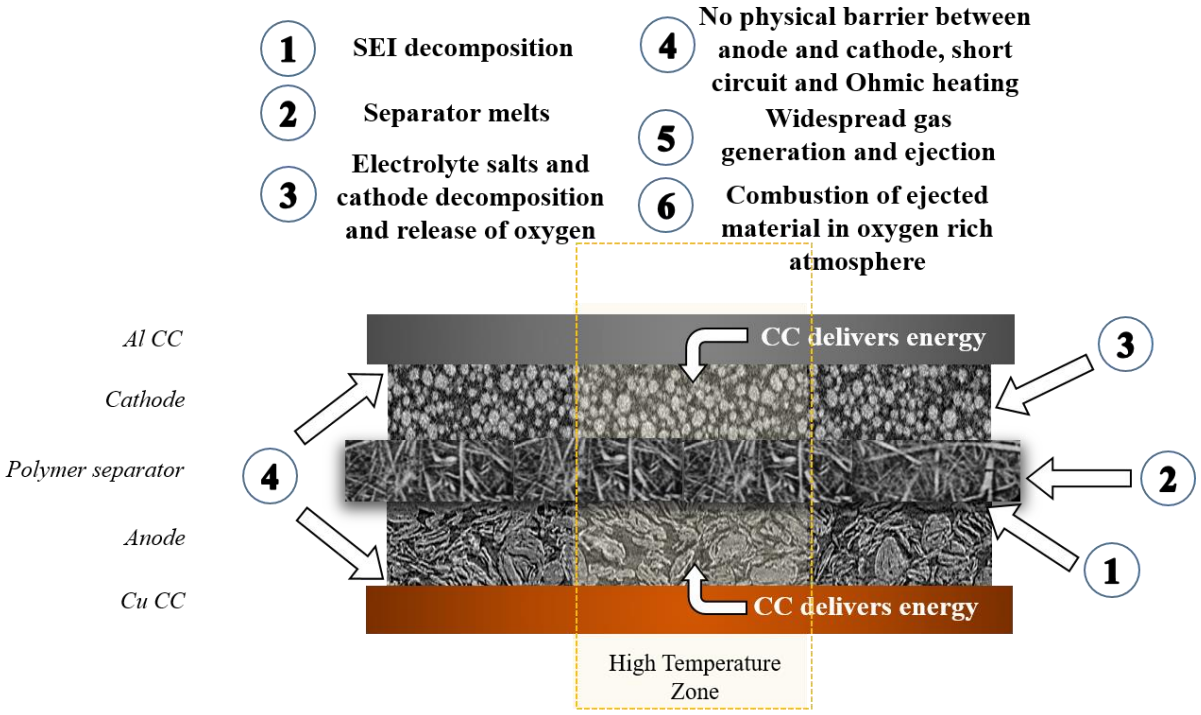

Figure 2-1: The broad sequence of steps which encompass a typical thermal runaway event with commercial materials and no mitigating factors. These steps are described in further detail on the next page and this figures provide a preliminary understanding of the events that occur and where in the electrode assembly, if applicable with arrows.

This can be grouped into three significant temperature ranges: at ca. 80 °C, the SEI starts to exothermically decompose. As the anode loses this protective layer, a loss of capacity occurs via de-intercalation of lithium-ions from the lithiated graphite anode and the carbon reacts with the electrolyte producing heat. This process is reported to continue until the widespread structural fracture and decomposition through reduction of alkyl carbonate electrolytes by lithium-ions accessible due to instability of the graphite phase in the local environment until ca. 220 °C. Subsequently, the accessible intercalated lithium is depleted and with continuous reformation and decomposition of the SEI, the lithium released reacts with PVDF and electrolyte decomposition by-products to generate more heat [121].

At ca. 130 °C; the rate of temperature increase slows, and the separator begins to melt (the majority of polyolefin commercial separators consists of polyethylene or polypropylene, which have melting points of ca. 105 °C – 180 °C depending on the grade). As the separator melts, this causes micro 'soft' short circuits of the anode and cathode, thereby considerably increasing the rate of reaction, current flow and energy delivered to the regions of short-circuit. These local regions experience greater heating, causing further degradation of the separator. Furthermore, less thermally stable cathode materials and typical lithium salts start to exothermally decompose at 150 – 200 °C, such as $LiPF_6$ [122]. These decomposition of these produce oxygen and highly combustible alkyl gases respectively.

At ca. 220 - 240 °C, there processes such as onset of widespread gas generation and decomposition of the cathode, electrolyte and polyvinylidene fluoride binder (PVDF). Transition metal oxide cathodes will release oxygen [85] which is highly influential in other decomposition reactions and combustion of flammable gaseous products, mostly produced from decomposition of the electrolyte previously. Golubkov *et al*. investigated three type of cathode materials in thermal runaway tests, which exhibited a correlation between greater energy density, with higher rates of heating, heat output and maximum temperature during thermal runaway (lowest to highest; LFP, NMC, LCO) [91]. To simulate the worst case scenario of failure which would replicate likely operating conditions, cells were tested at full SOC (voltage dependent on cell chemistry). Further work from Golubkov *et al*. found that lower onset critical temperatures and maximum temperatures reached after failure were measured in investigations on SOC impact on NCA cathodes during failure of 18650-cells [123], which was exacerbated with overcharge voltage ranges. The extremely low lithium content in the transition metal oxide cathode, increases the oxidation potential, thus, the electrode is volatile to the organic solvent electrolyte.

2.2.2 Gas generation

Given the myriad of possible permutations of cell chemistry and electrode assembly material, the extent at which the decomposition reactions are completed to produce gases fluctuate broadly. However, gas chromatography (GC) analysis conducted in literature [91,123–125] can provide average final ejected gas compositions for 18650-cells [91], however, set-ups can leave undetected species such as HF [123,126]. 18650-cells typically are 2.0 – 3.5 Ah capacity and at this capacity range, up to 7 L of gas [90,91] can be produced during thermal runaway. Golubkov *et al.* [91] investigated the ejected gas volumes with GC for commercial 18650-cells consisting of graphite and LCO-NMC, NMC and LFP chemistries, the composition of which are shown in

Table 2-1.

Comparisons between the compositions of gases show H_2 and CO_2 are the most abundantly produced gaseous species which are detected during failure at full SOC. CO is produced and was measured to be in greater proportions of the total gas volume from LCO-NMC and NMC cell chemistries with trace amounts of hydrocarbon gases present in all chemistries. Gas generation reaction pathways and their relative extents with the complex mechanics of failure which can vary from cell to cell of the same specification highlight the challenges that is posed with quantification of the individual reactions which may occur, though, the most probable postulated reactions to produce each gas species are reported hereafter.

Table 2-1: Composition of gases reflective of the molar amount detected in GC analysis of thermal runaway of 100% SOC 18650-cells, reproduced from [91].

Composition of species in gas (mol %)	LCO-NMC	NMC	LFP
H_2	30.0	30.8	30.9
CO_2	24.9	41.2	53.0
CO	27.6	13.0	4.8
CH_4	8.6	6.8	4.1
C_2H_4	7.7	8.2	6.8
C2H6	1.2	-	0.3

Production of H_2

Probable sources of hydrogen gas production stem from the reaction of exposed intercalated lithium with binder material after decomposition of the graphite anode to allow accessibility [85,91,127]. These reactions typically occur above 260 °C after the graphite structure has been delaminated, the lithium reacts with the PVDF and carboxymethyl cellulose (CMC), which are common binder materials, in the following reactions [127]:

$$(-CH_2 - CF_2) + Li \rightarrow LiF + (-CH = CF -) + 0.5H_2 \quad [2\text{-}3]$$

$$(CMC - OH) + Li \rightarrow (CMC - O - Li) + \frac{1}{2}H_2 \quad [2\text{-}4]$$

Production of CO_2

There are multiple probably sources of carbon dioxide generation, through thermal decomposition of the SEI [128,129]:

$$(CH_2OCO_2Li)_2 \rightarrow Li_2CO_3 + C_2H_4 + CO_2 + \frac{1}{2}O_2 \quad [2\text{-}5]$$

Reactions with trace amounts of impurities such as water or HF can also occur [91]:

$$ROCO_2Li + HF \rightarrow ROH + CO_2 + LiF \quad [2\text{-}6]$$

$$2ROCO_2Li + H_2O \rightarrow 2ROH + Li_2CO_3 + CO_2 \quad [2\text{-}7]$$

Furthermore, electrolyte and the intercalated lithium may react as shown in CROSSREF for the production of flammable hydrocarbons which can produce further Li_2CO_3, which can react with HF to produce further carbon dioxide:

$$Li_2CO_3 + 2HF \rightarrow 2LiF + CO_2 + H_2O \quad [2\text{-}8]$$

Oxygen generation from the thermal decomposition of the delithiated metal oxide cathode partakes in oxidation of the electrolyte [130] and it has been measured that carbon dioxide is predominantly produced at the cathode side of an overcharged cell [131]. Thus plausible for greatest proportion of carbon dioxide to be attributed to this reaction. Here, the example of EC reduction at the carbon anode where SEI reformation occurs [119] to produce carbon dioxide is shown:

$$C_3H_4O_3 + 2.5O_2 \rightarrow 3CO_2 + 2H_2O \quad [2\text{-}9]$$

Production of CO

There are two proposed reactions for the production of CO amidst thermal runaway, the first is the reduction of CO_2 at the anode with the intercalated lithium [127,128]:

$$2CO_2 + 2Li^+ + 2e^- \rightarrow Li_2CO_3 + CO \quad [2\text{-}10]$$

It has been suggested that CO is also produced from incomplete combustion of carbonaceous species that compete for the limited O_2 that is released from the thermal decomposition of the cathode. Ohsaki *et al.* [130] reported the greatest contributor of CO came from the cathode side in overcharge of LCO cells.

Production of CH_4, C_2H_4 and C_2H_6:

Organic solvent reduction is attributed to the alkyl and alkenyl hydrocarbons produced and detected in failure, the production of these highly combustible hydrocarbons are accompanied by lithium carbonate. The production of methane:

$$2Li^+ + 2e^- + C_3H_6O_3 + H_2 \rightarrow Li_2CO_3 + 2CH_4 \quad [2\text{-}11]$$

The production of ethylene at the lithiated anode by two possible reactions at the lithiated graphite anode [119,128]:

$$2Li + C_3H_4O_3 \rightarrow Li_2CO_3 + C_2H_4 \quad [2\text{-}12]$$

$$2Li + 2C_3H_4O_3 \rightarrow (CH_2OCO_2Li)_2 + C_2H_4 \quad [2\text{-}13]$$

Or ethylene by SEI decomposition [129]:

$$(CH_2OCO_2Li)_2 + 2Li \rightarrow 2Li_2CO_3 + 2C_2H_4 \quad [2\text{-}14]$$

Production of ethane at the lithiated anode:

$$2Li + C_3H_6O_3 \rightarrow Li_2CO_3 + C_2H_6 \quad [2\text{-}15]$$

The amount of combustible material which in produced within the cell at high temperature and the volume of gas that is measured subsequently which is initially pressurized within the 18650-cell poses an extreme hazard risk. For example, explosive ejection of such material from a pressurized steel casing vessel into a much more oxygen rich atmosphere will induce combustion of significant force and is a risk to the surrounding environment.

2.2.3 Thermal runaway characterisation

Characterisation methods facilitate measurements of properties to deduce the internal phenomena within lithium-ion batteries during failure, which is typically a rapid event occurring within 5 s, thus temporal and spatial resolution are significant considerations for failure testing. Thus, it remains difficult to detect internal mechanical deformation and gas-induced degradation in lithium-ion batteries, especially outside specialized diagnostics laboratories. Furthermore, internal structural insights garnered through these techniques will be linked with external measured thermal and cell voltage responses to explain the failure mechanisms which have occurred and for use as a reference standard of commercial material responses for safety attributed components in research.

Lithium-ion batteries can generate significant amounts of heat associated with both electrochemical reactions and ohmic losses. When the rate of heat generation exceeds the rate of heat dissipation, the cell begins to increase in temperature and at a critical temperature, highly exothermic decomposition reactions occur with ejection of these materials. This process, referred to as thermal runaway, rapidly degrades the anode, cathode, electrolyte, separator and SEI [85–89,132] and ultimately results in catastrophic failure of the cell. Therefore, understanding the mechanism and onset of thermal runaway is essential for the design of safer lithium-ion batteries. Feng *et al.* [97] utilised the 'heat-wait-seek' method with extended volume accelerated rate calorimetry to deconstruct the sequence of events during thermally induced failure at increasing temperature. The process of thermal runaway has been deconstructed [87,89,97,132,133], widely-reviewed [14,85,119,134–136] and evaluated with multiple direct and in-direct techniques [92,96,100,137–142] and has informed complementary kinetic-thermal models [88,98,106,119,143–145]. High-speed *operando* X-ray radiography and CT [95] has previously been used to evaluate thermal runaway mechanisms of overcharge [86], internal short circuits [93], nail penetration [146], the mechanics of mechanical safety designs [147] and has been correlated with modelling [85,88,94,103–107].[94] Feng *et al.* [14,97–99] have investigated failure with numerous abuse techniques, predominantly in large format prismatic cells. Yang *et al.* [102] subjected a flexible lithium-ion battery to bending and cutting without catastrophic failure. These techniques have facilitated characterisation of failure testing with broad approaches to improving lithium-ion battery safety.

Typically, the focus of research into CCs for lithium-ion energy storage has been in the morphology of current collectors to accommodate the structures of novel electrodes [73,76–78,148]. However, due to recent failure events, battery safety has seen greater scrutiny and motivated research in component level safety functionality. Xu *et al.* [149], Chombo *et al.* [150] among other reviews [151–155] have

previously reviewed a range of mitigative materials, components and strategies for cell safety and design. These cell components are designed to target specific events in the thermal runaway initiation process such as local temperature and the internal short circuit to improve safety through mitigation. These safety additions are often properties enhancements, such as thermal or mechanical stability or reduction in flammability to components, which include; electrolyte [156–160], separator [161–167] and thermally responsive materials (cathode coatings [168], current collectors [151,169–172], separators [173]). Positive temperature coefficient (PTC) CCs are those with significantly greater resistance at higher temperatures [151,169–172], these have been proposed as safety features which can mitigate failure, however, limitations arises with high C-rate and temperature operations. A current collector redesign utilising the PTC mechanism by Liu *et al.* [80] has demonstrated the ability to isolate the region of short circuit from the battery.

Several authors [164,174,175] have examined and reviewed separators pioneered for safety advancements. Common commercial polymer separators in 18650-cells usually comprise of an amalgamation of PE or PP and are typically ca. 10 – 30 μm thick [175], therefore, depending on the grade, they have an approximate melting point of ca. 130 ^{o}C. Multilayers of different polyolefins can introduce time delay during the separator failure process due to the differing melting points [173,176,177]. Improvements in thermal stability to prevent shrinkage have been achieved with a variety of methods which include the application of a ceramic coatings [178,179] or the use of polyester [180].

Recently reported re-engineering of the current collector to improve battery safety by Naguib *et al.* [79] restructured the electrode and current collector design to produce impact-tolerant “slitted” construction which could withstand mechanical impact and by and Liu *et al.* [80] using a positive temperature coefficient material within a current collector configuration to isolate the region of short-circuit from the rest of the battery. It is notable that connection of the two most electrically conductive materials within a cell (the current collectors) leads to the most severe internal short circuit thus one of the most probable conditions for thermal runaway to occur. Thus removal or isolation of the CC during an internal short circuit holds great promise for significantly reducing the risk of thermal runaway initiating and propagating through the cell.

2.3 Lithium Ion Cell Components and Safety

2.3.1 Electrode considerations

Electrochemical degradation and poor capacity retention are common features of certain lithium-ion chemistries as discussed previously in Chapter 1 for each major cell component. For example, battery safety considerations for the positive electrode; the spinel based structures have shown excellent relative thermal stability and resistance to thermal runaway due to greater heat dissipation but are known to suffer from lower energy and power densities than competing cell chemistries such as the cobalt electrode compositions. There is considerable and diverse research into alternative materials to mitigate this, while improving upon other performance parameters such as specific capacity, cell energy and power density. These innovative active materials require greater understanding and characterisation during operation and failure before widespread commercial acceptance and uptake can occur.

Cells of similar capacity constructed of electrodes of different cell chemistries present significant differences in thermal responses due to the availability of active materials that may cause exothermic reactions which produce greater heat. Such instances have been observed in 18650-cells with silicon doped graphite [92]. Oxygen evolution from thermal degradation of the positive electrode such as LCO present a greater challenge than LFP and the relatively inert Mn^{4+} in NMC for thermal stability considerations.

2.3.2 Commercial cells safety components

Lithium ion cells describe an individual electrochemical energy storage unit, when these are constructed together for larger commercial use, they are typically modules which together form the battery pack. Additional components are required at each stage to ensure stringent safety regulations are adhered to as well as providing safe operating conditions for the cells. Cells of different format contain very different approaches to cell structures due to their intended applications, in this thesis, pouch cells and cylindrical 18650-cells were of interest due to their prevalence in consumer products.

Pouch cells offer advantages in cooling, packing in modules and volumetric energy density to due minimal mass that is inherent with a typically aluminium-plastic multilayer foil exterior which is heat sealed. Consequently, the lack of structural support provided by the foil cell casing, cells are more susceptible to deformation and when operated in abusive conditions, gas induced swells are observed.

Pouch cells are constructed of a repeated planar electrode unit of alternating positive and negative electrodes which are electrically connected via the current collectors welded to the respective terminals at one side of the cell. This cell structure allows for more effective cooling, packing, less strain on the electrode assembly as the layers are flat and greater volumetric (and gravimetric) energy density than cylindrical 18650-cells. To appropriate these characteristic advantages inherent to the cell format, containment and mitigation systems are considerations made at the pack-level design. The lack of structural support was evident in first generation Samsung Galaxy Note 7 battery designs. The negative electrodes bent in the top right-hand corner due to a restrictively smaller battery casing. This caused deformation along the top edge and when combined with high mechanical stress on a thin separator resulted in extreme high-profile failures.

High energy density cylindrical cells of the 18650-format can exceed 3 Ah, for which a myriad of applications exists in aerospace and powertrains in electric vehicles (EVs) with varying high-energy and high-power demands [10–12]. Safety components of commercial 18650-cells have been introduced with the advancement of lithium-ion battery technology, shown in Figure 2-2. As electric vehicles require number of cells that can be into the thousands, it is important for the packaging of modules, cells and electrodes to be as efficient as possible in the cell to maximise energy density.

Cylindrical cell of which the 18650-design has been a popular geometry (ca. 18mm in diameter and ca. 65 mm in height) consists of a spirally wound assembly in housed in an electrolyte filled usually stainless steel cylindrical casing which provides a protective housing. This differs prominently from pouch cells as the steel casing provide significant advantages in mechanical properties, however, this strengthened exterior structure can also transform the cell into a pressure vessel with the generation of gases within. The positive electrode current collectors are welded together above the electrode assembly and is connected to the positive exterior terminal known as the cell cap. The negative electrode current collectors are commonly welded together below the electrode assembly to a much larger current collector welded to the inside cylindrical surface of the stainless steel casing. These terminals are isolated by an insulative ring surrounding the cap at the top of the cell.

The Current Interrupt Device (CID), PTC, top vent disk are common components found in the 18650-cell design. These dynamic structural changes induced by the activation of 18650-cell safety devices have been investigated by several authors [86,96,103,165,170,171]. The PTC shown in Figure 2-2, is located just under the positive electrode cap acts as a method of limiting the current flow from the cell. During ambient room temperature, the thin PTC is a polymer washer with an embedded conductive path of particles. However with increasing temperature due to Joule heating (ca. 125 ^{o}C), the resistance of the PTC increases dramatically as the polymer changes from a crystalline to amorphous state, thus reducing the current flow.

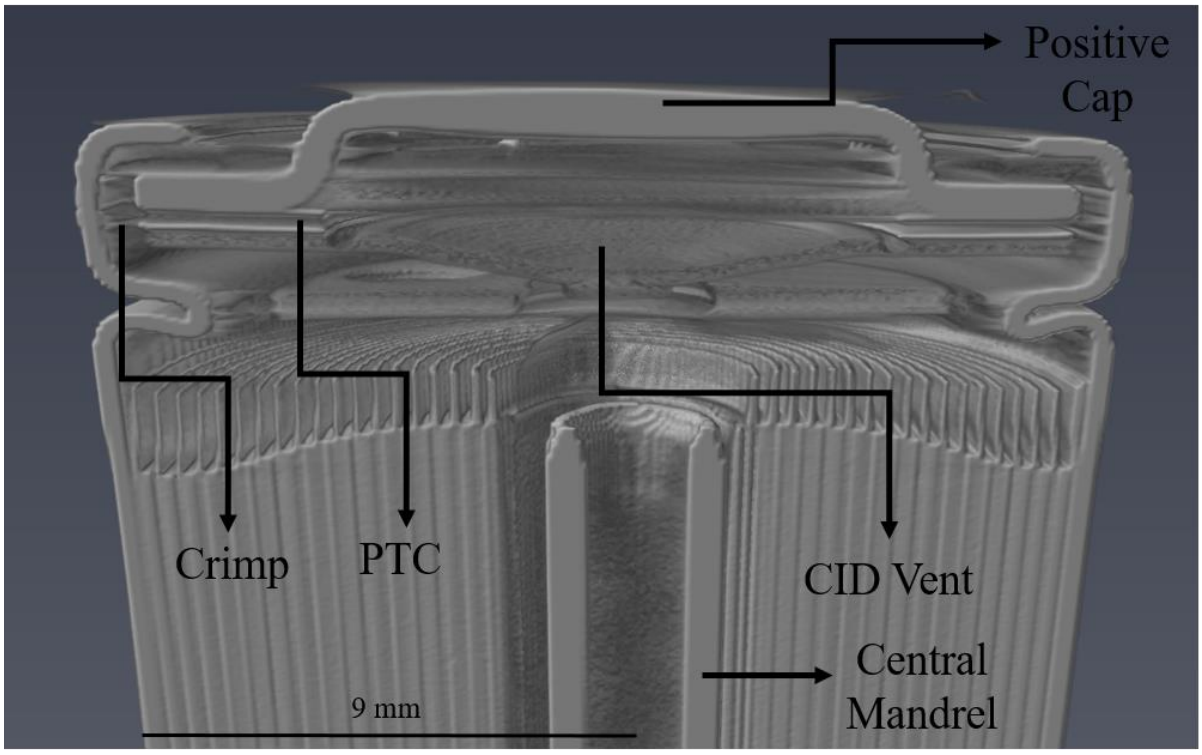

Figure 2-2: Common safety components in the header of a Moli Energy ICR-18650J.

The CID and top safety disk vent shown in Figure 2-2 acts as an internal pressure valve to prevent excessive gas generation and the stainless steel housing transforming the cell into a higher risk pressure vessel. The pressure increase within a cell due to the gas generation reactions, the product of which accumulates at the crimp below the PTC and the CID vent, during electrolyte decomposition and other exothermic thermal runaway reactions. The top safety vent disc bursts at a given pressure pre-determined, causes disconnect of the conductive path. Many commercial designs exist which can lead to different mechanisms to disrupt the flow of current. Typically a thin disc of aluminium with a depression in the centre, the CID is located between the positive header and the electrode assembly. At the centre of the spiral wound electrode assembly, a hollow central mandrel can be found which typically provides structural reinforcement to mitigate external crushing forces and provide a facile path for gases to flow to reach the CID vent during failure.

2.4 Thermal Runaway Failure Initiation Methods

2.4.1 Introduction and types of failure methods

Failure or abuse methods typically fall into three broad categories; thermal, mechanical and electrical abuse (external or internal short circuiting or excessive charge or discharge) with the majority of failure testing utilizing the first two [94]. However, disadvantages exist with these techniques [94,95,97,108] as the worst-case scenario of failure (whereby all the energy capacity is ejected in one direction), cannot be reliably induced. This is especially true for failure produced as a result of thermal abuse as there is a lack of precision in determining when and where thermal runaway will initiate. There are other experimental limitations which must be considered, but most prominent is the time taken to achieve the critical temperature to initiate thermal runaway as electrolyte may evaporate from initial venting. A drying electrode assembly [97] also poses challenges to other failure methods such as oven tests or accelerating rate calorimetry. These drawbacks are not observed in FTRC nail penetration failure tests, however: as a consequence of the nail penetration of the electrode assembly inside the cell casing, the nail provides a heat sink path from the cell, decreasing the total energy available released in thermal runaway thus a less violent failure event [93,109,110]. The third means of inducing failure is electrically, this has been previously performed by a hard internal short-circuit [93,94,111], propagating widespread thermal runaway throughout the cell thus impeding the escape of electrolyte via venting. During the process of failure, surface temperatures in excess of 600 ˚C are common for an event which elapses within a few seconds [93–95]. Therefore in battery packs, the ability to forecast violent ruptures and failures will provide key insight into the safety and performance of such powertrains [112].

Another influential factor in determining the cell's thermal runaway behaviour is understanding the cell chemistry and influence of the components during operation, abnormal conditions and failure. The characterisation of this is crucial, as some chemistries and internal cell components are inherently more thermally stable than others; this acts as a basis from which inherently safe design can improve upon. [17,63,64].

The severity and consequences of these failures have provided the impetus for the development in rigorous *in-situ* and *operando* characterisation of failure in energy-dense high performance cells. The risks and consequences associated with batteries have increased with the greater capacity, energy and power densities seen in commercial applications, thus characterisation techniques to accelerate research into innovative cell designs and integrated safety mechanisms are crucial. High energy density batteries

may be prone to catastrophic failure events rather than gradual performance decline and manufacturers need to be able to guarantee the safety and performance of a complex electrical power train, in a simple and cost effective manner.

2.4.2 Cell Abuse Testing and Safety Standards

High profile failure of lithium-ion energy storage which have been well reported provided impetus for widespread review and implementation of compulsory safety standards for operation, storage and transportation with abuse test requirements for cell acceptance before approval in applications. There are many certifications standards, notable examples are: UN 38.3, IEC 62133-2:2017, UL 1642 with regards to abuse tests, operation, storage and transportation [14].

UN 38.3

Cell response is evaluated at temperature extremes are evaluated between at -40 ^{o}C and 70 ^{o}C, whereby, cells are stored at -40 ^{o}C for six hours. Then six hours at 75 ^{o}C for a total of ten cycles, this changes to 12 hours for larger format batteries. A pass given for no leakage, venting, rupture or fire and the cell retains 90% of OCV from starting at full SOC OCV.

Mechanical abuse aims to simulate impact during shipping of lithium-ion cells; the impact test consists of a 9.1 kg bar of 0.158m diameter is dropped from a height of 0.61 m on the cell. A pass is given when the external casing temperature remains below 170 ^{o}C, with no fire or rupture for six hours after the test. Crush abuse tests also exists, with the cell crushed between two flat surfaces at rate of 1.5 cm/s until force reaches 13 kN or voltage drops by 0.10 V or cell deforms to more than 50% of its original thickness. The cell casing should remain below 170 ^{o}C

UL 1642

For thermal abuse tests, cells are to be heated in a convection oven from 20 ^{o}C to 130 ^{o}C and remain there for 10 minutes at a rate of 5 ^{o}C a minute before returning to 20 ^{o}C. Cells should not explode or catch fire. For mechanical abuse, both crush and impact tests are the same requirements as the UN 38.3 standards.

IEC 62133-2:2017

Thermal abuse and mechanical abuse crush tests for IEC 62133 are the same specification as the UL 1642 standards.

2.4.3 Accelerating Rate Calorimetry (ARC)

A widely used evaluation method for thermal runaway characterisation, the “heat-wait-seek” too facilitates a specified rate of thermal heat and measures the temperature through external thermocouples attached to the lithium-ion cell. Cell temperature measured can be expected to increase linearly with specific heat capacity and thermal input, however, at higher temperatures – internal cell components are observed to decompose with thermal abuse. These structural changes are exothermic overall, thus heat-generation from within the cell increases the cell temperature in excess to the expected amount from the resistance heaters. This excess self-generated heat is measured as a spike in the rate of temperature increase and indicative of these processes at specified temperatures.

ARC methods for determining the cell originated heat generation has been insightful to the temperatures and processes which produce exothermic ejection, which can be correlated with other methods to deduce the architectural phenomena responsible – there are inherent disadvantages with the method [94,95,97,108]. Examples such as inducing the worst-case scenario of failure, whereby all the energy capacity in released in one direction, or precision in determining where thermal runaway will initiate. Experimental limitations also arises which must be considered, most prominently the drying electrode assembly as a result of prolonged heating methods to measure cell-generated heat accurately. ARC requires a significantly extended amount of time to achieve critical temperature to initiate thermal runaway and thus the electrolyte may evaporate from initial venting. Other issues with ARC for applicability for work presented in this thesis is the suitability for beamtime experiments, where the imaging stage has a relatively lower maximum weight requirement, X-ray transparency also an issue with the typical steel or denser construction and difficulties with high rate acquisition acoustic spectroscopy experimental set-up. These considerations and characterisation methods are described in Chapter 3 and the relevant results section later.

2.5 Summary

The internal responses of the cell to the abuse methods are described in this chapter for typical commercial lithium-ion battery components with the reactions highlighting the significant volume of combustible gases ejected at high temperature. Cell safety components, cell testing standards and ARC are reviewed to provide an understanding of the present lithium-ion battery safety landscape which provide a standard for cell safety investigations to be based upon and perhaps results which stem from such work can inform and revise such standards with the development of new active materials.

The effects on component failure through exothermic degradative reactions, propagation of the micro-scopic short-circuit, physical and mechanical considerations within the electrode assembly of the lithium-ion battery are discussed here and can be used as a typical comparative standard with commercial components to those investigated in the later results chapters. The understanding of the interactions between components at each temperature range and the chronological sequence provide insight into the severity or absence thereof during failure.

3 Review of Characterisation Techniques and Methodology

Background theory and general experimental methodology are discussed for the techniques used in this thesis. Specific experimental set-ups and particular nuances for each experiment are elaborated further in each respective results section.

3.1 X-Ray Imaging

3.1.1 Introduction

The term X-ray was referred to as such by Röntgen in his initial report, 'On a new kind of ray: A preliminary report' in 1898 [181], when he first observed the characteristic fluorescent glow from an unknown new type of ray or electromagnetic wave being emitted from his cathode-ray tube. The term X was used to refer to the radiation (Bremsstrahlung), and stemmed from mathematics where X denoted an unknown.

Since then, rapid advancement in technology has produced modern X-ray apparatus capable of diverse applications, from medical imaging to non-destructive imaging diagnostic tools for materials. Now, with achievable resolutions in the tens of nanometres range available in laboratories, and the processing time for image development during reconstruction for 3D X-ray CT scans quicker than ever, micro-structural imaging has never been so advanced. Equipment and complementary software has seen X-rays finely specified to fulfil the specific criteria for every scan required. For example, X-ray CT settings such as the accelerating voltage, current, exposure time, rate of imaging acquisition, resolution reconstruction algorithms, are crucial to spatially resolve accurately the internal microstructure obscured by complex architecture.

The developments in X-ray technologies has seen understanding, characterisation and subsequent designs for lithium-ion batteries improve immeasurably, with investigations ranging from real time 4D tomography of thermal runaway and post-mortem analysis after failure, to electrode characterisation at the microstructural level. Visualising details such as structural degradation on the micro- and nano-scale, evolution of particle morphology and investigating the mass transport phenomena has seen consistent advancement of performance parameters of active materials.

A plethora of X-ray systems and the respective capabilities are available with varying brilliance and photon fluxes with comparable spatial resolutions. Synchrotron imaging offers the highest temporal resolutions with over 20000 frames per second and versatile imaging modalities. However, experiment time at such synchrotron beamline are extremely limited hence the highly competitive proposal system for evaluating research and providing access to such facilities. In lithium-ion batteries, catastrophic failure occurring over sub-second time frames can be visualised in three-dimensions in real-time and such rapid structural evolutions detail important information regarding failure. However, such facilities are very expensive which is reflected in the competitive application process for short periods of allocated use, which for commercial research can be very expensive. Thereby, justification for experimental plans at each X-ray source should be carefully considered with respect to the objectives of the experiment.

Many applications will favour spatial resolution rather above temporal resolution, and laboratory imaging sources are available which offer competitive spatial resolutions with synchrotrons. These X-ray CT systems are more readily accessible, available and come with more modest operating costs. Thus, laboratory radiography and tomography has seen greater application due to the accessibility. Disadvantages however, include a much lower photon flux and consequently slower acquisition times. In this work, synchrotron and laboratory X-ray imaging has been applied, and therefore both modalities are considered in the following sections.

3.1.2 Synchrotron Originated Radiation

Synchrotrons are specialised particle accelerators, which accelerate thermionically emitted electrons through sequences of magnets until they asymptotically approach (nearly) the speed of light, typically with energies in the order of GeV. Subsequently, the electron is released with a polygonal circulating trajectory guided by a large electromagnet framework once released into a closed vacuum primary storage ring [182] (which minimises electron scattering via air molecules). The structure of the bending magnets at each angled section of the storage ring accelerates the electrons and changes the electron direction of travel hence the polygonal trajectory. Electromagnetic waves of high intensity radiation, predominantly in the form of X-rays, are a result of lost kinetic energy from the electron during deceleration (following the curved path) in the magnetic field, known as synchrotron light.

Early particle accelerators did not appreciate synchrotron light, which was considered an inconvenient by-product, however synchrotrons have evolved with technology and are widely used in a range of scientific and engineering research.

Diamond Light Source (DLS) and The European Synchrotron Radiation Facility (ESRF) are third-generation synchrotrons using special arrays of magnets called insertion devices, which cause the electrons to follow an undulating path, creating even more *brilliant* radiation – ten orders of magnitude greater than laboratory-based rotating target CT systems – where brilliance, *B* is defined by Equation 1-1:

$$B = \frac{\left(\frac{photon}{second}\right)}{(mrad)^2(mm^2 source\ area)(0.1\%\ bandwidth)} \quad [3\text{-}1]$$

Electrons are added to the ring every ca. 10 minutes in a process known as ‘top-up’ thus allowing synchrotron light delivered to the beamlines to be more stable and to retain maximum intensity. Electron beam energy in the closed vacuum storage ring determines the X-ray spectrum emitted to each beamline and the current influencing the X-ray flux.

Beamlines allow the division of the storage synchrotron to be accessible to diverse experimental research. Beamlines typically consist of three ‘hutches’; a control cabin, experimental hutch and an

optics hutch; the Bremsstrahlung from the storage ring enters the ‘front end’ of the beamline via the bending magnets, where the beam is collimated and low energy X-rays are filtered out. Proceeding onto the next stage, the beam is refined to the requisite specifications of the users, through a series of filters, mirrors, mono-chromators and slits to potentially produce a parallel polychromatic or monochromatic X-ray beams. Monochromatising the beam is typically required when beam hardening occurs during acquisition of radiographys during X-ray tomography, whereby lower energy X-rays experience greater attenuation. Samples are placed in the experimental hutch for imaging meanwhile the users observe and set beam configurations in the control hutch.

3.1.3 X-ray Imaging Theory: Matter Interaction

As X-rays pass through a material, due to absorption and scattering of the incident radiation beams, the number of photons (intensity) of X-rays decrease exponentially. The degree to which this occurs is quantitatively described by the linear attenuation coefficient (μ), defined as the fraction of intensity lost due to absorption or scattering per unit thickness of material. For an incident, monochromatic X-ray beam of intensity, I_0, the expected intensity, I, at a distance, η, in the incident direction into a material is given by Equation 1-2:

$$I(\eta) = I_0 e^{-\mu\eta} \qquad [3\text{-}2]$$

The correlation is known as Beer's law of attenuation and is applicable for monochromatic X-rays and for a non-divergent beam where scatted radiation is completely removed. Generally, the linear attenuation coefficient (μ) is given by:

$$\mu = \frac{\rho N_A}{m_A}\sigma_{tot} \qquad [3\text{-}3]$$

Where ρ is the density, N_A is Avogadro's constant, m_A is the atomic molar mass, and σ_{tot} is the total photon atomic cross section. Attenuation coefficients are well documented and can be referred to [183,184] for prospective samples to estimate the suitability of X-ray systems.

The total photon atomic cross-section (σ_{tot}) and thus the attenuation coefficient (μ) is determined by the extent to which elastic and inelastic interactions, as well as pair production and photoelectric emissions, occur upon interaction with incoming photons. The most significant contributions to attenuation in the keV range are elastic, inelastic (Compton), and photoelectron emission.

Equation 3-4 defines the substantial contributing components of the total photon atomic cross-section (σ_{tot}) and therefore the attenuation coefficient (μ). The mechanisms by which the incident photons are attenuated by are elastic (σ_{el}), inelastic (Compton, σ_{comp}) interactions, pair production, photoelectron emissions (σ_{pe}), with the most significant shown in Equation 3-4:

$$\sigma_{tot} \approx \sigma_{el} + \sigma_{comp} + \sigma_{pe} \quad [3\text{-}4]$$

Elastic scattering occurs when an incident electromagnetic photon wave conserves wavelength and energy but changes direction as the interacting particle remains in its ground state. Compton scattering occurs when a photon of lower energy is emitted upon interaction due to the transfer of energy. Photoelectron emissions are due to the photoelectric effect, whereby an ejected electron with energy equal to the energy of photon is emitted minus the binding energy. A characteristic electromagnetic wave is emitted once another electron fills the remaining hole left behind. The extent of each attenuating interaction mechanism is dependent on the atomic number of the material involved and the wavelength of the incident X-rays, thus the composition and phase identification within a sample can be deduced.

In a lab system, the greater the accelerating voltage of the cathode ray tube, the greater the kinetic energy of the electron thus the greater the converted energy is to radiation. Hence there is a dependence of energy level of Bremsstrahlung spectrum on the accelerating voltage of the cathode ray tube. The emission spectrum also contains signature emission peaks from collisions between electrons of the target metal and the electron beam, with characteristic emissions akin to de-excitation of electrons (radiative electron relaxation), whereby the emitted radiation is equal to the difference between electron orbital energy levels due to a photoelectron emission. K_α *and* K_β representing subsequently high energy outer orbital electrons filling in the inner orbital vacancy (L-orbital to K-orbital and M-orbital to K-orbital respectively). Therefore, in laboratory based systems, where X-rays are produced by cathode ray tubes, the spectrum will contain characteristic emission peaks from the target electrode overlaid on the Bremsstrahlung. Higher voltages used to produce characteristic emission spectrums will provide a greater relative intensity.

3.1.4 X-ray Computed Tomography (CT)

Hounsfield conceived and developed X-ray CT publishing the landmark manuscript 'Computerized transverse axial scanning (tomography): I. Description of system' in 1972. This revolutionised the medical imaging field during this time and led to the award of a Nobel Prize. He successfully demonstrated that by acquisition of 2D orthogonal slices at tiny angular increments around the central vertical axis of rotation it would be possible to produce a 3D reconstruction.

In the resultant set of images from the X-ray acquisition, known as radiographs, the species within the sample are identified based on their attenuation coefficient, which is a function of the density ρ, the atomic molar mass m_A and the energy of the incident photon shown in Equation 1-2 and Equation 1-3.

Before reconstruction can begin, rectifications of the radiographs need to be made through flat-field corrections which remove visible artefacts on the radiographs (which would be seen as ring artefacts in later tomograms). Thus, each radiograph or projection at each incremental angle proceeds through correction to ensure the correct intensity due to attenuation by the sample is acquired. Additionally, potentially defective pixels are present but are removed in the corrected image and subsequent reconstruction following flat field correction.

In this work, reconstruction is done using the computationally efficient mathematical process of Filtered Back Projection; the corrected radiographs are used to form a 3D image of the material from multiple images taken at equal angular increments. In the resultant 3D image, the position and shape of features within a sample can be precisely identified. More complex samples with irregular shape and overlapping geometries require additional projection angles as determined by the Nyquist-Shannon theorem, otherwise significant interference between transmitted X-rays may occur and thus there may not be sufficient contrast to distinguish finer features. Zhao *et al.* [185] discusses a suggested general 'rule of thumb' for cone beam CT where the minimum number of projections (N_{proj}) should be such that the angular increments between projections ($\Delta\theta$) amounts to a distance at the edge of the field of view (FoV) equal to the voxel size (b_{vox}) defined in Equation 3-5:

$$N_{proj} \geq \frac{2\pi}{\arctan\left(\frac{2b_{vox}}{FoV}\right)} \quad [3\text{-}5]$$

Before X-ray CT reconstruction of radiographs, there is a decision on the number of radiograph projections required. By decreasing the incremental angles at which each projection is taken, and thereby decreasing the total number of projections (radiographs) artefacts can be identified.

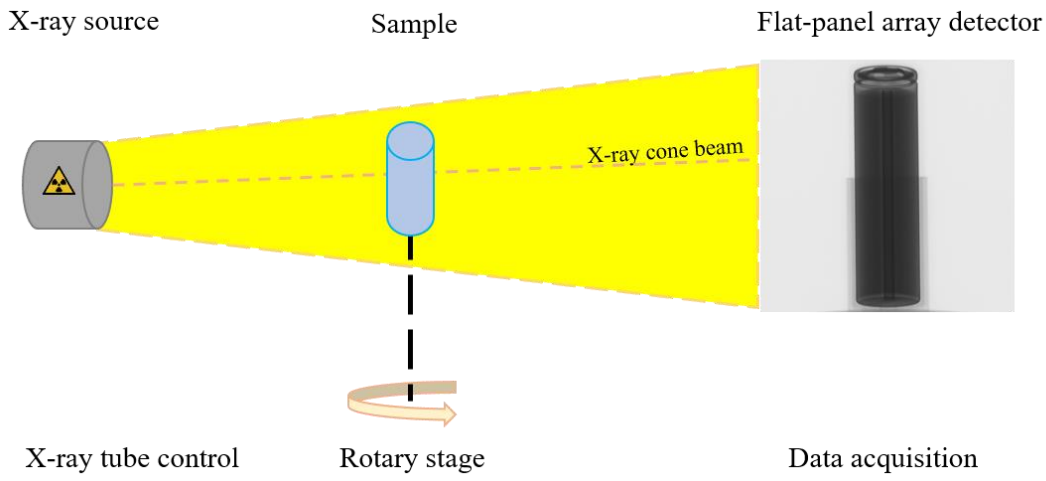

Figure 3-1: A typical rotary stage laboratory based X-ray CT system configuration.

The second step in the Filtered Back Projection approach is the application of a filter to remove low frequency blurring or noise – components of which are investigated further with increasing number of projections by Zhao *et al.* [185]. In Figure 3-2, the significance of the number of projections can be observed; although the global structure, such as the shape of the cylindrical electrode assembly can be seen at 180 projections, there is much noise therefore the double anode and cathode layers are not visible. Further detail, reduced artefacts and improved signal to noise is obtained with large projection numbers.

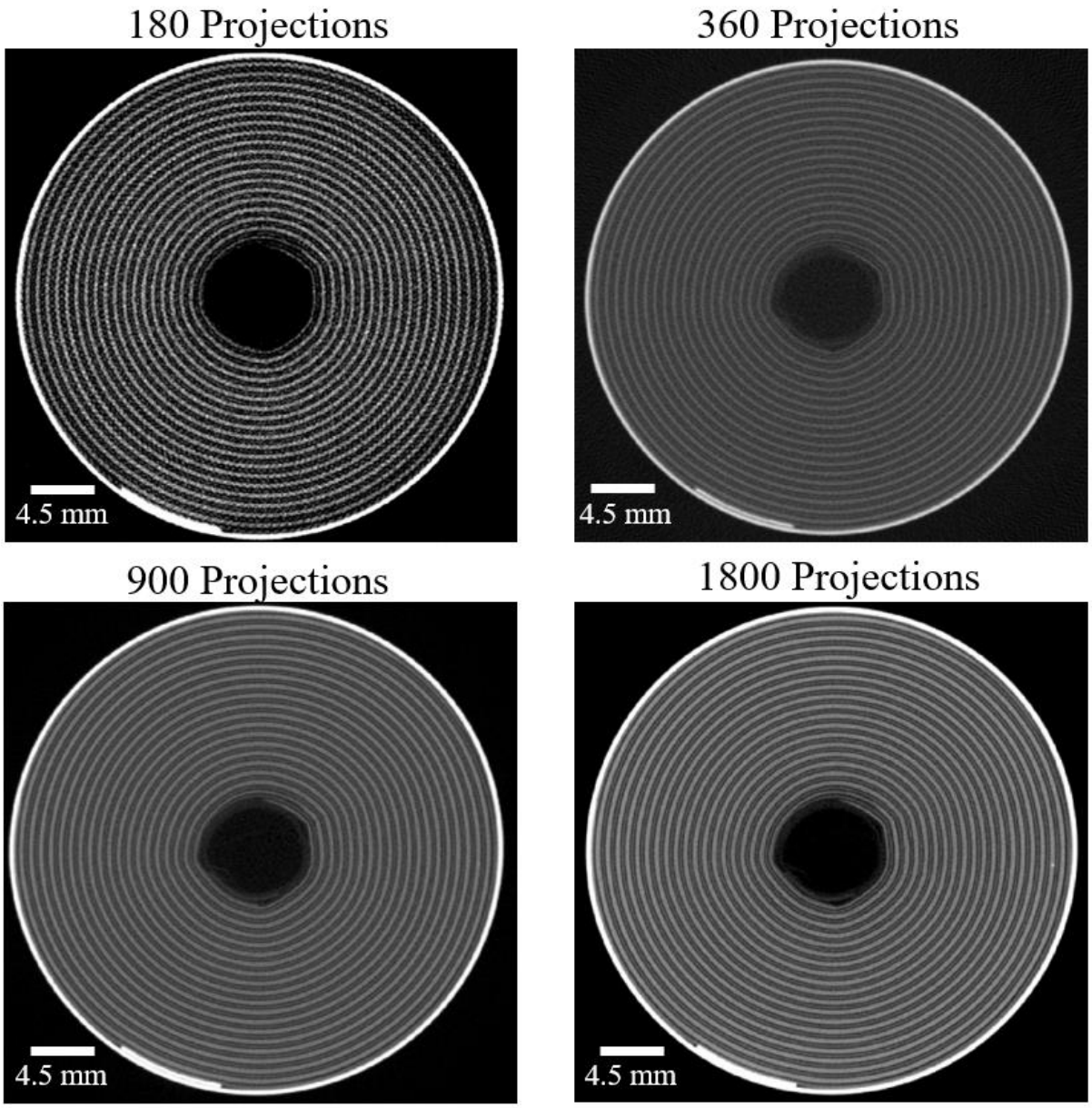

Figure 3-2: Single XY orthogonal slices from flat field corrected reconstructions of an 18650-cell showing structural detail and noise as a function of number of projections used for projection acquisition. Pixel size was 35.5 µm, the width of the cell was 18 mm.

3.1.5 X-ray Computed Tomography Laboratory Systems

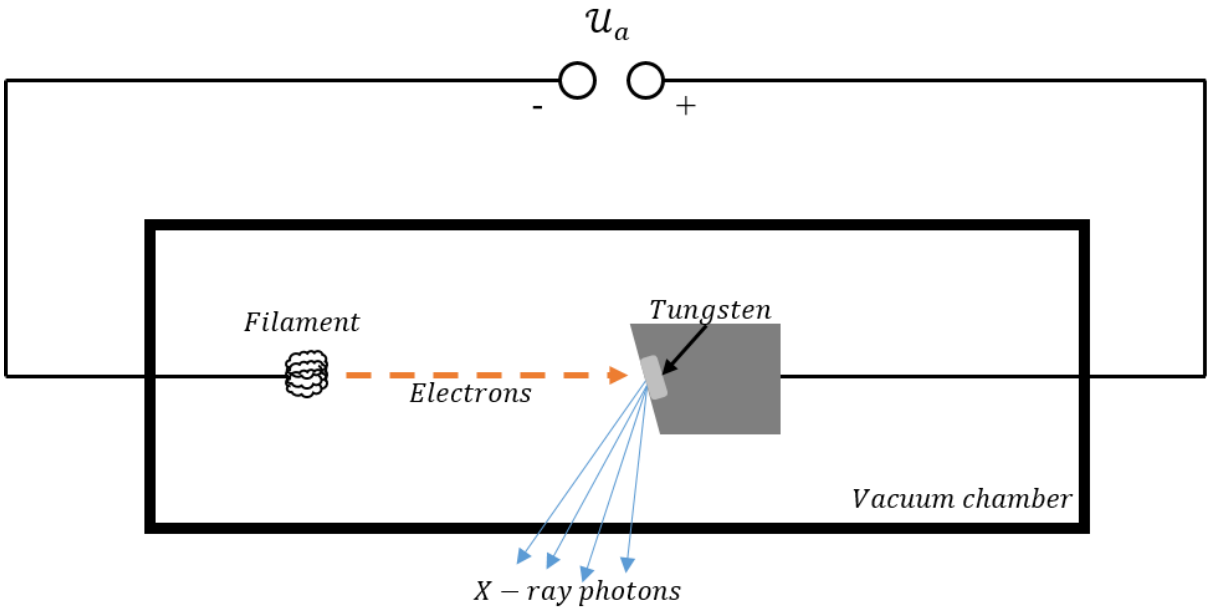

Figure 3-3: Illustration of the basic components and operation of an X-ray tube system, where U_a is the accelerating voltage.

Virtually all sources of X-rays in laboratory-based CT systems employ the acceleration of electrons generated via thermionic emission from a hot filament, into a metal target, shown in Figure 3-3. Electrons interacting with the metal target produce two differing emissions: continuous Bremsstrahlung and characteristic fluorescence radiation. A tungsten source produces one of the highest continuous Bremsstrahlung radiation spectra in commercial CT systems, whilst the melting point, thermal stability and mechanical properties ensure longevity as a target source. A filter such as 0.1 mm copper or aluminium reduces the low energy distribution of the Bremsstrahlung. For a tungsten tube, no characteristic radiation is produced when the binding energy of tungsten is exceeded.

In this thesis, two lab-based X-ray CT systems were used: the Nikon XT H-225 (Nikon Metrology, UK) and the Zeiss Xradia Versa 520 (Carl Zeiss, Pleasanton, CA, USA). Both the Nikon XT H-225 and the Versa 520 were used for X-ray CT at the micro-scale, both providing a divergent cone beam X-ray radiation. The Nikon XT H-225 offers high power (up to 225 W, an accelerating voltage of 225 kV) and a larger FoV but a lower maximum resolution of ca. 3.5 µm. The Nikon uses a PerkinElmer 1620 Detector and offers greater flexibility in sample size and weight, and can produce tomograms within 20 seconds but up to approximately one hour for greater resolution as shown in Figure 3-2. A slot in front of the X-ray source is available for a filter to be placed in to remove any low

energy radiation for contrast. CT Pro 3D provided by Nikon Metrology also facilitated reconstruction of acquired datasets.

The Versa 520 also utilises a tungsten target, however, a lower accelerating voltage from 30 kV to 160 kV for a much smaller sample stage and field of view. 1×, 4×, 20× and 40× objective lenses for optimal magnifications are available, and pixel resolutions of 150 nm are possible. The source-to-sample and sample-to-detector ratios automatically move to the right positions to provide the geometric magnification but can be altered to preference. For example, doing an interior scan of a sample, one may use a 0.4× magnification scan before using the Scout-and-Zoom functionality to narrow down the desired field of view to produce much higher pixel resolution scans. Scans typically take eight to sixteen hours. A carousel of filter materials in front of the source is available, to mitigate beam hardening which is more prominent and again filter out low energy X-rays for samples which are highly attenuating to improve contrast between similarly attenuating materials. The Zeiss XMReconstructor performed Filtered Back Projection algorithm reconstructions on tomography data sets which could account for beam hardening and centre shifts tailored to the user's discretion.

3.1.6 Image Visualisation: Histogram Filtering (Post Reconstruction) and Artefacts

Current software for image analysis and segmentation such as Avizo (Thermo Fisher Scientific, France) allows for 3D visualisation and image analysis. Reconstructions of the radiographic data yields a 3D matrix of information. Each element consisting of a voxel, a volume equivalent of pixel which contains the data regarding the attenuation of material at that point. Using algorithms in modules incorporated within programs like Avizo (Figure 3-4), visualisation of the internal architecture of a lithium-ion 18650-cell is possible. Post-reconstruction software has many applications to imaging techniques not limited to data visualisation capabilities from X-ray reconstructions but also image analysis for data evaluation, 3D reconstruction modelling, material properties computation and 4D visualisation of structural transformations.

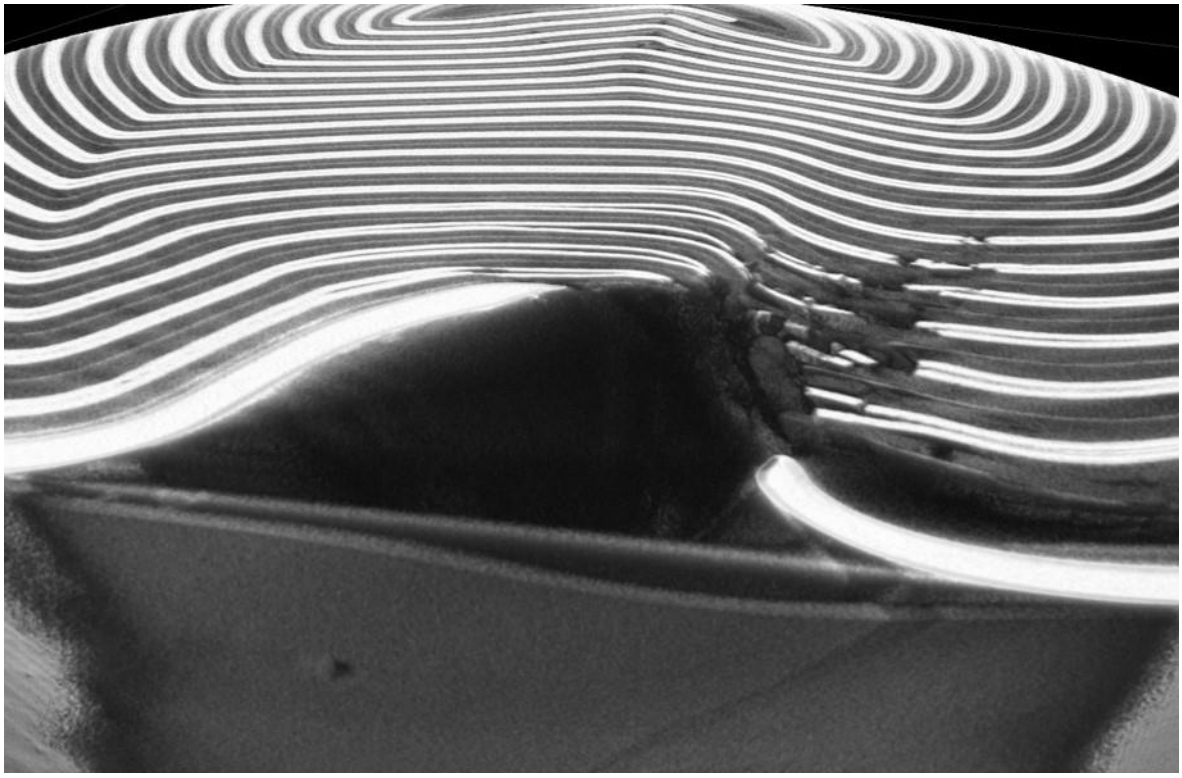

Figure 3-4: A 3D rendering of the internal structure of a commercial 18650-cell, acquisation at 6.05 µm pixel size.

The filtering and later separation of materials based on their attenuation is done by segmentation of materials and is largely based on the differences between their greyscale values. For example, in Figure 3-4 there are distinct phases that differ greatly in greyscale value. The highly attenuating materials are shown as white and the weakly attenuating materials as black. In Figure 3-4, the high contrast difference between the electrode and missing portions permits facile identification of the pore. In Figure 3-4, there

is contrast between for distinct phases, the highly attenuating steel can, the cathode which can be identified as axial brighter streaks in the electrode assembly, the lowly attenuating graphite (the dark axial streaks) can also be identified. Structural information such as deformation and electrode damage can be made visible with proper filtering and segmentation. This is achieved initially by filtering out phases by virtue of their threshold using the histogram of greyscale values of the reconstruction voxel dataset shown in Figure 3-5.

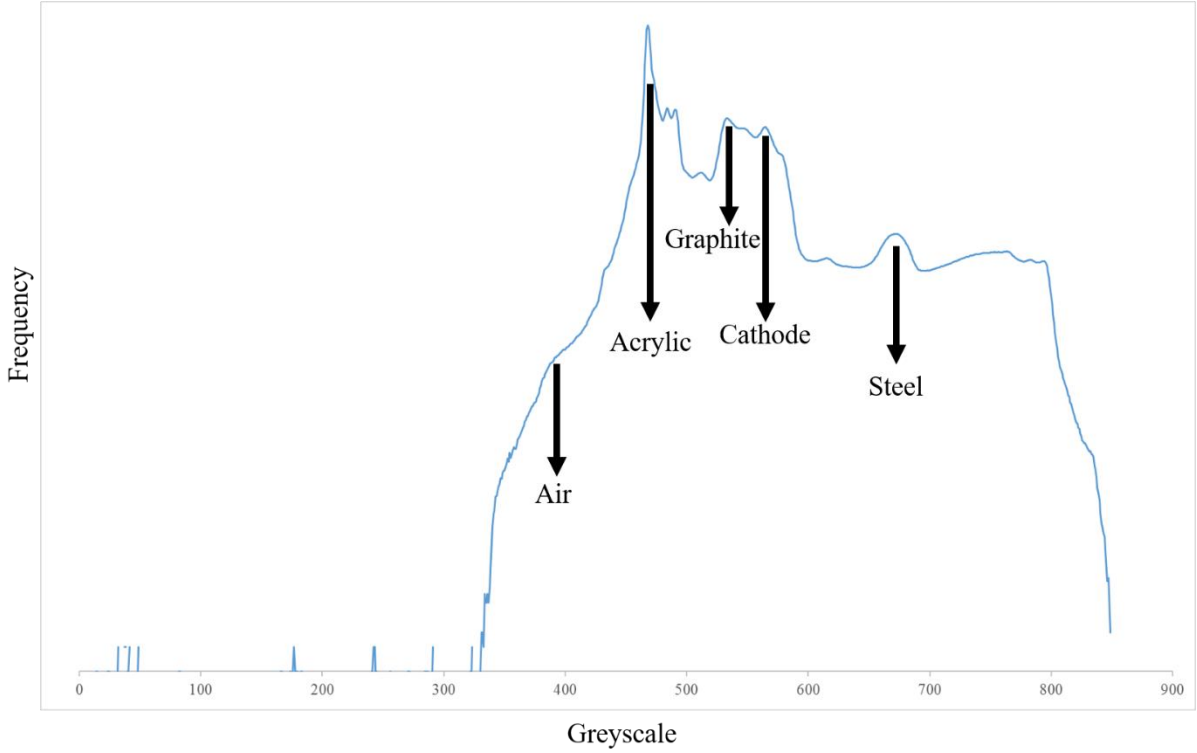

Figure 3-5: Greyscale histograms derived from the counts and the absorption threshold of the materials of substantial amounts within a Moli Energy ICR-18650J cell.

Common difficulties encountered with this process occur via overlapping normal distribution peaks associated with similarly attenuating material, insufficient contrast by low current or exposure time. The use of histogram filtering in visualisation software such as Avizo is shown Figure 3-6. Differences in attenuation can be filtered out with the greyscale histogram, which represents the difference in attenuation of each material in the Moli-Energy 18650-cell. In Figure 3-6(a), none of the components have been filtered out, with each subsequent image, an additional species has been filtered out so it is possible to correlate the greyscale histogram with the material; starting with air in (b), the acrylic sample holder in (c), the light metals in the electrode assembly such as the graphite anode, aluminium and copper current collectors shown in (d), the lithium cobalt oxide is removed in (e) with the inner mandrill and steel cell casing visible only. These two components look to be of similar attenuation in Figure

3-6e, however, by changing the limit of the upper filter, it is possible to differentiate these smaller differences in attenuation.

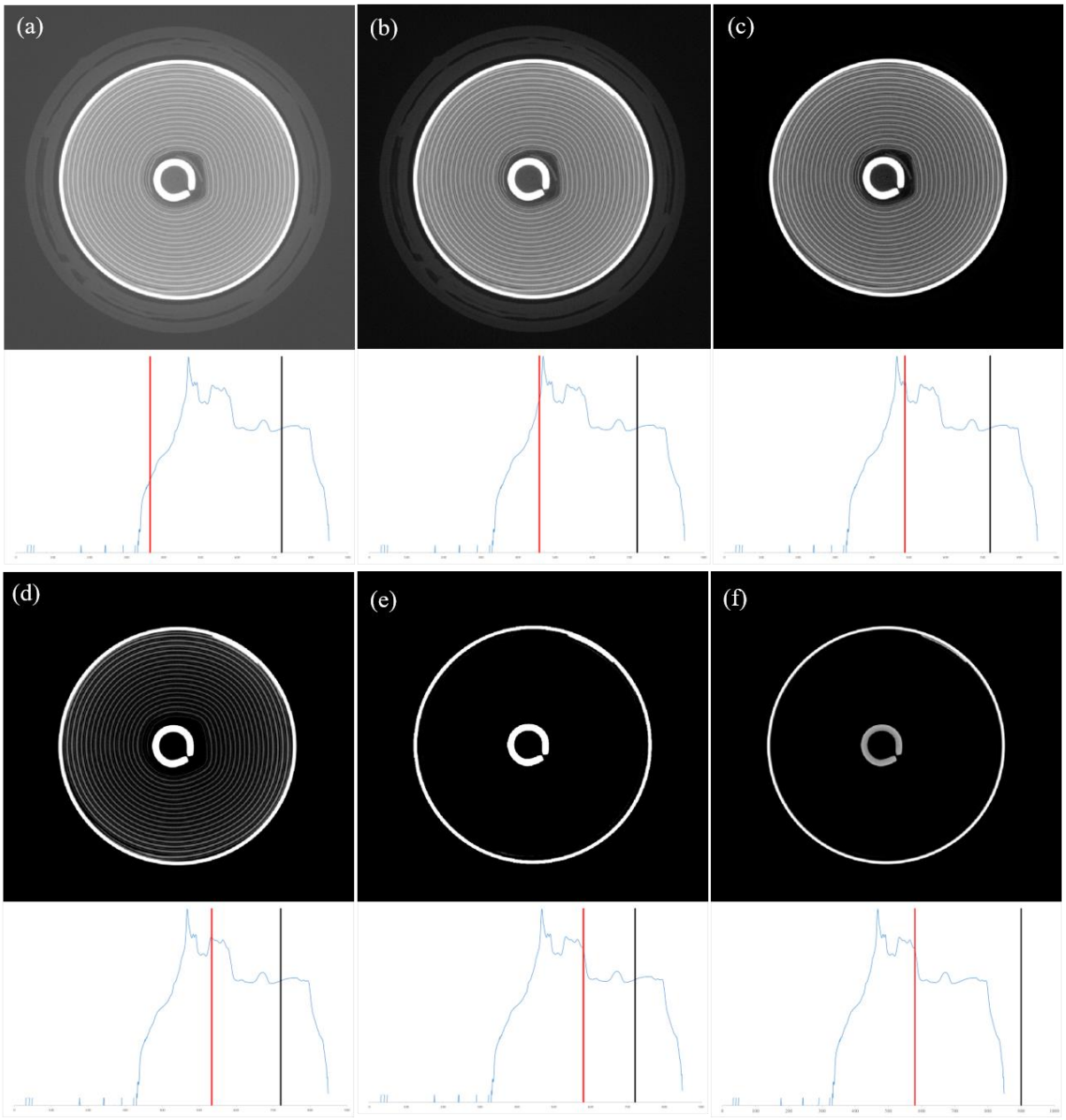

Figure 3-6: Orthoslices from X-ray CT commercial Moli-Energy ICR-18650J cell with different histogram filtering used to highlight differences in attenuation, the filtering is shown by the red line with the histogram area to the right of this line depicted in the corresponding orthoslice. The upper limit of the filter was set at the histogram maximum, 848, the effect of this is shown in (f).

Additionally, tomograms with low pixel resolution often cannot resolve fine features and species or boundaries between similar materials due to the merged greyscale histogram. Beam

hardening due to highly attenuated low energy radiation in polychromatic X-ray beams [186] resulting in ring artefacts [187] and image artefacts [188] are covered in depth by Banhart [189], Hsieh [190] and briefly in Chapter 3.1.2 and Chapter 3.1.3. These artefacts can be mistaken for foreign high attenuating particles or species of different attenuation within a continuous phase.

Ring artefacts can often appear due to streaks occurring from material which may be outside the field of view but still interacts with X-rays which can interfere with detector. Minimising ring artefacts can be achieved via movement of the sample to compare the radiographs with the reference image and at two positions during imaging. A comparison between these frames allows the software to compute and identify the features on the radiographs which are artefacts artificially imposed on the ortho-slice but not actually present in the sample field of view.

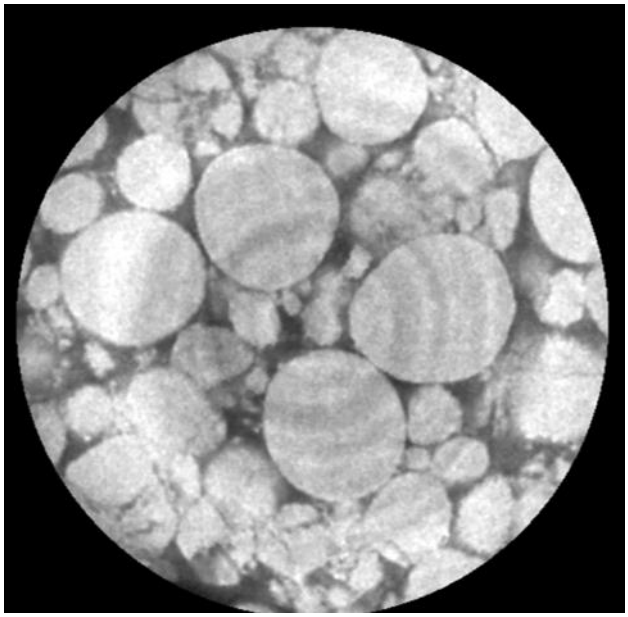

Figure 3-7: Example of artefacts in projections which when reconstruction around the centre rotation axis creates ring artefacts.

The ‘Filter Sandbox’ function can also be applied within Avizo or as an option during reconstruction. A set of algorithms functions can be applied to the attenuation voxels, with the kernel weighting of each filter adjustable to find optimal signal to noise, some filters are discussed in work by Ozcan *et al.* [191].

3.2 Acoustic Spectroscopy (AS)

Acoustic spectroscopy (AS) by use of ultrasonic probing is based on the principle of differing propagation speeds of sound waves through different materials. In this work, ultrasonic waves are transmitted perpendicular to the electrode layers and the reflection caused by material interfaces of different properties are shown in Figure 3-8, with ToF difference, between each reflected signal peak.

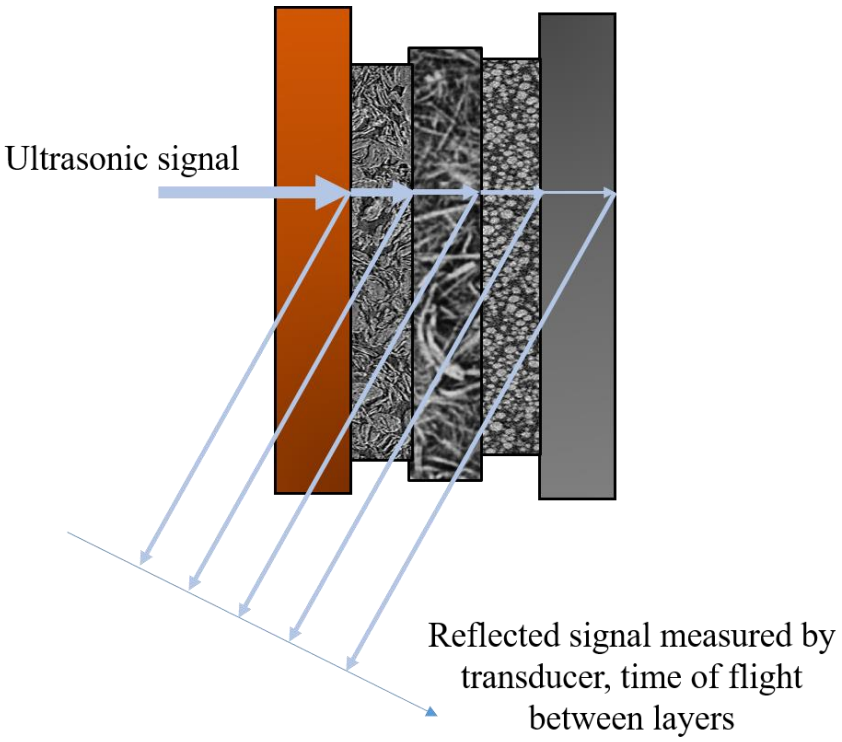

Figure 3-8: As the ultrasonic pulse propagates through each layer, each interface produces an observed reflection, with insight into the state of charge (SoC), state of health (SoH) and mechanical evolutions given by the attenuation and observed ToF shift. The reflections of the ultrasonic signal in this figure are to allow for easier interpretation – in reality, the ultrasonic signal is reflected at all angles in spatially in three dimensions with the transducer only measuring those reflected back to the interface of the sensor whereby the average of each reflection measured by the transducer interface was used for analysis.

Reflections of the propagated ultrasonic wave with ToF differences, can be correlated to a material thickness. These sequences of ultrasonic reflections which are picked up by the transducer, give rise to the waveform signal peaks shown in Figure 3-9. These characterisation acoustic spectroscopy measurement instances are highly dependent on the contact of the transducer to the battery surface, the propagation through use of couplants, the intended region of interested which defines the

voltage applied to the piezoelectric component of the transducer, the ultrasonic amplitude gain, the range to which the reflected ultrasonic signal is observed and thereby the resolution. Not planar surfaces such as cylindrical cells also pose a challenge with interference with the ultrasonic signal echoing around the steel cell casing. These variables along with a consistent contact and applied pressure behind the transducer to ensure uniform conditions for each measurement pose a challenge experimentally, as expounded upon initially in preliminary acoustic spectroscopy work by Copley *et al.* [192].

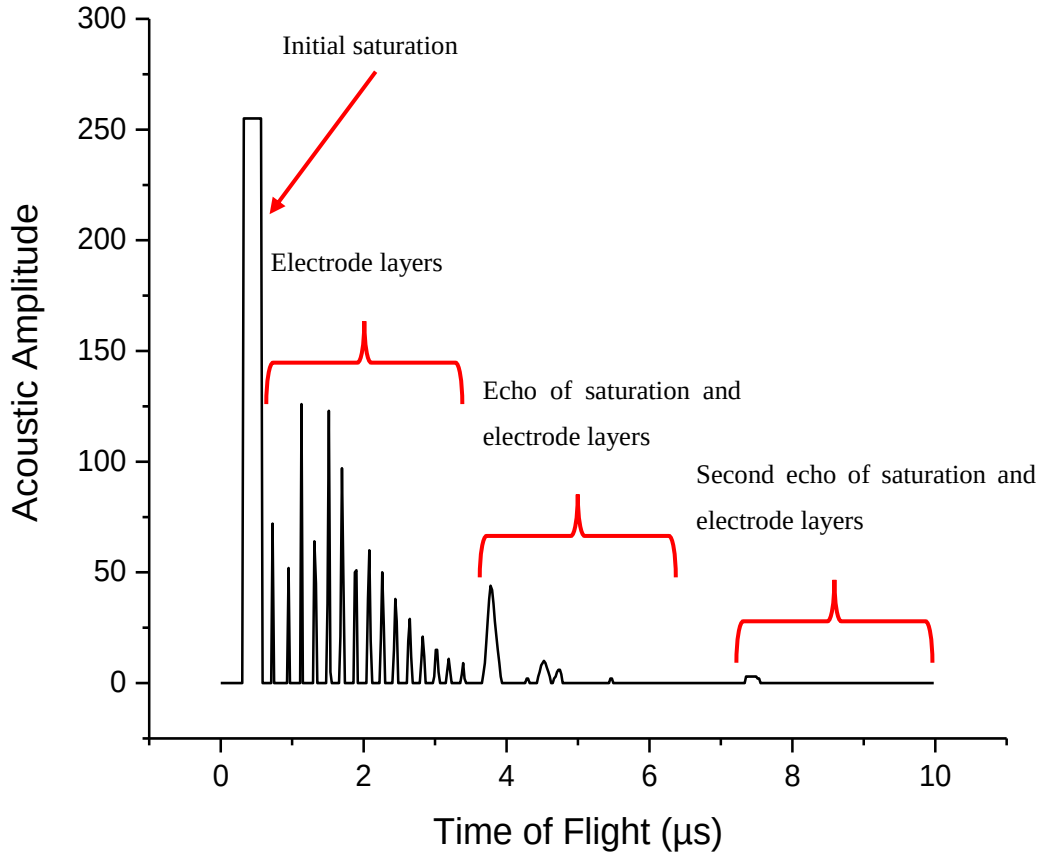

Figure 3-9: The initial waveform typically observed at the start of an experiment using AS probing, this data set is a static acoustic ToF response with continuous acquisition providing the ToF shift analysis. AS data is plotted as a spectrogram for time resolved AS analysis with the correlative X-ray imaging and X-ray CT.

AS is applicable in circumstances when materials are not stressed in tension or compression beyond their elastic limit. The relationship between the speed of sound (c) of the ultrasonic wave used in AS, is based upon elastic modulus (E) and density (ρ) as defined by the Newton-Laplace equation shown in Equation 1-6.

$$c = \sqrt{\frac{E}{\rho}} \quad [3\text{-}6]$$

The difference in time of flight between interfaces is also dependent on the thickness of each layer, with a thicker layer producing a proportionately delayed ToF. Hsieh *et al.* [193] have previously discussed the importance of material density on acoustic wave propagation in electrode assembly materials. Robinson *et al.* [194] inferred changes in electrode locations as a result of changes in the acoustic signal at the same SoC. In addition to ToF shifts, another important change in AS signals is the variations in acoustic intensity is known as attenuation. When the waveform transmitted through each material or medium is scattered, reflected and/or absorbed by different extents, the acoustic impedance of a system ΔZ, as a function of the change in density $\Delta\rho$ and the elastic modulus E, is given by:

$$\Delta Z = \sqrt{|\Delta\rho|E} \quad [3\text{-}7]$$

Due to the properties of gases, its attenuation is much greater than solids or liquids, thus resulting in a dramatic reduction in transmission. This is shown as a reduction in acoustic intensity or loss of reflected signal during AS analysis. Quantifying these values through the electrode assembly with heterogeneous lithiation at realistic C-rates at different SOC presents a challenge due to the amalgamation of materials in the electrode assembly. Moreover, during the complex process of thermal runaway reactions, transient electrode architectural changes and the time scales involved increase this difficulty. As such, analysis of the acoustic spectrogram through relative changes in attenuation (acoustic amplitude represent by colour intensity) and the time of flight (the speed of sound propagation through the layers) are used to link spectrogram characteristics to the sequence of events that occur during thermal runaway.

Hsieh *et al.* [193] introduced the capability of AS to determine SoC and the SoH of pouch cells at low C-rates (C/5, C/10, C/20), given prior acoustic measurements and voltage correlation to deduce relative ToF shift. Models developed by Davies *et al.* [195] displayed robustness in predicting SoC to 1 % accuracy for intact and damaged cells due to shifts in the transmitted ultrasonic signals which was attributed to variations in bulk moduli and electrode density.

Spatially resolved acoustic ToF characterisation by Robinson *et al.* [194] has shown promise in probing the internal structure with SoC. Further spatially resolved ultrasonic measurements conducted

by Chang *et al.* illustrated local variations in phase through the cell thickness with varying C-rates, with lithium metal plating near the welded tab locations exhibiting significant amplitude attenuation [196]. This work was furthered by Bommier *et al.* [197] with operando ultrasonic probing, *ex situ* characterisation studies and post-mortem confirmation of lithium plating. As labelled in Figure 3-9, echo peaks can be observed during acoustic probing, whereby the ultrasonic pulse has travelled through the entirety of the cell and reflected off the surface behind, typically the testing bench, and an echo is formed. The cumulative time of flight attenuation due to cell properties changes within the probed region and can be observed and used for bulk temperature analysis as shown by Owen *et al.* [198]. Their work decoupled temperature effects and SoC through material property changes independently of the rate of operation on AS characterisation.

Other broader applications of acoustic characterisation can be found in the wider electrochemical energy storage literature not limited to ultrasonic pulses and lithium-ion batteries. Ladpli *et al*. [199] used algorithms to decompose the acoustic waveforms into simpler constituents to analyse the acoustic-electrochemistry phenomena to predict SoC and SoH. Gold *et al*. [200] have also utilised ultrasonic waves at 200 kHz to resolve SoC determination over one cycle. The use of the lower frequency facilitated the analysis of a graphite electrode by analysis of the slower, compressional waves' arrival times at different states of charge. Also characterisation of a vanadium redox flow battery at different SoC has been demonstrated by Chou *et al*. [201]. The internal structure and flow characteristics in polymer electrolyte membrane water electrolysers were imaged by *Maier et al.* [202], whereby acoustic intensity decreased with increasing amount of gas production. A recent review of acoustic characterisation methods conducted by *Majasan et al.* [203] surveys broader applications and prospective suitability for energy storage technology not limited to lithium-ion batteries.

The principles of acoustics spectroscopy is based upon propagation and attenuation of ultrasonic signals are used, constructive and destructive interference of signals are inherent to the act of propagation and reflection. This is observed in Figure 3-9, where after the initial saturation, the acoustic amplitude of the characteristic waveform varies between higher and lower acoustic amplitude before steadily decreasing due to interference. Thus, in analysis, it is important to distinguish this attenuation of the acoustic amplitude from the time-of-flight delay associated with density and elastic modulus. Transducers are typically operationally limited in temperature window due to the construction from less thermally stable components for typical commercial use, high temperature grade couplants whether liquid or solid based can provide thermal protection for the measurement sensor simultaneously with the propagative contact purpose. Preliminary tests conducted in a range of temperature environments were conducted to examine the sensitivity to temperature of acoustic spectroscopy measurements with

elastic modulus and density, prior to the work conducted and presented here. Higher order reflections observed can also be used for analysis as shown by Owen *et al*. [198] who examined the temperature and cycling rate influences on acoustic signal. Further AS literature to investigate X-ray imaging for single crystal electrochemical performance [204] and a broader review into recent advances for the technique in electrochemical power systems [203] highlight the promise, impact and relevance of the technique to the field.

In this thesis, the electrode delamination and gas formation in lithium-ion batteries with coupled AS and X-ray imaging has been examined. These events are known causes of electrochemical degradation and precursors to the onset of thermal runaway. These gas induced delaminations from a planar electrode assembly are failure characteristics which will be prominently visible due to the changes in the measured attenuation and shift in the waveform peak location, identified using AS measurements and analysis. Laboratory and synchrotron X-ray imaging with X-ray CT is used to highlight the internal phenomena which occur during defect driven gas-induced delamination and thermal abuse pouch-cell calorimetry to provide correlative validation. The results produced are split into two parts, the first demonstrates the application of laboratory X-ray imaging with AS to identify gas formation in a cell cycling under normal conditions; the second utilises AS with high speed synchrotron imaging to observe and characterise thermal runaway.

3.3 Scanning Electron Microscopy

Scanning electron microscopy (SEM) detects secondary and backscattered electrons (depending on the mode of operation) from an irradiated electron beam to produce topographic images with nm resolution. The Zeiss EVO MA 10 (Zeiss, UK) was used for SEM imaging, typical parameters were: accelerating voltage 10 kV, gun vacuum below 5×10^{-7} bar and 8 mm working distance.

Energy dispersive X-ray spectroscopy (EDX) performed using INCAx-act X-ray detector and software (Oxford Instruments) provided spatial mapping of component elements within the sample. High energy electrons irradiated upon the sample cause emission of electrons from inner shell orbital electrons; the energy difference between the inner orbital and an outer orbital is characteristic for every element as an outer shell electron fills the inner hole left by the emitted electron, producing a characteristic photon equal to the energy difference between the orbitals. Thus, it is possible by detection of these photons of characteristic energy to produce a spatially resolved 2D map of elements within the sample. Typically, an adhesive carbon disc of ca. 0.8 cm was used as a sample holder for topographic imaging or a small sample clamp for cross-section imaging.

3.4 Fractional Thermal Runaway Calorimetry

3.4.1 Background

A spectrum of variables influence each thermal runaway event, with unique circumstances, no event is identical regardless of the cell model and state of charge. Cell designs to mitigate failure should cater for the worse possible scenario, which could see the total energy potentially ejected in any direction, leading to additional parasitic mass and volume.

FTRC was instigated by the NASA Johnson Space Centre (JSC), NASA Engineering and Safety Centre (NESC) and Science Applications International Corp. (SAIC) as an important technique to improve lithium-ion battery safety. This is achieved by quantify the total heat during thermal runaway and the fraction of heat released through the cell casing versus the ejecta material thus decoupling the heat generated inside and outside the cell. This proportion is determined by an energy yield algorithm which processes transient temperature versus time using the specific heat formula:

$$Q = \sum m_i C_{p_i} dT_i \qquad [3\text{-}8]$$

3.4.2 Calorimeter design and purpose

An ambidextrous calorimeter design accommodating multiple cell designs for gas and material ejection during potential cell rupture in both the top and bottom directions has been used shown in Figure 3-10.

After the cell chamber, there are ejecta containment components which features ejecta material capture and tortuous flow paths to accurately capture the energy in the ejected gas with the potential for gas capture and gas chromatography. The calorimeter can induce thermal abuse via high flux cartridge heaters to simulate failures and nail penetration mechanical abuse to puncture the cell casing.

FTRC has yielded a comprehensive insight into the characterization of thermal runaway behavior with a variety of cell architectures, chemistries, novel materials and safety features. By the

tandem use X-ray radiography, the mechanism by which failure occurs have been very well characterized by Finegan *et al.* [86,93,94] and has led to further work in evaluating novel battery innovations.

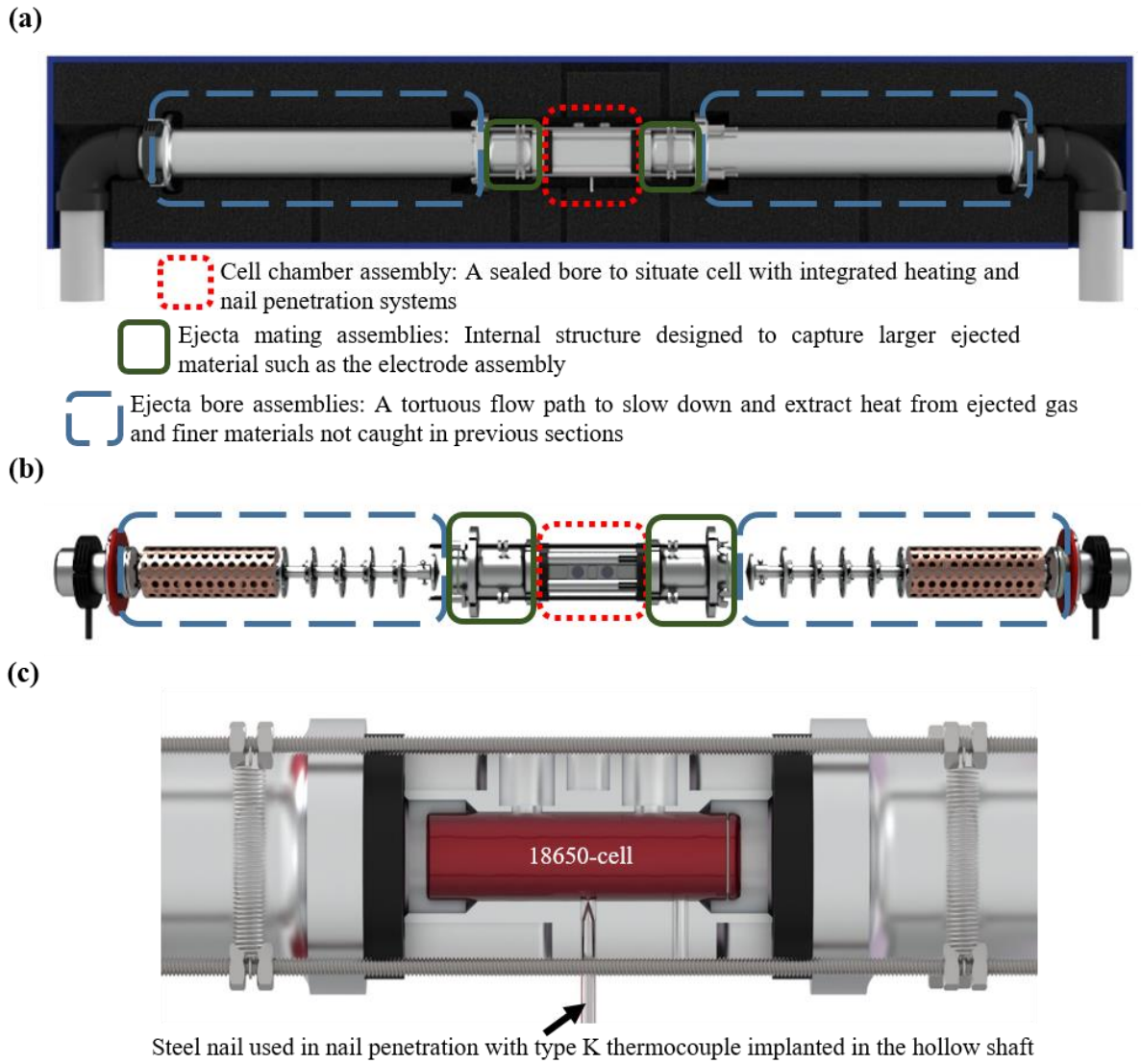

Figure 3-10: (a) Render of the fully assembled calorimeter inside a thermally insulating casing, with sections circled and functionality described. (b) An exploded view of the internal structure of the FTRC unit. (c) Rendering of the aluminium nail penetration cell chamber using a steel nail with an internal thermocouple. Additional features include spring pressurized cell surface thermocouples, gas sealing O-ring and thermally isolating ceramic.

Bottom vent mechanisms exhibit consistently less heat release during thermal runaway and have higher remaining cell mass than cells without bottom vents. This is due to the two pressure relief points in bottom vent cells which alleviate the pressure drop between the inside and outside of the cell, and therefore provides a lower driving force for materials to eject. Thicker cell casing reinforces the mechanical integrity of the steel can structure and has reduced the risk of bursting and breaching,

especially highlighted by deflection points within cells (spin-groove and base plate) which were most vulnerable to thermally-induced breaches.

FTRC has eliminated the random variables which are not inherent to the cell design and provides a method to characterize behaviour during thermal runaway, with 3D thermal profiling of heat released complemented by X-ray radiography. However, for statistical significance, multiple experiments of at least ten runs are recommended to establish a statistically significant data sample set to produce any meaningful conclusions. The latest iterations of FTRC were designed in collaboration with NASA and NREL to accommodate simultaneous correlative high speed synchrotron X-ray imaging and rapid acquisition acoustic ToF probing which are shown in Chapter 4.1.

3.5 Overview

Thus far in the literature review, the underpinning theory for characterisation methods are explored with respect to lithium-ion battery safety literature. Practical and laboratory considerations of acoustic spectroscopy, X-ray imaging and computed tomography during battery abuse experiments. These failure tests were facilitated at high speed X-radiography synchrotrons with a large working distance and imaging rig which permitted a large design envelope for the *in-situ* FTRC. Aluminium as the material for the FTRC unit permitted X-ray transmission for radiography analysis and the high temperature environment of abuse testing required high temperature couplants for AS.

Spatial and temporal resolutions of each method were examined in literature where possible to identify aspects of the technique which could be utilised to enhance insights into internal mechanical and thermal responses of the lithium-ion batteries tested. Examples such as the propagation of ultrasonic waves through different mediums or lack thereof would provide sensitivity to phase changes or temperature changes attributed to density changes in the medium. Furthermore, regions of interests can be feasibly scanned with the Versa-520 across multiple length-scales. Thus, an analysis of the inferred measurements from a combination of these techniques *in-situ* and post-mortem provide a correlative and more complete deduction of the contribution to safety of the function materials investigated in this thesis.

4 Simultaneous Acoustic Spectroscopy and X-ray Radiography

The work and results reported in this chapter have been peer reviewed and published in Journal of Power Sources (Pham MTM, Darst JJ, Finegan DP, Robinson JB, Heenan TMM, Kok MDR, Iacoviello F, Owen R, Walker WQ, Magdysyuk OV, Connolley T, Darcy ED, Hinds G, Brett DJL, Shearing PR. ***Correlative acoustic time-of-flight spectroscopy and X-ray imaging to investigate gas-induced delamination in lithium-ion pouch cells during thermal runaway.*** J Power Sources. 2020; 470:228039. doi:10.1016/j.jpowsour.2020.228039.).

4.1 Introduction

It remains difficult to detect internal mechanical deformation and gas-induced degradation in lithium-ion batteries, especially outside specialized diagnostics laboratories. Despite their widespread application, concerns regarding the safe deployment of batteries across a range of challenging applications persist. Lithium-ion batteries can generate significant amounts of heat associated with both electrochemical reactions and ohmic losses. When the rate of heat generation exceeds the rate of heat dissipation, the cell begins to increase in temperature and at a critical temperature, highly exothermic decomposition reactions occur – this process is referred to as thermal runaway. Identification of these characteristic markers in degrading cells would aid the development of improved BMSs which can prevent further degradation and eventual failure.

AS can be used as an insightful and field-deployable diagnostic or prognostic technique to sense the onset of failure. Internal structural changes, such as gas-induced delamination, are identified using ultrasonic pulse-echo probing due to variations in the attenuation and signal peak shifts. The change in the speed of the ultrasonic wave through different phases within the electrode assembly is apparent due to the order of magnitude difference of elastic moduli and densities in phases of matter. These properties are also subject to temperature dependency, hence with increasing temperatures as seen in thermal runaway – this can be inferred and measured with acoustic time of flight. Thus with sufficient temporal

and spatial resolution, through-plane structural changes in thermal runaway can be characterised. These insights can be correlated with existing thermal runaway elucidative techniques which have been developed and provided prior understanding in literature.

AS through ToF analysis has provided methods to evaluate the SoC and SoH of the electrode assembly [193,195], spatial imaging and analysis of high rate cycling behaviour [194,196,205]. Prior to this work, acoustic spectroscopy had predominantly focussed on longer term SoH inferred degradation and charge-discharge on the magnitude of minutes to hours, contrastingly to a thermal runaway event which can elapse in seconds.

Inferred relative structural AS insights are correlated with X-ray imaging (both laboratory and synchrotron sources), thermal responses measured through FTRC and electrochemical cycling data. FTRC data has also been used to support statistical assessments which describe the event-to-event variability in thermal runaway responses for a given cell format [92].

Here, thermal abuse FTRC is used to analyze the thermal evolutions as thermal runaway progresses with acoustic spectroscopy probing and co-incident X-ray imaging for internal mechanical changes. [92–94,97]. Electrode delamination and gas generation are known precursors and nucleation points for degradation and eventual failure, characteristics prominently visible via ToF AS due to the significant changes in the measured attenuation and shift in the waveform peak location. This work is split into two parts, the first demonstrates the application of laboratory X-ray imaging with ToF AS to identify gas formation in a cell cycling under normal conditions; the second utilises ToF AS with high-speed synchrotron imaging to observe and characterise thermal runaway.

4.2 Experimental

4.2.1 ToF AS integrated FTRC

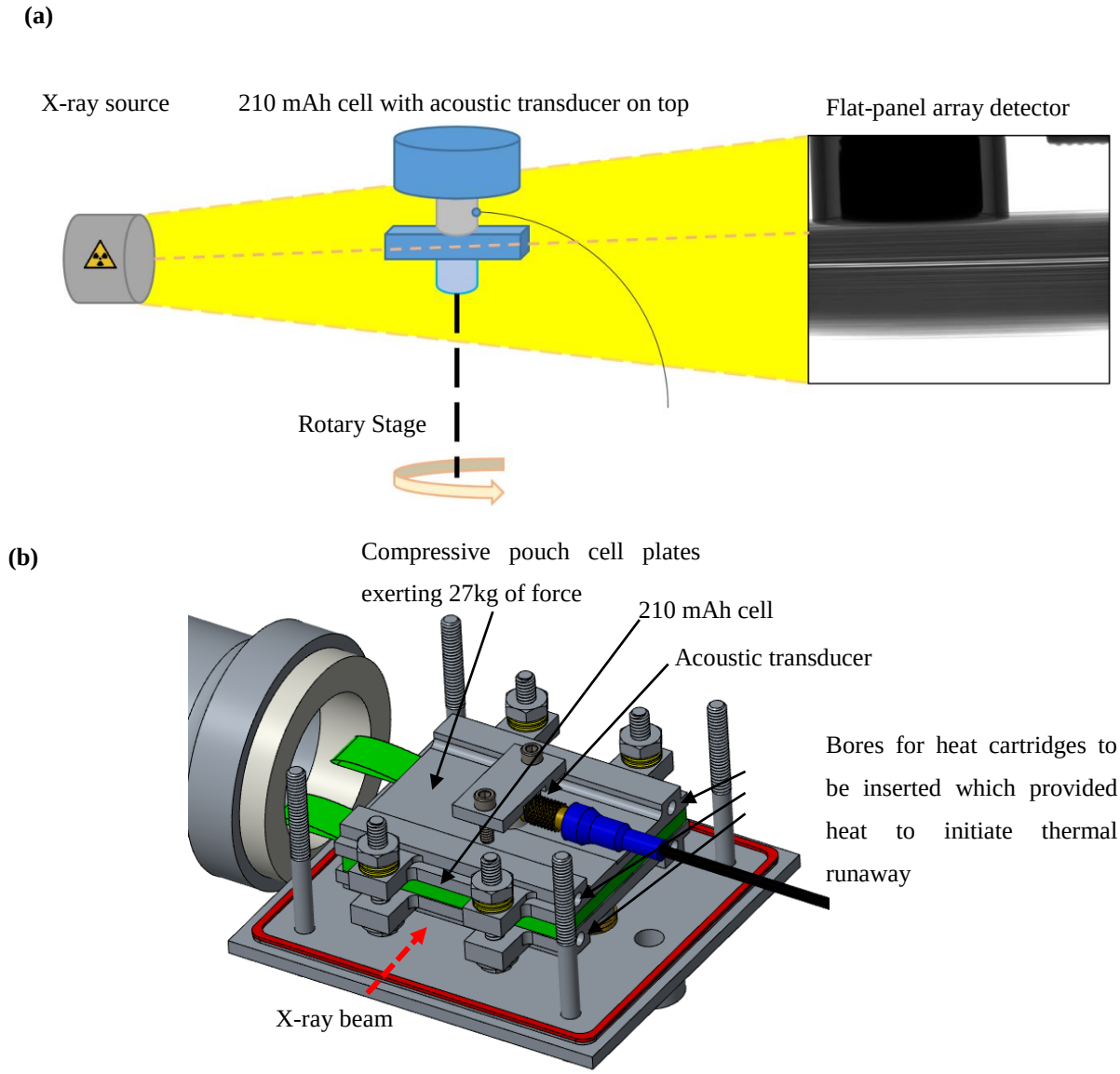

Figure 4-1: (a) A simple schematic of the experimental set-up used in the Nikon XT H225 to produce simultaneous AS and X-ray imaging. (b) 3D rendering of the ultrasonic transducer in the pouch cell calorimeter cell chamber stack under compression.

All acoustic ultrasound ToF measurements were obtained via an Olympus Epoch 650 ultrasonic flaw detector (Olympus Corp, Japan) with a pulse-echo contact transducer (M110-RM, Olympus Corp, Japan). The 6 mm piezoelectric transducer element is capable of frequencies up to 5 MHz, with the chosen frequency of 2.25 MHz used for all measurements. Couplant suitable for high temperature

applications (H-2, Olympus Corp, Japan) was applied to maintain interfacial contact between the cell and transducer to facilitate propagation of the ultrasound wave into the cell. Constant pressure was applied behind the transducer during simultaneous X-ray imaging. *Operando* laboratory X-ray imaging was conducted with a 200 g weight placed on top of the sensor. During synchrotron fractional thermal runaway calorimetry, a compressive force of ca. 27 kg (82.74 $N \cdot cm^{-2}$ measured by a torque wrench, correlating torque to compression) was applied. The experimental set-ups are shown in Figure 4-1. This force was to promote better contact between the transducer and the cell throughout abuse testing, high temperature graded couplant was used to ensure better propagation of ultrasonic signals.

The magnitude of the measured reflected ultrasonic signal by the transducer is determined by the gain magnification, which was set at 60 dB. The voltage applied to the piezoelectric transducer was 200 V. The resolution of each waveform data sample, with 495 discrete mapping points equally spaced across the range of 10 μs, provides a ToF resolution of 20.2 ns for each data point. The ultrasound waveform data was transferred from the Epoch 650 through an RS232 connection and output files acquired by an open-source Python code described in previous work by Steingart *et al.* [193,195,206].

A pouch cell calorimeter was designed to accommodate thermal, mechanical and electrochemical abuse for a range of pouch cell dimensions (up to 50 mm × 50 mm). The temperature was measured at the surface of the cell with type-K thermocouples. The experimental set-up [Figure 4-1 (b)] served multiple purposes; the bores seen in Figure 4-1(b) were fitted with heater cartridges which provided heat to initiate failure. The compressive plates containing the heater cartridges ensured more effective thermal contact between the heated plates and the surface area of the cell through the duration of the test. This also counteracted any insulation effect of gas generation which may reduce thermal conductivity between the heater cartridges and the cell. This facilitated reliable initiation of thermal runaway as the active materials within the cell could be reliably heated until failure occurred as swelling due to gas production did not occur at the cell-compression plate interface. This compression also ensured that ToF probing was possible throughout the duration of the test as gas accumulation did not occur through the acoustic probe plane, which caused loss of signal shown in Part I, where no compression of the cell was used.

Commercial 210 mAh $LiCoO_2$ cathode pouch cells with a graphite anode (PL-651628-2C, AA Portable Power Corp., CA, USA) were charged to 4.2 V using a constant current, constant voltage (CCCV) protocol. The constant current charge was performed at 0.5 C with the voltage then held constant at 4.2 V until the current dropped below 0.05 C. The cell was then left at open circuit potential

for 20 min before being put into compression plates for failure testing. During calorimetry testing, failure was induced at different heat fluxes to provide varied insight into the processes of thermal abuse leading to thermal runaway, which may have different time constants. Heating was applied using heater cartridges inserted into the compressive plates seen in Figure 2b. Heating was switched off immediately after the onset of widespread thermal runaway which was observed using X-ray radiography.

The compressive plates were designed with a hole for the transducer to fit in with a back plate providing continual compression, with couplant to provide as close to a homogeneous force on the cell without impingement which may affect thermal runaway characteristics. In larger cells where impingement might be of concern due to a change in compression locally that could be a nucleation point for failure and affect results in thermal abuse tests. However, dimensionally the cells used in this work were chosen for their small size to increase likelihood of capturing thermal runaway mechanisms within the transducer field of view.

Electrochemical testing was achieved using a Gamry Interface 1010E potentiostat (Gamry Instruments, Pennsylvania, USA). During defect identification cycling, the cell CCCV cycling was conducted at 0.5 C constant current, from ca. 3.6 V to 4.2 V, then using a constant voltage protocol until the current cut-off of 0.1 C. Discharge cut-off was 2.75 V, with a discharge current of 0.5 C.

4.2.2 X-ray radiographic imaging:

Laboratory-based X-ray radiographic imaging was conducted using a Nikon XT H225 (Nikon Metrology, UK), with a 2K × 2K PerkinElmer 1620 Detector; this was performed simultaneously to the ToF measurements. The imaging parameters were chosen to ensure appropriate X-ray penetration of the cell as well as sufficient contrast to show gas-induced delamination and other structural changes. An accelerating voltage of 130 kV and a current of 70 µA were used. No filter was used and one frame per second (fps) radiograph acquisition was achieved with a pixel resolution of 5.55 µm.

High-speed X-ray radiography at 20 fps and 580 µs exposure time was performed at the I12 beamline [207] at DLS), the radiography was used to capture the transient internal architecture throughout testing, whilst simultaneously capturing ToF data. The cells were imaged under a 74 keV monochromatic parallel beam with a pixel size of 16.26 µm and a field-of-view (FOV) of 20 mm × 12 mm (Horizontal × Vertical). A $Gd_3Ga_5O_{12}$ (GGG) scintillator and Miro 310 detector were used for all high-speed imaging experiments.

Selected frames highlighting the significant structural evolution during gas formation and thermal runaway from these radiographic videos are shown in this paper, with the videos illustrating failure provided in the Supplementary Information.

4.2.3 X-ray micro-CT:

Non-destructive X-ray CT was conducted using two systems, a Nikon XT H 225 (Nikon Metrology, UK) and a Zeiss Xradia 520 Versa (Carl Zeiss, USA). Both CT systems utilise a tungsten target. The accelerating voltages and beam energy were selected based on the attenuation of the samples and the contrast of materials. Radiographs were obtained at incremental angles while rotating the vertical axis in the middle of the region of interest. These acquired radiographs were subsequently reconstructed using commercial software packages (CT Pro 3D and Zeiss XMReconstructor for Nikon and Zeiss CT systems respectively), which use algorithms based on the standard filtered back-projection or the Feldkamp-David-Kress (FDK) method. Collection parameters are described in Table 1.

Table 4-1: Imaging configurations for X-ray CT. 0.4X magnification used for Versa CT scan.

	Voxel Size	**FOV**	**Exposure Time**	**Accelerating voltage**	**Power**	**Filter**	**Projections**
Nikon XT H 225	24.5 µm	40 × 40 mm	1 s	180 kV	18.5 W	1 mm Cu	3176
Zeiss Xradia 520 Versa	7.7 µm	10 × 10 mm	25 s	160 kV	10 W	N/A	3201

Post collection segmentation and visualisation of the reconstructed tomograms were processed using Avizo Fire 9.5 software (Thermo Fisher Scientific, France).

4.3 Laboratory Imaging

A static cone-beam tungsten source was used for the laboratory X-ray imaging; as a result, layers that were horizontally co-incident or parallel to the centre of this beam were much brighter in the radiograph due to the lack of flat-field corrections applied to radiography. In each of the frames seen in Figure 4-2, the brighter horizontal layer co-incident with the centre of the X-ray beam was used as a reference point due to the stationary source and a fixed sample holder below the cell. As the cell was discharged at 0.5 C, a greater proportion of the cell above this reference point was observed and therefore it can be observed that the pouch cell experiences mechanical expansion, which is corroborated by a reduced proportion of the transducer in the FoV. At 162 min, delamination of the electrode layers under the sensor and gas generation can be observed and correlated with the loss of ultrasonic signal. Correlating ToF AS shown in Figure 4-3.

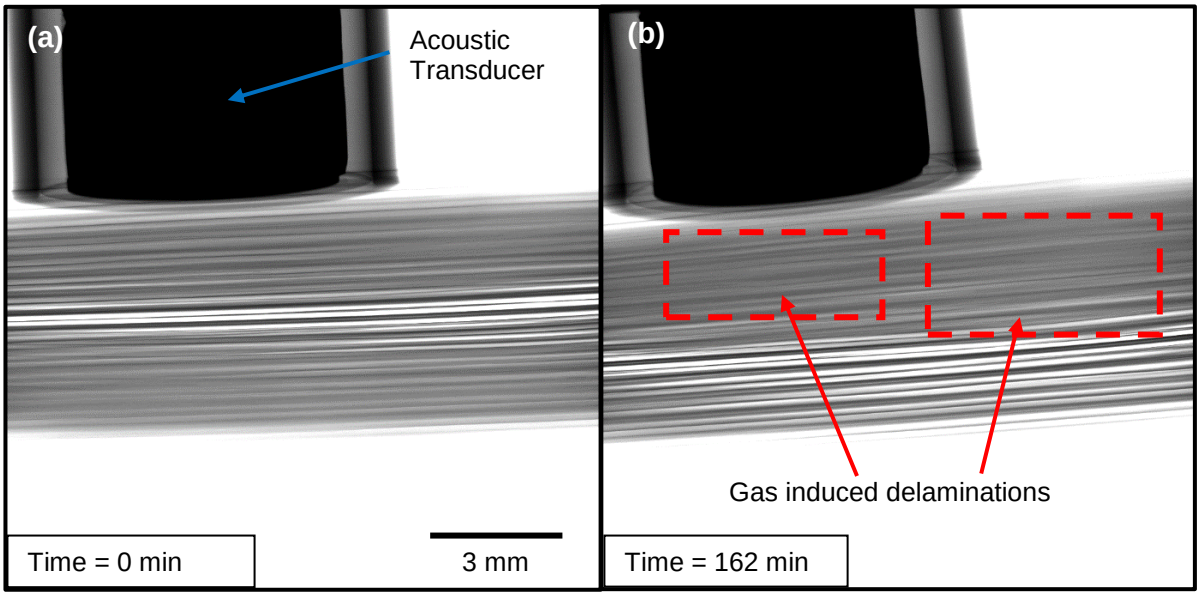

Figure 4-2: Radiographs depicting the expansion of the pouch cell layers, with the horizontal bright-line being the centre of cone-beam with no incident angle. The radiography video can be seen in Supplementary Materials. (a) Initial radiograph from which relative comparisons were made. (b) Gas-induced delamination during discharge observed.

The acoustic spectrogram shown in Figure 4-3 represents the individual ToF snapshot data acquired throughout the duration of the experiment with the amplitude of the waveform depicted by the colour-map key. Given the nature of the acoustic response signals, the first horizontal white line (located at ca. 0.625 µs – 1.25 µs seen in Figure 4-3(a)) describes the initial saturation of the transducer which does not change with time. The subsequent red lines provide information pertaining to the first electrode

and subsequent material interfaces until a ToF of ca. 7.5 µs, where the sensed ultrasonic wave reflections are echoed.

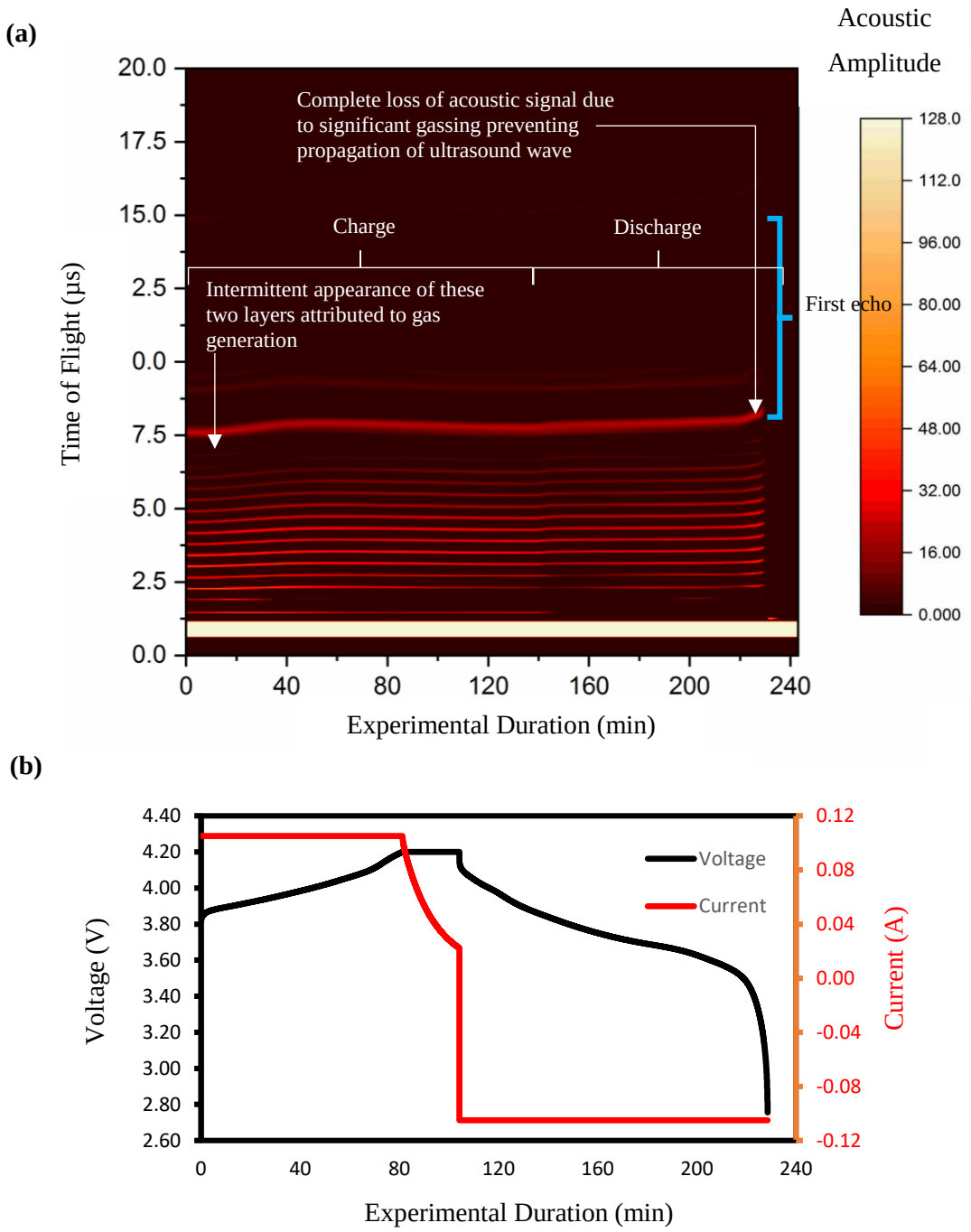

Figure 4-3: ToF acoustic spectrogram plotted with respect to experimental duration which can be correlated to voltage or SOC, the characteristic wave amplitude is shown by the colour scheme. Shifts in ToF through the battery were observed; with significant changes at ca. 40 min, 45 min and 230 min. The highly reflected first wave consistent throughout all ultrasonic measurements and observed at ca. 1.3 µs. At ca. 7.5 µs, the first echo of the reflected signals appears, with a fainter second echo at ca. 14.9 µs. The acoustic amplitude is displayed in arbitrary units.

The commercial 210 mAh cell has seen consistent and reliable operation when cycled within the specified operating parameters of voltage, current and temperature in previous work [205]. ToF shifts and attenuation associated with density changes due to lithiation and delithiation are immediately observable and have been explained previously [205]. However, in this experiment, the cell was cycled with a constant force applied behind the transducer. Gas formation and mechanical delamination was observed in both X-ray imaging and ToF AS.

Initial indicators of gas generation were observed with ToF AS [Figure 4-3], as the cell was cycled. An intermittent appearance of the internal electrode layers at ca. 6.25 µs ToF can be observed during the duration of the experiment. The final two layers of the electrode assembly, observed with ToF AS disappeared and reappeared. This can be ascribed to gas generation and then gas movement away from the ToF probed region because of the additional force behind the transducer. This gradual accumulation and movement of gas reduced the acoustic amplitude, which is reflected in the diminished intensity of the colour in Figure 5.

A further indication of the formation of gas was the fluctuation in the intensity of the waveform at ca. 140 min, represented by the acoustic amplitude (measured in arbitrary units, AU) – which decreased from approximately 96 to below 32, as highlighted in Figure 5. At the start of the experiment, at ca. 6.25 µs ToF, there was a clear reduction in the acoustic intensity (ca. 24 AU). This intensity fluctuated throughout the experiment; the signal was lost intermittently and gradually declined in acoustic intensity (ca. 12 AU at 140 min). This intensity drop was also observed at the two ToF reflected peaks adjacent to the 2.5 µs ToF (seen as red adjacent lines either side of the 2.5 µs ToF marker).

At 230 min, a second more apparent feature is observed in Figure 4-3, after a rapid increase in ToF, loss of signal was observed. This coincided with decreased acoustic intensity of reflections of the layers close to the acoustic sensor beforehand (at 2.5 µs ToF and from 150 min to 230 min). This can be attributed to the formation of gas during cycling. This was a key indicator in cell failure, as previous literature has shown the onset of gassing within the cell predicates actual thermal runaway and ejection of material [95,141]. There were portions of the transducer which could successfully transmit and sensed the reflected signals and some which did not. This lack of homogeneity in the gas, liquid and solid phases with the electrode assembly was responsible for the presence of acoustically visible electrode layers further away but not those adjacent across the surface area of the transducer as the transducer averaged the reflected signal sensed across its surface area.

The region of interest where acoustic ToF measurements were taken [shown inset in Figure 4-4], was observed and shown as an orthogonal slice from the reconstructed tomogram of the electrode layers before degradation and after gas generation. At the start of the experiment, the uniformity of the electrode layers at the centre of the cell is evidenced by the inset cross-sectional orthoslice [Figure 4-4(a)], which was also reflected in the acoustic data [Figure 4-3].

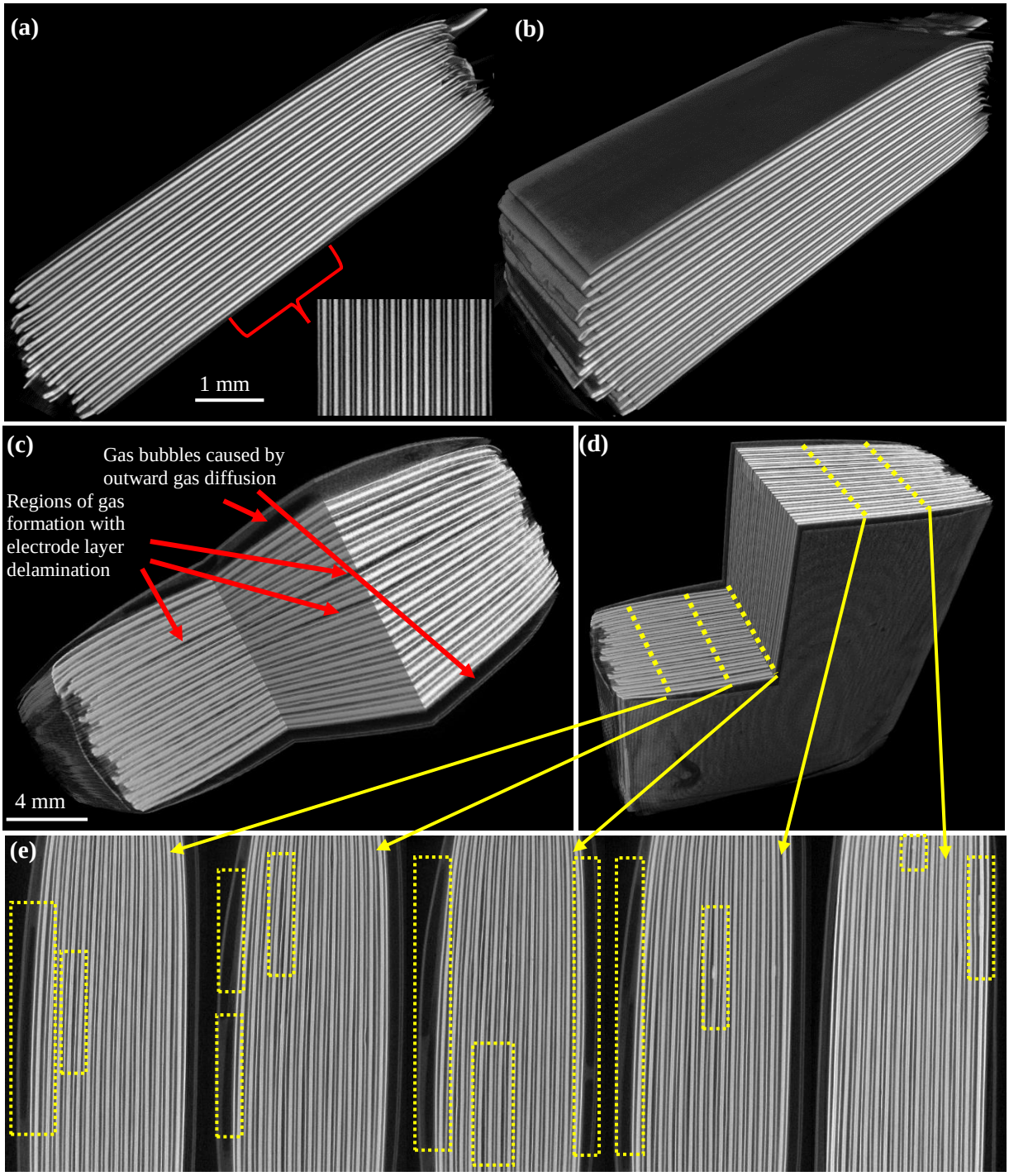

Figure 4-4: (a) An X-ray orthoslice cross-section of the cell prior to cycling and failure, the ToF probed region is shown inset. (b) An X-ray CT of the 210 mAh lithium-ion pouch cell before the detection of

defect or failure. (c) Post-mortem X-ray CT of the region of interest, which was probed via ToF AS during cycling. The highly attenuating gas pocket at the edge of the pouch cell, outside the electrode assembly and within the outer casing, is responsible for the loss in the acoustic signal. This provided visualisation via CT after gas-induced delamination with regions of interest depicted. (d). Side profile of the acoustic region of interest, with the location of the orthoslice provided. (e). Orthoslices highlighting some of the mechanical defects and features visible via acoustic ToF. Scale bar used in (c) applicable to (d) and (e). X-ray CT acquisition parameters can be found in Table 4-1.

Figure 4-4 highlights multiple instances of electrode delamination as well as accumulation of the gases produced at the surface of the electrode assembly in contact with the polymer cell casing after cycling was completed. Comparison of X-ray CT before [Figure 4-4(a) and Figure 4-4(b)] and after failure [Figure 4-4(c), Figure 4-4(d) and Figure 4-4(e)], shows the increasing delamination of the electrode, with the defects and gas regions circled in Figure 4-4. Additional comparison between the acoustic and X-ray imaging data, highlighted that these regions were nucleation sites for gas formation. Throughout the duration of the experiment, the trend of fluctuating acoustic amplitude throughout the ‘deepest’ ToF observable electrode layers, can be attributed to gas formation and later movement away from the ToF AS probed region. This was due to the 200 g weight applied to the transducer which slowly forced the gas laterally, away from the probe. Eventually, gas generation and diffusion of gas through the electrode layer resulted in macroscopic gas accumulation between the electrode layer and the cell casing.

4.4 Correlative Synchrotron X-ray Imaging

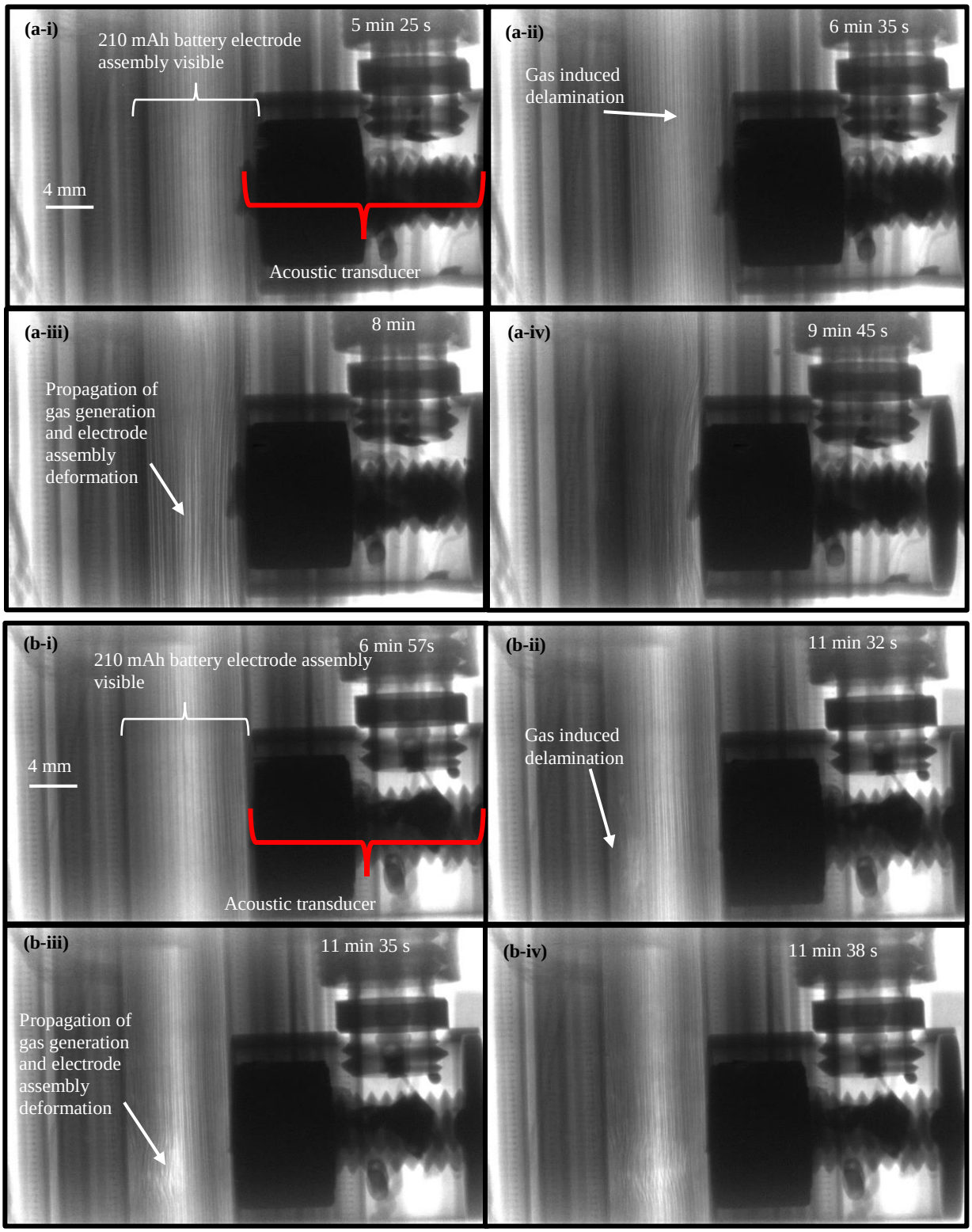

Figure 4-5: (a) Selected radiography frames from Cell 1 highlighting significant structural changes during thermal runaway in the first failure test. The pouch cell calorimeter was at an angle to the X-ray beam path during this first test, hence the visible screw next to the transducer and the left-hand side of

the cell was covered by some of the aluminium compression plate. Delamination and gas generation predicated the initiation of widespread thermal runaway. Thermal runaway, the ejection of gas and material and the subsequent recompression of the cell are shown in the four frames. (a-i) Heating has been applied for a minute and minor delamination was observed, this radiograph can be used as a reference for significant changes induced due to thermal abuse. (a-ii) After 2 min 10 s of heating, the first major signs of delamination can be observed. (a-iii) Widespread gas generation and thermal runaway occurred. (a-iv) Thermal runaway and gas generation ended, the compressive pouch cell chamber stack has forced the electrode layers together. (b) The radiography of Cell 2 during the second thermal abuse test conducted at a higher heat flux in the aluminium plates of the 210 mAh commercial lithium-ion cell. (b-i) At 6 min 57 s, the cell has expanded with increasing temperatures as heating had been applied for ca. 30 s. (b-ii) Formation of the gas phase was visible. (b-iii) Onset of widespread thermal runaway caused further gas generation. (b-iv) Widespread thermal runaway and gas generation which led to pressure build-up and eventually ruptured the cell casing.

To further evaluate the value of ToF AS to characterise thermal runaway, co-incident high speed X-ray imaging and ToF probing was conducted at a synchrotron facility during thermal abuse testing of two identical cells to those used in the laboratory tests described above.

Radiography captured the failure process of both Cell 1 and Cell 2 [Figure 4-5 (a) and Figure 4-5(b) respectively] in the two thermal runaway tests conducted. This provided insight into correlating acoustic signatures shown in ToF AS with internal phenomena seen by X-ray imaging and post-mortem CT. Due to the experimental set-up in a synchrotron experimental hutch, the acquisition of the ToF data commenced at experimental time = 0 s; however, X-ray imaging started later due to safety protocols to ensure no personnel were present in the experimental hutch. Thus, the onset of thermal abuse via the heater cartridges occurred several min (ca. 6 min 20 s and ca. 4 min 30 s for Cell 1 and Cell 2 respectively) into the experiments when both ToF AS probing and X-ray imaging data could both be acquired simultaneously. For Cell 1, heating started at 6 min 20 s in the first thermal runaway experiment seen in Figure 4-5(a-i). The structural changes seen in Figure 4-5(a-ii), recorded at 20 fps, and were correlated with the ultrasonic ToF reflections sensed by the transducer in Figure 4-5(a). After 6 min 35 s, shown in the Figure 4-5(a-ii), mechanical deformation of the layers adjacent to the transducer was observed, which preceded local gas formation. The shadow which is seen to appear adjacent to the face of the transducer [Figure 4-5 (a-ii)] indicates the disintegration of the laminar electrode format, thus less distinct and high contrast edges are seen in Figure 4-5(a-i).

The onset of widespread thermal runaway of Cell 1 during the first experiment was seen in the third radiograph frame [Figure 4-5 (a-iii)]. Through the X-ray visible plane, the entire electrode assembly exhibited delamination. Thermal decomposition of the $LiCoO_2$ cathode, electrolyte and other active material was seen as fracture of the electrode assembly with rapid gas generation. The gas-induced delamination observed throughout the cell, caused the pressure to peak as observed by the maximum swelling of the cell. The increased pressure due to gas generation, coupled with the force of the compressive plates resulted in a breach of the external casing of the cell. These dynamic structural evolutions were are apparent in Supplementary Material.

After 9 min 45 s, thermal runaway had concluded, with no generation and ejection of gas and no ejection of material. The compressive plates applied continual force to the transducer to ensure perpendicular movement of gas to the ultrasonic imaging plane and allowed the layers to be acoustically propagative as well as preserving the intimate contact of the cell-transducer interface. Thermal runaway caused the electrode to compress in a deformed manner. This reduced distance between electrode layers was correlated and seen in Figure 4-6(a) after 10 min, as the reduced distance between electrode layers has yielded a greater acoustically visible depth and higher acoustic amplitude.

For Cell 2, in the second thermal runaway experiment seen in Figure 4-5(b), heating started at ca. 4 min 20 s [Figure 4-5 (b)]. The electrode rupture can be observed in Figure 4-5(b-ii) from the gradual formation and accumulation of the gas from exothermic decomposition of the materials, which was not as severe as previously seen in Figure 4-5(a). This rupture occurred in the ToF AS probed region and therefore was reflected in a slower progression in the delay of the ToF shift in Figure 4-6. In Figure 4-5(b-ii), the initial formation of gas visible in the X-ray and acoustic FOV correlated with the acoustic ToF shift at 11 min 32 s. Despite the greater heat flux applied to Cell 2, a less violent failure was observed; as shown by the predominantly intact electrode assembly with a gaseous void at the end of the experiment. This is due to the greater temperature gradient from the heater to the entire battery and the temperature gradient across the battery, as a result of the greater heat flux. The high heat flux resulted in a higher local cell temperature adjacent to the cartridge heater, which caused local thermal runaway but did not allow enough time for the entire cell's contents to reach the critical temperature.

Given the compressive force provided by the experimental set-up [Figure 4-1(b)], the ultrasound wave propagated further through the pouch cell, therefore, more layers of the electrode assembly were identified without saturation of the transducer's reflection sensor or increasing the sensor's FOV. In addition, the initial four layers experienced a greater acoustic amplitude and a reduced

ToF between the characteristic waveform peaks seen in Figure 4-6(a) and Figure 4-6(b). This can be explained by the compressive force applied, which reduced the acoustic amplitude losses between interfaces. Consequently, this improved propagation of the ultrasonic signal as there was improved interfacial contact between layers.

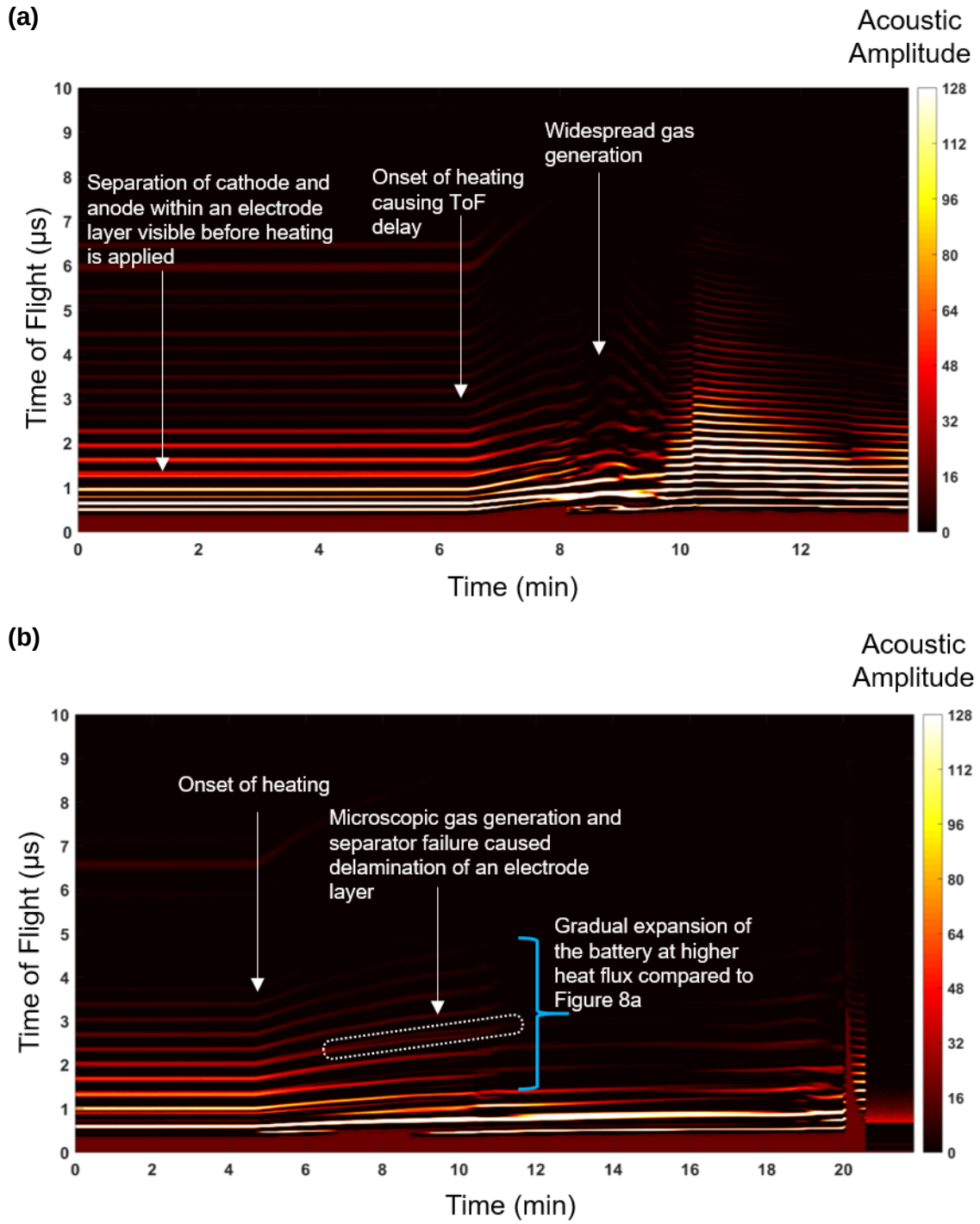

Figure 4-6: (a) ToF AS of Cell 1 during the first failure test, with highlighted regions of interest during induced thermal runaway of a 210 mAh commercial pouch cell. This spectrogram corresponded to the radiography shown in Figure 4-5(a). Onset of heating at approximately 6 min 20 s into the test. (b) ToF AS of Cell 2 during the second failure test, with highlighted regions of interest during thermal runaway

of a 210 mAh commercial pouch cell in the second test, corresponded to the radiography shown in Figure 4-5(b). Onset of thermal runaway at approximately 4 mins 20 s into the test with the main features of interest identified on the AS plot. The acoustic amplitude is displayed in arbitrary units. The cells were heated with different heat fluxes as mentioned in the experimental section of this chapter, the lower heating provided to Cell 2, showed a more gradual change in the acoustic spectrogram in (b).

During the gradual thermal abuse of Cell 1, the onset of heating is clear ca. 6 min 20 s into the test as shown in Figure 4-6(a), as there is a distinct trend of delayed ToF of the ultrasonic wave due to cumulative propagation through the previous layers. This was attributed to decreasing density with increasing temperature and therefore poorer propagation via molecules, which are further apart at greater temperatures due to greater kinetic energy. Consequently, this reduced the ultrasonic wave velocity through the solid electrodes which caused delays in propagation and reflection of the ultrasonic signal therefore a trend of delayed ToF during heating before thermal runaway. Microscopic gas formation and delamination of the electrode which causes expansion or spatially divergent electrode material was visible during radiography at every layer of the pouch cell seen in Figure 4-5(a-iv) with the layers seen by ToF AS, contorted away from the transducer on the right-hand side. The onset of widespread macroscopic gas generation is labelled at 8 min whereby widespread gas generation and rupture of the cell occurred. This gas-induced delamination contributed to the reduction in the ultrasonic wave velocity through the cell, which was exhibited in the ToF for each subsequent electrode layer, thus the cumulative effect of this delay was more apparent for the layers at greater ToF. As the cell progresses through thermal runaway despite the removal of heat at ca. 8 min, the significant gas volume which had formed internally away from the transducer, did not propagate the ultrasound wave and thus no reflection of the attenuated waves is observable despite the very high compressive force. Gas formation begins to occur throughout the cell and once the gas phase reaches a significant volume, each subsequently reflected wave declines in acoustic amplitude with a general trend of delayed shift in ToF. At later experimental duration, these reflected waves no longer appear as the gas propagation progresses. After ca. 8 min, the significant volume of gas has caused maximum expansion of the pouch cell, whereby the internal pressure causes the pouch cell to burst. The constant compressive force applied by the pouch cell chamber coupled with the lack of internal pressure after the cell ruptured and gas ejected, allowed visibility of electrode layers further away from the transducer. The highly compressed pouch cell, which has ruptured and ejected gas, seen in Figure 4-6(a) after ca. 10 min, as thermal runaway has passed and thermal decomposition to produce gas has stopped.

Initiation of failure of Cell 2 during the second thermal runaway test can be identified with heating induced and observed at ca. 4 min 30 s, as a result of thermal decomposition of the electrolyte

and density changes of the active material. Consequently, this exhibited a characteristically similar trend and change in waveform as shown previously in Figure 4-6(a). It is suspected that due to the higher heating rate applied to Cell 2, the heat was not uniformly distributed to the active material within the cell hence the longer duration of widespread thermal runaway and a gradual mechanical expansion of the electrode assembly. Once the onset of failure had occurred, thermal abuse was stopped and the process of failure was extended compared to the first abuse test. More gradual heating applied to Cell 1 during the first failure test ensured a lower temperature gradient across the cell and between the cell and the heat cartridges, thus all the active material within Cell 1 was at a higher average temperature than Cell 2. This higher temperature gradient between the heater cartridges and the cell and across the active material of Cell 2 was reflected in a slower propagation of thermal runaway and a less catastrophic failure probed by the acoustic transducer. This was observed via a more gradual ToF shift seen in Figure 4-6(b). This highlighted the difference in rate of loss of acoustic signal – which was seen to a much greater extent in Figure 4-6(a). However, as a consequence of the slower thermal runaway dynamics of Cell 2, the gas generation lasted longer and there was a longer time during which reflected ultrasonic signals were absent (ca. 11 min to 16.5 mins).

For Cell 2, an interesting phenomenon was observed at the electrode layer initially situated at 2.05 μs ToF, which began to split around 6 min. During the onset of thermal runaway, gas was observed to be generated between the anode and cathode with radiography; this is mirrored by the splitting of the single peak reflected wave shown and circled in Figure 4-6(b). The greater retention of the electrode structural integrity seen in Figure 4-5(b), which was reflected in acoustic measurements with a less sudden shift in ToF of the electrode layers adjacent to the cell, visible at low ToF. The progressive disappearance of reflected ultrasonic waveforms from a later ToF to an earlier ToF is suspected to be due to layers further away being hidden by macroscopic gas formation during thermal runaway and later rupture of the cell which caused widespread loss of ToF AS visible electrode layers.

It is difficult to quantitatively evaluate the degree to which ToF and attenuation have been affected by the gas phase. During thermal runaway, the dynamic fluidisation of the electrode assembly, especially with the transient nature of the composition of this gas-phase at different phases of thermal runaway rapidly changes due to the different extent of reactions and number of reactions that can occur. Later accumulation of the gas phase due to macroscopic gas generation and movement to the external surface of the electrode assembly but within the aluminium casing of the cell, formed a gas layer which attenuated the ultrasonic wave significantly. This physical phenomenon was also observed in Figure 4-6 before the ejection of gas and material in thermal runaway before recompression due to the plates of the pouch cell calorimeter chamber.

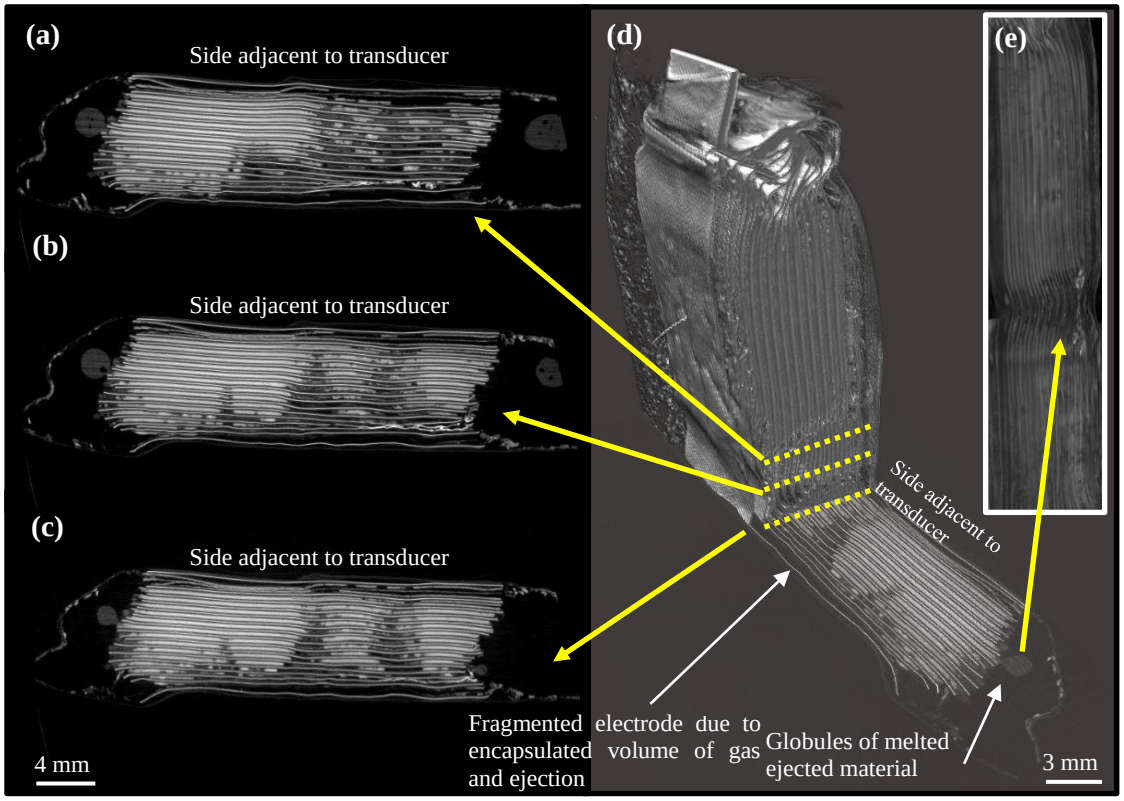

Figure 4-7: Radiography and tomography of Cell 2 after thermal runaway where: (a) top, (b) middle, (c) bottom are the corresponding orthogonal slices illustrating the gas formation regions in line with the ultrasonic transducer. This ToF AS probed region is ca. 6mm in diameter. (d) An internal and external view of the cell with the side profile view of the damage caused by pathway formed for gas and material ejection shown inset (e).

The remains of Cell 1 were insufficiently intact for post-mortem CT. Thus, only the tomogram of Cell 2 from the second thermal runaway experiment cell is seen in Figure 4-7. The internal pouch cell architecture was assessed with post-mortem tomography, for which the Nikon CT imaging configurations can be found in Table 4-1. Reconstruction and visualisation with Avizo 9.5 software, exposed the mechanical damage during thermal runaway. There were some internal un-combusted remains of the cell electrode assembly which have remained intact, primarily the highly attenuating cathode and copper current collector, which were visible on the acoustic transducer side of the cell and on the left side in the radiographs. The damaged electrode layers and ejection of material was stark on the highly attenuating cathode layers, with the two furthest layers from the transducer undergoing complete delamination and structural collapse.

The encapsulated gas volume observed due to the loss of material by ejection seen in Figure 4-7(d), reinforced the loss of acoustic signal at later ToF. Ejected material was seen on the external far side of the cell with some globules of previously melted material visible. The fragmented structure supported the hypothesis of loss of reflected ultrasound signal depth due to a lack of transmission through the gas gap seen in Figure 4-7.

The ToF AS probing analysed in Figure 4-6 was correlated with time to the X-ray imaging, which produced radiographs shown in Figure 4-5. The expansion of the electrode layers and attenuation of the acoustic signal was observed in the radiography seen in Figure 4-6. The expansion of the electrode layers during cycling, gas-induced delamination and gas formation throughout the three experiments detailed here were consistent with the ToF delay in the acoustic spectrogram and X-ray imaging.

4.5 Conclusions

In-situ and *operando* ToF AS has been demonstrated to be a robust tool in identifying gas formation and probing mechanical deformation within cells, which has been coupled with X-ray radiography and CT to provide a comprehensive tool for cell failure analysis. Through-plane, temporally-resolved structural changes contributing to the onset of degradation and failure have been identified using ToF AS. These sequences of events causing mechanical failure have been linked to degradation in electrochemical performance, capacity retention and thermal response. *In-situ* X-ray imaging and *ex-situ* X-ray CT confirmed these observations, which were also corroborated with the principles of ToF AS.

Due to the propagative properties of ultrasound through different phases such as attenuation and wave velocity, integration into battery management systems would allow direct measurement and analysis of the onset of gassing within complex modules; as well as SoC, SoH and electrochemical performance. Gas formation and delamination are prime indicators of impending thermal runaway, which could be prevented with acoustic analysis implemented in the BMS, with a spatially resolved array of transducers offering potential for prognostic, temporally resolved, *in-situ* and *operando* ultrasonic-based analysis. However, limitations arise in precisely quantifying the attenuation and ToF shifts compared to the theoretically expected values. ToF AS has potential as a powerful, non-destructive and field-accessible technique which would see applications in EV battery modules on-board or in-line metrology during battery manufacture or evaluation for second-life/recycling.

5 Prevention of Thermal Runaway

The work and results reported in this chapter have been peer reviewed and published in Cell Reports (Pham MTM, Darst JJ, Walker WQ, Heenan TMM, Patel D, Iacoviello F, Rack A, Olbinado MP, Hinds G, Brett DJL, Darcy ED, Finegan DP, Shearing PR. ***Prevention of lithium-ion battery thermal runaway using polymer-substrate current collectors.*** Cell Reports Phys Sci. 2021. doi:10.1016/j.xcrp.2021.100360.).

5.1 Introduction

Isolating electronically conducting material from internal short circuits is a promising way to prevent the onset of thermal runaway within lithium-ion cells. The sequence of precursor events indicative of widespread thermal runaway has been widely investigated [87,89,97,132,133] and reviewed [14,85,119,134] through the use of multiple direct and indirect techniques [92,96,100,138–142,208]. During nail penetration of an 18650-cell, internal cell temperatures over 800 ˚C [146] and surface temperatures over 600 ˚C are common [93–95,209] due to the ca. 70 kJ of heat [92] that is typically produced. . Common failure modes and means to prevent failure have been reviewed in-depth [81,108,143,210–213], but little change has ever been made to the architecture of current collectors for improved battery safety commercially.

Recently reported re-engineering of the current collector to improve battery safety by Naguib *et al.* [79] restructured the electrode and current collector design to produce impact-tolerant “slitted” construction which could withstand mechanical impact and by and Liu *et al.* [80] using a positive temperature coefficient material within a current collector configuration to isolate the region of short-circuit from the rest of the battery. It is notable that connection of the two most electrically conductive materials within a cell (the current collectors) leads to the most severe internal short circuit thus one of the most probable conditions for thermal runaway to occur. Thus removal or isolation of the CC during an internal short circuit holds great promise for significantly reducing the risk of thermal runaway initiating and propagating through the cell.

Here, a metal-coated polymer current collector, that is designed to disconnect internal short circuits by withdrawing from the heating region, is tested in 18650 cells. In addition to having lower mass and manufacturing costs, cells with metal-coated polymer current collectors demonstrate reduced risk of thermal runaway during nail penetration. High speed synchrotron X-ray radiography of 18650-cells during nail penetration testing, in tandem with *pre-* and *post- mortem* X-ray computed tomography, provides insights into the function of the novel current collectors. The results are compared with those of 18650-cells with standard commercial aluminium and copper current collectors.

5.2 Experimental

5.2.1 Cell preparation

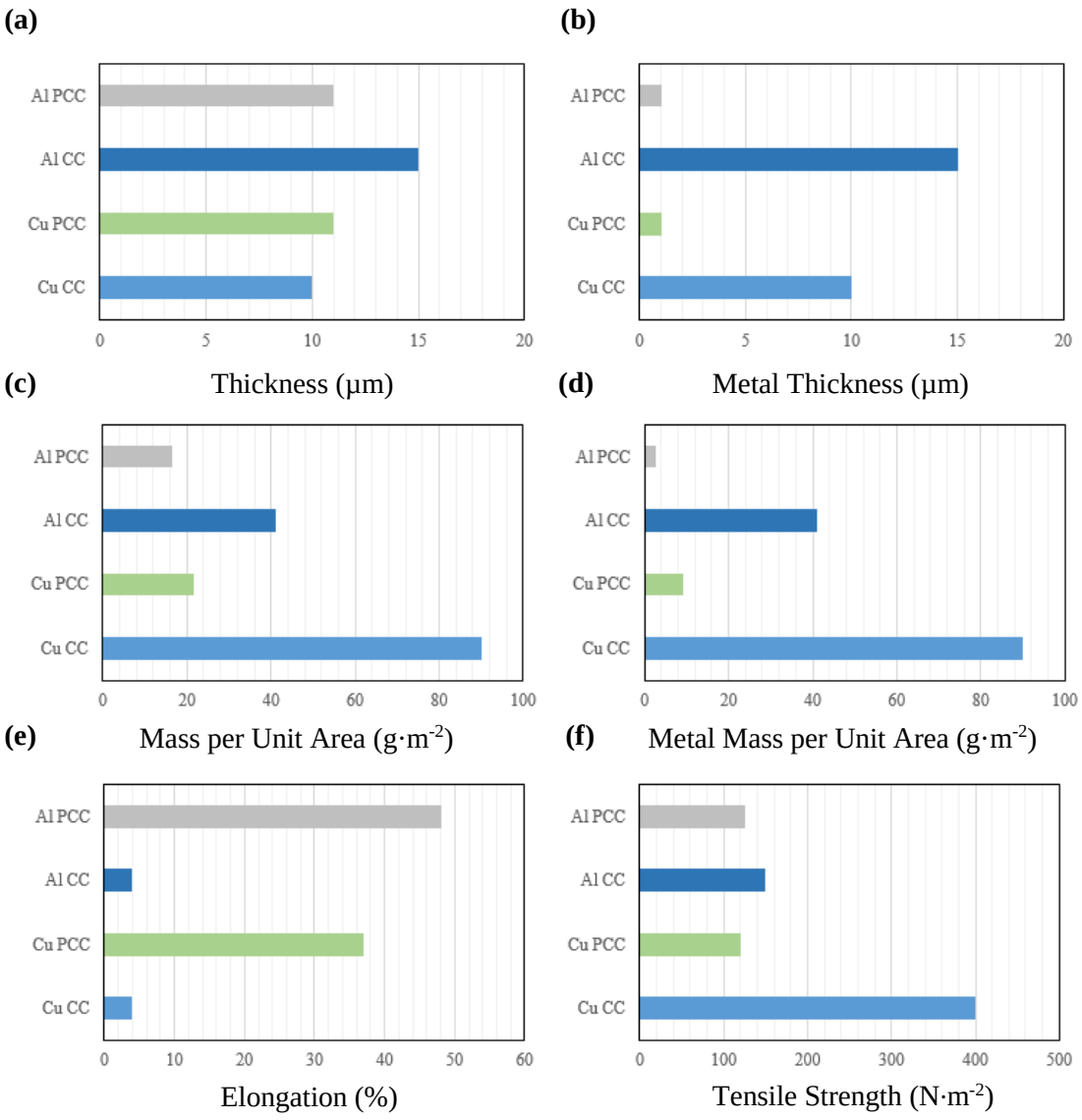

Figure 5-1: Comparison of (a) thickness (b) metal film thickness (c) mass per unit area (d) metal mass per unit area (e) elongation and (f) tensile strength of standard commercial metal CCs and PCCs.

Cells were manufactured with both commercial CCs and their PCC counterparts, comparative material properties and thicknesses are shown in Figure 5-1. Nail penetration and PCC evaluation was investigated by *operando* X-ray imaging, *post-mortem* X-ray micro-CT and thermal statistical analysis to understand the internal phenomena and external thermal response. In all tests conducted, the internal CC tabs were avoided during nail penetration, guided by *a priori* tomogram acquisition. Penetration of the negative tab welded to the cell casing would not have impacted the outcome as the Al PCC would

have protected the cathode layers. However, nail penetration of the positive tab in the electrode assembly would cause the cell to fail as there is no Al PCC present to protect this tab, however doing so would not provide evaluation of the Al PCC, and hence the internally welded tabs were avoided.

Four configurations of cells (G1, G2, G3, and G4) with different current collectors that were tested were tested. A combination of the standard metal current collectors (Al CC, Cu CC), the polymer aluminium current collector (Al PCC), the polymer copper current collector (Cu PCC) and both polymer aluminium and copper current collectors (Al + Cu PCC) were used in non-bottom vent and otherwise identical 18650-cells. The PCC materials were manufactured and provided by the Soteria Battery Innovation Group (South Carolina, USA). Lithium-ion 18650-cells consisting of $LiNi_{0.5}Mn_{0.3}Co_{0.2}O_2$ (NMC-532) and graphite electrodes were used in this work and were custom manufactured by Coulometrics (Tennessee, USA). Multiple abuse tests were conducted to ensure repeatability of results. Cells were rated at 2.10 Ah capacity at 0.20 C and were charged using a constant current, constant voltage (CC-CV) protocol. Cells were charged to 4.20 V at 0.50 C constant current and then held at constant voltage until the current was less than 0.02 C before abuse testing. Cells were tested at 4.20 V to provide the worst case scenario outcome should it occur as well as increasing the likelihood for a microscopic short-circuit to initiate and develop into a macroscopic short-circuit whereby the heat generation from thermal decomposition propagates cell-level thermal runaway.

The effectiveness of the safety mechanism of the PCC is predicated on whether it deploys before separator failure. Thus, in order to investigate the most challenging environment for the PCC to function, a 10 µm thick single layer polypropylene separator was used. For comparison, typical commercial separators are usually less than 25 µm in thickness [173,175,214,215] and are single layer, tri-layer or ceramic-coated polyolefin separators and therefore would likely in most cases be more thermally stable than a 10 µm thick single layer polypropylene separator. As the mechanism is theorised to enact before any other non-polymer electrode assembly component, this would enable the PCC to operate independently of cell chemistry.

5.2.2 X-ray Radiography

High-speed X-ray imaging at 2000 frames per second was performed at beamline ID19 at the European Synchrotron Radiation Facility (ESRF) in order to capture the internal dynamic structural phenomena during testing. The cells were imaged under a 74 keV polychromatic beam with a pixel size of 10.00 µm and a 2016 × 1111 pixel (horizontal × vertical) field of view (FOV). A PCO.Dimax (PCO AG, Germany) detector and LuAG:Ce ($Lu_3Al_{15}O_{12}$:Ce) scintillator (Crytur, Czech Republic) were used for all high-speed imaging experiments. The radiographs were flat-field corrected and enhanced using MATLAB's adaptive histogram equalisation (adapthisteq) function.

5.2.3 X-ray Micro-CT

Table 5-1: Imaging configurations for lab-based X-ray micro-CT. Zeiss HE3 filter is a proprietary filter provided by Zeiss as part of the Xradia 520 Versa.

Technique	Voxel Size	Field of view	Accelerating voltage	X-ray Tube Power	Filter	Projections
XRM – Nikon XT 255	35.5 µm	70 mm × 70 mm	200 kV	35 W	0.1 mm Cu	1848
XRM – Nikon XT 255	10.5 µm	20 mm × 20 mm	200 kV	35 W	0.1 mm Cu	3176
XRM – 520 Versa (4 × magnification)	1.77 µm	3.6 mm × 3.6 mm	160 kV	10 W	Zeiss HE3	1801

Laboratory-based X-ray CT was used to evaluate the safety mechanism of the PCC non-destructively by interior tomography acquisition across multiple length-scales. Non-destructive X-ray CT was conducted using laboratory X-ray systems: a Nikon XT H225, 225 kV with a PerkinElmer 1620 Detector and a Zeiss Xradia 520 Versa (Carl Zeiss, USA) were used to acquire flat-field corrected orthogonal radiographs to be reconstructed into 3D volumetric data. Both CT systems utilise a tungsten target, accelerating voltages and beam powers are shown in Table 5-1, and were selected based on the attenuation of the samples and the contrast of the component materials to ensure features of interest were resolvable. The resulting radiographs were reconstructed using commercial software packages (CT Pro 3D and Zeiss XMReconstructor), which use algorithms based on standard filtered back-projection or Feldkamp-David-Kress (FDK).

Cells were scanned with an increasingly focussed FOV and greater resolution; from 35.5 µm pixel size, corresponding to a 70 mm × 70 mm FOV, to 1.76 µm × 1.76 µm pixel resolution and 3.6 mm × 3.6 mm FOV (imaging configurations are shown in Table 5-1). The highest resolution interior volumetric data acquisitions were required to provide visualisation of the electrode layers post testing – in particular the PCC which surrounded the nail. Tomograms were acquired using the Zeiss Xradia 520 Versa utilising the "Scout & Zoom" technique [216–219]. This was required to visualise the current collector adequately. An initial coarse scan was conducted to establish the orientation and axes of the sample before a more detailed interior tomography was acquired. Post reconstruction, visualisation of the reconstructed tomograms was processed using Avizo Fire 9.5 software (ThermoFisherVSG, France).

5.2.4 Fractional Thermal Runaway Calorimetry

A custom-designed FTRC was used as described in Chapter 3.4. An ambidextrous design accounted for the permutations of failure such as bottom vent cell ejection or spin groove breaches. Figure 3-10(a) displays the fully assembled calorimeter enclosed in thermally insulating blocks composed of sealed glass cells, FOAMGLAS^{TM} (Pittsburgh Corning, Toledo US). For this study, the aluminium calorimeter design allows for X-ray transparency to probe the internal phenomena, nail penetration functionality, portability and the ability to perform high-throughput failure testing.

An interchangeable aluminium 18650-cell chamber enclosed the cell, as shown in Figure 3-10(c), capable of testing 18650-format commercial cells with varying chemistries, capacities and safety mechanisms, such as bottom vents. It is designed to discern the energy from the casing of the cell and the ejected contents; the cell chamber was thermally insulated from the rest of the calorimeter with thermally insulative ceramic. The aluminium designed allowed for X-ray transparency and thus visualisation of the internal phenomena that occurred during nail penetration experiments. The lightweight and portability of the unit also facilitated beamline hutch use with larger and much heavier calorimetry systems surpassing the imaging stage weight limit at beamlines.

The nail penetrated to a depth of 9 mm, an event which took ca. 1.1 – 1.6 s and was similar to nail penetration in previous studies [94]. The temperature at the tip of the nail was recorded via an additional thermocouple placed inside the hollow shaft of the nail [146,209]. Statistical analysis derived from the thermal runaway temperature data, provided by thermocouples throughout the axial direction, yielded insight into the total thermal runaway calorific output, with the decoupled heat contributions correlated with the cell casing and ejected material.

5.2.5 SEM Material Analysis

SEM provided insight into the structure of the PCCs after the nail penetration tests. Samples were cut into 20 mm × 20 mm squares with a fresh scalpel, coated with a nano-layer of gold to inhibit charging by improving conductivity and then vertically clamped into a sample holder to orientate the cross section vertically, parallel to the imaging path. Material analysis was provided by an EVO MA 10 (Carl Zeiss, USA) SEM. SEM micrographs were taken of the cross-section. Magnification at 10000-14000× at a working distance of 8.5 mm, an electron accelerating voltage of 10 kV and pixel resolution of ca. 29 nm was used to acquire material analysis of the PCC cross-section.

5.3 Prevention of Thermal Runaway: FTRC Data

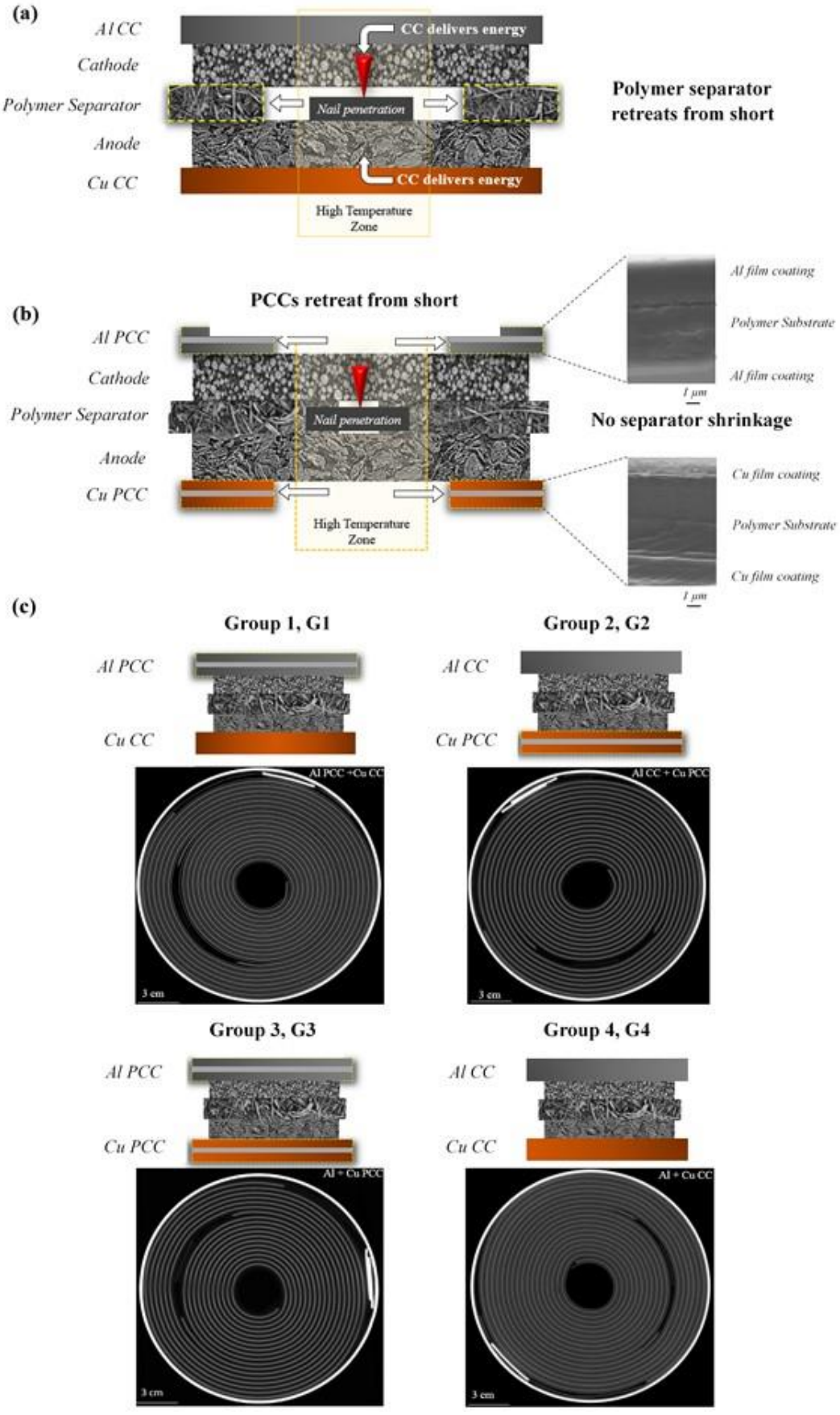

Figure 5-2: (a) Nail penetration of a standard commercial metal CC cell. (b) Failure mitigation mechanism of Al PCC + Cu PCC cell during nail penetration; SEM insets of the PCC cross-sections illustrate the ca. 8 μm polymer substrate 'core' and ca. 0.5 μm metal film coating. (c) Cell specifications of CCs used in this work. Cells are manufactured with one or both PCC, with G4 used as the standard commercial control group. Cylindrical cross section ortho-slices are shown with the corresponding cell group. Tomograms were acquired at 10 μm pixel size for each cell group.

The nail penetration process for cells with a conventional metal foil CC and those with PCCs are illustrated schematically in Figure 5-2(a) and Figure 5-2(b), respectively. In the conventional metal foil CC cell, the short circuit is maintained between adjacent electrode layers by the presence of the nail, leading to continuous heat generation and eventually thermal runaway. The principle of the PCC safety mechanism is that the initial heat generation caused by the short circuit causes thermal degradation thus the PCC periphery to shrink away from the nail, breaking the short circuit and preventing thermal runaway.

A variety of cell configurations were used to provide a basis for comparison of the Al PCC and Cu PCC and are grouped into four categories, G1 (Al PCC, Cu CC), G2 (Cu PCC, Al CC), G3 (Al + Cu PCC), G4 (Al + Cu CC) as shown in Figure 5-2(c). Therefore, comparison of G1 with G4 (and G2 with G3) provided insights into the effectiveness of the Al PCC in preventing thermal runaway. Similarly, evaluation of the Cu PCC could be made by comparison of G2 with G4 (and G1 with G3), which can be found in Supplemental Material. Lastly, both PCCs together could be evaluated via comparison between G3 and G4.

Tomograms of the fresh cells, acquired at 10 μm voxel resolution [Figure 5-2 (c)], were able to identify and resolve the commercial CCs within the 18650-cells (G1, G4). However, as the metal film coatings on the PCC were approximately 0.5 μm thick (G2, G3), they were not sufficiently resolved and were not apparent in the ortho-slices shown, thus leading to the contrasting cylindrical ortho-slices between the cell groups [Figure 5-2 (c)]. Mass differences between the commercial CCs and the PCCs are shown in Figure 5-1. Significant reduction in cell mass was observed and further analysis on gravimetric energy density increase due to the PCCs was observed.

The increase in gravimetric energy density associated with the use of PCCs instead of standard metal CCs is highlighted in Figure 5-1, together with a comparison of their mechanical properties. The mass reduction is significant, especially when comparison is made of the mass of constituent metal per

m^2. For the Cu PCC, the mass per unit area of Cu decreased from 90 $g \cdot m^{-2}$ to 9 $g \cdot m^{-2}$, while for the Al PCC, the mass per unit area of Al dropped from 41 $g \cdot m^{-2}$ to 2.7 $g \cdot m^{-2}$. The PCCs also exhibit comparable tensile strength to Al and considerably more favourable ductility at similar thicknesses to commercial metal CCs.

The introduction of the PCCs into the 18650s resulted in mass disparities between the groups of cells using different CC/PCC specifications, with an average mass difference of approximately 2.2 g (ca. 5%) between cells with standard metal CCs and those employing PCCs [Figure 2(a)]. This highlights the potential for gravimetric energy density increases as cells of the same capacity exhibited a reduction in overall mass.

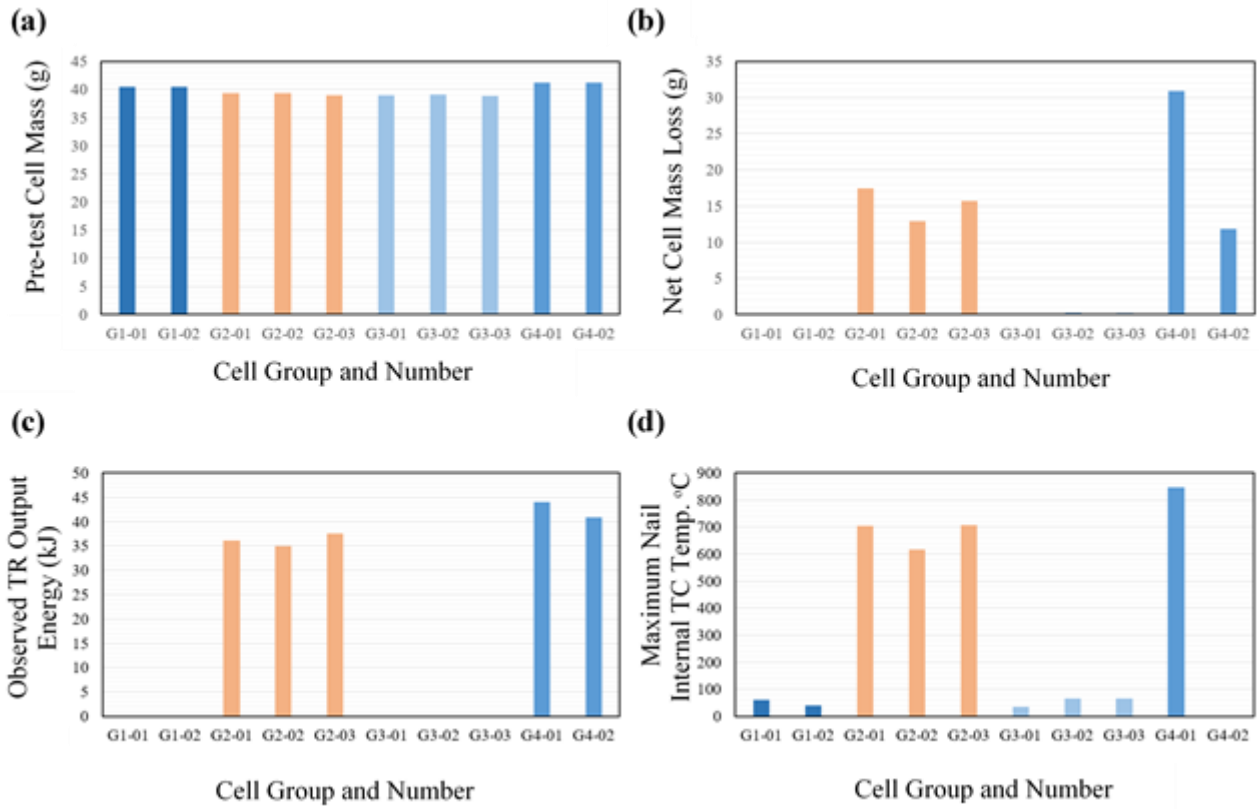

Figure 5-3: For each CC configuration in the four cell groups, multiple failure tests were conducted. Repeated tests of the cell group 1 is denoted as G1-0#. (a) Pre nail penetration test mass of each cell. (b) Cell mass loss after the nail penetration tests. (c) Calculated thermal runaway calorific output derived from the fractional thermal runaway calorimeter. (d) Maximum temperature measured by the thermocouple within the tip of the nail. Please note that for the G4-02 cell, the thermocouple within the nail failed and no temperature was recorded for this test.

Fractional thermal runaway calorimetry (FTRC) and analysis of the thermal data provided by thermocouple instrumentation facilitated analysis of the impact of nail penetration, with concurrent visualisation provided by high speed X-ray radiography. In the nail penetration tests conducted with FTRC and reported in this work, thermal runaway was not observed in any of the cells that contained the Al PCC (G1 and G3). This was supported by comparison of mass loss [Figure 5-3 (b)], calorific output [Figure 5-3 (c)] and maximum nail tip temperature [Figure 5-3 (d)] for cells which contained the Al PCC and those which did not. In contrast, thermal runaway was initiated in cells that contained only the Cu PCC (G2) and in the cells with only standard commercial metallic CCs (G4). The Cu PCC is examined further in Supplemental Material.

As the CC provides an electrical pathway for the micro short-circuit, the greatest elevated temperature will be experienced by the CC due to Ohmic heating before dissipating heat to the adjacent electrodes and then the separator. Therefore, in instances with the PCC, the PCC will experience a higher temperature than the separator thus thermal degradation of the PCC will occur first.

5.4 Operando Synchrotron Radiography of Nail Penetration Experiments

Different materials and phases were identifiable during *operando* X-ray radiography. In the central core, typically filled with weakly attenuating electrolyte, gases and materials with different contrast were observed to flow upwards, providing indicators of thermal decomposition of electrolyte and of the active materials in the electrode assembly. These observations were further reinforced by evidence of electrode disintegration and upward flow of electrode layers.

In Figure 5-4(a), various stages of the nail penetration of cell G4-01 (standard commercial Al CC + Cu CC) are shown. At 0.4545 s, as the nail penetrated the cell wall and began to impinge on the structure of the cylindrical electrode assembly, the initial bend in the electrode layer was followed by a firm spring back into position as the nail proceeded to the next layer. In this radiography frame, after the nail had penetrated through the outer four electrode layers, the first two layers had sprung back into position and were already showing signs of splitting and thermal degradation. These sites acted as nucleation points for thermal runaway via micro- and later macro- short circuiting.

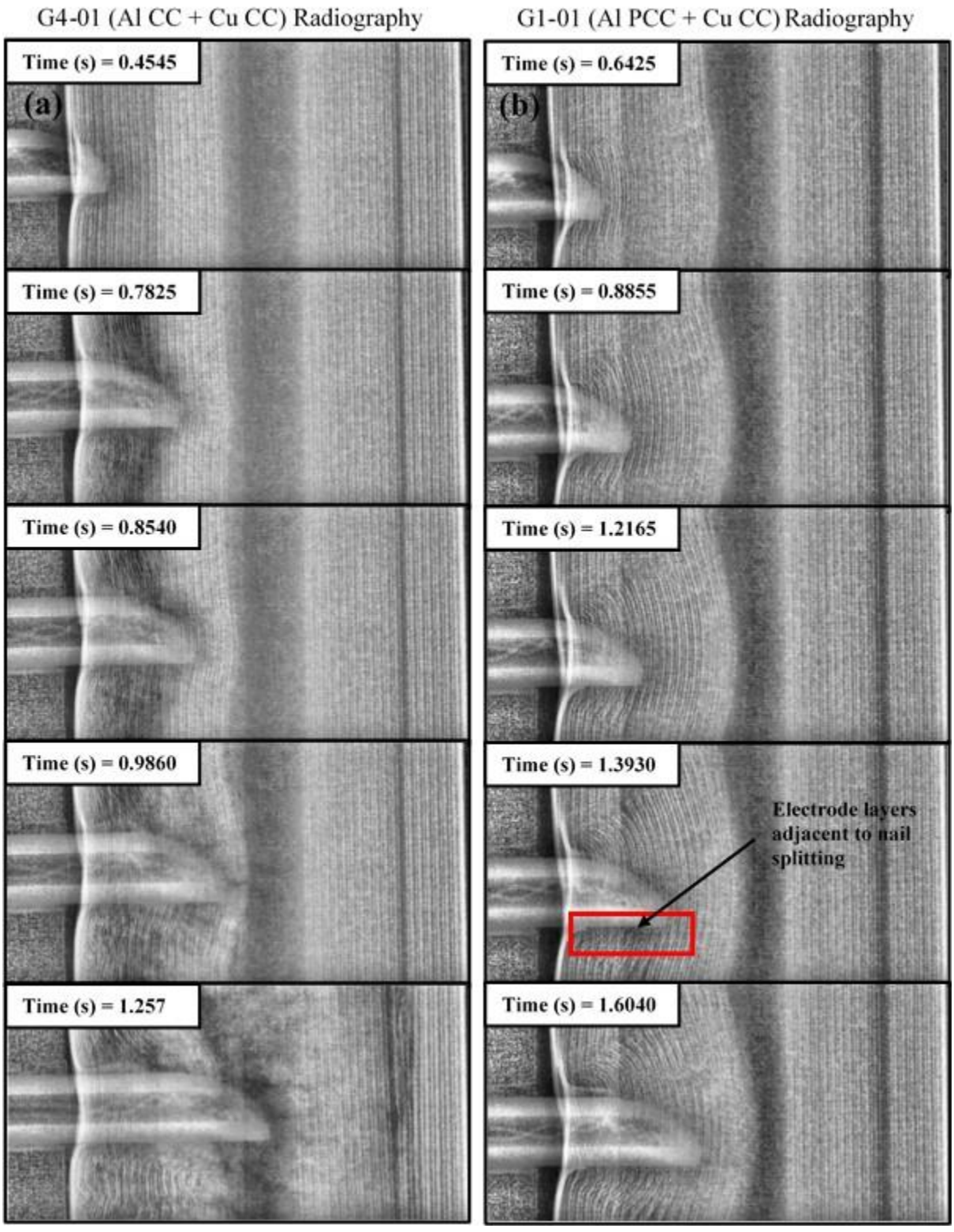

Figure 5-4: Radiography of cells undergoing nail penetration with time stamps shown in the top left of each frame. Penetration continues until a depth of 9 mm, or until the nail fails to penetrate further. (a) G4-01 (standard commercial Al CC + standard commercial Cu CC) – the onset of thermal runaway occurs immediately upon penetration and in the fourth frame cracking of the electrode assembly is evident. (b) G1-01 (Al PCC + standard commercial Cu CC) – complete absence of thermal runaway

and clear shear stress exerted on the cylindrical electrode assembly. Videos of each of these tests are provided as Supplementary Material.

As the macro short-circuiting of the nail-penetrated electrode layers occurred, electrolyte and active material decomposition led to macroscopic gas generation, which resulted in flow of material towards the cell cap prior to cell rupture. At 0.7825 s in Figure 5-4(a), thermal runaway had initiated in the previously penetrated layers and fluidisation of these layers was observed. Penetration continued into the inner half of the cylindrical electrode assembly, shown at 0.8540 s in Figure 5-4(a); thermal degradation observed in the form of electrode disintegration around the nail was also initiated locally and later propagated to widespread thermal runaway at 0.9860 s. At the tip of the nail at 0.9860 s, the inner electrode layers were seen to be cracking horizontally. At 1.257 s in Figure 5-4(a), widespread thermal runaway on the other side of cell was observed. The mechanism of thermal runaway observed in Figure 5-4(a) for cell G4-01 was consistent with that for cell G4-02. The dynamic process is illustrated in Supplementary Material.

In Figure 5-4(b), corresponding stages of the nail penetration of Cell G1-01 (Al PCC + Cu CC) are shown. The characteristic behaviour during nail penetration contrasted greatly to cell G4-01, with a significantly more ductile response of the electrode assembly to the penetration of the nail and very little evidence of electrolyte decomposition or widespread fracture of electrode layers. As the first five electrode layers were penetrated at 0.6425 s, the shear stress imposed by the nail on the electrode assembly caused the material to shift. This force can be observed by the deformed electrode assembly layers adjacent to the nail. This cumulative displacement of electrode layers resulted in curvature of the internal layers of the electrode assembly into the central core region. However, in contrast to the behaviour observed for cell G4-01, local heat generation was evidently rapidly curtailed by shrinkage of the Al PCC from the nail and all layers remained largely intact despite the significant curvature.

Some localised damage was evident close to the surface of the nail, where the electrode assembly was observed to have split (highlighted at 1.3930 s in Figure 5-4(b)); this was especially visible along the bottom edge of the nail. From 1.2165 s to 1.6040 s, in Figure 5-4(b), the shear stress which impacted on the electrode layers caused further deformation of the layers, and displacement of the electrode assembly in the central core of the cell. Further splitting of the tips of the electrode assembly in contact with the penetrating nail was observed, with a maximum temperature of 61.4 °C recorded. This temperature was measured by a thermocouple at the tip of the nail, thus it was lower than the actual temperature of the PCC. However, the temperature experienced was much lower than the

melting point of the polymer substrate, therefore, this provided further evidence to the hypothesized shrinkage of the PCC at the periphery where the nail had penetrated, rather than melting of the PCC.

The rigid spring back of electrode layers observed in cell G4-01 was not evident for cell G1-01. This more ductile response was likely to be a result of the elongation property of the PCC shown in Figure S1. Additionally, the interruption of thermal breakdown of material local to the surface of the nail, which maintained the integrity of the electrode assembly, allowing it to deform plastically as penetration progressed. Further analysis of these findings was provided by *post-mortem* CT shown later in Figure 5-5.

No thermal runaway of cell G1-01 occurred after waiting 10 minutes with the nail inside the cell. Subsequent removal and voltage measurement revealed an open circuit voltage (OCV) of 4.077 V for G1-01. After 8 months, the OCV of the cell was measured as ca. 3.60 V, which demonstrated a highly effective isolation of electrically conducting paths between the punctured electrode layers.

From these tests on the Al CC + Cu CC (G4 cells) and the Al PCC + Cu CC (G1 cells), primary indicators of the safety mechanisms of the Al PCC could be observed. The prevention of thermal runaway can be attributed to the Al PCC providing electrical isolation of the cathode and the nail (which is electrically connected to the anode via the cell can and the Cu CC). Secondly, due to the temperature sensed by the nail thermocouple, it could be ascertained that the polypropylene separator had not failed and that the Al PCC had indeed operated with the hypothesized shrinking mechanism as detailed in Figure 5-2(b). This was due to the initial micro short-circuit, which occurred as the nail penetrated the cell and came into contact with the Al PCC and the cathode; this ‘soft’ short circuit caused an initial surge of current to the local area which caused elevated local temperatures as measured by the thermocouple at the tip of the nail. As the temperature increased to ca. 60 °C, the Al PCC polymer core began to experience thermal damage and shrink from the nail, which was observed as a frayed electrode assembly adjacent to the nail tip (highlighted at 1.3930 s in Figure 5-4(b)). As a result, the Al film coating on either side of the PCC lost electrical contact with the nail as it also retreated with the polymer core of the Al PCC. This is in stark contrast with the mechanisms observed in Figure 5-4(a) for standard commercial cells, whereby the Al CC did not retreat and remained electrically connected. This enabled a continuous positive feedback between cell short-circuit and temperature elevation, which resulted in separator failure prior to thermal runaway.

Cells with the Al PCC did not undergo thermal runaway, as the PCC isolated the cathode from the nail by polymer shrinkage as the temperature increased. However, as the penetrating nail was in continuous contact with the negative steel cell casing, the Cu PCC was ineffective in preventing thermal runaway in the absence of the Al PCC. Further work in other cell geometries and structures is needed to objectively evaluate the potential mitigation of thermal runaway, especially in the absence of the Al PCC.

5.5 Post-mortem X-ray CT

The 3D reconstructions from *post-mortem* CT scans of the G3 cells (Al PCC + Cu PCC) are shown in Figure 5-5 and were used to validate the hypotheses deduced from the radiographs in Figure 5-4. The cathode is represented by the thicker bright grey layers due to the high level of X-ray attenuation, the thin dark line in the middle of the layers is the Al film coated PCC, as the polymer and Al film coated on the PCC have much lower attenuation. Graphite also has relatively low attenuation and is shown by the thicker dark grey layers.

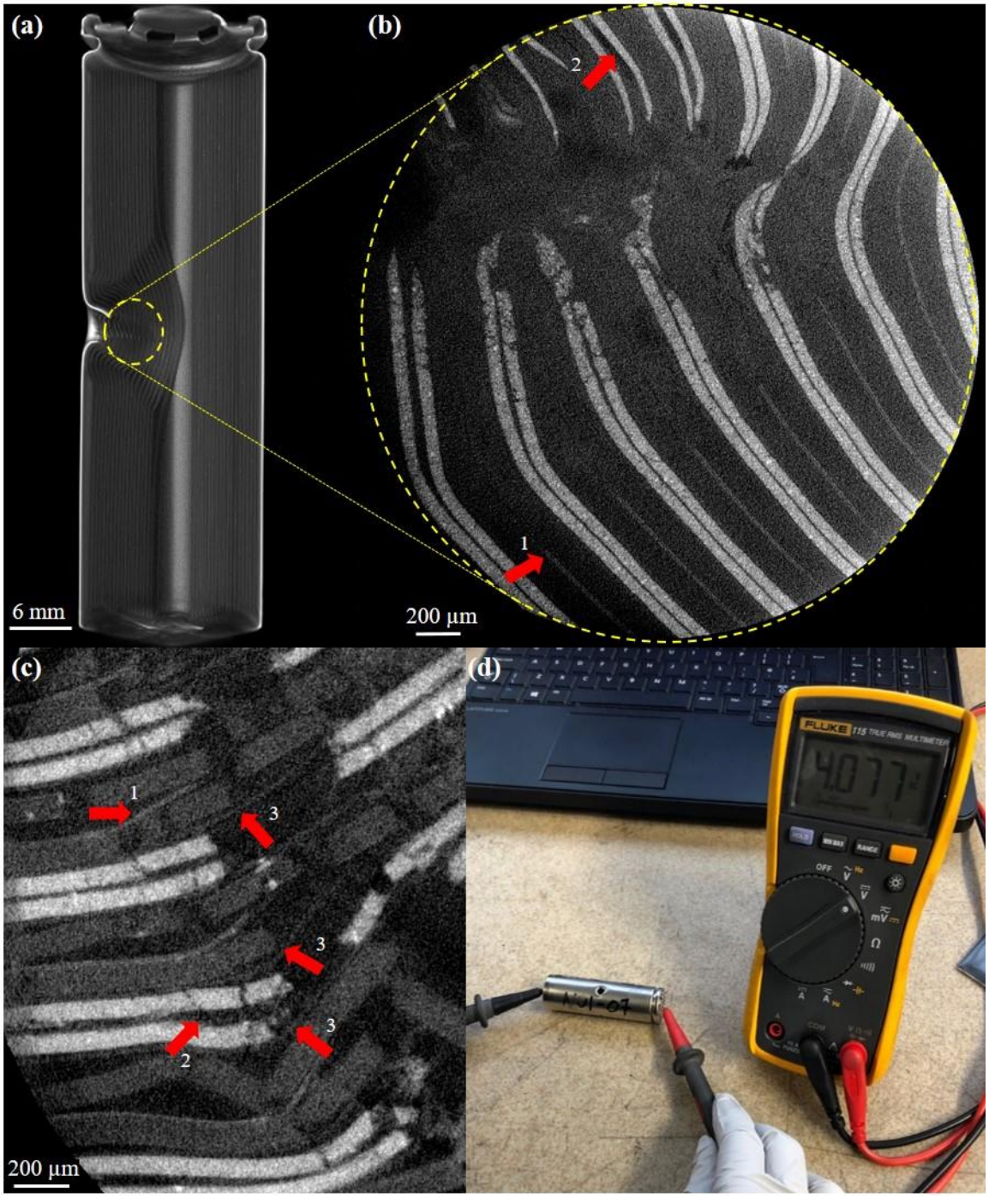

Figure 5-5: Post mortem analysis of G3 cells. Numbered arrows represent the same feature observed across multiple locations and are not limited to the examples marked where 1 shows the negative Cu PCC, 2 shows the positive Al PCC and 3 shows the separator. (a) Reconstructed tomogram of the entire nail penetrated cell (G3-02, Al PCC + Cu PCC), showing evidence of the shear forces exerted on the electrode assembly. (b) Cylindrical cross-section of the nail penetration path shown in (a) of cell G3-02 (Al PCC + Cu PCC) providing visualisation of the structure and indicators of the phenomena that occurred during mechanical abuse. (c) Cylindrical cross-section ortho-slice of the nail penetration path in the penetrated direction for cell G3-03 (Al PCC + Cu PCC). This interior focussed field of view provided visualisation of the internal structure after nail penetration at 1.76 μm pixel size. (d) Post nail penetration test OCV measurement showed 4.077 V for Cell G1-01.

Figure 5-5 (a) highlights the flexibility of the PCC electrode assembly to accept the mechanical deformation from the nail penetration. Additionally, the preventative mechanism in Al PCC cells occurred prior to the compromise of the safety components, as the CID, the CID vent and the PTC device remained intact. These safety measures specific to the cylindrical cell format (18650, 21700, 26650 etc) at the cell casing level, highlight the rapid preventative response of the PCC local to the region of short-circuit at the electrode level. Consequently, it can be inferred that the cell level safety devices common to most cylindrical cell formats (i.e. PTCs etc) did not respond sufficiently fast to the internal short-circuit via the nail. This highlights the significance in preventing the development of microscopic failures into cell level thermal runaway. Fractured electrodes can be observed along the nail penetration path, which were subsequently investigated using region of interest (RoI) CT as displayed in Figure 5-5(b). RoI X-ray CT was acquired with 1.76 μm pixel resolution, which was sufficient to resolve both the polymer and the metal coating of the PCC, and to deduce the sequence of events during nail penetration.

Both PCCs were visible in the ortho slices [Figure 5-5 (b) and Figure 5-5(c)] and the Al PCC and Cu PCC were observed to have shrunk away from the region of elevated temperature around the path of the nail, as shown by arrow 1 and 2, respectively, in both Figure 5-5(b) and Figure 5-5(c). In regions where the PCC had withdrawn from the elevated temperature region, a black void is visible indicating the complete absence of the PCC, as highlighted for example by arrow 2 in Figure 5-5(b). The lack of PCC to bind the double electrode layer together caused the double anode and cathode layers to split apart. These findings reaffirm the observations of the *operando* radiography.

Higher resolution imaging focussed on the damaged electrode layers adjacent to the nail, as shown in Figure 5-5(c) for cell G3-03. Material was visible between the cathode and anode at a similar attenuation level to the polymer core of the PCC, shown by arrow 3. This material was concluded to be the separator, which had maintained its integrity and was still found between the anode and cathode, despite the fact that adjacent PCCs on either side had melted or shrunk away from the path of the nail. This is significant as it provides further evidence that the PCC thermal degradation shrinking safety mechanism had operated as expected, deploying before any separator failure and isolated the cathode sufficiently to prevent further short-circuiting leading to thermal runaway.

5.6 Conclusions

Multi-length scale analysis with high speed X-ray radiography and *post-mortem* CT, combined with fractional thermal runaway calorimetry provided a detailed comparison between the thermal runaway mechanism during nail penetration of PCC cells and that of standard commercial CC cells. The mechanical abuse tests conducted provide evidence that the Al PCC demonstrated complete prevention of thermal runaway in an 18650 geometry cell with lithium-ion nickel-manganese-cobalt (NMC) cathode and graphite anode. In both Al and Cu PCCs, shrinkage of the core polymer layer from the interface between nail and electrode assembly caused the anode and cathode layers to split apart due to a lack of bonding with the PCC. The absence of the PCC in close proximity to the elevated temperature nail penetrated path in high resolution X-ray CT, coupled with the intact separator provides solid evidence for the hypothesized shrinking safety mechanism of the Al PCC.

Cells with the Al PCC showed potential for functionality after nail penetration, as the cells held voltage above 3.60 V for 8 months. The Cu PCC by itself is insufficient to prevent thermal runaway during this method of mechanical abuse. This is attributed to the nail bridging the electrically negative can, which is connected to the graphite anode, with the Al CC and the cathode. Therefore, despite the protection offered to the graphite local to the nail, the Al CC offered no additional protection to the cathode, and this resulted in thermal runaway. However, further testing would be required with different format cells where the cell casing is not electrically conductive to provide an unbiased evaluation of the Cu PCC. This would be possible in pouch or prismatic cells where the cell casing is not electrically connected to either of the electrodes and the Cu PCC could potentially isolate the negative electrode from the positive electrode. Adoption of the Al PCC in pouch cells would provide a thermal runaway contingency which would contribute immensely to reducing the consequences of failure in a cell geometry with much fewer safety components than an 18650-cell.

The results presented here demonstrate a great advancement in improving the safety of lithium-ion batteries, while also reducing cost and increasing the energy density of cells when scaled to manufacturing commercial cell formats as well as at the module level. Typically, efforts into the advancement of battery safety to ensure commercial adaptation is driven by development of new materials, examples include new electrodes, non-flammable electrolytes, the adoption of which requires time intensive, multi-variate, experimental optimisation of these novel components. The innovative structure provided by the PCC architecture offers the safety advances reported in this work which is independent of cell chemistry (provided the PCC is stable in the operating environment), moreover, the

properties of the PCC allow for assimilation with current cylindrical cell roll-to-roll manufacturing technology.

The promise shown by the polymer current collector in prevention and potential for mitigation presents scope for future work into other failure mechanisms such as thermal and internal short circuit abuse. We acknowledge that only 10 tests were conducted in total for this work and therefore we cannot say with statistical confidence that this material will withstand nail penetration thermal runaway 100% of the time, but this work nonetheless demonstrates a substantial improvement in safety with 5 out of 5 successful demonstrations with the Al PCC, where otherwise thermal runaway would certainly occur.

6 Mitigation of Thermal Runaway

6.1 Introduction

Metal-coated PCCs have demonstrated the promise in their ability to electrically isolate conductive materials in the previous chapter, which may mitigate against internal short circuit and subsequent thermal runaway in Li-ion batteries. Here, PCCs are tested in with and without a TSS and evaluate the mitigative impact on the total thermal energy released compared with industrial standard materials in an 18650 lithium-ion NMC cell. Fractional thermal runaway calorimetry was used to evaluate the thermal energy released during thermal runaway for these novel materials which were compared against widely deployed commercial counterparts as a control group. High speed synchrotron X-ray radiography provided internal structural insights during the process of failure.

Thermal runaway nucleation from microscopic internal shorts usually occurs due to failure of the separator. Alongside the cell electrolyte, typical commercial separators are one of the most susceptible components to degradation and structural compromise at high temperatures. Thus, a combination of both CC and separator safety innovations would provide the greatest promise to the mitigation of thermal runaway by limiting the current delivery to the short circuit and by isolating the electrodes with a TSS.

The major focus of research into CCs for lithium-ion batteries has been in tailoring the morphology of current collectors to accommodate the structures of novel electrodes [73,76–78,148]. However, due to recent failure events, battery safety has seen greater scrutiny and motivated research in component level safety functionality. Xu *et al.* [149], Chombo *et al.* [150] among other reviews [151–155] have previously reviewed a range of mitigative materials, components and strategies for cell safety and design. These cell components are designed to target specific events in the thermal runaway initiation process such as local temperature rise and the internal short circuit to improve safety through mitigation. These safety additions are often materials property enhancements, such as thermal or mechanical

stability or reduction in flammability, which include; electrolyte [156–160], separator [161–167] and thermally responsive materials (cathode coatings [168], current collectors [151,169–172], separators [173]). PTC CCs are those with significantly greater resistance at higher temperatures [151,169–172], these have been proposed as safety features which can mitigate failure, however, limitations arises with high C-rate and variable temperature operation. For example, a current collector redesign utilising the PTC mechanism by Liu *et al.* [80] has demonstrated the ability to isolate the region of short circuit from the battery.

Several authors [164,174,175] have examined and reviewed separators pioneered for safety advancements. Common commercial polymer separators in 18650-cells usually comprise of PE and/or PP and are typically ca. 10 – 30 µm thick [175], therefore, depending on the grade, they have an approximate melting point of ca. 130 ^{o}C. Multilayers of different polyolefins can introduce time delay during the separator failure process due to the differing melting points [173,176,177]. Improvements in thermal stability to prevent shrinkage have been achieved with a variety of methods which include the application of a ceramic coatings [178,179] or the use of polyester [180].

Results demonstrated in Chapter 5 highlighted the functionality of the Al PCC in prevention of thermal runaway during nail penetration with a 100% success rate [220]. This confirmed the promise of isolation of electrically conductive components in preventing microscopic short circuits developing into thermal runaway. Furthermore, mitigation of thermal runaway was also observed with the Cu PCC compared with the commercial Cu CC counterpart. This was attributed to the reduction in current delivery to the region of high temperature, which inhibited self-heat generation and thus limited development of a more severe thermal runaway and therefore a lower total calorific output by the cell. This was calculated to be a 14.8% reduction in the total thermal energy released compared to a control cell composed of commercial materials.

6.2 Experimental

18650 cells with PCC and TSS mitigation were used in this work and were manufactured with a selection of these components and their commercial counterparts (Al + Cu CC and PS). Both thermal and internal short-circuit device (ISCD) abuse techniques were conducted with high speed X-ray radiography and thermal statistical analysis provided by the FTRC. Cells containing the ISCD were positioned with the centre of the component parallel to the beam direction, to evaluate the local PCC and TSS characteristics when inducing failure. Thermal abuse simulates instances where cells are subject to high environmental temperatures such as operating a cell beyond the recommended limits, insufficient cooling during operation of a battery or propagation of failure through a module. The internal short circuit device reproduces examples where manufacturing defect, design flaws or internal degradation resulting in electrode cracking and deformation which may occur prior-to or during failure.

6.2.1 Information regarding 18650 cells and testing

Seven custom configurations of a 2.10 Ah capacity NMC-532 18650-cell shown in Table 6-1 were manufactured by Coulometrics (Tennessee, USA). A combination of the standard metal CCs (Al CC, Cu CC), the polymer counterparts (Al PCC, Cu PCC), a 10 µm thick single layer polypropylene separator and a 25 µm thick thermally stable polyaramid fibre (Twaron® [221–224]) separator were used in construction of the electrode assembly. The Soteria Battery Innovation Group (South Carolina, USA) manufactured and provided the PCCs, and Dreamweaver International (South Carolina, USA) provided the TSS used in the construction of cells in this work. The Dreamweaver Gold 25 µm thickness thermally stable separators used in cells consisted of non-woven aramid fibres, which were thermally stable up to 300 °C without change in chemical stability and less than 3% shrinkage. Other notable properties are: Gurley Number (JIS) of 150 s, 61% porosity, Young's Modulus of 1.177 GPa. Further information regarding the PCC and TSS can be found in Supplementary Information.

NMC532 and graphite electrode choices were chosen for relevancy to commercial trends to move away from LCO and the highest nickel content blends of NMC. NMC provides greater thermal stability than LCO, thus during the phases of thermal runaway precursor reactions prior to ejection of material, less oxygen is released during the thermal decomposition of the positive electrode and electrolyte. The 10 µm separator was used to provide emphasis on the protection provided in the worst case component scenario where the separator would be most prone to failure.

A constant current, constant voltage (CC-CV) protocol was used to charge the cells to 4.20 V at 0.50 C constant current. Cells were then held at constant voltage until the current was less than 0.02 C. Cells were tested at 4.20 V to provide the greatest heat output during failure. Multiple abuse tests were conducted to ensure repeatability of results.

6.2.2 X-ray Radiography

High-speed X-ray imaging was performed at beamline ID19 at the ESRF. In order to capture the internal dynamic structural phenomena during testing, temporal resolutions of 2000 frames per second (fps) were used for radiograph acquisition. The field of view of the cell was 2016 × 1111 pixel (horizontal × vertical) with a pixel size of 11.35 µm. A 74 keV polychromatic beam, PCO.Dimax (PCO AG, Germany) detector and LuAG:Ce ($Lu_3Al_{15}O_{12}$:Ce) scintillator (Crytur, Czech Republic) were used for all high-speed imaging experiments.

High-speed X-ray radiography at 2000 fps was performed at the I12 beamline [207] at DLS. Radiographs were acquired with a 74 keV monochromatic parallel beam with a pixel size of 17.90 µm and a FOV of 1280 × 800 pixel (Horizontal × Vertical). A $Gd_3Ga_5O_{12}$ (GGG) scintillator and Miro 310 detector were used for all high-speed imaging experiments.

6.2.3 Fractional Thermal Runaway Calorimet

As described in previously in Chapter 3 and Chapter 5, FTRC was designed in-house and utilised an ambidextrous design to safeguard for the uncertainties of failure and the direction of ejection from failure events such as bottom vent cell ejection or spin groove breaches. The fully assembled calorimeter (as shown in Figure 3-10) utilises thermally insulating blocks composed of sealed glass cells, FOAMGLAS™ (Pittsburgh Corning, Toledo US) to provide a near-adiabatic system, an assumption used in subsequent heat calculations. The calorimeter was made using aluminium to allow for X-ray transparency revealing the internal phenomena during high speed radiography. An array of thermocouples distributed axially and radially on the FTRC unit constituted the basis of calculations for calorific output during failure.

6.2.4 PCC safety mechanism and TSS effects

Thermal runaway within commercial 18650-cells predominantly nucleates through microscopic short circuits during separator failure. The effects of defects or abusive environmental conditions on standard commercial materials are shown in Figure 6-1(a), within an electrode assembly used in common, commercial lithium-ion batteries. Microscopic short-circuits originating from this abuse causes a local high temperature zone, through the following sequence of events, assuming the defect or degradative conditions persists: A continuous rise in temperature locally will cause separator damage and failure, this will compromise the physical isolation of each electrode causing short circuiting and significant current delivery via the current collector escalating into widespread cell thermal runaway (Figure 6-1a).

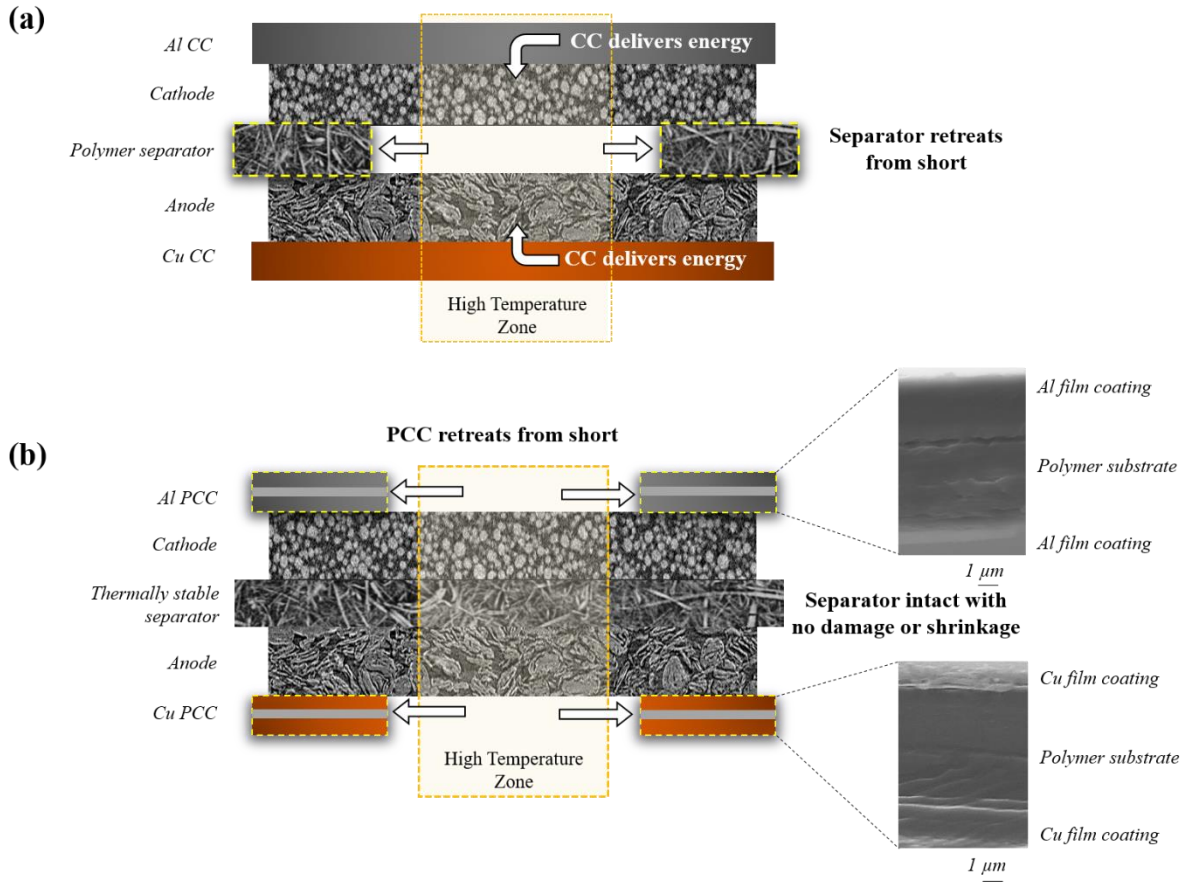

Figure 6-1: (a) Thermal runaway nucleation induces local high temperature in the assembly which causes the separator to thermally degrade and structurally fail first in standard commercial metal CC and polymer separator 18650-cell. (b) The failure mitigation functionality of the Al + Cu PCC and the TSS. PCC cross-sections are shown inset to provide visualisation of the ca. 8 μm polymer substrate 'core' and ca. 0.5 μm metal film coating.

The preventative mechanism of the Al PCC was elucidated with high speed X-ray radiography in Chapter 5, whereby the initial temperature increase caused the Al PCC to shrink away from the defect or high temperature region [Figure 5-2(b)] during mechanical abuse through nail penetration. This occurred before a 10 µm thick single layer polypropylene separator would observe any degradation and prevent subsequent microscopic short circuits from developing onto the macroscopic level. Mitigation with reduction in Cu-PCC was also observed in cells which did not have cathode protection of the Al PCC.

Mechanical deformation represents one likely scenario a cell may experience failure abuse, however, there have been many well reported incidences of thermal and internal short circuit thermal runaway of commercial devices too [14,15,81]. In these instances, whereby external temperature or internal defects could propagate the cell to failure, the addition of the TSS may provide further protection. The implementation of the TSS is proposed to provide further mitigation with minimal separator shrinkage up to 300 °C and would provide a greater degree of isolation of active materials from oxygen present in the air. This would, in turn, prevent a greater proportion of active material undergoing combustion, and therefore a reduction in output energy release during failure.

Table 6-1: 7 cell groups manufactured for mitigative evaluation experiments through both thermal abuse and ISCD initiated failure. Mass mean averages were calculated from cells without the ISCD to remove any effects the ISCD and the process of the ISCD implementation may have on the 18650-cell mass. Reduction in cell mass observed with the cells containing PCC compared with the commercial CC, as the PCC is primarily constructed of a less dense polymer substrate and not pure metal.

Cell Configurations			**Average Cell**	**Number of**
Cell Group	**Current Collector**	**Separator**	**Mass (g)**	**Cells Tested**
Group 1, G1	Al + Cu CC	PP	41.09	10
Group 2, G2	Al PCC + Cu CC	PP	40.55	8
Group 3, G3	Al CC + Cu PCC	PP	39.24	8
Group 4, G4	Al + Cu PCC	PP	39.03	6
Group 5, G5	Al + Cu CC	TSS	41.39	6
Group 6, G6	Al PCC + Cu CC	TSS	40.40	4
Group 7, G7	Al PCC + Cu PCC	TSS	38.23	6

7 cell configurations with unique current collectors and separator configurations were selected to provide comparison of the PCC and TSS with their commercial counterparts, to quantitatively ascertain the mitigative effects of the Al PCC and TSS on the cell output heat. The cells were specified to evaluate the performance of the Al PCC and the TSS when the cells were thermally abused or failed via an ISCD. The cell specifications in Table 6-1 were used in this work to provide a comparative basis between commercial materials and each of the mitigative components. All cell groups listed underwent abuse of both thermal and ISC abuse.

These cell configurations were selected to provide a comparative basis for the PCCs and the TSS. Comparison between G1, G2, G3 and G4, would provide insights into the PCCs' effect on the energy released during thermal runaway. Similarly, evaluating the differences between G1 and G5, G2 and G6, G3 and G7 respectively, would garner information into the TSS mitigative effects on the total energy release during thermal runaway, as the CC configuration remain the same within those pairs of cell groups. Furthermore, a comparison between G1 and G7 would provide a total mitigation assessment of both the PCCs and the TSS with their commercial counterparts.

6.3 Thermal Abuse – Calorimetry Analysis: PCC mitigation effectiveness

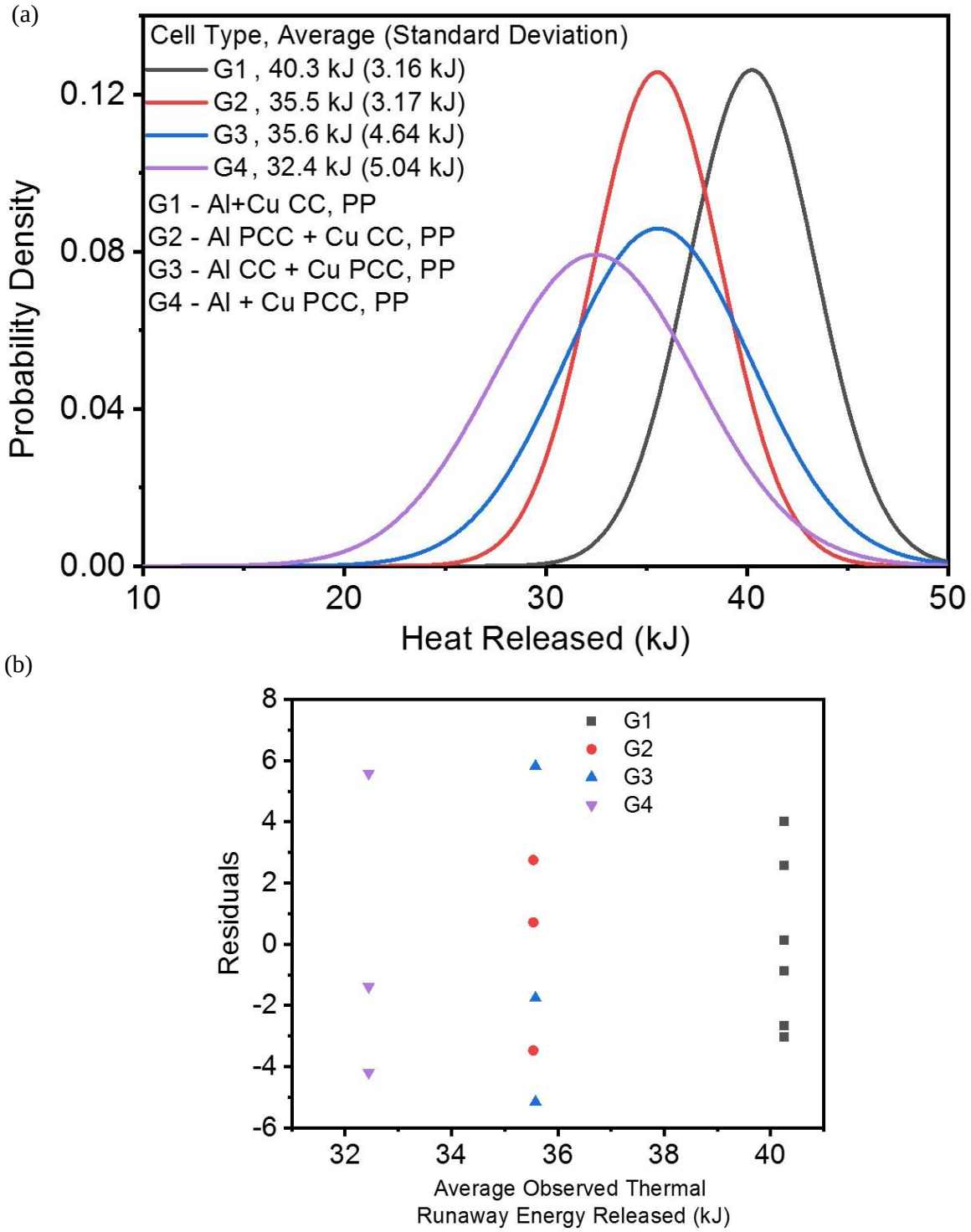

Figure 6-2: (a) Normal distributions derived from the heat released during thermal abuse initiated cell failure for G1, G2, G3 and G4. The comparison of these four cell groups would provide analysis of the mitigative effects of the Al PCC, Cu-PCC and both together. The peak of the normal distribution curves represent the mean average, the value of which can be found in the key in the top left of the figure. (b) The observed residuals for individual data elements in each distribution.

Cell failures by thermal abuse were achieved using the FTRC calorimeter and all cells in this work were continually heated at a rate of 960 W until failure, for consistency with results in Chapter 5 which have already examined the preventative success of the PCC [220]. From Figure 6-2, G1 (commercial materials) displayed the highest ejection of energy during thermal runaway with an average calorific output of 40.3 kJ. G3 (Cu-PCC) provided a degree of mitigation with average energy ejection measured at 35.6 kJ, whereas, cell group G2 (Al PCC) exhibited a greater mitigative effect, as cells ejected 35.5 kJ during failure. The isolative mechanism of the PCC and reduction in the energy delivery during thermal abuse is demonstrated by an 11.7% and 11.9% reduction in thermal energy released with G3 and the G2 respectively. G2 and G3 both provide similar mitigation: as all cells were subjected to thermal abuse until failure occurred, the initial isolation of the electrodes provided by the respective PCC at the microscopic short-circuit was overwhelmed as temperatures increased and the PP separator structurally failed due to melting. Thereafter, contact of the anode and cathode initiated further short-circuiting, with the PCC retreating from the short. However, with this continuous heating, thermal degradation of the electrolyte and active materials developed into thermal runaway. A combination of both PCCs with the polypropylene separator resulted in a further reduction of 19.6% in the thermal energy released by the cells in G4, with a mean average of 32.4 kJ. This highlighted the PCCs mitigative effects during failure initiated by thermal abuse. The high temperature of the electrode assembly and short-circuiting, instigated the isolation of active material and reduced the current delivery to the failure region by thermally driven PCC retreat, the function of which is shown in Figure 1b.

6.4 Thermal Abuse – Calorimetry Analysis: TSS mitigation effectiveness

(a)

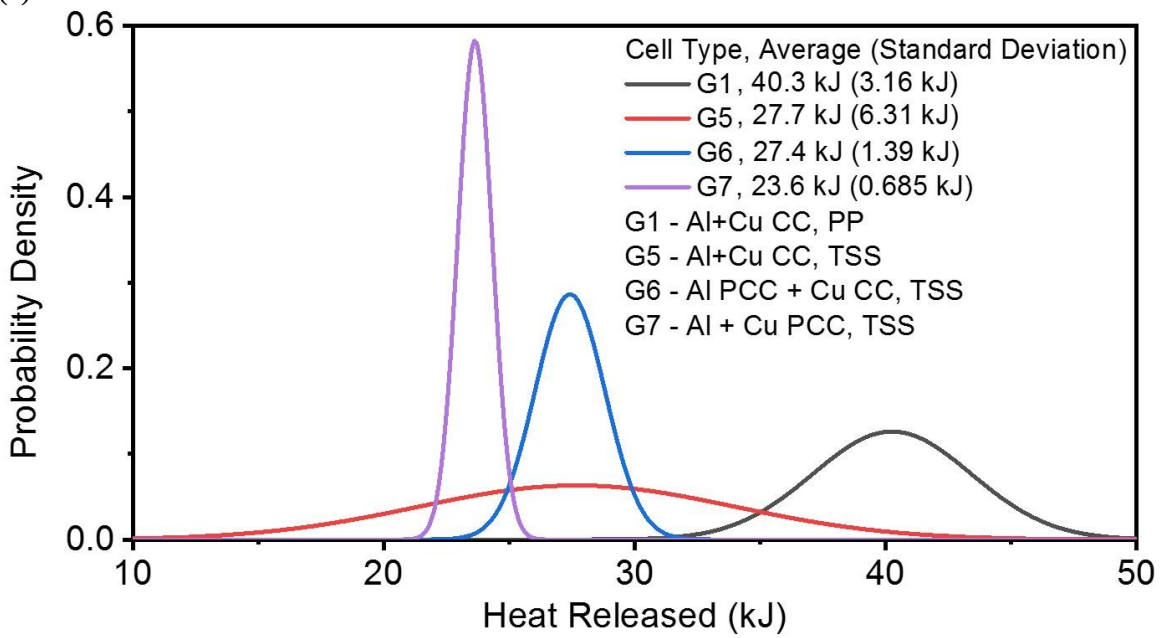

(b)

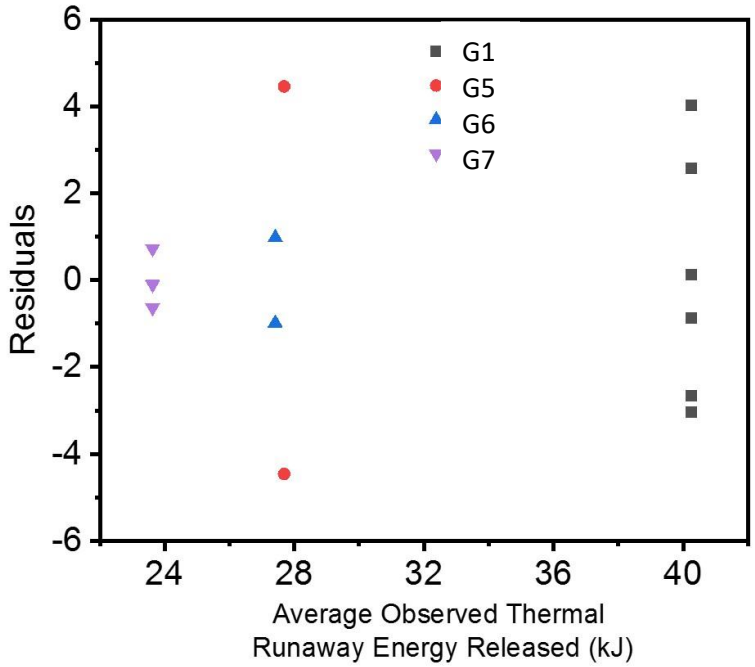

Figure 6-3: (a) Normal distributions derived from the energy observed during thermal abuse initiated cell failure for G1, G5, G6 and G7. The comparison of these four cell groups would provide analysis of the mitigative effects of the TSS and both the PCCs and TSS together. The peak of the normal distribution curves represent the mean average, the value of which can be found in the key in the top right of the figure. (b) The observed residuals for each distribution.

From the value of averages of each cell group shown in the top right of Figure 6-3, (also shown by the peak of the normal distribution), the thermal energy released by G1 (40.3 kJ) is significantly higher compared with G5 (27.7 kJ), G6 (27.4 kJ) and G7 (23.6 kJ). G1 and G5 both were manufactured from commercial metal film CC and differ by the separator alone (a TSS compared to PP). Therefore, the 31.3% reduction in energy observed can be attributed to the mechanism of the TSS during failure. The action of the TSS is explained as follows: during the sequence of events leading up to cell venting, the quantities of oxygen released from degradation of cathode materials is limited. Therefore, external oxygen present in the environment is required for further combustion of flammable active materials, electrolyte and gases [91,122,126,225,226]. The impact of the TSS on combustion and thermal degradation of the electrode assembly during thermal runaway was quantified by the reduction in energy released. The TSS provided a protective barrier from oxygen in the surrounding environmental air as the TSS retained its structural integrity during ejection of the jelly-roll electrode assembly. This characteristic is observed in high-speed synchrotron radiography, where before jelly-roll ejection, cells with the TSS were observed to have intact jelly-rolls whereas those with a commercial separator had already undergone significant electrode damage.

Comparison of G5 and G6, where the only change of material is the Al PCC replacing the commercial aluminium metal film current collector, shows only a reduction of 0.3 kJ, which is relatively minor. This reduction of 0.3 kJ may initially seem insignificant for the addition of the Al PCC, which has previously prevented failure in nail penetration. In this scenario, the isolation of the cathode is not of notable consequence as the TSS is still present to provide a barrier between the anode and cathode compared as the cell was continually heated and the polymer substrate of the PCC melted. The TSS does not display any structural degradation until 300 ^{o}C, a temperature which is typically not reached until cell ejection of flammable gases and material which undergoes combustion. Therefore, the isolation of the cathode is not significant as the TSS is still present to provide a barrier between the anode and cathode compared to cells containing conventional polymer separators (G1).

The impact of the TSS on the thermal runaway energy release is significant as the combustion of components and short-circuiting between electrodes are predominantly removed. Therefore, it is the other reactions which can occur (preceding ejection of flammable gases and material) which have a greater influence on the total energy released. Consequently, for a fully charged cell, reactions such as the highly exothermic breakdown of the cathode and electrolyte and the continuous heat generation and gas evolution at the lithiated graphite anode after SEI breakdown provide a greater proportion of the total energy released.

G7 provides further mitigation (compared to G5 and G6) when both anode and cathode PCCs were used in addition to the TSS. As the cell temperature increased during failure, the functional mechanism of the PCC activated; the polymer substrate of the PCC melts and this caused the electrode to delaminate from the PCC due to a lack of binding. This phenomena was widespread across the electrode assembly and changed the structure of the layers. In the G7 cell, the electrode assembly as manufactured is cathode-PCC-cathode-TSS-anode-PCC-anode-TSS. After PCC activation whereby the polymer substrate melts, this changed to cathode-cathode-TSS-anode-anode-TSS, thus leaving spacing between the cathode-cathode and anode-anode layers. The thermal degradation of the cathode (releasing oxygen at ca. 220-235 ^{o}C [225]) tends to follow two prevailing reaction pathways, with the electrolyte and with the lithiated anode. Hou *et al.* [225] investigated these anode-cathode-electrolyte reactions in NMC-811 vs. graphite cells to determine the proportion of oxygen as a precursor reactant in oxygen-electrolyte and oxygen-lithiated anode chemical reactions. The resultant heat released with the oxygen and lithiated anode produced ca. 2-3 times more heat per unit volume of oxygen reacted than with electrolyte. Thus, the spacing provided by the PCC failure provides a much more facile transport path (between the cathode-cathode layers) for the oxygen generated by thermal decomposition of the cathode rather than through the TSS to the anode. This space would be increased by the cumulative absence of PCC on both the anode and cathode throughout the electrode assembly, resulting in significantly reduced mass transport resistance for the evolved gas between the electrode layers. Thus, we hypothesise that the oxygen reacted primarily with the electrolyte [122] and produced much less energy than if the oxygen had reacted with the lithiated anode. The combination of the PCCs and the TSS mitigative effects were able to achieve a significant 41.4% reduction in energy released compared to G1 composed of commercial counterpart materials.

6.5 Thermal Abuse – X-ray radiography and post mortem analysis

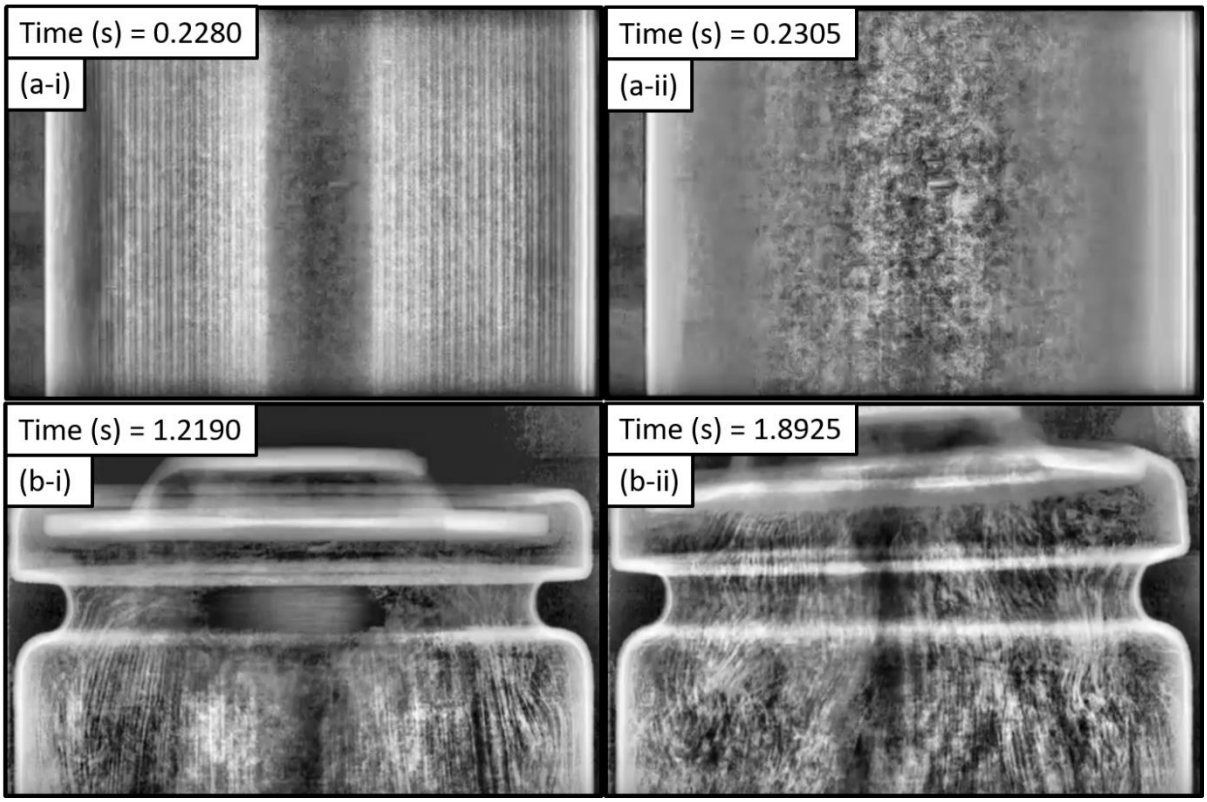

Figure 6-4: Two radiographs taken frames before and after complete ejection of the electrode assembly. (a) G6 cell (Al PCC, Cu CC and TSS). Please note the difference between the time indicated by the time stamp and thus the speed at which electrode ejection occurred (0.0025 s). Moments before ejection, the electrode assembly exhibits insignificant damage, which was confirmed with post-mortem physical examination, whereby the electrode jelly-roll was predominantly intact. (b) A G1 cell composed of commercial CC and separator which underwent failure. The first radiograph is taken at 1.2190 s (ca. 0.6735 s before ejection) displays considerable electrode damage from thermal decomposition which significantly precedes ejection. The second at 1.8925, the moment before ejection, shows electrode displacement into the cell header, structural compromise of the vent and substantial electrode deformation.

During post-mortem analysis conducted on all cell groups, it was observed that TSS cells typically ejected predominantly intact jelly-roll electrode assemblies, with little damage visible externally. A phenomena confirmed with simultaneous high-speed X-ray radiography during cell testing as shown in Figure 6-4a – which was representative of TSS constructed cells. In Figure 6-4a-i, the radiograph provided by high speed X-ray imaging reveals a predominantly intact electrode assembly on the verge of being ejected. 5 frames later (equating to 2.5ms at 2000 fps temporal resolution) in Figure 6-4a-ii, the jelly-roll electrode assembly has ejected.

Contrastingly, in Figure 6-4b-i for cell G1 (commercial materials), the radiograph was acquired 1347 frames (or 0.6735 s) before the cell is on the verge of ejection, which is shown in Figure 6-4b-ii. Significant non-uniform X-ray attenuation across the width of the cell was observed which can be correlated to the damage experienced to the electrode assembly due to thermal decomposition.

This confirms that by comparison, cells manufactured with the TSS (G5, G6, G7) displayed a propensity to ‘protect’ the electrode assembly and eject a structurally sound, predominantly undamaged jelly-roll. Given the uniformity in heating provided by the calorimeter design, the assumption that these characteristics were also observed along the length of the cell is reasonable. This provides evidence that the TSS provided structural protection during thermal abuse, and the potential for combustion and exothermic anode-cathode-electrolyte reactions were limited.

6.6 ISC – Calorimetry Analysis: PCC mitigation effectiveness

(a)

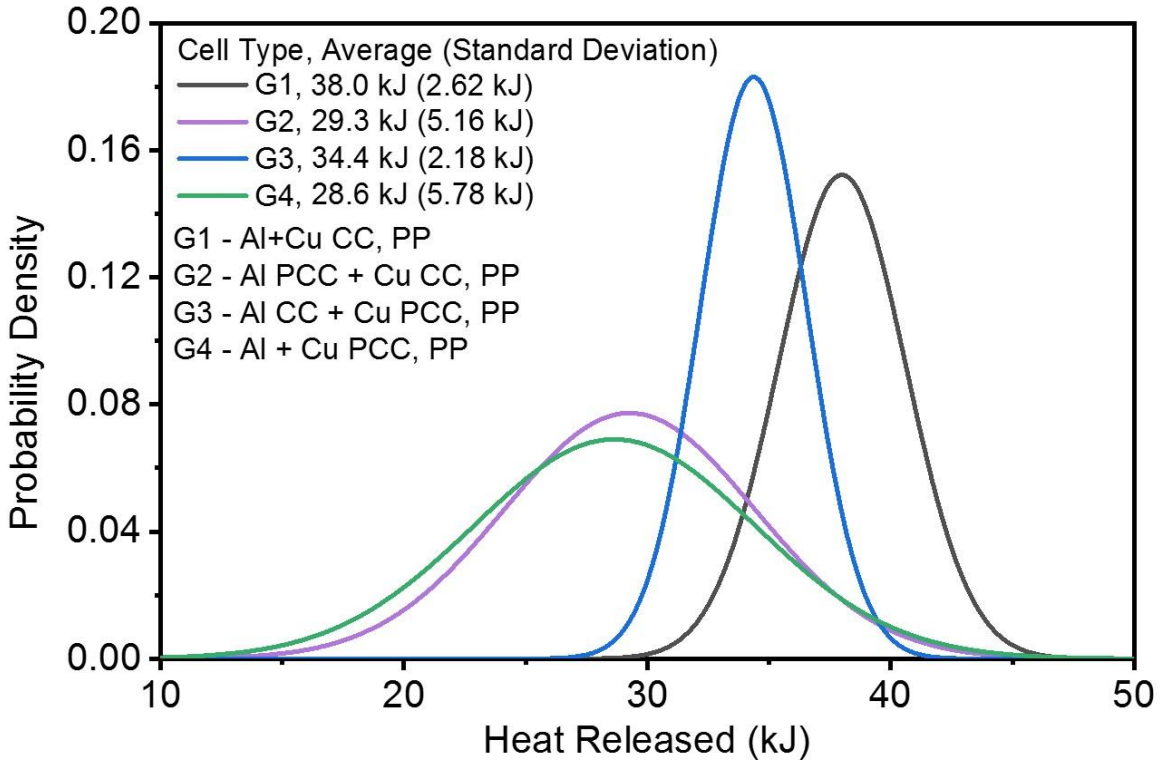

(b)

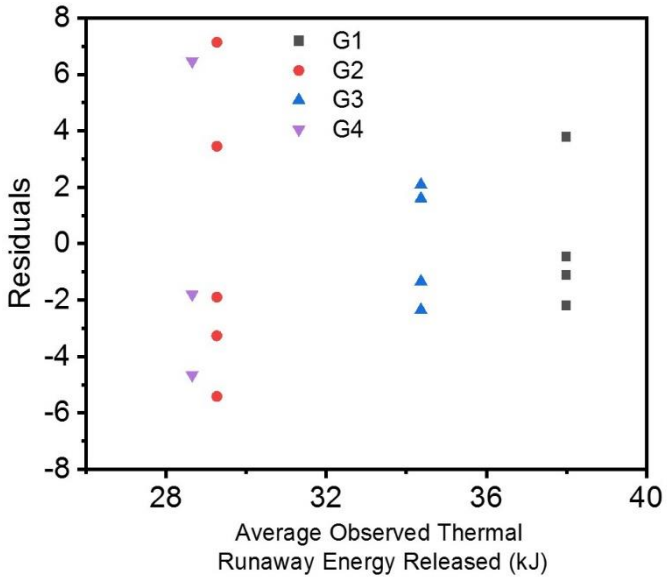

Figure 6-5: (a) Normal distributions derived from the energy observed during the activation of the ISCD implanted with the cell failure for G1, G2, G3 and G4. The comparison of these four cell groups would provide analysis of the mitigative effects of the PCC when an internal short circuit occurs, which propagates into cell level failure. The peak of the normal distribution curves represents the mean

average, the value of which can be found in the key in the top left of the figure. (b) The observed residuals for each distribution.

The ICSD replicates examples where defects during cell production, inherent design flaws and structural damage to the electrode assembly can cause cell shorting. Here, we have used ICSDs in conjunction with PCCs and TSSs to evaluate the mitigation of thermal runaway initiated by internal short. In these instances, the PCC has isolated the local region where the internal short-circuit device is located and reduced the current delivery to that region, thus the severity of the short circuit and the subsequent thermal runaway is mitigated. For the internal short circuit tests, the same 7 cell groups were used and implanted with an ISCD [93,111,227] .

As shown in Figure 6-5, G1 (composed of commercial materials for the CC and separator), failed on average with 38.0 kJ thermal energy released; significantly more than the other three groups which consisted of one or two of the PCCs. G2 (Al PCC) and G3 (Cu-PCC) observed a reduction in output energy by 22.9% and 9.47% respectively, which highlighted the greater protection provided by the Al PCC when only one of the two CCs were replaced as previously observed in Chapter 5 [220]. When the activation of the ISCD occurred, the microscopic short-circuit and elevated local temperatures causes the PCC to retreat from the ISCD and due to the structure of a lithium-ion electrode assembly, the Al PCC is of higher impact. Conductive additives and binders are added to the cathode during production as most cathode materials display relatively low electronic conductivity [228]. NMC materials increase in conductivity with decreasing lithiation (or increasing cell level state of charge) [229,230]. In these tests where the cell was fully charged, the graphite anode displayed several orders of magnitude greater electronic conductivity than the NMC cathode [231,232]. Therefore, if the Al PCC retreated from the local short circuit for cells in G2, the NMC cathode could only electrically conduct along the axial length and radial spiral from non-localised regions where there was no short circuit and there was PCC present in the electrode assembly. However, the electronic conductivity of this current pathway was several orders of magnitude less if the CC were present, thus a significantly mitigated short circuit.

Comparatively, for G3 where the Cu-PCC retreats from the localised region of the ISCD, the graphite anode is several orders of magnitude greater in electronic conductivity than the cathode and therefore will experience a more severe short-circuit than G2 despite the mitigation provided by the Cu-PCC. This difference in conductivity of the anode and cathode is responsible for the difference in mitigation provided by the PCCs in G2 and G3. Subsequent Ohmic heating causing separator failure and propagation of heat across the cell was followed by ejection of flammable gases and material for combustion.

G4 observed, on average, a 24.7% reduction in total thermal energy released by cells during thermal runaway, as both the mitigative effects of each PCC were experienced. The mitigation provided by the PCCs for the internal short circuit abuse via the ISCD initiation was greater than that afforded to the thermal abuse of the same G2 and G4 cells. This can be attributed to the abuse technique and the failure mechanism which the electrode assembly undergoes. For thermal abuse, the PCCs offer the initial isolation of the electrodes, however, once temperatures are in excess of 130 ^{o}C and separator failure ensues, highly exothermic anode-cathode-electrolyte reactions are unmitigated and the temporary isolation provided by the PCC is not as influential. In comparison, the ISCD requires ca. 47 – 57 ^{o}C to actuate [227,233,234] and the subsequent Ohmic heating is required to propagate thermal energy throughout the active material within the electrode assembly for cell level thermal runaway to ensue. Therefore, the PCC intervenes and mitigates this severity at a crucial stage where internal short circuit failures may develop into a severe failure. Thus, there is a greater mitigative effect provided by the PCCs in internal short-circuit failures compared to thermal abuse-initiated failures.

6.7 ISC – Calorimetry Analysis: TSS mitigation effectiveness

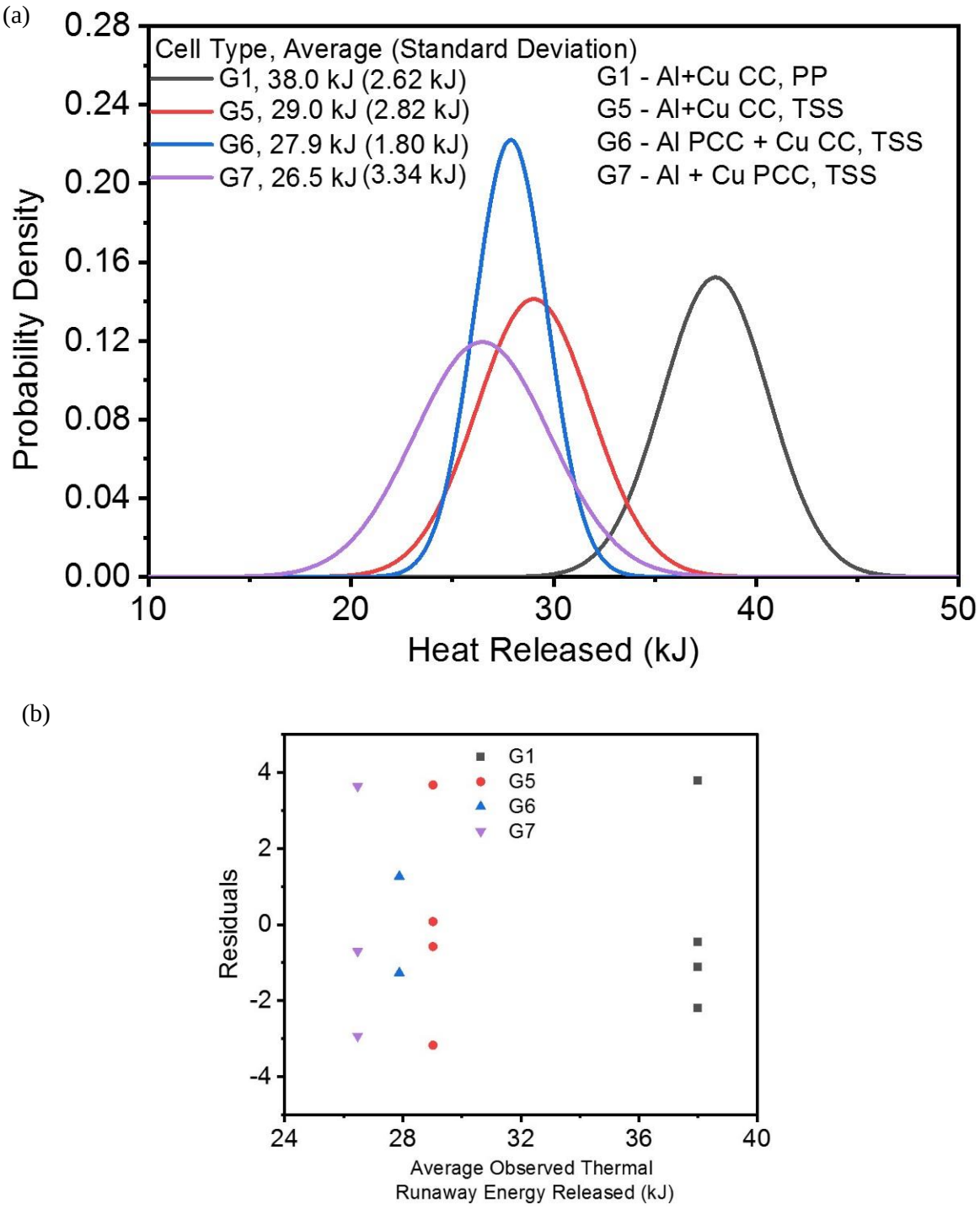

Figure 6-6: (a) Normal distributions derived from the energy observed during the activation of the ISCD implanted with the cell failure for G1, G5, G6 and G7. The comparison of these four cell groups would provide analysis of the mitigative effects of the TSS and both PCCs and TSS together when an internal short circuit occurs, which propagates into cell level failure. The peak of the normal distribution curves

represent the mean average, the value of which can be found in the key in the top right of the figure. (b) The observed residuals for each distribution.

G5, G6, G7 provide similar mitigative effects compared to G1 (which is manufactured with commercial standard materials for the CC and separator). The distribution of each cell group's energy ejected is also more consistent here and the difference in mitigation between having both PCCs with the TSS here is less prominent than that observed that observed in thermal abuse. G5 (TSS) and G6 (Al PCC, TSS) measured a 23.7% and 26.6% reduction in released energy during thermal runaway. Considering G5, the TSS alone provides a significant and comparative mitigation to G4 (Al + Cu PCC) despite differences in mitigation methods. Here, the TSS in G5 could not prevent short-circuit from developing in severity with commercial metal film CC. Following Ohmic heating, the surrounding electrode assembly experienced elevated temperatures which caused thermal decomposition of the anode, cathode and electrolyte; however, importantly the TSS remains structurally intact where polymer separators would have melted and caused a greater surface area of anode and cathode to potentially come into contact. This inhibited internal cell exothermic reactions prior to venting of flammable gases and ejection of material from the cell. The TSS provided structural protection, limited the presence of oxygen to the high temperature electrode assembly, and thus, combustion was mitigated and a reduction in total energy output from thermal runaway for G5.

Comparing the mitigation provided by G2 (Al PCC) and G6 (Al PCC, TSS) to G1, the difference between the two cell groups (G2 and G6) is that the addition of the TSS provided only 3.7% or 1.4 kJ reduction in thermal energy released. This is noticeably less substantial mitigation than when both of these materials were tested earlier for thermal abuse, (8.1 kJ or 20.1% reduction when comparing the G2 and G6 to G1 for thermal abuse). For internal short-circuit of G6, the mechanism of the PCC activated first, isolating the ISCD on the cathode side. In the absence of the PCC in the localised region of the ISCD, the severity of the short is reduced due to the less electronically conductive cathode. Ohmic heating ensues with increasing temperatures and thermal degradation and highly exothermic decomposition reactions occur, with the majority of the anode and cathode separated with the intact TSS. However, compared to thermal abuse of G6, the average temperature of the electrode assembly is less, due to the mitigated short circuit and the inherent nature of thermal abuse adding heat to the system. Despite the lower average temperature, the mechanism of the ISCD causes localized elevated temperature, which causes structural damage locally, exacerbated by the hole in the TSS to accommodate the ISCD, thus combined with a lower electrode temperature, the effectiveness of the TSS is reduced. For G7, a reduction of 30.3% in total energy output was observed, with a similar

mechanism as previously described, with the addition of the Cu PCC providing an initial mitigation to the graphite anode.

6.8 Conclusions

High speed X-ray radiography and FTRC provided insights into the mitigation mechanism of the PCCs and the TSS during thermal abuse and internal short circuit initiated thermal runaway. Through isolation of the electrodes during thermal abuse and limiting current to the short circuit once the separator failed, cells G2 (Al PCC), G3 (Cu-PCC) and G4 (Al + Cu PCC) provided reduction in thermal energy release of 11.7%, 11.9%, 19.6% respectively. However, in these cell groups the polypropylene separator failed and thus, thereafter, the PCC offered little protection. Further thermal abuse tests were conducted with the PCCs and the TSS, with cells G5 (TSS), G6 (Al PCC, TSS), G7 (Al + Cu PCC, TSS) where the safety advantages of both materials were accrued and mitigation reductions of 31.3%, 32% and 41.4% in thermal energy released were observed. The TSS was shown to protect the electrode assembly with isolation of the anode and cathode, inhibiting the oxygen transport with the PCC retreating and creating a void between the double-sided electrode layers; this provided protection to the electrode assembly from oxygen to prevent a greater amount of flammable material undergoing combustion. This phenomena was captured by the high speed X-ray imaging shown in Figure 6-4(a), where the electrode assembly was observed to be predominantly intact, in stark contrast to G1 cells made of commercial counterparts shown in Figure 6-4(b). Thus, generally undamaged jelly-rolls were witnessed in *post-mortem* analysis, indicative of TSS protection and lack of combustion. For thermal abuse, mitigative synergy of both materials contributed to the substantial 41.4% reduction in thermal energy.

For ISCD initiated failure, the PCC was highly effective during the initial short circuit due to the reduction in conductivity with the absence of the PCC in the localized region of the ISC. This effectiveness was greater than that observed in the thermal abuse of the same cells, however, this mechanism was effective until separator failed at temperature above 130 ^{o}C. When the TSS was implemented into cells G5, G6 and G7 for internal short circuit failure, the reduction observed were 23.7%, 26.6% and 30.3% compared to G1. The lower average temperature of the electrode assembly in ISCD initiated failures reduced the total average energy release of G1 compared to thermal abuse due reduced contributions of the exothermic thermal decomposition of electrodes and electrolyte above ca. 200-220 ^{o}C. Furthermore, the lack of oxygen release from the NMC cathode prevents further exothermic decomposition and combustion reactions.

These materials have been demonstrated to be highly effective in mitigation of thermal energy released during thermal runaway, and demonstrate flexibility towards cell chemistry, fast

implementation scalability with current production methods, cost and performance benefits with the reduction in metal used for the PCC, and therefore lower cell mass. These materials represent a significant step in reducing the severity of thermal runaway with mitigation reduction (in terms of energy released) comparative to bottom vents in 18650-geometry cells which have been widely adopted. These findings also help identify the mitigation contributions of certain aspects of the failure mechanisms before thermal runaway, and highlight the requirement for further advancements in battery safety through prevention and mitigation particularly as cell energy density increases. The results highlight the robustness of the PCC building upon previous work by the authors in prevention and now mitigation of thermal runaway. Moreover, the TSS emphasized the importance of structural dynamics and oxygen deprivation in combustion reactions during cell venting of flammable gases and material to reduce the total energy release.

Variability in total energy released during thermal runaway experiments was observed, this can be attributed to many factors such as differences in short circuit severity, heterogeneity within the cylindrical electrode assembly will cause differences in thermal decomposition reactions cell-to-cell, the degree of mitigation afforded by the function materials, the PCC and TSS. However, in each scenario, a significant portion of the energy ejected was mitigated. This consistent reduced total of a lower magnitude released represents a significant contribution to safety and electrical powertrain design due to the reduced risks from combustion, cell-to-cell thermal runaway propagation at the pack level and in design scopes where containment of failure is important, a lower total energy release will aid in reducing the mass and design criteria to reach containment or mitigation. Electrode material choice could be considered to have a lesser impact in thermal runaway in this instance as the material stifles oxygen evolution from the cathode from facile combustion and protection of the electrode assembly from the oxygen rich atmosphere too.

7 Characterisation of Pure Silicon Anode Lithium-ion Cells

7.1 Introduction

Silicon (Si) as an anode material for Li-ion batteries offers a specific capacity that is much greater than that of graphite (3579 $mAh \cdot g^{-1}$ vs. ca. 372 $mAh \cdot g^{-1}$). However, limitations are posed due to the significant volume change (ca. 300% on full lithiation), leading to capacity loss and performance degradation. Despite Si becoming increasingly prevalent in commercial cells, its failure mechanisms are also not well understood, this is furtherly complicated with the requirement of specialised electrochemical diagnostics facilities as well as synchrotron imaging. Chapter 1.8.2 discussed the literature survey with regards to pure silicon anodes in lithium-ion energy storage literature.

In Chapter 5 and Chapter 6, the PCCs exhibited significant contributions to safety improvement with the prevention of thermal runaway in 18650-format cylindrical cells and reduced calorific output. It remains difficult to characterise these internal mechanical responses leading up to failure especially the polymer of the PCC. Chapter 4 demonstrated thermal runaway characterisation with acoustic spectroscopy for through plane electrode deformation and detection of gas generation within the electrode assembly. Reviewers for these previously submitted manuscripts expressed an enquiring interest whether the technique and materials with safety functionality would continue to operate as expected independently of chemistry and cell format which motivation for the selection of this cell chemistry and format.

In this chapter, pure silicon anodes of a nano-wire architecture (which help mitigate mechanical challenges that lead to capacity loss) are investigated with acoustic spectroscopy and X-ray radiography to ascertain the thermal runaway characteristics. Insights through these characterisation methods will be used to linked internal structural phenomena with externally measured thermal and cell voltage responses. Advancements in greater energy density and high rate capabilities provide further impetus to understand degradation and failure associated with these new materials and architectures. Here, AS

will be used to identify phase changes associated with silicon failure and investigate the features which may arise due to the presence of an internal short circuit device with melting internal components and the Al PCC. Multifaceted characterisation to inform future electrode design and battery safety is critical for the acceleration of adoption and commercialization of silicon cell chemistries and functional materials alongside contributions to safety through components such as PCCs. The Si NW structures explored here are designed to maximise surface area to improve electrochemical reaction kinetics, a factor which could result in a more severe thermal runaway.

7.2 Experimental

The internal responses of commercial 3.6 Ah LCO and Si-NW anodes pouch cells (Amprius, CA,USA) consisting of commercial materials and their Al PCC counterparts were tested to evaluate the thermal runaway mechanisms of silicon and the preventative mechanism of the PCC with this cell chemistry and format. These cells are also tested with Al PCC to scrutinise the effectiveness of the functional mechanism to battery safety, independent of cell chemistry and geometry with thermal and internal short circuit abuse.

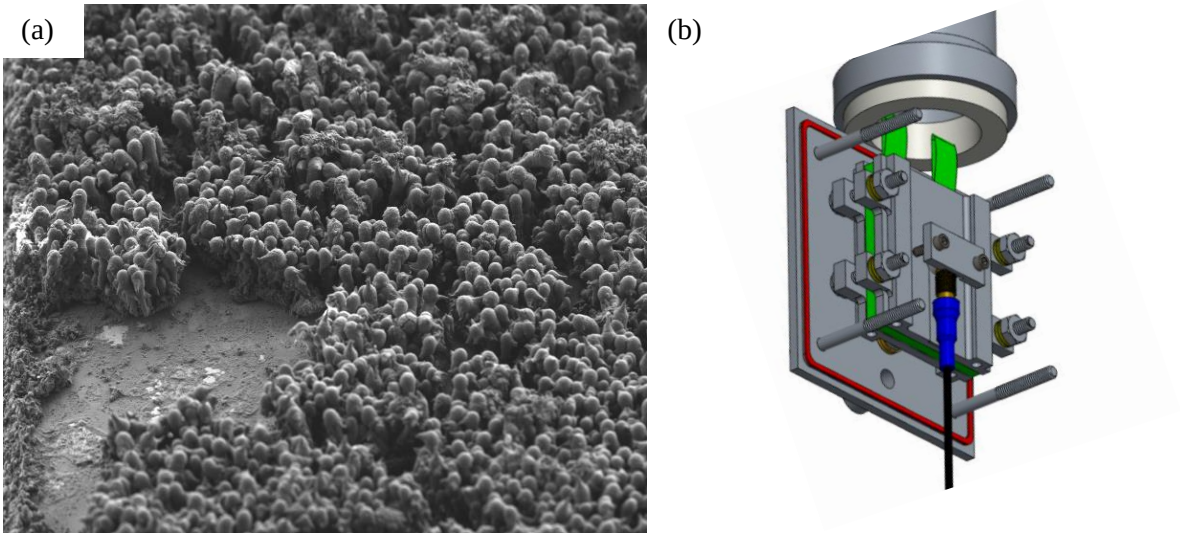

Figure 7-1: (a) SEM side profile of Si-NW anode used in Si-NW cells tested during thermal runaway. Some Si nano-wires detached from the current collector during sample preparation. (b) The orientation of the pouch cell chamber assembly. This is of the same design as shown previously in Figure 4-1(b). The brass plate was placed beneath the cell in the encapsulating cell chamber to collect high temperature molten material which could melt the aluminium containment.

Three cell configurations were used in this work, commercial cells constructed of Si-NW anodes with commercial components and their ISCD counterpart (A and A-ISC respectively). This was to examine the differences in AS signal responses and provide understanding of the structural evolution as a result of a pure silicon anode. A further cell group which consisted of the Al PCC and ISC (B-ISC) was also tested to evaluate the Al PCC in a scenario which can be considered worst-case. Cell groups A and A-ISC required no voltage sensor as cells were taken to failure with commercial materials.

The 50 mm × 55 mm × 4.5 mm (width-height-thickness) Si-NW anode pouch cells consisted of 16 repeat unit anode-cathode electrode layers and the ISCD was implanted in the centre of the flat electrode surface eight layers in. The acoustic pulse-echo transducer was also placed externally to the cell at this centre position to provide through-plane understanding of the mechanical evolution of the ISC device and electrode assembly layers.

The cells were constructed of a single layer polypropylene separator (similarly to Chapter 5 and 6) to evaluate whether the functional PCC would activate before separator failure and to evaluate the effectiveness of the PCC. However, these Si-NW PCC cells contained an implanted ISCD which has an activation temperature at ca. 57 ^{o}C whereby it connects the negative electrode active material to the positive electrode current collector is due to the melting point of the wax component of the ISCD which separated these components. The latent ISCD has without exception initiated consistent failure in previous testing in literature [93,111,227,233,234].

The connection of the negative electrode active material and positive electrode current collector has been proposed and confirmed as the most probable short circuit to induce failure [235] due to the high electrical conductivity but lower thermal conductivity of the graphite carbon negative electrode comparatively to the copper current collector. Furthermore, the activation of the ISCD at 57 ^{o}C is achieved through an etched separator to accommodate the ISCD, which occurs at much lower than the expected melting point range of polymer separators at ca. 130 ^{o}C and closer to the temperature at which PCC which retreated in Chapter 5. Therefore, to mitigate or prevent failure, the Al PCC will have to isolate the microscopic short circuit through disconnecting the PCC to the ISC and thereby the negative electrode to prevent propagation of mechanisms predicating failure such as rapid short circuit and heat generation. Cell OCV was measured for cells in B-ISC to evaluate the contributions to cell safety the PCC offers in the silicon pouch cell.

FTRC provided thermal data analysis with concurrent X-ray radiography visualization of the internal structural evolution. Thermal abuse through four cartridge heaters provided a total of 112 W heating until failure. A-ISC and B-ISC cells were heated until the thermocouple measured 70 – 85 ^{o}C as there is expected temperature difference between that measured at the cartridge heaters and the cell electrode assembly. Onset of failure was observed with self-generated heat from exothermic decomposition of electrode materials which caused a significant temperature increase and ejection of material observed with X-ray radiography.

Synchrotron X-ray radiography allows visualization of the cell cross-section, with attenuation based upon absorption, distinguishing the alternating anode-cathode layers and in instances of the ISCD implantation, identification of the device location. The X-ray and acoustic 'transparent' experimental set-up shown in Figure 4-2 was used to conduct failure testing. X-ray imaging at 2000 frames per second was performed the European Synchrotron Radiation Facility (ESRF) on beamline ID19. The cells were imaged with a field of view (FOV) of 2016 × 1111 pixel (horizontal × vertical) under a polychromatic 74 keV beam with a pixel size of 10.00 µm. A PCO.Dimax (PCO AG, Germany) detector and LuAG:Ce ($Lu_3Al_{15}O_{12}$:Ce) scintillator (Crytur, Czech Republic) were used for these high-speed imaging experiments. The radiographs were flat-field corrected and enhanced using MATLAB's adaptive histogram equalisation (adapthisteq) function.

The PCC materials were manufactured and provided by the Soteria Battery Innovation Group (South Carolina, USA). Multiple abuse tests were conducted to ensure repeatability of results, further results which followed observed trends can be found in Supplementary Materials. Cells were rated at 3.60 Ah capacity and were charged at using a constant current, constant voltage (CC-CV) protocol. Cells were charged to 4.05 V at 0.3 C constant current and then held at constant voltage until the current was less than 0.02 C before abuse testing.

The effectiveness of the safety mechanism of the PCC is predicated on whether it deploys before separator failure as shown in Figure 6-1(b) and whether it can prevent or mitigate the B-ISC cell from failure at the expected 57 ºC. Thus, in order to investigate the most challenging environment for the PCC to function, a 10 µm thick single layer polypropylene separator was used. For comparison, typical commercial separators are usually less than 25 µm in thickness [173,175,214,215] and are single layer, tri-layer or ceramic-coated polyolefin separators and therefore would likely in most cases be more thermally stable than a 10 µm thick single layer polypropylene separator adopted here as a 'worst case scenario'.

7.3 Thermal and ISC abuse of Cell Groups A and A-ISC

Characterisation of the cell responses during abuse and initiation of thermal runaway was conducted with the set-up shown in Figure 7-2(a). The acoustic probe is centred on the flat surface area of the cell and in the location where the ISCD would be located. Thermocouples were screwed down on the bottom and top aluminium plates to provide cell temperature measurements. Cell Groups A and A-ISC were heated at 112 W until thermal runaway occurred, which allowed for the visualisation through X-ray radiography and examining with AS and post-mortem analysis.

Figure 7-2: (a) Photograph of the experimental set-up shown in Figure 4-2. The cell chamber stack assembly with the brass plate taped down to the bottom of the cell chamber enclosure to collect high temperature material ejected from thermal runaway to prevent damage to the aluminium cell chamber enclosure. (b) Post-test cell chamber assembly photograph, high temperature ejection of materials caused the aluminium cell chamber plates to melt. (c) Post-test photograph of the brass plate, showing multiple locations where high temperature material from cell thermal runaway caused the brass to melt.

(d) Photograph of Si-NW cell within the cell chamber stack assembly post thermal runaway testing, the laminated aluminium exterior remains with the electrode assembly melted and ejected during failure.

7.3.1 Thermal abuse of Cell Group A

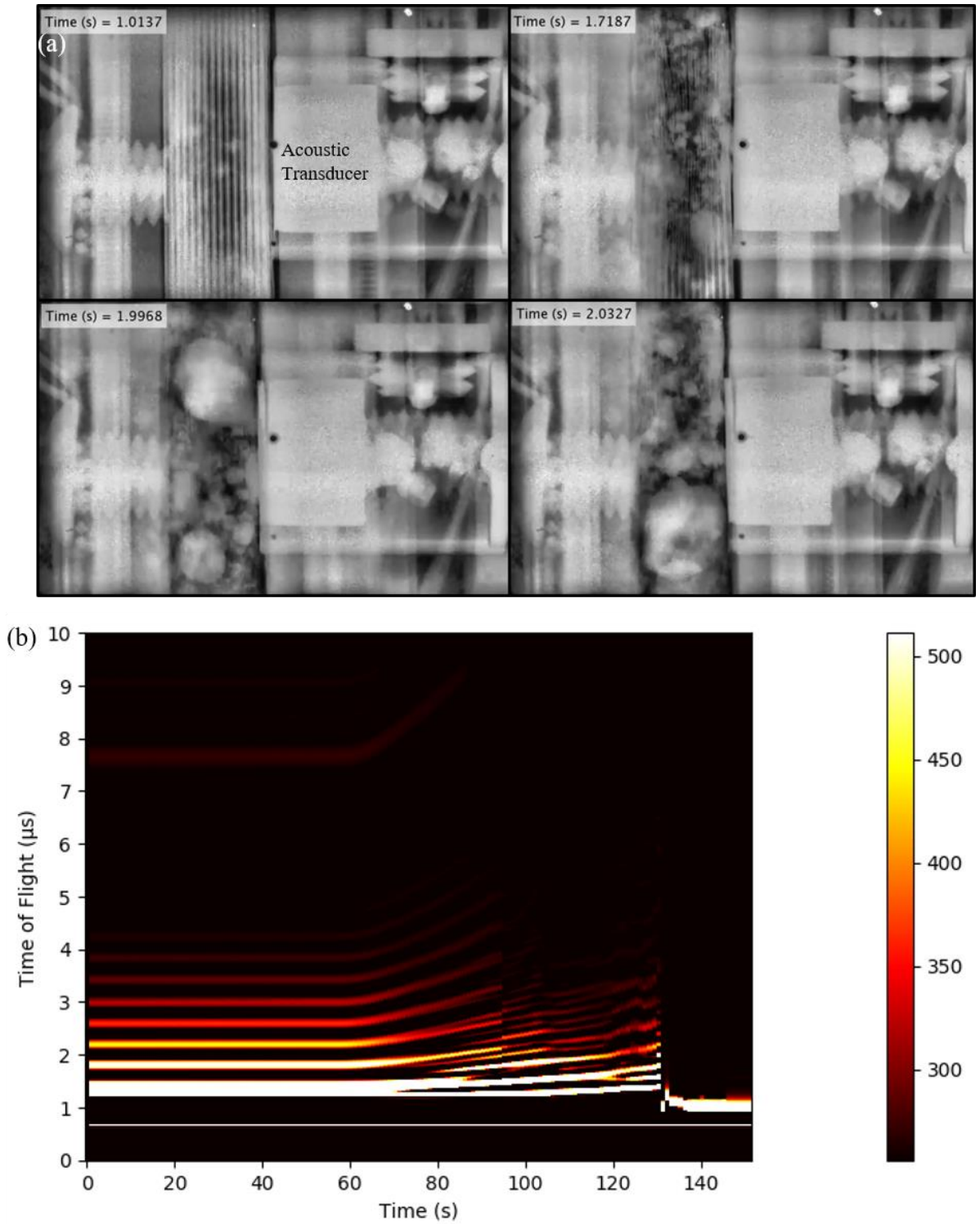

Figure 7-3: (a) Selected X-ray radiographs from a cell in cell group C, Si-NW pouch cell with commercial materials (polymer separator and metal foil current collector). The X-ray radiography

captures the 4 seconds preceding widespread ejection of material. (b) Acoustic spectrogram of the test shown in (a). The acoustic spectrogram captures the entirety of the set-up, heating and failure of the cell in this test.

Thermal abuse is observed in Figure 7-3(b) at a start of ca. time = 65 s with a trend of delayed time of flight observed through-out the cell. In Figure 7-3(a), thermal decomposition of the electrode assembly occurs in the middle layers of the pouch cell as the attenuation of X-rays decrease resulting in a darker central region as the material structure disintegrates with the formation of molten material seen as small brighter circles at time = 1.0137 s. This is reflected in Figure 7-3(b), at time = 65 s and at 3 – 4.5 μs time of flight, where the acoustic signal experiences continual time of flight increase until ca. 95 s, highlighting the generation of gases.

At time = ca. 95 s in Figure 7-3(b), the thermal decomposition of the electrode layers is widespread causing the electrode assembly material to melt and the associated generation of gases. The acoustic signal can no longer propagate to those layers and the attenuation of the signal due to presence of gaseous phases which also prevented a reflected signal resulted in little to no acoustics measurements at 3 – 4.5 μs time of flight after time = ca. 95 s.

Between time = 1.9968 s and time = 2.0327 s, shown in Figure 7-3(a), molten electrode material spheres can be seen to move downwards in the radiograph shown due to gravity, towards the brass plate shown in Figure 7-2(a) and Figure 7-2(c). The temperature of the molten material exceeded the melting point of brass (930 ^{o}C), thus the spheres of molten material melted through the brass protective plate at the bottom of the cell chamber enclosure shown in Figure 7-2(c). The aluminium cell chamber stack assembly with a melting point of 660.3 ^{o}C were also melted during the ejection of molten electrode material shown in Figure 7-2(b) and Figure 7-2(d). At time = 2.0327 s, the electrode assembly within the cell has undergone thermal decomposition during thermal runaway and the majority of it has been ejected, shown in Figure 7-2(d). This characteristic was observed throughout all groups tested of the Si-NW pouch cell.

The acoustic spectrogram trends examined in Figure 7-3(b) were also observed in repeated tests shown in Supplementary Materials. Cells from Group A typically failed for 70 – 80 s upon start of heating until signal failure of the acoustic transducer due to thermal damage of internal components.

7.3.2 ISC Abuse of Cell Group A-ISC

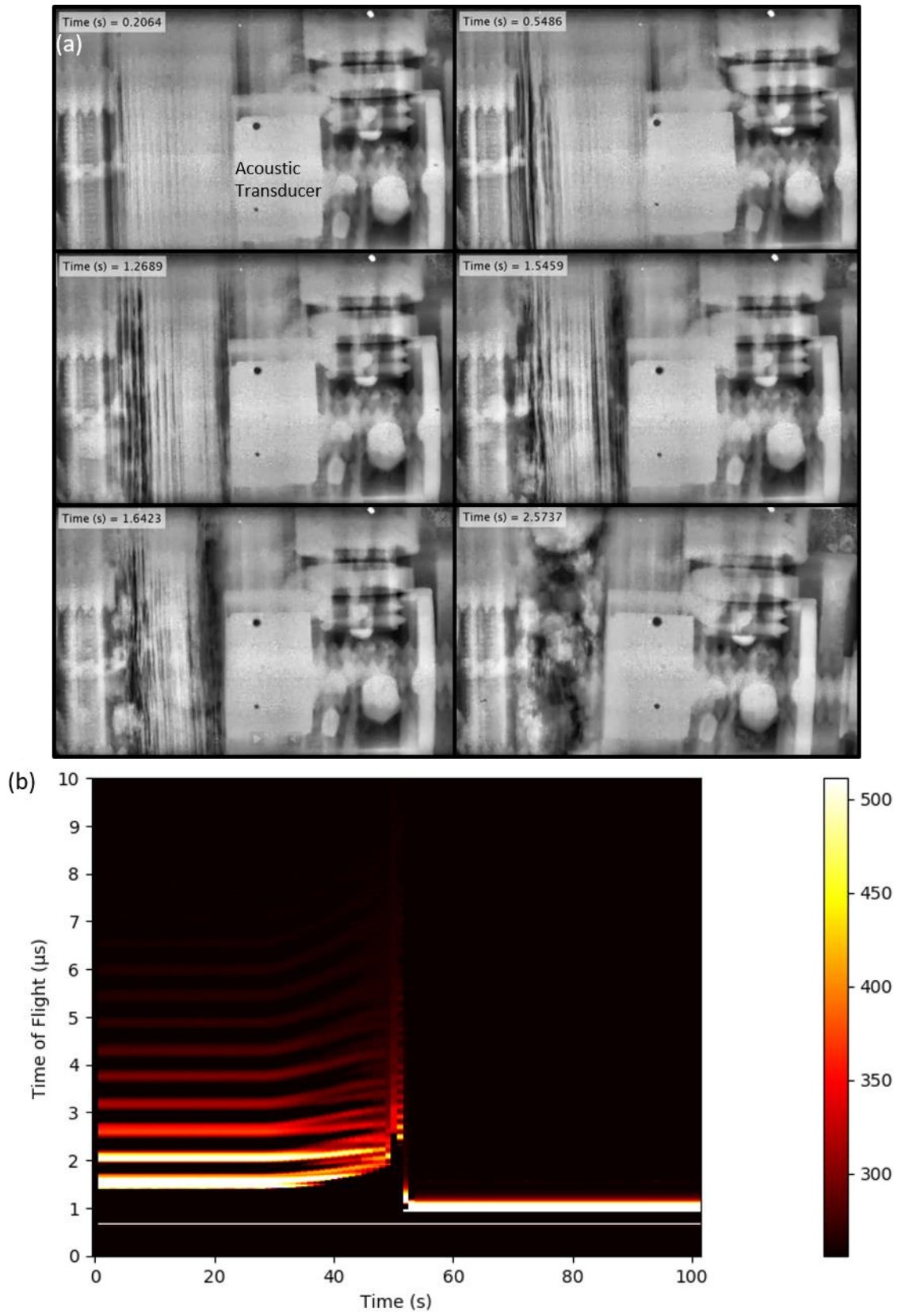

Figure 7-4: (a) Selected X-ray radiographs from a cell in cell group A-ISC, where the commercial materials Si-NW pouch cells have an implanted ISCD in the centre of the cell. (b) Acoustic spectrogram of the commercial materials ISC cell shown in (a) undergoing thermal runaway.

The internal short-circuit device activates at ca. 57 °C, when the coating of wax melts and produces a hard short between the aluminium and copper current collectors. Heating at 112 W to 57 °C to failure, the test elapsed time is significantly shorter than cells from group A (commercial cell) where there is no ISCD and the critical temperature for widespread cell failure is ca. 200 °C. From Figure 7-4(a), failure initiated further away from the transducer (centre of the cell where the ISCD is located) before propagating to the electrode layers closer to the transducer due to the exothermic decomposition of electrode material spreading heat. This is shown in Figure 7-4(b), where the loss of acoustic signal intensity progresses from later time of flight (ca. 6 – 7 μs) to electrode layers closer to the transducer (2 – 4 μs). Disintegration of the electrode structure due to separator failure and gas generation can be observed with the splitting of acoustic signals through-out the cell, most prominently at ca. 35-50 s for time of flight 2.6- 3.8 μs. It remains difficult to detect ISCD activation and probe further details into failure for A-ISC as the event is very rapid as failure occurred at 57 °C which also caused early onset of gas generation and thermal damage of the acoustic transducer and loss of signal at time = ca. 50 s.

Cell groups A and A-ISC required no voltage sensor as cells were taken to failure with commercial materials.

7.4 ISC Abuse of Cell Group B-ISC (Si-NW, PCC and ISCD)

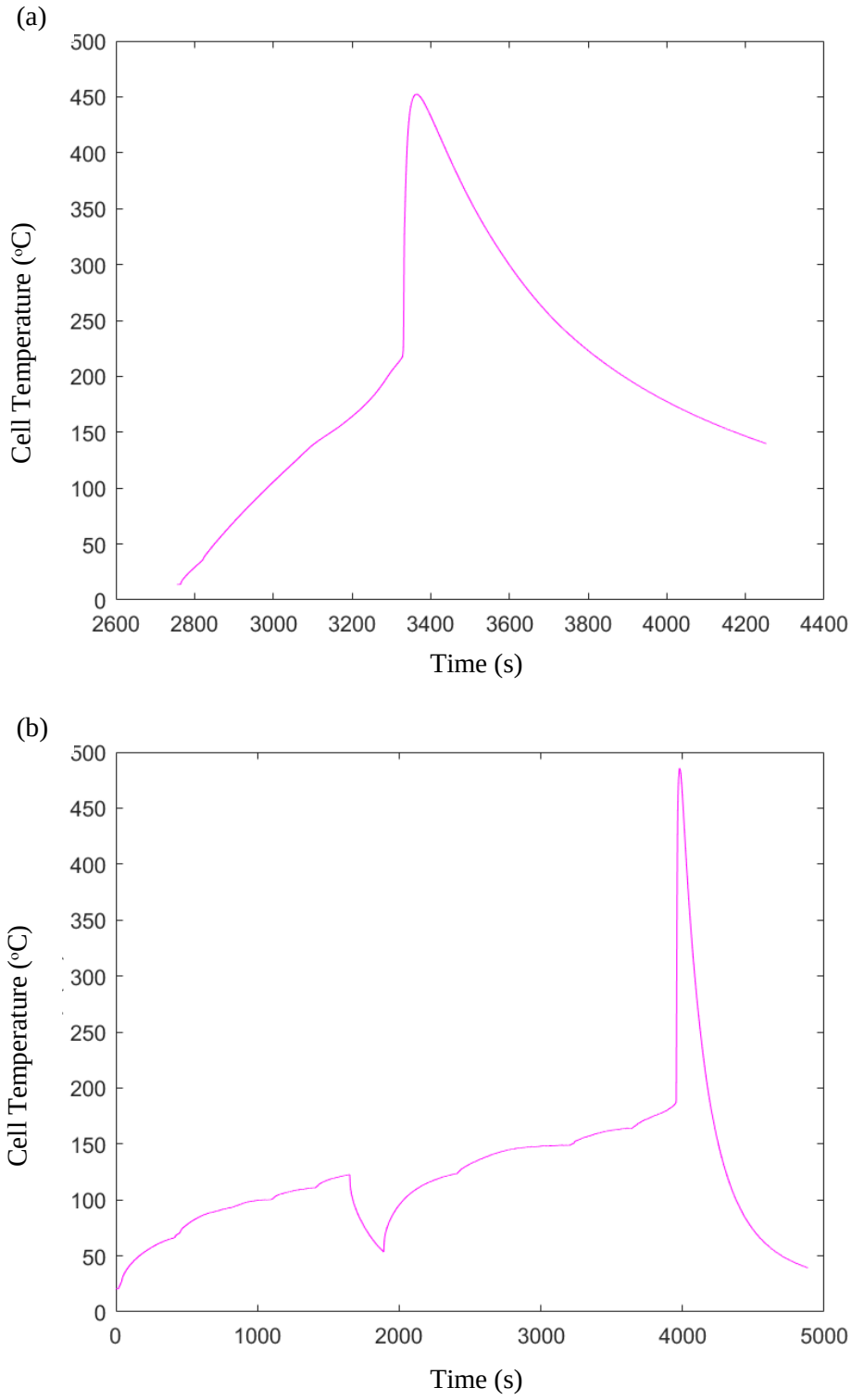

Figure 7-5: Cell temperature for two B-ISC cells from when 112 W heating was applied via cartridge heaters. In both instances, the expected failure critical temperature is ca. 57 °C. (a) B-ISC Cell 1 - Heating was continually applied until the cell reached ca. 210 °C before macro-scopic short-circuit which caused widespread failure and sudden ejection of heat. Temperature of 450 °C reached. (b) B-

ISC Cell 2 – 66 W heating was applied until OCV dropped was observed, after observation where the cell did not progress into thermal runaway and OCV returned to 4.05 V. Cell underwent thermal runaway at ca. 180 °C.

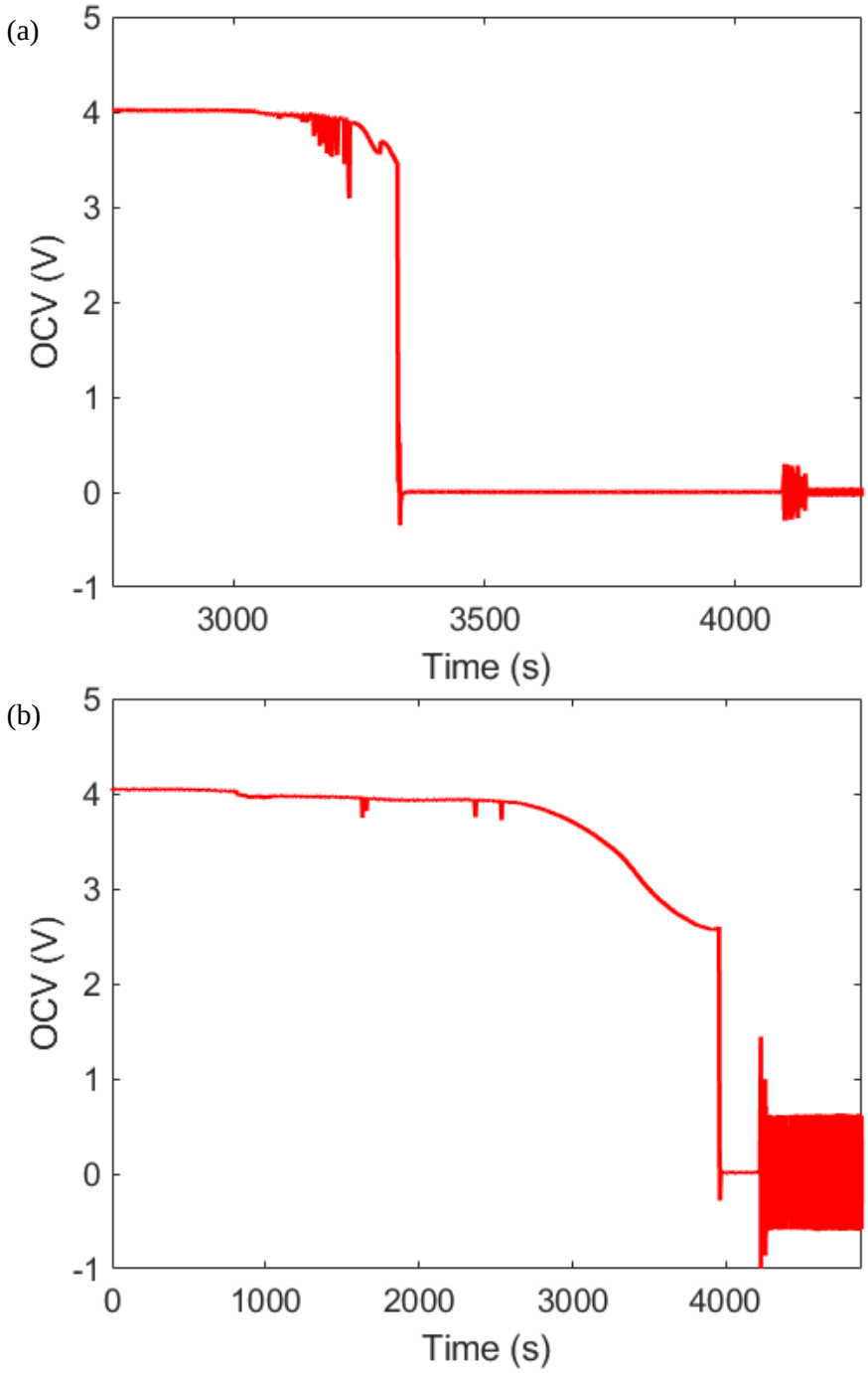

Figure 7-6: OCV measurements for B-ISC during ISC abuse tests. (a) B-ISC Cell 1. (b) B-ISC Cell 2.

The experiment time on the x-axis of Figure 7-5 and Figure 7-6 are consistent for each cell and measurement started after the FTRC was set up in the imaging hutch at ESRF to ensure OCV connection were correct and held through set up. As the experiments conducted with PCC cell configurations did not fail at the expected temperature but had prolonged structural responses to the combination of the

ISC and PCC activation, synchrotron facilities are limited in data acquisition to 4.2 s of 2000 fps, thus it was no possible to acquire X-ray radiography data for B-ISC cells.

For both Cell 1 and 2 from B-ISC, throughout heating to initiate the ISCD device seen in Figure 7-5, the cell has fluctuations in OCV measurement but continues to maintain voltage greater than 3.95 V until widespread thermal runaway at time = ca. 3300 s and 3950 s respectively shown in Figure 7-6. The critical temperature and initiation of widespread thermal runaway is reflected in Figure 7-5 where the measured temperature suddenly increases in both instances to above 450 ^{o}C. As previously seen in Figure 7-2(b-d), the actual temperatures during failure are significantly higher than measured with the thermocouples as evidenced with the aluminium cell chamber and brass protective plate melting. At 150 ^{o}C and 170 ^{o}C for Cell 1 and Cell 2 respectively, the OCV no longer recovers to 4.05 V and continues to deteriorate with heating until failure thereafter.

As the temperature reaches 57 ^{o}C and continues to rise towards the cell critical temperature, the ISCD has activated causing a microscopic short between the anode current collector (copper foil) and the cathode polymer-substrate current collector (Al PCC). These microscopic short-circuits are observed and measured in Figure 7-6. Ohmic heating which caused local temperature increase around the ISCD device and thereby the current collectors, resulted in the Al PCC polymer-substrate core retreating from the region of high temperature and disconnecting the microscopic short-circuit. This is observed through the OCV recovery to 4.05 V until the cell OCV deteriorates permanently until failure. The lengthy deterioration of OCV with heating, despite the ISCD device activation and short-circuiting of the current collector, suggests the PCC activation mitigated the short circuit. This is done through the activation of the safety mechanism, the melting of the polymer substrate due to Ohmic heating isolated the short-circuiting from the ISCD. The electrode assembly delaminated across the cell, until the separator melts at higher temperatures, which caused further macro-scopic short-circuiting until the cell’s critical temperature.

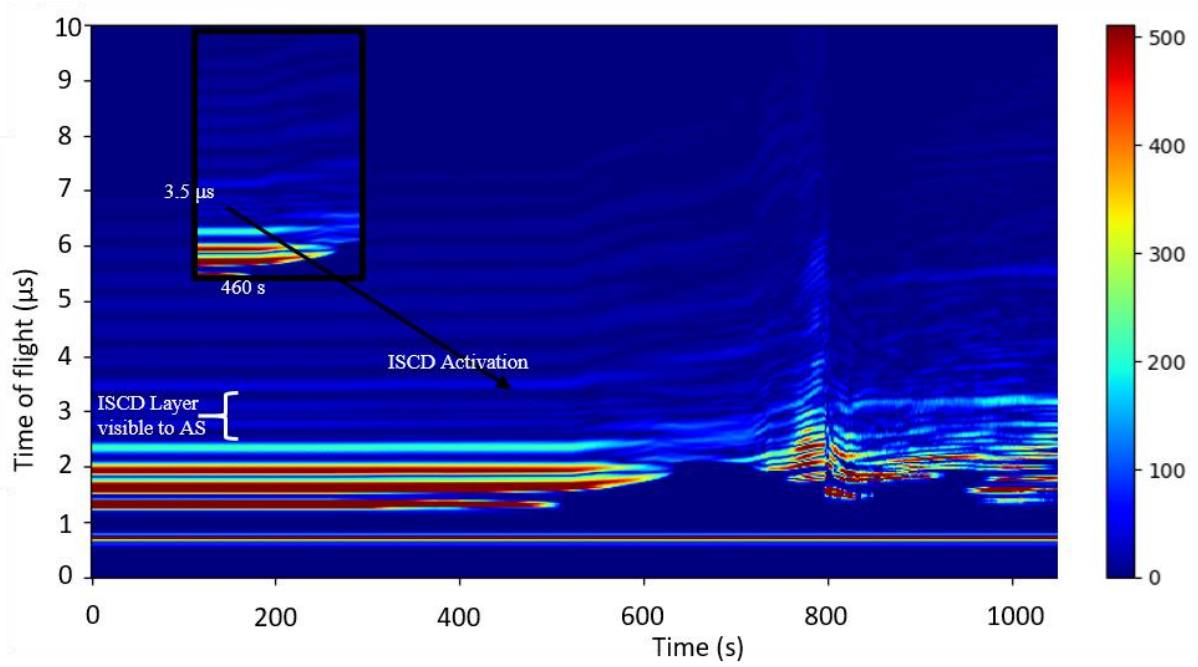

Figure 7-7: Acoustic spectrogram of a cell from B-ISC heated at 112 W until failure. Shown inset is the moment the ISC activates and the corresponding acoustic time-of-flight response at ca. time = 460 s and time of flight = 3.5 µs. The experiment time on this axis is relative to when the AS acquisition equipment start recording, however, signal changes allows for identification of onset of heating and ISCD activation (shown inset) and widespread gas generation.

The design of the cell chamber stack assembly ensured through-plane alignment of the acoustic transducer with the ISCD during failure, allowing the structural evolution of the ISCD during heating to be examined with AS. In Figure 7-7, the decision was made to saturate the signal at low time-of-flights to ensure strong signal to resolve the layer where the internal short-circuit device was located, and to characterise evolution of attenuation and time-of-flight during failure. At ca. 3 µs time of flight in Figure 7-7 (labelled), the effect of ISCD implantation can be observed with AS immediately at time = 0 – 200 s, as there is an observable thin layer between the electrode layers. Additionally, 8 subsequent layers after the ISCD can be counted at later time of flight after 3 µs, as the 16 layer pouch cell has the ISCD implanted in the middle of these layers.

Shown in the inset in Figure 7-7 is the activation of the ISCD device causing a “ripple” on the acoustic spectrogram at ca. time = 460 s and time of flight = ca. 3.5 µs. The retreat mechanism of the polymer-substrate in the Al PCC due to the elevated temperature thereafter, can be observed by the greater delay in time of flight and loss of signal for electrode layers at time = 520 s for times of flight

greater than 3 μs due to the electrode layers no longer bound to the Al PCC. Significant gas generation and molten material due to thermal decomposition of the electrode materials at time = ca. 720 s caused a significant delay in time of flight, due to the substantial attenuation and reduction in time of flight posed by liquid and gaseous phases to ultrasonic signals. Widespread cell failure occurred at t = ca. 790 s whereby gas and molten material were ejected from the cell casing, caused loss of signal at later time of flight (5 – 8 μs).

In comparison to spectrograms for A and A-ISC (Figure 7-3 (b) and Figure 7-4(b) respectively), the sequence of events predicating failure occurred over a much longer timeframe. The polymer-substrate core which continually activates and retreats from regions of high temperature across the cell can be observed in Figure 7-7, as the ultrasonic signal at time = 520 – 720 s, there is substantial perturbation in the ultrasonic signal. Due to the sensitivity of the acoustic signal to phase changes (due to difference in elastic modulus and density), the melting of the wax to short the anode and cathode current collector can be observed immediately before significant OCV drop and the mechanism of the Al PCC can be observed through-out. Furthermore, the ISCD activated at ca. 57 ^{o}C was prevented from developing into cell thermal runaway which can be attributed to the mechanism of the Al PCC polymer-substrate retreating from the ISCD, consequently, this disconnected the initial microscopic short-circuit. As the cell was continually subjected to thermal abuse, the temperature increased throughout the cell, the separator and the polymer-substrate core of the Al PCC melted. Slow OCV deterioration can be attributed to the disconnection of active material from the current collector due to the structural damage of the Al PCC, rather than a slow short-circuit as temperatures during heating before failure remained at a constant rate rather than sudden rises. This highlighted the success of the Al PCC which prevented initial failure (expected and observed in other cells at 57 ^{o}C), until the cell reached the critical temperature range where a nominal (non-ISCD) cell would be expected to fail. Furthermore, the principles of ultrasonic acoustic spectroscopy facilitated the characterisation of phase change of the ISCD and the signal oscillation on the spectrogram which represented the activation of the polymer-substrate mechanism of the Al PCC.

7.5 Conclusions

The suite of characterisation techniques used were able to provide insights into the failure of a pure silicon anode, identification of the ISCD wax phase change which predicates short circuiting and thereby voltage drop and the effectiveness of the PCC with ISCD abuse in a pouch cell geometry with a new cell electrochemistry (LCO and silicon anode compared to NMC-graphite previously). Silicon anodes have shown unprecedented high temperatures, sufficient to melt the aluminium calorimeter, the brass plate used to capture cell ejecta and formation of glass beads. The double-walled hollow nanowire morphology which have micro- and macro- porosity to accommodate high rate capability with low tortuosity and silicon expansion through cycling provide a significantly greater surface area to volume than graphite. During thermal runaway, the highly exothermic decomposition reactions between silicon anode, the LCO positive electrode and the electrolyte ensued at a very rapid rate of reaction and thus substantial generation of heat due to this easily accessible silicon anode surface area above the critical temperature. There is limited research insights into the failure mechanisms of a lithium-ion and pure silicon negative electrode chemistry, due to the challenge of producing a pure silicon electrode which will provide competitive cycle life and capacity retention. The quantification of exact reactions and contributions to the exothermic output are difficult to expound. A combination of accelerating rate calorimetry and modelling may provide future insights into silicon anode thermal runaways.

Graphite anode lithium-ion batteries have reported temperatures in excess of 600 ^{o}C, however the formation of glass beads require the reaction of silicon and oxygen at a temperature in excess of 1400 ^{o}C [236]. This highlights the importance in battery safety testing and review when implementing new materials for greater performance, existing lithium-ion energy storage and the surrounding contingencies for failure and safety are designed for the current graphite iteration. These safety mechanisms would be considerably inadequate for the failure observed with silicon anodes observed and would require new lithium-ion standards for pure silicon negative electrodes.

The introduction of novel materials for cell chemistries pushes the impetus on improving the understanding and methods of thermal runaway, as previous FTRC literature have had no experience of such high temperature during cell failure. AS highlighted the significance of phase change within the electrode assembly during failure of nominal and ISCD cell groups due to the order of magnitude difference in elastic moduli and density but also density as a function of temperature as reported by Rhod *et al*. [198]. The wax which melts at 57 ^{o}C before the negative electrode and positive electrode current collector connect, was detected immediately through AS pulse-echo probing, the effect of the event was

also detected in the surrounding layers – which allows for specific layer identification of defects, degradation and short-circuiting.

PCC abuse testing highlighted the robustness of acoustic spectroscopy as an emerging alternative to established electrochemical diagnostics methods for degradation and failure such as X-ray radiography, OCV measurements which may not be as easily field deployable. Limitations in acquisition due to the unexpectedly prolonged failure of the two B-ISC cells (which have without exception underwent thermal runaway at 57 ^{o}C), mitigated the effects of the ISCD short-circuit and prevented failure until temperature in excess of 170 ^{o}C, a temperature range where you'd expect a nominal commercial cell to fail under thermal abuse. Cells maintained OCV over 3.90 V until after 150 ^{o}C with ISCD activation and continuous thermal abuse due to the PCC isolating the short circuit from propagating initially. The cell took ca. 330 s to fail from ISCD activation with the PCC as seen in Figure 7-7. This would be of great impact in BMS for cell SOH management and provide rapid analysis to respond to, comparatively, the ISCD commercial cell failed 20 s into heating detection visible to AS.

A comparison of the acoustic spectroscopy data from Chapter 4 and work presented here highlighted the similarities of the relative trend observed in the characteristic signals. Time-of-flight delay due to the expanding battery due to gas generation from the electrolyte-electrode and thermal decomposition reactions, moreover, the changes in density associated with temperature are both observed relative trends in each. An increase in the gain of the acoustic signal was chosen to maximise the acoustic amplitude of the waveform, thus, bringing prominence to layers deeper within the electrode and in particular the ISCD. Other differences which were significant were the variability in the measured reflected acoustic signal, this is due to the experimental interest in the field of view, differences in signal properties determined by the piezoelectric control system to determine the best ultrasonic wave to provide insights and differences in contact, thus, ultrasonic wave propagation through the cell. This highlighted best practices with the method for ensure repeatability, the signal properties which yielded the most insight and that each acoustic spectrogram is unique to the measurements in that configuration for each cell, thus relative changes in the acoustic amplitude and ToF for each spectrogram are the characteristics for analysis.

8 Conclusions and Future Work

8.1 Acoustic spectroscopy

This thesis has described and highlighted the use of multifaceted diagnostic techniques pertaining to failure of lithium-ion batteries. The work presented initially utilised the insights provided by multi-length and time scale X-ray imaging and CT as a correlative technique for acoustic spectroscopy, as a proof of concept for the technique in rapid failure diagnostics. Combined understanding of ultrasound propagation and reflection through multi-layered electrode materials during failure and equivalent architectural evolutions measured through calorimetry and X-ray imaging as a proxy for characteristic signals. This facilitated identification of gas generation and electrode delamination, typically precursor events to subsequent capacity loss and eventually failure. The propagation of ultrasonic waves are significantly sensitive to the onset of external factors which affect material density and elastic modulus, such as temperature, as temperature changes were detected instantaneously.

This work has been extended to cylindrical cell geometry lithium-ion batteries, though the curvature poses a challenge with interfacing and ultrasound waves echoing around the structure. High rate cycling and conditions that induce significant structural change such as delamination are of interest for characteristic signal analysis. Furthermore, ongoing multiple cell scrutiny such as battery pack structures have been investigated for depth diagnostics and identification of specific cell irregularities if cycled together. All such continuing acoustic spectroscopy work will be with metrology at the forefront, to produce an accurate standardised and comparable measurement, thus, continuation of X-ray and ultrasound transparent cell chambers with fractional thermal runaway calorimetry.

Other possible avenues for acoustic spectroscopy which utilise the sensitivity to density and elastic modulus is the rapid spatial mapping of heterogeneous lithiation of electrodes, quantification of state of charge and temperature with respect to degradation experiments and thereby state of health. The relative changes in these properties allows the technique to be applied to different electrochemistries too.

Moreover, there exists further considerations of the impact of acoustic spectroscopy in the wider lithium-ion energy storage field, these are not limited to but include: in-line cell production metrology and standards evaluation, as an assessment proxy tool for second life purposes. As the uptake of EVs increase in the general population, AS can be used as a rapid non-invasive prognostic method for state of health of battery packs equivalent to present ministry of transport (MOT) tests for combustion engines. Compared to specialised and very limited X-ray imaging facilities, AS provides a relatively much more affordable option of field-deployable lithium-ion diagnostics.

8.2 Polymer Current Collectors (PCCs)

The prevention of thermal runaway with metal coated polymer current collectors (PCCs) was investigated and elucidated with X-ray imaging and region of interest micro-CT in Chapter 5. Safety functionality provided by the PCCs was tested to target the short-circuit which predicates failure, in the worst case scenario, whereby a 10 μm polypropylene separator was used in conjunction as a component which could fail simultaneously or beforehand. The difference between commercial CCs and PCCs was evident in radiographic imaging as the commercial cells experienced electrode cracking during nail penetration whereas the electrode assembly with the PCC was displaced into the empty cell core with the shear stress. Cells with the Al PCC, which were at full state of charge, prevented failure in all instances with the protection provided to the cathode. The PCC was observed to have retreated from the nail penetration region of high temperature (as the nail acted as the electrical pathway for short-circuit), thus prevented further electrical contact with the positive electrode thereafter. The PCC's mechanism also responded prior to separator failure or any other safety cell component. Micro-CT provided visualisation of the retreated PCC, non-failed separator and disconnect from the nail penetration region in adjacent electrode assemblies.

The results of the Al PCC 18650s highlighted the importance of the protection of the cathode with the electrically negative can in this cell geometry and isolation of the micro-scopic short-circuit for prevention as lithium-ion battery failure. The results presented here demonstrate a great advancement in improving the safety of lithium-ion batteries, while also reducing cost and increasing the energy density of cells. Typically, efforts into the advancement of battery safety to ensure commercial adaptation is driven by development of new materials, examples include new electrodes, non-flammable electrolytes, the adoption of which requires time intensive, multi-variate, experimental optimisation of these novel components. The innovative structure provided by the PCC architecture offers the safety advances reported in this work which is independent of cell chemistry (provided the PCC is stable in

the operating environment), moreover, the properties of the PCC allow for assimilation with current cylindrical cell roll-to-roll manufacturing technology.

In addition to uptake and construction of other cell chemistries and geometries to further prevention tests with the Al PCC, ongoing work to optimise the PCC design to facilitate higher rate capabilities with the metal coated film is also of importance to prevent the thin film being a nucleation point for high temperature generation. The impact of abuse methods on the Al PCC mechanism, in addition to, performance and safety contributions during operations in conditions of high degradation to provide a more comprehensive analysis of the type of battery failure or prevention due to the change in current collector design. Pack level failure and cell-to-cell propagation would be of high interest to EVs uptake and therefore the mitigation to ejection of flammable gases, side-wall or burst disks ruptures in a closed environment with possible heat sinks or cell-to-cell contact. Further work with the PCCs was combined with implementation of further components with an active contribution to safety, a thermally stable separator (TSS). Furthermore, understanding the operating principles of these cells which have prevented failure, as these cells in this work were isolated immediately, whether the cells can have safely discharged or recycled could be work of interest.

8.3 Thermally Stable Separators (TSS)

Cells which contained the Cu-PCC only, which propagated into thermal runaway, were measured to have mitigated and reduced the total ejected output energy during failure, which was investigated in Chapter 6. PCCs were investigated in tandem with a thermally stable separator (until 300 ˚C). Cells were taken to failure thermally and with an internal short circuit device to quantify the mitigation provided by the materials with FTRC. X-ray imaging highlighted the thermal stability of the electrode assembly exactly prior to ejection as the internal cell pressure exceeded the vent/crimp permitted pressure. A 19.6% and 41.4% reduction in total failure energy released with PCCs and with both PCCs and TSS components respectively during thermal abuse. Moreover, this was also reflected in internal short circuit failure, at 24.7% and 30.3% respectively. Following the publication of this thesis, the work presented in Chapter 6 will be disseminated through an energy storage and safety peer-review journal.

These results demonstrate the mitigative and preventative mechanisms of the PCCs and TSS provided to cylindrical cell lithium-ion batteries. The implementation of these materials in new cell chemistries and cell geometries will test the robustness of the safety functionality an important factor

in future uptake of these materials commercially. Future work to include gas composition analysis to provide a more comprehensive analysis of the reactions which occur or do not due to the mitigation of the PCCs and TSS. Other avenues of interest are the high rate capabilities possibility with these materials and optimisation of design for such performance. As with the PCCs previously, the mitigation provided by the TSS and as a combination with the PCC within pack-level powertrains.

TSS greatly hinders the combustion proportion of the thermal runaway energy ejection, thus placing greater importance on electrode selection and their thermal stability. Future work with positive electrode changes to evaluate those thermal decomposition reactions and electrode-electrolyte interactions will provide insights into those mechanisms and the effect on the TSS on those reaction pathways. Less thermally stable positive electrodes such as LCO will produce more oxygen from the electrode during thermal decomposition, the degree to which that oxygen affects thermal runaway responses can be evaluated with a comparative LFP cell for instance.

8.4 Pure Silicon Nanowire Anodes, X-ray imaging, computed tomography and FTRC

The Al PCC was investigated in Chapter 7 through silicon nanowire negative electrode and a commercial pouch cell format with acoustic spectroscopy, FTRC and X-ray imaging. This work was motivated by the suggestion from a peer reviewer of the manuscript of Chapter 5, whereby the reviewer expressed an interest in the work being expanded to more experimental or research stage electrochemistries which are not widely adopted. The data storage and acquisition limitations were encountered here with the significantly longer failure sequence of events, X-ray imaging for Al PCC cells were not possible. Internal temperatures in excess of 1400 ˚C were observed with glass bead products and molten portions of a brass plate, a scenario previously never encountered with graphite anodes or doped graphite anodes. Acoustic spectroscopy permitted distinct phase changes and onset of heating with activation of the ISCD visible due to the sensitivity of ultrasound propagation through matter temperature and phase changes. The Al PCC allowed for the Si-NW cell to ‘resist’ widespread cell failure with the ISCD until the expected 200 ˚C for thermal abuse failure, whereby normal cell failure occurred.

The temperatures observed in the failure of pure silicon anodes also poses the challenge of whether present lithium-ion standards for safety are relevant with the newest cell chemistries in

development as it is evident the risks associated are much greater with higher performance parameters. Additionally, the micro- and nano-structure considerations for high performance and safety for electrode design are apparent which are juxtaposed here due to inherent link to specific surface area and the effect on exothermic thermal runaway reactions as shown in Chapter 7.

Design alteration to improve cell rate capability and heat dissipation associated with high rate cycling would see less resistance to adoption of materials. Furthermore, characterisation and investigation of silicon nano-wires into the heterogeneous alloying of the nano-wire structure which has seen amorphous and crystalline structures with micro- and nano- CT and synchrotron imaging methods have continued to provide greater understanding into pure silicon anode chemistries and the effect of the heterogeneity on failure.

Ongoing work in collaboration with NASA Johnson Space Centre into greater FTRC functionality, implementation of the PCCs and TSS into a greater variety of cell chemistries and geometries of high interest and impact in electrochemical energy storage. FTRC also experienced temperatures in excess of all previous tests and revised iterations to prevent FTRC damage for future work would improve the cell abuse testing process. X-ray imaging at synchrotron facilities also were limited by memory/storage issues, thus perhaps redesign of testing process or working in tandem with beamline scientists to provide solutions to this would provide greater insights into X-ray characterisation.

9 References

1. REN21. *Renewable 2017, Global Status Report*.; 2017.

2. Bogdanov D, Ram M, Aghahosseini A, et al. Low-cost renewable electricity as the key driver of the global energy transition towards sustainability. *Energy*. 2021. doi:10.1016/j.energy.2021.120467

3. Qazi A, Hussain F, Rahim NABD, et al. Towards Sustainable Energy: A Systematic Review of Renewable Energy Sources, Technologies, and Public Opinions. *IEEE Access*. 2019. doi:10.1109/ACCESS.2019.2906402

4. IEA. 2018 World Energy Outlook: Executive Summary. 2018:11. www.iea.org/t&c/.

5. Mwasilu F, Justo JJ, Kim EK, Do TD, Jung JW. Electric vehicles and smart grid interaction: A review on vehicle to grid and renewable energy sources integration. *Renew Sustain Energy Rev*. 2014. doi:10.1016/j.rser.2014.03.031

6. Anair D, Mahmassani A. *State of Charge: Electric Vehicles' Global Warming Emissions and Fuel-Cost Savings across the United States*.; 2012. http://www.ucsusa.org/clean_vehicles/smart-transportation-solutions/advanced-vehicle-technologies/electric-cars/emissions-and-charging-costs-electric-cars.html.

7. Su W, Eichi H, Zeng W, Chow MY. A survey on the electrification of transportation in a smart grid environment. *IEEE Trans Ind Informatics*. 2012. doi:10.1109/TII.2011.2172454

8. Chen T, Jin Y, Lv H, et al. Applications of Lithium-Ion Batteries in Grid-Scale Energy Storage Systems. *Trans Tianjin Univ*. 2020. doi:10.1007/s12209-020-00236-w

9. Sinsel SR, Riemke RL, Hoffmann VH. Challenges and solution technologies for the integration of variable renewable energy sources—a review. *Renew Energy*. 2020. doi:10.1016/j.renene.2019.06.147

10. Zaghib K, Dontigny M, Guerfi A, et al. Safe and fast-charging Li-ion battery with long shelf life for power applications. *J Power Sources*. 2011;196(8):3949-3954.

doi:10.1016/j.jpowsour.2010.11.093

11. Fan J. Studies of 18650 cylindrical cells made with doped linio2 positive electrodes for military applications. *J Power Sources*. 2004;138(1-2):288-293. doi:10.1016/j.jpowsour.2004.06.010

12. Larcher D, Tarascon JM. Towards greener and more sustainable batteries for electrical energy storage. *Nat Chem*. 2015;7(1):19-29. doi:10.1038/nchem.2085

13. Wang XL, An K, Cai L, et al. Visualizing the chemistry and structure dynamics in lithium-ion batteries by in-situ neutron diffraction. *Sci Rep*. 2012. doi:10.1038/srep00747

14. Feng X, Ouyang M, Liu X, Lu L, Xia Y, He X. Thermal runaway mechanism of lithium ion battery for electric vehicles: A review. *Energy Storage Mater*. 2018;10(May 2017):246-267. doi:10.1016/j.ensm.2017.05.013

15. Williard N, He W, Hendricks C, Pecht M. Lessons learned from the 787 dreamliner issue on Lithium-Ion Battery reliability. *Energies*. 2013;6(9):4682-4695. doi:10.3390/en6094682

16. Yoshio M, Brodd RJ, Kozawa A. *Lithium Ion Batteries Science and Techonologies*.; 2009.

17. Nitta N, Wu F, Lee JT, Yushin G. Li-ion battery materials: Present and future. *Mater Today*. 2015;18(5):252-264. doi:10.1016/j.mattod.2014.10.040

18. Ye Y, Saw LH, Shi Y, Somasundaram K, Tay AAO. Effect of thermal contact resistances on fast charging of large format lithium ion batteries. *Electrochim Acta*. 2014;134:327-337. doi:10.1016/j.electacta.2014.04.134

19. Tippmann S, Walper D, Balboa L, Spier B, Bessler WG. Low-temperature charging of lithium-ion cells part I: Electrochemical modeling and experimental investigation of degradation behavior. *J Power Sources*. 2014;252:305-316. doi:10.1016/j.jpowsour.2013.12.022

20. Reddy TB, Linden D. *Linden's Handbook of Batteries*. Fourth. New York: McGraw-Hill; 2011.

21. Darcy E, Scharf S. Safe, High Performing Li-ion Battery Designs: Summary of 2015 Findings. In: *2015 NASA Aerospace Battery Workshop*. Huntsville, AL; 2015:1-78. https://www.nasa.gov/sites/default/files/atoms/files/darcy_-_nasa_batt_workshop_2015.pdf.

22. Boukamp BA. All-Solid Lithium Electrodes with Mixed-Conductor Matrix. *J Electrochem Soc*. 1981;128(4):725-729. doi:10.1149/1.2127495

23. Kaskhedikar NA, Maier J. Lithium storage in carbon nanostructures. *Adv Mater*. 2009. doi:10.1002/adma.200901079

24. Sphar ME, In:, Yoshio M, Brodd RJ, Kozawa A. Lithium-Ion Batteries: Science and Techonologies. In: *Lithium-Ion Batteries*. Springer; 2009:117. doi:10.1007/978-0-387-34445-4

25. Levi MD, Aurbach D. Diffusion Coefficients of Lithium Ions during Intercalation into Graphite Derived from the Simultaneous Measurements and Modeling of Electrochemical Impedance and Potentiostatic Intermittent Titration Characteristics of Thin Graphite Electrodes. *J Phys Chem B*. 1997. doi:10.1021/jp9701911

26. Markevich E, Levi MD, Aurbach D. Comparison between potentiostatic and galvanostatic intermittent titration techniques for determination of chemical diffusion coefficients in ion-insertion electrodes. *J Electroanal Chem*. 2005;580(2):231-237. doi:10.1016/j.jelechem.2005.03.030

27. Persson K, Sethuraman VA, Hardwick LJ, et al. Lithium diffusion in graphitic carbon. *J Phys Chem Lett*. 2010;1(8):1176-1180. doi:10.1021/jz100188d

28. Billaud D, McRae E, Hérold A. Synthesis and electrical resistivity of lithium-pyrographite intercalation compounds (stages I, II and III). *Mater Res Bull*. 1979;14(7):857-864. doi:10.1016/0025-5408(79)90149-1

29. Qi Y, Guo H, Hector LG, Timmons A. Threefold Increase in the Young's Modulus of Graphite Negative Electrode during Lithium Intercalation. *J Electrochem Soc*. 2010;157(5):558-566. doi:10.1149/1.3327913

30. Takami N, Hoshina K, Inagaki H. Lithium Diffusion in Li4/3Ti5/3O4 Particles during Insertion and Extraction. *J Electrochem Soc*. 2011;158(6):725-730. doi:10.1149/1.3574037

31. Wunde F, Berkemeier F, Schmitz G. Lithium diffusion in sputter-deposited Li 4Ti 5O 12 thin films. *J Power Sources*. 2012;215:109-115. doi:10.1016/j.jpowsour.2012.04.102

32. Scharner S, Weppner W, Schmid-Beurmann P. Evidence of Two-Phase Formation upon Lithium Insertion into the Li1. 33Ti1. 67 O 4 Spinel. *J ….* 1999;146(3):857-861. doi:10.1149/1.1391692

33. Wagemaker M, Simon DR, Kelder EM, et al. A kinetic two-phase and equilibrium solid solution in spinel Li 4+xTi5O12. *Adv Mater*. 2006;18(23). doi:10.1002/adma.200601636

34. Colin JF, Godbole V, Novák P. In situ neutron diffraction study of Li insertion in Li4Ti 5O12. *Electrochem commun*. 2010;12(6):804-807. doi:10.1016/j.elecom.2010.03.038

35. Jain A, Ong SP, Hautier G, et al. Commentary: The materials project: A materials genome approach to accelerating materials innovation. *APL Mater*. 2013;1(1). doi:10.1063/1.4812323

36. Hatchard TD, Dahn JR. In Situ XRD and Electrochemical Study of the Reaction of Lithium with Amorphous Silicon. *J Electrochem Soc*. 2004;151(6):838-842. doi:10.1149/1.1739217

37. Chandrasekaran R, Magasinski A, Yushin G, Fuller TF. Analysis of Lithium Insertion/Deinsertion in a Silicon Electrode Particle at Room Temperature. *J Electrochem Soc*.

2010;157(10):1139-1151. doi:10.1149/1.3474225

38. Ding N, Xu J, Yao YX, et al. Determination of the diffusion coefficient of lithium ions in nano-Si. *Solid State Ionics*. 2009;180:222-225. doi:10.1016/j.ssi.2008.12.015

39. Xie J, Imanishi N, Zhang T, Hirano A, Takeda Y, Yamamoto O. Li-ion diffusion in amorphous Si films prepared by RF magnetron sputtering: A comparison of using liquid and polymer electrolytes. *Mater Chem Phys*. 2010;120:421-425. doi:10.1016/j.matchemphys.2009.11.031

40. Li J, Xiao X, Yang F, Verbrugge MW, Cheng YT. Potentiostatic intermittent titration technique for electrodes governed by diffusion and interfacial reaction. *J Phys Chem C*. 2012;116(1):1472-1478. doi:10.1021/jp207919q

41. Pharr M, Zhao K, Wang X, Suo Z, Vlassak JJ. Kinetics of initial lithiation of crystalline silicon electrodes of lithium-ion batteries. *Nano Lett*. 2012;12(9):5039-5047. doi:10.1021/nl302841y

42. Ong SP, Richards WD, Jain A, et al. Python Materials Genomics (pymatgen): A robust, open-source python library for materials analysis. *Comput Mater Sci*. 2013;68:314-319. doi:10.1016/j.commatsci.2012.10.028

43. Sun L, Liu Y, Shao R, Wu J, Jiang R, Jin Z. Recent progress and future perspective on practical silicon anode-based lithium ion batteries. *Energy Storage Mater*. 2022. doi:10.1016/j.ensm.2022.01.042

44. Zuo X, Zhu J, Müller-Buschbaum P, Cheng YJ. Silicon based lithium-ion battery anodes: A chronicle perspective review. *Nano Energy*. 2017. doi:10.1016/j.nanoen.2016.11.013

45. Huang JY, Zhong L, Wang CM, et al. In situ observation of the electrochemical lithiation of a single SnO 2 nanowire electrode. *Science (80-).* 2010;330(6010):1515-1520. doi:10.1126/science.1195628

46. Sethuraman VA, Srinivasan V, Newman J. Analysis of Electrochemical Lithiation and Delithiation Kinetics in Silicon. *J Electrochem Soc*. 2013. doi:10.1149/2.008303jes

47. Ogata K, Salager E, Kerr CJ, et al. Revealing lithium-silicide phase transformations in nano-structured silicon-based lithium ion batteries via in situ NMR spectroscopy. *Nat Commun*. 2014. doi:10.1038/ncomms4217

48. Paz-Garcia JM, Taiwo OO, Tudisco E, et al. 4D analysis of the microstructural evolution of Si-based electrodes during lithiation: Time-lapse X-ray imaging and digital volume correlation. *J Power Sources*. 2016. doi:10.1016/j.jpowsour.2016.04.076

49. McDowell MT, Lee SW, Nix WD, Cui Y. 25th anniversary article: Understanding the lithiation of silicon and other alloying anodes for lithium-ion batteries. *Adv Mater*. 2013.

doi:10.1002/adma.201301795

50. Misra S, Liu N, Nelson J, Hong SS, Cui Y, Toney MF. In situ X-ray diffraction studies of (de)lithiation mechanism in silicon nanowire anodes. *ACS Nano*. 2012. doi:10.1021/nn301339g

51. Liu N, Wu H, McDowell MT, Yao Y, Wang C, Cui Y. A yolk-shell design for stabilized and scalable Li-ion battery alloy anodes. *Nano Lett*. 2012. doi:10.1021/nl3014814

52. Chan CK, Peng H, Liu G, et al. High-performance lithium battery anodes using silicon nanowires. *Nat Nanotechnol*. 2008. doi:10.1038/nnano.2007.411

53. Cui Y. *Designing Silicon Nanostructures for High Energy Lithium Ion Battery Anodes*.; 2012. https://www.energy.gov/sites/prod/files/2014/03/f9/es148_cui_2012_p.pdf.

54. Cui Y. *Wirnig Up Silicon Nanostructures for High Energy Lithium Ion Battery Anodes*.; 2013. https://www.energy.gov/sites/prod/files/2014/03/f9/es148_cui_2012_p.pdf.

55. Cui Y. *Wiring Up Silicon Nanostructures for High Energy Lithium Ion Battery Anodes*.; 2014. https://www.energy.gov/sites/prod/files/2014/03/f13/es148_cui_2013_o.pdf.

56. Shen C, Ge M, Luo L, et al. In Situ and Ex Situ TEM Study of Lithiation Behaviours of Porous Silicon Nanostructures. *Sci Rep*. 2016. doi:10.1038/srep31334

57. Stefan CI. High Energy Density and Specific Energy Silicon Anode-Based Batteries. In: *Power Sources Conference*. Denver, CO; 2018. http://www.powersourcesconference.com/Power Sources 2018 Digest/docs/13-2.pdf.

58. Martha SK, Haik O, Zinigrad E, et al. On the Thermal Stability of Olivine Cathode Materials for Lithium-Ion Batteries. *J Electrochem Soc*. 2011. doi:10.1149/1.3622849

59. Cho J, Kim YW, Kim B, Lee JG, Park B. A breakthrough in the safety of lithium secondary batteries by coating the cathode material with AIPO4 nanoparticles. *Angew Chemie - Int Ed*. 2003. doi:10.1002/anie.200250452

60. Lin F, Markus IM, Nordlund D, et al. Surface reconstruction and chemical evolution of stoichiometric layered cathode materials for lithium-ion batteries. *Nat Commun*. 2014. doi:10.1038/ncomms4529

61. Lee MJ, Lee S, Oh P, Kim Y, Cho J. High performance LiMn2O4 cathode materials grown with epitaxial layered nanostructure for Li-Ion batteries. *Nano Lett*. 2014. doi:10.1021/nl404430e

62. Yamada A, Chung SC, Hinokuma K. Optimized LiFePO[sub 4] for Lithium Battery Cathodes. *J Electrochem Soc*. 2002. doi:10.1149/1.1348257

63. Scrosati B, Garche J. Lithium batteries: Status, prospects and future. *J Power Sources*. 2010.

doi:10.1016/j.jpowsour.2009.11.048

64. Schmuch R, Wagner R, Hörpel G, Placke T, Winter M. Performance and cost of materials for lithium-based rechargeable automotive batteries. *Nat Energy*. 2018. doi:10.1038/s41560-018-0107-2

65. Myung ST, Maglia F, Park KJ, et al. Nickel-Rich Layered Cathode Materials for Automotive Lithium-Ion Batteries: Achievements and Perspectives. *ACS Energy Lett*. 2017. doi:10.1021/acsenergylett.6b00594

66. Sun YK, Myung ST, Kim MH, Prakash J, Amine K. Synthesis and characterization of Li[(Ni0.8Co 0.1Mn0.1)0.8(Ni0.5Mn 0.5)0.2]O2 with the microscale core-shell structure as the positive electrode material for lithium batteries. *J Am Chem Soc*. 2005. doi:10.1021/ja053675g

67. Lim BB, Myung ST, Yoon CS, Sun YK. Comparative Study of Ni-Rich Layered Cathodes for Rechargeable Lithium Batteries: Li[Ni0.85Co0.11Al0.04]O2 and Li[Ni0.84Co0.06Mn0.09Al0.01]O2 with Two-Step Full Concentration Gradients. *ACS Energy Lett*. 2016. doi:10.1021/acsenergylett.6b00150

68. Schipper F, Nayak P, Erickson E, et al. Study of Cathode Materials for Lithium-Ion Batteries: Recent Progress and New Challenges. *Inorganics*. 2017. doi:10.3390/inorganics5020032

69. Saubanère M, McCalla E, Tarascon JM, Doublet ML. The intriguing question of anionic redox in high-energy density cathodes for Li-ion batteries. *Energy Environ Sci*. 2016. doi:10.1039/c5ee03048j

70. Janek J, Zeier WG. A solid future for battery development. *Nat Energy*. 2016. doi:10.1038/nenergy.2016.141

71. Bachman JC, Muy S, Grimaud A, et al. Inorganic Solid-State Electrolytes for Lithium Batteries: Mechanisms and Properties Governing Ion Conduction. *Chem Rev*. 2016. doi:10.1021/acs.chemrev.5b00563

72. Lu LL, Ge J, Yang JN, et al. Free-standing copper nanowire network current collector for improving lithium anode performance. *Nano Lett*. 2016;16(7):4431-4437. doi:10.1021/acs.nanolett.6b01581

73. Myung ST, Hitoshi Y, Sun YK. Electrochemical behavior and passivation of current collectors in lithium-ion batteries. *J Mater Chem*. 2011;21(27):9891-9911. doi:10.1039/c0jm04353b

74. Zhu P, Gastol D, Marshall J, Sommerville R, Goodship V, Kendrick E. A review of current collectors for lithium-ion batteries. *J Power Sources*. 2021. doi:10.1016/j.jpowsour.2020.229321

75. Hu CC. Soteria Architecture Cell Materials. In: *48th Power Sources Conference*. Denver, CO; 2018:93-96. http://www.powersourcesconference.com/Power Sources 2018 Digest/docs/6-4.pdf.

76. Yang CP, Yin YX, Zhang SF, Li NW, Guo YG. Accommodating lithium into 3D current collectors with a submicron skeleton towards long-life lithium metal anodes. *Nat Commun*. 2015;6(May):1-9. doi:10.1038/ncomms9058

77. Zielke L, Barchasz C, Walu S, et al. Degradation of Li/S battery electrodes on 3D current collectors studied using X-ray phase contrast tomography. *Sci Rep*. 2015;5:10921. doi:10.1038/srep10921

78. Braithwaite JW. Corrosion of Lithium-Ion Battery Current Collectors. *J Electrochem Soc*. 2002;146(2):448. doi:10.1149/1.1391627

79. Naguib M, Allu S, Simunovic S, Li J, Wang H, Dudney NJ. Limiting Internal Short-Circuit Damage by Electrode Partition for Impact-Tolerant Li-Ion Batteries. *Joule*. 2018. doi:10.1016/j.joule.2017.11.003

80. Liu S, Trela JA, Karimi KJ. US2018/0269535A1: Battery cell design for preventing internal short circuits from occurring and propagating using positive temperature coefficient (PTC) materials. 2017. https://patentscope.wipo.int/search/en/detail.jsf?docId=US226140746&tab=NATCOLLDOCUMENTS.

81. Liu B, Jia Y, Yuan C, et al. Safety issues and mechanisms of lithium-ion battery cell upon mechanical abusive loading: A review. *Energy Storage Mater*. 2019. doi:10.1016/j.ensm.2019.06.036

82. Dreamweaver. Dreamweaver Gold: The Lowest Cost , Highest Performance Battery Separators Available. https://www.dreamweaverintl.com/uploads/5/7/8/8/57886015/dwi_brochure-_gold_170419.pdf.

83. Dreamweaver. Dreamweave Titanium: Nanofiber-based separators with lower ESR & superior chemical resistance. https://www.dreamweaverintl.com/uploads/5/7/8/8/57886015/dwi_brochure_titanium_170306.pdf.

84. Dreamweaver. Dreamweave Silver: Nanofiber-based battery separators with improved energy density and recharge rate. https://www.dreamweaverintl.com/uploads/5/7/8/8/57886015/dwi_brochure_silver_170306.pdf.

85. Wang Q, Ping P, Zhao X, Chu G, Sun J, Chen C. Thermal runaway caused fire and explosion of lithium ion battery. *J Power Sources*. 2012;208:210-224. doi:10.1016/j.jpowsour.2012.02.038

86. Finegan DP, Scheel M, Robinson JB, et al. Investigating lithium-ion battery materials during overcharge-induced thermal runaway: An operando and multi-scale X-ray CT study. *Phys Chem Chem Phys*. 2016;18(45):30912-30919. doi:10.1039/c6cp04251a

87. Chen Z, Qin Y, Ren Y, et al. Multi-scale study of thermal stability of lithiated graphite. *Energy Environ Sci*. 2011;4(10):4023-4030. doi:10.1039/c1ee01786a

88. Ren D, Liu X, Feng X, et al. Model-based thermal runaway prediction of lithium-ion batteries from kinetics analysis of cell components. *Appl Energy*. 2018;228(January):633-644. doi:10.1016/j.apenergy.2018.06.126

89. Lopez CF, Jeevarajan JA, Mukherjee PP. Experimental Analysis of Thermal Runaway and Propagation in Lithium-Ion Battery Modules. *J Electrochem Soc*. 2015;162(9):A1905-A1915. doi:10.1149/2.0921509jes

90. Orendorff CJ, Lamb J, Nagasubramanian G, Fenton KR, Langendorf JL. Through Materials Development Lithium - Ion Battery Safety Challenges. 2015.

91. Golubkov AW, Fuchs D, Wagner J, et al. Thermal-runaway experiments on consumer Li-ion batteries with metal-oxide and olivin-type cathodes. *RSC Adv*. 2014;4(7):3633-3642. doi:10.1039/c3ra45748f

92. Walker WQ, Darst JJ, Finegan DP, et al. Decoupling of heat generated from ejected and non-ejected contents of 18650-format lithium-ion cells using statistical methods. *J Power Sources*. 2019;415(January):207-218. doi:10.1016/j.jpowsour.2018.10.099

93. Finegan DP, Darcy E, Keyser M, et al. Characterising thermal runaway within lithium-ion cells by inducing and monitoring internal short circuits. *Energy Environ Sci*. 2017;10(6):1377-1388. doi:10.1039/c7ee00385d

94. Finegan DP, Darst JJ, Walker WQ, et al. Modelling and experiments to identify high-risk failure scenarios for testing the safety of lithium-ion cells. *J Power Sources*. 2019;417:29-41.

95. Finegan D, Scheel M, Robinson JB, et al. In-operando high-speed tomography of lithium-ion batteries during thermal runaway. *Nat Commun*. 2015;6(1):1-10. doi:10.1038/ncomms7924

96. Robinson JB, Darr JA, Eastwood DS, et al. Non-uniform temperature distribution in Li-ion batteries during discharge - A combined thermal imaging, X-ray micro-tomography and electrochemical impedance approach. *J Power Sources*. 2014;252:51-57. doi:10.1016/j.jpowsour.2013.11.059

97. Feng X, Fang M, He X, et al. Thermal runaway features of large format prismatic lithium ion battery using extended volume accelerating rate calorimetry. *J Power Sources*. 2014;255:294-301. doi:10.1016/j.jpowsour.2014.01.005

98. Feng X, Sun J, Ouyang M, et al. Characterization of penetration induced thermal runaway propagation process within a large format lithium ion battery module. *J Power Sources*. 2015. doi:10.1016/j.jpowsour.2014.11.017

99. Feng X, Sun J, Ouyang M, et al. Characterization of large format lithium ion battery exposed to extremely high temperature. *J Power Sources*. 2014. doi:10.1016/j.jpowsour.2014.08.094

100. Yokoshima T, Mukoyama D, Maeda F, et al. Direct observation of internal state of thermal runaway in lithium ion battery during nail-penetration test. *J Power Sources*. 2018;393:67-74. doi:10.1016/j.jpowsour.2018.04.092

101. Ruiz V, Pfrang A, Kriston A, Omar N, Van den Bossche P, Boon-Brett L. A review of international abuse testing standards and regulations for lithium ion batteries in electric and hybrid electric vehicles. *Renew Sustain Energy Rev*. 2018. doi:10.1016/j.rser.2017.05.195

102. Yang C, Ji X, Fan X, et al. Flexible Aqueous Li-Ion Battery with High Energy and Power Densities. *Adv Mater*. 2017. doi:10.1002/adma.201701972

103. Coman PT, Rayman S, White RE. A lumped model of venting during thermal runaway in a cylindrical Lithium Cobalt Oxide lithium-ion cell. *J Power Sources*. 2016. doi:10.1016/j.jpowsour.2015.12.088

104. Wang Q, Jiang B, Li B, Yan Y. A critical review of thermal management models and solutions of lithium-ion batteries for the development of pure electric vehicles. *Renew Sustain Energy Rev*. 2016. doi:10.1016/j.rser.2016.05.033

105. Liu H, Wei Z, He W, Zhao J. Thermal issues about Li-ion batteries and recent progress in battery thermal management systems: A review. *Energy Convers Manag*. 2017. doi:10.1016/j.enconman.2017.08.016

106. Abada S, Marlair G, Lecocq A, Petit M, Sauvant-Moynot V, Huet F. Safety focused modeling of lithium-ion batteries: A review. *J Power Sources*. 2016. doi:10.1016/j.jpowsour.2015.11.100

107. Sato N. Thermal behavior analysis of lithium-ion batteries for electric and hybrid vehicles. *J Power Sources*. 2001. doi:10.1016/S0378-7753(01)00478-5

108. Lamb J, Orendorff CJ. Evaluation of mechanical abuse techniques in lithium ion batteries. *J Power Sources*. 2014;247:189-196. doi:10.1016/j.jpowsour.2013.08.066

109. Zhang M, Du J, Liu L, et al. Internal Short Circuit Trigger Method for Lithium-Ion Battery

Based on Shape Memory Alloy. *J Electrochem Soc*. 2017;164(13):A3038-A3044. doi:10.1149/2.0731713jes

110. Orendorff CJ, Roth EP, Nagasubramanian G. Experimental triggers for internal short circuits in lithium-ion cells. *J Power Sources*. 2011;196(15):6554-6558. doi:10.1016/j.jpowsour.2011.03.035

111. Keyser M, Darcy E, Long D, Pesaran A. Passive Safety Device and Internal Short Tested Method for Energy Storage Cells and Systems. 2015:1-16. https://patentimages.storage.googleapis.com/0b/ce/a0/8ee68aaabbe10f/US9142829.pdf.

112. Darcy E, Darst JJ, Walker WQ, Finegan DP, Shearing PR. Design Guidelines for Safe , High Performing Li-ion Batteries with 18650 cells Applications and Motivation 5 Battery Design Guidelines Trading thermal isolation vs heat dissipation • Risk of side wall breaches during thermal runaway • Insights from cell c. In: *JRC Exploratory Research Workshop*. Petten, Netherlands; 2018. https://ec.europa.eu/jrc/sites/jrcsh/files/eric-darcy-nasa-lessons-learned-passive-thermal-runaway-propagation-resistant-designs-spacecraft-batteries.pdf.

113. Berdichevsky G, Kelty K, Straubel J, Toomre E. The Tesla Roadster Battery System. *Tesla Mot Inc*. 2007:1-5. doi:10.1109/VPPC.2007.4544139

114. Quinn JB, Waldmann T, Richter K, Kasper M, Wohlfahrt-Mehrens M. Energy Density of Cylindrical Li-Ion Cells: A Comparison of Commercial 18650 to the 21700 Cells. *J Electrochem Soc*. 2018. doi:10.1149/2.0281814jes

115. Sun J, Li J, Zhou T, et al. Toxicity, a serious concern of thermal runaway from commercial Li-ion battery. *Nano Energy*. 2016. doi:10.1016/j.nanoen.2016.06.031

116. Chen S, Wang Z, Yan W. Identification and characteristic analysis of powder ejected from a lithium ion battery during thermal runaway at elevated temperatures. *J Hazard Mater*. 2020. doi:10.1016/j.jhazmat.2020.123169

117. Zhang L, Duan Q, Meng X, et al. Experimental investigation on intermittent spray cooling and toxic hazards of lithium-ion battery thermal runaway. *Energy Convers Manag*. 2022. doi:10.1016/j.enconman.2021.115091

118. Kim GH, Pesaran A, Spotnitz R. A three-dimensional thermal abuse model for lithium-ion cells. *J Power Sources*. 2007. doi:10.1016/j.jpowsour.2007.04.018

119. Spotnitz R, Franklin J. Abuse behavior of high-power, lithium-ion cells. *J Power Sources*. 2003;113(1):81-100. doi:10.1016/S0378-7753(02)00488-3

120. Hatchard TD, MacNeil DD, Basu A, Dahn JR. Thermal Model of Cylindrical and Prismatic

Lithium-Ion Cells. *J Electrochem Soc*. 2001. doi:10.1149/1.1377592

121. Wang Q, Sun J, Yao X, Chen C. Thermal Behavior of Lithiated Graphite with Electrolyte in Lithium-Ion Batteries. *J Electrochem Soc*. 2006. doi:10.1149/1.2139955

122. Roth EP, Orendorff CJ. How electrolytes influence battery safety. *Electrochem Soc Interface*. 2012. doi:10.1149/2.F04122if

123. Golubkov A, Scheikl S, Planteu R, Voitic G, Thaler A, Hacker V. Thermal Runaway of a Commercial 18650 Li-Ion Battery with a NCA Cathode - Impact of SOC and Overcharge. *ECS Meet Abstr*. 2015. doi:10.1149/ma2015-03/2/555

124. Chen S, Wang Z, Wang J, Tong X, Yan W. Lower explosion limit of the vented gases from Li-ion batteries thermal runaway in high temperature condition. *J Loss Prev Process Ind*. 2020. doi:10.1016/j.jlp.2019.103992

125. Koch S, Fill A, Birke KP. Comprehensive gas analysis on large scale automotive lithium-ion cells in thermal runaway. *J Power Sources*. 2018. doi:10.1016/j.jpowsour.2018.07.051

126. Ribière P, Grugeon S, Morcrette M, Boyanov S, Laruelle S, Marlair G. Investigation on the fire-induced hazards of Li-ion battery cells by fire calorimetry. *Energy Environ Sci*. 2012. doi:10.1039/c1ee02218k

127. Pasquier A Du, Disma F, Bowmer T, Gozdz AS, Amatucci G, Tarascon J -M. Differential Scanning Calorimetry Study of the Reactivity of Carbon Anodes in Plastic Li-Ion Batteries. *J Electrochem Soc*. 1998. doi:10.1149/1.1838287

128. Onuki M, Kinoshita S, Sakata Y, et al. Identification of the Source of Evolved Gas in Li-Ion Batteries Using [sup 13]C-labeled Solvents. *J Electrochem Soc*. 2008. doi:10.1149/1.2969947

129. Richard MN, Dahn JR. Accelerating Rate Calorimetry Study on the Thermal Stability of Lithium Intercalated Graphite in Electrolyte. I. Experimental. *J Electrochem Soc*. 1999. doi:10.1149/1.1391893

130. Ohsaki T, Kishi T, Kuboki T, et al. Overcharge reaction of lithium-ion batteries. In: *Journal of Power Sources*. ; 2005. doi:10.1016/j.jpowsour.2005.03.105

131. Belharouak I, Lu W, Vissers D, Amine K. Safety characteristics of Li(Ni0.8Co0.15Al 0.05)O2 and Li(Ni1/3Co1/3Mn 1/3)O2. *Electrochem commun*. 2006. doi:10.1016/j.elecom.2005.12.007

132. Fu Y, Lu S, Li K, Liu C, Cheng X, Zhang H. An experimental study on burning behaviors of 18650 lithium ion batteries using a cone calorimeter. *J Power Sources*. 2015;273:216-222. doi:10.1016/j.jpowsour.2014.09.039

133. Zheng S, Wang L, Feng X, He X. Probing the heat sources during thermal runaway process by thermal analysis of different battery chemistries. *J Power Sources*. 2018;378:527-536. doi:10.1016/j.jpowsour.2017.12.050

134. Bandhauer TM, Garimella S, Fuller TF. A Critical Review of Thermal Issues in Lithium-Ion Batteries. *J Electrochem Soc*. 2011;158(3):R1. doi:10.1149/1.3515880

135. Feng X, Ren D, He X, Ouyang M. Mitigating Thermal Runaway of Lithium-Ion Batteries. *Joule*. 2020. doi:10.1016/j.joule.2020.02.010

136. Lyu P, Liu X, Qu J, et al. Recent advances of thermal safety of lithium ion battery for energy storage. *Energy Storage Mater*. 2020. doi:10.1016/j.ensm.2020.06.042

137. Pastor-Fernández C, Uddin K, Chouchelamane GH, Widanage WD, Marco J. A Comparison between Electrochemical Impedance Spectroscopy and Incremental Capacity-Differential Voltage as Li-ion Diagnostic Techniques to Identify and Quantify the Effects of Degradation Modes within Battery Management Systems. *J Power Sources*. 2017;360:301-318. doi:10.1016/j.jpowsour.2017.03.042

138. Hausbrand R, Cherkashinin G, Ehrenberg H, et al. Fundamental degradation mechanisms of layered oxide Li-ion battery cathode materials: Methodology, insights and novel approaches. *Mater Sci Eng B Solid-State Mater Adv Technol*. 2015;192:3-25. doi:10.1016/j.mseb.2014.11.014

139. Sharma N, Peterson VK, Elcombe MM, et al. Structural changes in a commercial lithium-ion battery during electrochemical cycling: An in situ neutron diffraction study. *J Power Sources*. 2010;195(24):8258-8266. doi:10.1016/j.jpowsour.2010.06.114

140. Waag W, Käbitz S, Sauer DU. Experimental investigation of the lithium-ion battery impedance characteristic at various conditions and aging states and its influence on the application. *Appl Energy*. 2013;102:885-897. doi:10.1016/j.apenergy.2012.09.030

141. Ren D, Feng X, Lu L, et al. An electrochemical-thermal coupled overcharge-to-thermal-runaway model for lithium ion battery. *J Power Sources*. 2017;364:328-340. doi:10.1016/j.jpowsour.2017.08.035

142. Yokoshima T, Mukoyama D, Maeda F, Osaka T, Takazawa K, Egusa S. Operando analysis of thermal runaway in lithium ion battery during nail-penetration test using an X-ray inspection system. *J Electrochem Soc*. 2019;166(6):A1243-A1250. doi:10.1149/2.0701906jes

143. Liao Z, Zhang S, Li K, Zhang G, Habetler TG. A survey of methods for monitoring and detecting thermal runaway of lithium-ion batteries. *J Power Sources*. 2019;436:226879.

doi:10.1016/j.jpowsour.2019.226879

144. Feng X, Zheng S, Ren D, et al. Investigating the thermal runaway mechanisms of lithium-ion batteries based on thermal analysis database. *Appl Energy*. 2019. doi:10.1016/j.apenergy.2019.04.009

145. Zhao R, Liu J, Gu J. Simulation and experimental study on lithium ion battery short circuit. *Appl Energy*. 2016. doi:10.1016/j.apenergy.2016.04.016

146. Finegan DP, Tjaden B, M. M. Heenan T, et al. Tracking Internal Temperature and Structural Dynamics during Nail Penetration of Lithium-Ion Cells. *J Electrochem Soc*. 2017;164(13):A3285-A3291. doi:10.1149/2.1501713jes

147. Finegan DP, Darcy E, Keyser M, et al. Identifying the Cause of Rupture of Li-Ion Batteries during Thermal Runaway. *Adv Sci*. 2018. doi:10.1002/advs.201700369

148. Wang Y, Cao G. Developments in nanostructured cathode materials for high-performance lithium-ion batteries. *Adv Mater*. 2008. doi:10.1002/adma.200702242

149. Xu B, Lee J, Kwon D, Kong L, Pecht M. Mitigation strategies for Li-ion battery thermal runaway: A review. *Renew Sustain Energy Rev*. 2021. doi:10.1016/j.rser.2021.111437

150. Chombo PV, Laoonual Y. A review of safety strategies of a Li-ion battery. *J Power Sources*. 2020. doi:10.1016/j.jpowsour.2020.228649

151. Liu K, Liu Y, Lin D, Pei A, Cui Y. Materials for lithium-ion battery safety. *Sci Adv*. 2018. doi:10.1126/sciadv.aas9820

152. Wu X, Song K, Zhang X, et al. Safety issues in lithium ion batteries: Materials and cell design. *Front Energy Res*. 2019. doi:10.3389/fenrg.2019.00065

153. Xu B, Kong L, Wen G, Pecht MG. Protection Devices in Commercial 18650 Lithium-Ion Batteries. *IEEE Access*. 2021. doi:10.1109/ACCESS.2021.3075972

154. Venugopal G. Characterization of thermal cut-off mechanisms in prismatic lithium-ion batteries. *J Power Sources*. 2001. doi:10.1016/S0378-7753(01)00782-0

155. Kaliaperumal M, Dharanendrakumar MS, Prasanna S, et al. Cause and mitigation of lithium-ion battery failure—a review. *Materials (Basel)*. 2021. doi:10.3390/ma14195676

156. Zeng Z, Murugesan V, Han KS, et al. Non-flammable electrolytes with high salt-to-solvent ratios for Li-ion and Li-metal batteries. *Nat Energy*. 2018. doi:10.1038/s41560-018-0196-y

157. Chawla N, Bharti N, Singh S. Recent advances in non-flammable electrolytes for safer lithium-ion batteries. *Batteries*. 2019. doi:10.3390/batteries5010019

158. Ding J, Tian T, Meng Q, et al. Smart multifunctional fluids for lithium ion batteries: Enhanced rate performance and intrinsic mechanical protection. *Sci Rep*. 2013. doi:10.1038/srep02485

159. Hyung YE, Vissers DR, Amine K. Flame-retardant additives for lithium-ion batteries. In: *Journal of Power Sources*. ; 2003. doi:10.1016/S0378-7753(03)00225-8

160. Shi Y, Noelle DJ, Wang M, et al. Mitigating thermal runaway of lithium-ion battery through electrolyte displacement. *Appl Phys Lett*. 2017. doi:10.1063/1.4975653

161. Shi C, Dai J, Shen X, et al. A high-temperature stable ceramic-coated separator prepared with polyimide binder/Al2O3 particles for lithium-ion batteries. *J Memb Sci*. 2016. doi:10.1016/j.memsci.2016.06.035

162. Jiang X, Zhu X, Ai X, Yang H, Cao Y. Novel Ceramic-Grafted Separator with Highly Thermal Stability for Safe Lithium-Ion Batteries. *ACS Appl Mater Interfaces*. 2017. doi:10.1021/acsami.7b05535

163. Liu K, Liu W, Qiu Y, et al. Electrospun core-shell microfiber separator with thermal-triggered flame-retardant properties for lithium-ion batteries. *Sci Adv*. 2017. doi:10.1126/sciadv.1601978

164. Liu X, Ren D, Hsu H, et al. Thermal Runaway of Lithium-Ion Batteries without Internal Short Circuit. *Joule*. 2018. doi:10.1016/j.joule.2018.06.015

165. Baginska M, Blaiszik BJ, Merriman RJ, Sottos NR, Moore JS, White SR. Autonomic shutdown of Lithium-ion batteries using thermoresponsive microspheres. *Adv Energy Mater*. 2012. doi:10.1002/aenm.201100683

166. Kang SM, Ryou MH, Choi JW, Lee H. Mussel- and diatom-inspired silica coating on separators yields improved power and safety in Li-ion batteries. *Chem Mater*. 2012. doi:10.1021/cm301967f

167. Park JH, Cho JH, Park W, et al. Close-packed SiO2/poly(methyl methacrylate) binary nanoparticles-coated polyethylene separators for lithium-ion batteries. *J Power Sources*. 2010. doi:10.1016/j.jpowsour.2010.06.112

168. Lin CC, Wu HC, Pan JP, et al. Investigation on suppressed thermal runaway of Li-ion battery by hyper-branched polymer coated on cathode. *Electrochim Acta*. 2013. doi:10.1016/j.electacta.2012.09.097

169. Chen Z, Hsu PC, Lopez J, et al. Fast and reversible thermoresponsive polymer switching materials for safer batteries. *Nat Energy*. 2016. doi:10.1038/nenergy.2015.9

170. Balakrishnan PG, Ramesh R, Prem Kumar T. Safety mechanisms in lithium-ion batteries. *J Power Sources*. 2006. doi:10.1016/j.jpowsour.2005.12.002

171. Feng XM, Ai XP, Yang HX. A positive-temperature-coefficient electrode with thermal cut-off mechanism for use in rechargeable lithium batteries. *Electrochem commun*. 2004. doi:10.1016/j.elecom.2004.07.021

172. Amine K. Batteries: Polymers switch for safety. *Nat Energy*. 2016. doi:10.1038/nenergy.2015.18

173. Zhang SS. A review on the separators of liquid electrolyte Li-ion batteries. *J Power Sources*. 2007;164(1):351-364. doi:10.1016/j.jpowsour.2006.10.065

174. Roth EP, Doughty DH, Pile DL. Effects of separator breakdown on abuse response of 18650 Li-ion cells. *J Power Sources*. 2007. doi:10.1016/j.jpowsour.2007.06.163

175. Lee H, Yanilmaz M, Toprakci O, Fu K, Zhang X. A review of recent developments in membrane separators for rechargeable lithium-ion batteries. *Energy Environ Sci*. 2014. doi:10.1039/c4ee01432d

176. Zhu Y, Wang F, Liu L, Xiao S, Chang Z, Wu Y. Composite of a nonwoven fabric with poly(vinylidene fluoride) as a gel membrane of high safety for lithium ion battery. *Energy Environ Sci*. 2013. doi:10.1039/c2ee23564a

177. Finegan DP, Cooper SJ, Tjaden B, et al. Characterising the structural properties of polymer separators for lithium-ion batteries in 3D using phase contrast X-ray microscopy. *J Power Sources*. 2016. doi:10.1016/j.jpowsour.2016.09.132

178. Choi JA, Kim SH, Kim DW. Enhancement of thermal stability and cycling performance in lithium-ion cells through the use of ceramic-coated separators. *J Power Sources*. 2010. doi:10.1016/j.jpowsour.2009.11.020

179. Shi C, Zhang P, Chen L, Yang P, Zhao J. Effect of a thin ceramic-coating layer on thermal and electrochemical properties of polyethylene separator for lithium-ion batteries. *J Power Sources*. 2014. doi:10.1016/j.jpowsour.2014.07.142

180. Orendorff CJ, Lambert TN, Chavez CA, Bencomo M, Fenton KR. Polyester separators for lithium-ion cells: Improving thermal stability and abuse tolerance. *Adv Energy Mater*. 2013. doi:10.1002/aenm.201200292

181. Röntgen WC. Ueber eine neue Art von Strahlen. *Ann Phys*. 1898;300(1):12-17. http://www.xtal.iqfr.csic.es/Cristalografia/archivos_10/Uber_eine_neue_art_von_strahlen_ocr.pdf.

182. Diamond Light Source Ltd. Diamond Light Source: About Synchrotrons. Diamon Light Source. https://www.diamond.ac.uk/Home/About/FAQs/About-Synchrotrons.html. Published 2018.

183. Chantler C, Olsen K, Dragoset R. X-ray form factor, attenuation and scattering tables (version 2.1). National Institute of Standards and Technology.

184. National Institute of Standards and Technology. X-Ray mass attenuation coefficients. *May 19, 2015*. 1994.

185. Zhao Z, Gang GJ, Siewerdsen JH. Noise, sampling, and the number of projections in cone-beam CT with a flat-panel detector. *Med Phys*. 2014. doi:10.1118/1.4875688

186. Hsieh J, Molthen RC, Dawson CA, Johnson RH. An iterative approach to the beam hardening correction in cone beam CT. *Med Phys*. 2000. doi:10.1118/1.598853

187. Hsieh J. Adaptive streak artifact reduction in computed tomography resulting from excessive x-ray photon noise. *Med Phys*. 1998. doi:10.1118/1.598410

188. F Edward B, Dominik F. CT artefacts: Causes and reduction techniques. *Imaging Med*. 2012. doi:10.2217/iim.12.13

189. Banhart J. *Advanced Tomographic Methods in Materials Research and Engineering*.; 2008. doi:10.1093/acprof:oso/9780199213245.001.0001

190. Hsieh J. *Computed Tomography: Principles, Design, Artifacts, and Recent Advances*.; 2015. doi:10.1117/3.2197756

191. Ozcan A, Bilenca A, Desjardins AE, Bouma BE, Tearney GJ. Speckle reduction in optical coherence tomography images using digital filtering. *J Opt Soc Am A*. 2007. doi:10.1364/JOSAA.24.001901

192. Copley RJ, Cumming D, Wu Y, Dwyer-Joyce RS. Measurements and modelling of the response of an ultrasonic pulse to a lithium-ion battery as a precursor for state of charge estimation. *J Energy Storage*. 2021. doi:10.1016/j.est.2021.102406

193. Hsieh AG, Bhadra S, Hertzberg BJ, et al. Electrochemical-acoustic time of flight: In operando correlation of physical dynamics with battery charge and health. *Energy Environ Sci*. 2015. doi:10.1039/c5ee00111k

194. Robinson JB, Maier M, Alster G, et al. Spatially resolved ultrasound diagnostics of Li-ion battery electrodes. *Phys Chem Chem Phys*. 2019. doi:10.1039/c8cp07098a

195. Davies G, Knehr KW, Van Tassell B, et al. State of Charge and State of Health Estimation Using Electrochemical Acoustic Time of Flight Analysis. *J Electrochem Soc*. 2017. doi:10.1016/j.amjcard.2005.12.032

196. Chang W, Steingart D. Operando 2D Acoustic Characterization of Lithium-Ion Battery Spatial

Dynamics. *ACS Energy Lett*. 2021. doi:10.1021/acsenergylett.1c01324

197. Bommier C, Chang W, Lu Y, et al. In Operando Acoustic Detection of Lithium Metal Plating in Commercial LiCoO2/Graphite Pouch Cells. *Cell Reports Phys Sci*. 2020. doi:10.1016/j.xcrp.2020.100035

198. Owen RE, Robinson JB, Weaving JS, et al. Operando Ultrasonic Monitoring of Lithium-Ion Battery Temperature and Behaviour at Different Cycling Rates and under Drive Cycle Conditions. *J Electrochem Soc*. 2022;169(4):040563. doi:10.1149/1945-7111/ac6833

199. Ladpli P, Kopsaftopoulos F, Chang FK. Estimating state of charge and health of lithium-ion batteries with guided waves using built-in piezoelectric sensors/actuators. *J Power Sources*. 2018. doi:10.1016/j.jpowsour.2018.02.056

200. Gold L, Bach T, Virsik W, et al. Probing lithium-ion batteries' state-of-charge using ultrasonic transmission – Concept and laboratory testing. *J Power Sources*. 2017. doi:10.1016/j.jpowsour.2017.01.090

201. Chou YS, Hsu NY, Jeng KT, Chen KH, Yen SC. A novel ultrasonic velocity sensing approach to monitoring state of charge of vanadium redox flow battery. *Appl Energy*. 2016. doi:10.1016/j.apenergy.2016.08.125

202. Maier M, Owen RE, Pham MTM, et al. Acoustic time-of-flight imaging of polymer electrolyte membrane water electrolysers to probe internal structure and flow characteristics. *Int J Hydrogen Energy*. 2021. doi:10.1016/j.ijhydene.2021.01.077

203. Majasan JO, Robinson JB, Owen RE, et al. Recent advances in acoustic diagnostics for electrochemical power systems. *JPhys Energy*. 2021. doi:10.1088/2515-7655/abfb4a

204. Michael H, Owen RE, Robinson JB, et al. Correlative Electrochemical Acoustic Time-of-Flight Spectroscopy and X-Ray Imaging to Monitor the Performance of Single-Crystal and Polycrystalline Nmc811/Gr Lithium-Ion Batteries. *SSRN Electron J*. 2022. doi:10.2139/ssrn.4041325

205. Robinson JB, Pham M, Kok MDR, Heenan TMM, Brett DJL, Shearing PR. Examining the Cycling Behaviour of Li-Ion Batteries Using Ultrasonic Time-of-Flight Measurements. *J Power Sources*. 2019;444. doi:10.1016/j.jpowsour.2019.227318

206. Steingart DA. Nodeforwarder. GitHub. https://github.com/dansteingart/nodeforwarder. Published 2018.

207. Drakopoulos M, Connolley T, Reinhard C, et al. I12: The Joint Engineering, Environment and Processing (JEEP) beamline at Diamond Light Source. *J Synchrotron Radiat*. 2015.

doi:10.1107/S1600577515003513

208. Pham MTM, Darst JJ, Finegan DP, et al. Correlative acoustic time-of-flight spectroscopy and X-ray imaging to investigate gas-induced delamination in lithium-ion pouch cells during thermal runaway. *J Power Sources*. 2020;470:228039. doi:10.1016/j.jpowsour.2020.228039

209. Hatchard TD, Trussler S, Dahn JR. Building a "smart nail" for penetration tests on Li-ion cells. *J Power Sources*. 2014;247:821-823. doi:10.1016/j.jpowsour.2013.09.022

210. Hendricks C, Williard N, Mathew S, Pecht M. A failure modes, mechanisms, and effects analysis (FMMEA) of lithium-ion batteries. *J Power Sources*. 2015;297:113-120. doi:10.1016/j.jpowsour.2015.07.100

211. Spielbauer M, Berg P, Ringat M, Bohlen O, Jossen A. Experimental study of the impedance behavior of 18650 lithium-ion battery cells under deforming mechanical abuse. *J Energy Storage*. 2019;26:101039. doi:10.1016/j.est.2019.101039

212. Chiu KC, Lin CH, Yeh SF, Lin YH, Chen KC. An electrochemical modeling of lithium-ion battery nail penetration. *J Power Sources*. 2014;251:254-263. doi:10.1016/j.jpowsour.2013.11.069

213. Mao B, Chen H, Cui Z, Wu T, Wang Q. Failure mechanism of the lithium ion battery during nail penetration. *Int J Heat Mass Transf*. 2018;122:1103-1115. doi:10.1016/j.ijheatmasstransfer.2018.02.036

214. Li Y, Pu H. Facile fabrication of multilayer separators for lithium-ion battery via multilayer coextrusion and thermal induced phase separation. *J Power Sources*. 2018;384:408-416. doi:10.1016/j.jpowsour.2018.02.086

215. Lagadec MF, Zahn R, Wood V. Characterization and performance evaluation of lithium-ion battery separators. *Nat Energy*. 2019. doi:10.1038/s41560-018-0295-9

216. Gelb J, Finegan DP, Brett DJL, Shearing PR. Multi-scale 3D investigations of a commercial 18650 Li-ion battery with correlative electron- and X-ray microscopy. *J Power Sources*. 2017;357:77-86. doi:10.1016/j.jpowsour.2017.04.102

217. Merkle AP, Gelb J. The Ascent of 3D X-ray Microscopy in the Laboratory. *Micros Today*. 2013;21(2):10-15. doi:10.1017/s1551929513000060

218. Feser M, Gelb J, Chang H, et al. Sub-micron resolution CT for failure analysis and process development. *Meas Sci Technol*. 2008;19(9):094001. doi:10.1088/0957-0233/19/9/094001

219. Burnett TL, McDonald SA, Gholinia A, et al. Correlative tomography. *Sci Rep*. 2014;4:4711. doi:10.1038/srep04711

220. Pham MTM, Darst JJ, Walker WQ, et al. Prevention of lithium-ion battery thermal runaway using polymer-substrate current collectors. *Cell Reports Phys Sci*. 2021. doi:10.1016/j.xcrp.2021.100360

221. Martinez-Cisneros C, Antonelli C, Levenfeld B, et al. Non-woven polyaramid porous membranes as separators for Li-ion batteries? *Electrochim Acta*. 2021. doi:10.1016/j.electacta.2021.138835

222. Deng Y, Pan Y, Zhang Z, et al. Novel Thermotolerant and Flexible Polyimide Aerogel Separator Achieving Advanced Lithium-Ion Batteries. *Adv Funct Mater*. 2022. doi:10.1002/adfm.202106176

223. Morin B, Hennessy J, Arora P. Developments in nonwovens as specialist membranes in batteries and supercapacitors. In: *Advances in Technical Nonwovens*. ; 2016. doi:10.1016/B978-0-08-100575-0.00011-5

224. Morin B, Hu C, Khokhlov P, Kaschmitter J, Cho S-J. Safety Testing with Nonwoven Nanofiber Separators: Comparing Shutdown Separators to Thermally Stable Separators. *ECS Trans*. 2016. doi:10.1149/07212.0001ecst

225. Hou J, Feng X, Wang L, et al. Unlocking the self-supported thermal runaway of high-energy lithium-ion batteries. *Energy Storage Mater*. 2021. doi:10.1016/j.ensm.2021.04.035

226. Abraham DP, Roth EP, Kostecki R, McCarthy K, MacLaren S, Doughty DH. Diagnostic examination of thermally abused high-power lithium-ion cells. *J Power Sources*. 2006. doi:10.1016/j.jpowsour.2006.04.088

227. Keyser M, Darcy E. NREL / NASA Internal Short-Circuit Instigator in Lithium Ion Cells. In: *JRC Lithium Ion Safety Workshop*. Petten, Netherlands; 2018:1-33. https://www.rechargebatteries.org/wp-content/uploads/2018/12/2-Initiation-presentation-MDBTC_matthew_keyser-nrel-nasa_internal_short_circuit_instigator_in_lithium_ion_cells_03_2018.pdf.

228. Hein S, Danner T, Westhoff D, et al. Influence of Conductive Additives and Binder on the Impedance of Lithium-Ion Battery Electrodes: Effect of Morphology. *J Electrochem Soc*. 2020. doi:10.1149/1945-7111/ab6b1d

229. Amin R, Chiang Y-M. Characterization of Electronic and Ionic Transport in Li 1- x Ni 0.33 Mn 0.33 Co 0.33 O 2 (NMC 333) and Li 1- x Ni 0.50 Mn 0.20 Co 0.30 O 2 (NMC 523) as a Function of Li Content . *J Electrochem Soc*. 2016. doi:10.1149/2.0131608jes

230. Du Z, Li J, Wood M, Mao C, Daniel C, Wood DL. Three-dimensional conductive network

formed by carbon nanotubes in aqueous processed NMC electrode. *Electrochim Acta*. 2018. doi:10.1016/j.electacta.2018.03.063

231. Wang M, Le A V., Shi Y, Noelle DJ, Qiao Y. Heterogeneous current collector in lithium-ion battery for thermal-runaway mitigation. *Appl Phys Lett*. 2017. doi:10.1063/1.4975799

232. Asenbauer J, Eisenmann T, Kuenzel M, Kazzazi A, Chen Z, Bresser D. The success story of graphite as a lithium-ion anode material-fundamentals, remaining challenges, and recent developments including silicon (oxide) composites. *Sustain Energy Fuels*. 2020. doi:10.1039/d0se00175a

233. Keyser M, Long D, Ireland J, et al. Emulating internal short circuit in lithium ion cells for understanding abuse behavior. In: *AABC 2014 - Advanced Automotive Battery Confernce, AABTAM Symposium - Advanced Automotive Battery Technology, Application and Market, AABTAM 2014*. ; 2014.

234. Darcy E, Keyser M, Long D, Jung YS, Kim G, Pesaran A. On-Demand Internal Short Circuit Device. In: *2010 NASA Aerospace Battery Workshop*. ; 2010.

235. Santhanagopalan S, Ramadass P, Zhang J (Zhengming). Analysis of internal short-circuit in a lithium ion cell. *J Power Sources*. 2009. doi:10.1016/j.jpowsour.2009.05.002

236. Dorner F, Sukurma Z, Dellago C, Kresse G. Melting Si: Beyond Density Functional Theory. *Phys Rev Lett*. 2018. doi:10.1103/PhysRevLett.121.195701

10 Appendix

10.1.1 Supplementary Video 1

Radiography video of Figure 4-2: Radiographs depicting the expansion of the pouch cell layers, with the horizontal bright-line being the centre of cone-beam with no incident angle

10.1.2 Supplementary Video 2

Radiography video of Figure 4-5 observing thermal runaway of a lithium-ion pouch cell imaged at synchrotron.

10.1.3 Supplementary Material

Supplementary material information for material properties of the PCCs.

10.1.4 Supplementary Video 3

High speed X-ray radiography of Cell G4-01 undergoing nail penetration where thermal runaway is observed. The G4 cell group contains commercial Al and Cu current collectors.

10.1.5 Supplementary Video 4

High speed X-ray radiography of Cell G1-01 underdoing nail penetration where thermal runaway was prevented. The G1 cell group contains the Al polymer current collector and commercial Cu current collector.

10.1.6 TSS data sheet

Dreamweaver Gold separator information.